



HAL
open science

The contribution of the grain boundary engineering to the problem of intergranular hydrogen embrittlement

Jiaqi Li

► **To cite this version:**

Jiaqi Li. The contribution of the grain boundary engineering to the problem of intergranular hydrogen embrittlement. Materials. Université de La Rochelle, 2017. English. NNT : 2017LAROS037 . tel-01941726

HAL Id: tel-01941726

<https://theses.hal.science/tel-01941726>

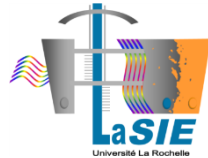
Submitted on 2 Dec 2018

HAL is a multi-disciplinary open access archive for the deposit and dissemination of scientific research documents, whether they are published or not. The documents may come from teaching and research institutions in France or abroad, or from public or private research centers.

L'archive ouverte pluridisciplinaire **HAL**, est destinée au dépôt et à la diffusion de documents scientifiques de niveau recherche, publiés ou non, émanant des établissements d'enseignement et de recherche français ou étrangers, des laboratoires publics ou privés.



Université de La Rochelle



Laboratoire des Sciences de
l'Ingénieur pour l'Environnement



UMR 7356

ÉCOLE DOCTORALE
SI-MMEA

Laboratoire des Sciences de l'Ingénieur pour l'Environnement

THÈSE

Présenté par :

Jiaqi LI

Soutenue le **20 décembre 2017**

Pour l'obtention du grade de Docteur de l'Université de La Rochelle

Discipline : *Science et Génie des Matériaux*

**Apport de l'ingénierie du joint de grain dans la problématique de
la fragilisation par l'hydrogène de nature inter-granulaire**

**The contribution of the grain boundary engineering to the
problem of intergranular hydrogen embrittlement**

Jury

| | | |
|------------------|---|------------------------|
| Yann CHARLES | MCF-HDR, LSPM, Université Paris 13 | Rapporteur |
| Afroz BARNOSH | Professor, NTNU, Norway | Rapporteur |
| Jun SONG | Assistant Professor, McGill University, Canada | Examinateur |
| Michel PEREZ | Professeur, Université de Lyon – INSA Lyon | Examinateur |
| Véronique DOQUET | Directrice de recherche, LMS, Ecole Polytechnique | Examinatrice |
| Arnaud METSUE | MCF, LaSIE, Université de La Rochelle | Examinateur |
| Abdelali OUDRISS | MCF, LaSIE, Université de La Rochelle | Invité |
| Jamaa BOUHATTATE | MCF-HDR, LaSIE, Université de La Rochelle | Co-Directrice de thèse |
| Xavier FEAUGAS | Professeur, LaSIE, Université de La Rochelle | Co-Directeur de thèse |

Acknowledgement

First of all, I would like to express my deepest and sincere gratitude to my advisors Xavier Feaugas and Jamaa Bouhattate, who supervised my work with continuous encouragement and support. Our scientific and non-scientific discussions always gave me new discoveries and reflections. It is really inspiring and rewarding to work with you. Xavier, thanks for your patience, motivation, and immense knowledge.

Furthermore, I want to thank all the committee members Dr. Véronique Doquet, Pr. Michel Perez, and particularly Dr. Yann Charles and Pr. Afroz Barnoush who accepted to review this thesis and contributed to its improvement. I would like to express my gratitude to Dr. Jun Song who joined the video dissertation in the wee hours of the morning.

I would like to thank Arnaud Metsue and Abdelmalek Hallil, whose support helped me a lot in the atomic scale calculations. Your scientific rigor and advice contributed so much to the improvement of this thesis.

I also especially want to thank Abdelali Oudriss and Remy Milet who were most closely involved in the experimental tests. It was a great time working on the electrochemical permeation, we spent many long but unforgettable hours together during the tests.

A very special thanks to Esaie Legrand and Bachir Osman-Hoch, who were always available spontaneous cooperativeness. You made FEM easier for me, it has been a pleasure working with you guys.

Special thanks to Sylvie Lartigue-Korinek and Louissette Priester for valuable explanations of grain boundary aspects and support of bi crystals with HRTEM.

I had a wonderful time in La Rochelle and I would like to thank all the colleagues and friends for their kindness. Thanks Martine, Isabelle(s), Jennifer, Camille for their administrative supports. I would like to thank Bruno, Stephane, Christelle, Cyril, Catherine, Stephanie, Juan, and Egle for their efficient help. I give my special thanks to the past and present PhD students, Ben, Germain, Daniela, Mat(t)hieu, Pierre(s), Rym, Yves, Niusha, Felana, Coralie, Clara, Milena and the others. Quoting all of you would be too long, but I had unforgettable moments with you in the Lab.

Finally, I must express my very profound gratitude to my parents for providing me with unfailing support and continuous encouragement throughout my years of study and through the process of researching and writing this thesis.

Content

| | |
|--|----|
| General introduction | 8 |
| Chapter 1. Literature Review | 12 |
| I. Hydrogen – metal and hydrogen embrittlement | 15 |
| I.1 Hydrogen-metal interactions | 15 |
| I.2 Hydrogen embrittlement | 15 |
| I.2.1 Hydrogen - hydride..... | 16 |
| I.2.2 Hydrogen - decohesion | 17 |
| I.2.3 Hydrogen - dislocation | 18 |
| I.2.4 Hydrogen - vacancy | 20 |
| I.2.5 Hydrogen – defactant..... | 21 |
| II. Hydrogen in Ni single crystals | 22 |
| II.1 Solubility..... | 23 |
| II.2 Diffusivity..... | 26 |
| III. Grain boundaries in metals | 30 |
| III.1 Grain boundaries (GBs) | 30 |
| III.1.1 Geometry..... | 30 |
| III.1.2 Classifications of grain boundaries..... | 31 |
| III.2 Free volume of grain boundary | 34 |
| III.3 Grain boundary energy | 35 |
| III.4 Defects in grain boundary | 40 |
| IV. Hydrogen in GBs-Intergranular segregation and diffusion | 44 |
| IV.1 Grain boundary segregation | 45 |
| IV.1.1 Driving force of segregation..... | 45 |
| IV.1.2 Experiments of segregation in polycrystals | 46 |
| IV.1.3 Atomic approaches of segregation in GBs | 48 |
| IV.2 Grain boundary diffusion | 53 |
| IV.2.1 Grain boundary diffusion model | 53 |
| IV.2.2 Experiments of GB diffusion in polycrystals | 57 |
| IV.2.3 Atomic approaches of GB diffusion | 58 |
| V. Summary | 61 |
| Chapter 2. Materials and methods | 62 |
| I. Materials and metallurgical characterization | 64 |
| I.1 Nickel single crystals..... | 64 |

| | |
|--|------------|
| I.2 Nickel bi crystals | 65 |
| II. Experimental and numerical methods | 67 |
| II.1 Experimental approaches..... | 67 |
| II.1.1 Hydrogen charging – thermal desorption spectroscopy (TDS) | 67 |
| II.1.2 Electrochemical permeation (EP)..... | 70 |
| II.2 Numerical approaches | 74 |
| II.2.1 Finite element method (FEM) | 74 |
| II.2.1.1 2D hydrogen transport models | 76 |
| II.2.1.2 3D hydrogen transport models | 77 |
| II.2.2 Atomic Simulation | 79 |
| III. Overview | 84 |
| Chapter 3. Impact of crystallographic orientation on the hydrogen transport | 86 |
| Chapter 3a. Hydrogen charging in nickel | 88 |
| I. Identification of the hydrogen charging conditions | 88 |
| I.1 Electrochemical kinetic model | 89 |
| I.1.1 Steady state | 91 |
| I.1.2 Thermodynamics | 96 |
| II. Equivalence conversion: Over potential – fugacity | 99 |
| Chapter 3b. Hydrogen in nickel single crystals | 105 |
| I. Hydrogen segregation and diffusion in Ni <001> | 105 |
| I.1 Hydrogen solubility in nickel <001> | 105 |
| I.2 Hydrogen diffusivity in nickel <001> | 110 |
| II. Orientations <100>, <110>, <219> and <111>..... | 111 |
| II.1 Anisotropic diffusion | 111 |
| II.2 Influence of self-stress on the diffusion process | 113 |
| II.2.1 Description of diffusion in the solids..... | 114 |
| II.2.1.1 Volume variation with the presence of a solute..... | 115 |
| II.2.1.2 Atomic and volume expansion | 116 |
| II.2.1.3 Strain state near the solute | 117 |
| II.2.1.4 Hydrogen flux and the apparent diffusion coefficient..... | 118 |
| II.2.1.5 In a solid with anisotropic elasticity properties | 119 |
| II.2.2 Confrontation of the thermodynamic approach with experimental data..... | 122 |
| III. Conclusions | 131 |

| | |
|--|-----|
| Chapter 4. Role of grain boundary character on the hydrogen segregation and diffusion | 133 |
| I. Grain boundaries structure | 136 |
| II. Hydrogen segregation states | 140 |
| II.1 Segregation energy..... | 140 |
| II.2 Stress states and hydrogen segregation | 146 |
| II.3 Segregation concentration | 150 |
| III. Hydrogen diffusion in GBs –atomic approach | 155 |
| IV. Experimental approaches | 161 |
| IV. 1 Hydrogen - twin boundaries in nickel polycrystals | 162 |
| IV. 2 Hydrogen - GBs in nickel bi crystals | 164 |
| IV. 3 FEM approaches..... | 167 |
| IV. 3.1 Pure diffusion | 167 |
| IV. 3.2 Stress near GB | 171 |
| V. Summary | 177 |
| Chapter 5. Conclusions and perspectives | 179 |
| Appendix | 187 |
| Appendix 2.1 EBSD and surface preparation | 188 |
| Appendix 2.2 TEM and sample preparation..... | 190 |
| Appendix 3.1 Diffusion tensor..... | 194 |
| Appendix 3.2 Sphere inclusion – Eshelby’s solution | 195 |
| Appendix 3.3 Solution for the static displacement waves..... | 196 |
| Appendix 3.4 Anisotropy of elasticity | 198 |
| Appendix 4.1 Hydrogen atom details at the segregation sites | 200 |
| Reference | 202 |

General introduction

Climate change and the coming energy crisis are definitely today's main social problems. The world's economically available supply of hydrocarbon resources is limited and the demand for hydrocarbon fuels is increasing for developing countries. Another problem related to the fuel consumption is the pollution of the environment, especially with the greenhouse-gas. Hydrogen as a potential substitutional fuel is one of the main technologies for research. This "hydrogen economy" is considered as a substitute to solve some of the negative effects of "hydrocarbon economy". However, there are still some challenges for applications of hydrogen such as production, storage, and infrastructure. Moreover, finding adaptable materials for applications of hydrogen is a major challenge for scientists and engineers.

The first challenge comes from the hydrogen itself, the hydrogen detection is difficult especially when the hydrogen distribution and the evolution with the time are appreciated. This is due to its small size and lightweight, moreover, the hydrogen atom presents the high mobility and low solubility in metals and alloys. Generally, experimental methods can provide information by indirectly analyzing or by conducting measurements with radioactive isotopes of hydrogen (deuterium and tritium). In order to get a complementary understanding of hydrogen's behavior, it is necessary to utilize numerical models which can simulate hydrogen in metals and its interactions.

Actually, with hydrogen's small size, it can easily penetrate and segregate in most metals, leading to a degradation of materials' mechanical properties, the effects of hydrogen on the ductility, toughness, and tensile strength are significant, and the performance and lifetime of materials are thus reduced with the presence of hydrogen. This phenomenon was first described in 1875 by Johnson [**Johnson 1875**], known as hydrogen embrittlement (HE). In his publication, the phenomenon was defined as:

"This change is at once made evident to anyone by the extraordinary decrease in toughness and breaking strain of the iron so treated, and is all the more remarkable as it is not permanent, but only temporary in character, for with lapse of time the metal slowly regains its original toughness and strength."

After 140 years of research, material scientists have had much success on the understanding of HE. This phenomenon results from a combination of different parameters related to the material characteristics, the source of the hydrogen (internal or external) and to the mechanical solicitations, as illustrated in *figure 1*. This type of corrosion is a process resulting in a decrease of the toughness or ductility of a metal due to the presence of atomic hydrogen. Most theories supported that HE initiated the process of hydrogen diffusion and segregation in the materials, this early stage of embrittlement is

strongly influenced by microstructural defects such as grain boundaries, precipitates, dislocations or vacancies.

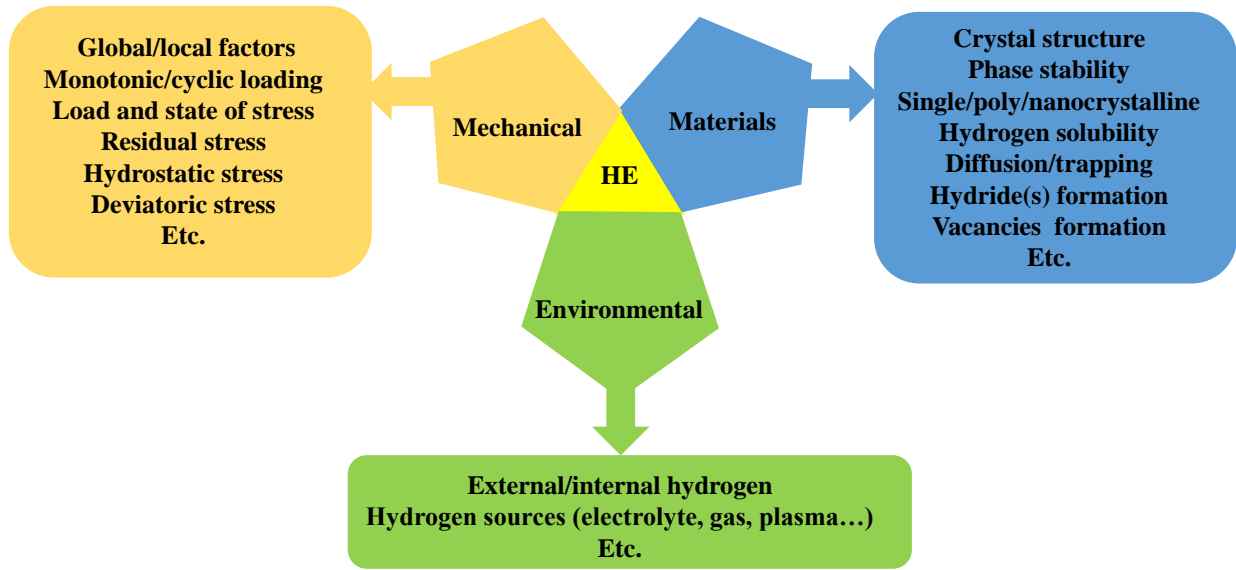


Figure 1 – Hydrogen embrittlement with three interaction factors.

Despite many achievements, there are still a lot of controversy among the influence of these defects, a more comprehensive understanding requires more research at different scales. With the rapid development of technology, especially the evolution of computer tools, HE has been widely studied at different scales as showed in *figure.2*.

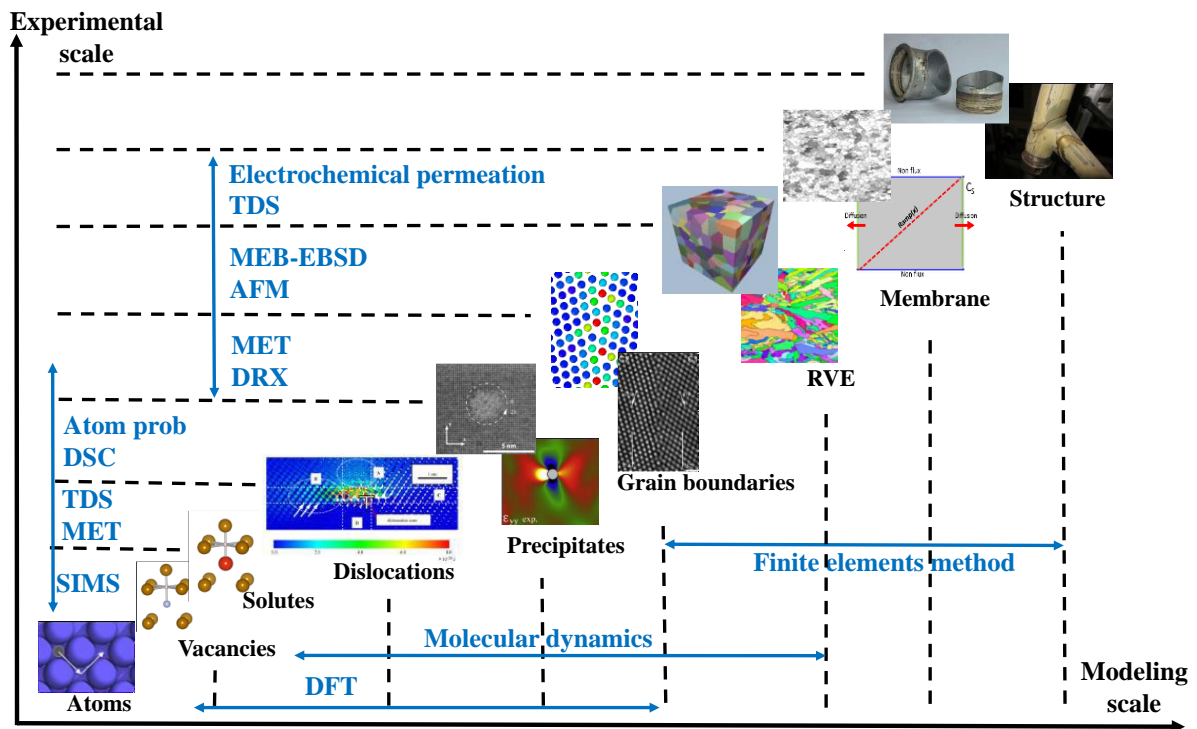


Figure 2 – Experimental and numerical methods at different scales

The analysis of HE is complex since all phenomena of all scales are linked altogether. For a more realistic approach, considering the early stage of HE in the materials, the mobility of hydrogen is a key parameter for understanding the mechanisms of diffusion and trapping of hydrogen within a crystal lattice. These mechanisms depend on the various microstructural heterogeneities and in particular the crystalline defects. The idea of this study is to investigate the hydrogen mobility within a material separately, the first step concerns the investigation of hydrogen behavior in a relative perfect crystal lattice, and later the contribution of crystalline defects such as grain boundaries on the hydrogen mobility. Moreover, the nature of grain boundaries presents different characters, it is appreciated to understand the hydrogen interactions with different types of grain boundaries. We have focused thus in this work on the diffusion and trapping of hydrogen in two elementary systems: single crystals (crystal lattice) and bi-crystals (different grain boundaries). The investigation material is nickel due to the high diffusivity of hydrogen in nickel, and particularly the absence of polymorphism have enabled both thermodynamic and kinetic data to be obtained in a large temperature range. There are many available experimental and numerical data for nickel in the literature and this material is well mastered in our laboratory. In this study, the hydrogen mobility in nickel has been investigated using a methodology combining experimental tools (electrochemical permeation / TDS, TEM/HRTEM, EBSD) and numerical methods (FEM-COMSOL / EAM-LAMMPS).

This manuscript consists of 5 chapters:

The first chapter is aimed at providing a literature review of experimental and numerical studies on the hydrogen transport in single/poly crystalline materials. A brief overview of HE mechanisms are presented which are directly linked to the microstructural defects, the interactions of hydrogen with these defects in metal are discussed with supports of the numerical and experimental evidences. A comparison between the single and poly crystalline fcc materials highlights the influences of grain boundaries on the hydrogen transport concerning the acceleration of diffusion and the hydrogen trapping. This literature study focus thus more on the grain boundaries and their interactions with hydrogen from theoretical and experimental aspects.

Then, we present in the second chapter all samples studied in this work and their microstructural characterizations. The experimental tools (EP, TDS, TEM...) are presented in details with their principles, and in particular the experiment conditions for the collected experimental data. Numerical simulations (FEM and MD) are also presented with different simulation models in details.

The experimental and numerical studies on the nickel single crystals are presented in the third chapter. The first part focuses on the hydrogen charging conditions by the electrochemical method, after studying the hydrogen evolution reactions at the surface and the charging current density identification, we focus then the driving force impact on the hydrogen solubility and diffusivity, a conversion model of the equivalent pressure to the current density is also discussed. The last part of this chapter, the

impact of the crystallographic orientation on the diffusion process is studied, by considering the stress state. In addition, a thermodynamic study has highlighted the importance of the vacancies clusters formed during the hydrogen charging on the diffusion process.

The fourth chapter comprises two parts on the nickel bi crystals. In the first part of this chapter, each grain boundary has been studied by molecular dynamics in a bi crystal system. For four different types of grain boundaries, we questioned the hydrogen-grain boundaries interactions particularly the hydrogen segregation and diffusion at the atomic scale. The hydrogen atom's behavior is extremely dependent on the locale grain boundary structure, the high excess volume grain boundaries have significant influences on the hydrogen diffusion and segregation. The segregation sites for the hydrogen atom in the grain boundary core are studied with their geometry and energy, the fast diffusion paths and trapping in boundaries will be discussed. In the end, we present experimental studies on the influence of grain boundaries on the hydrogen diffusion process. The results are discussed in regard to the stress state, fast diffusion and hydrogen – micro defects interactions.

At the end of this thesis, a summary of key findings and conclusions based on the different analyses of this work are presented. To finish, different perspectives are proposed to improve the experimental and numerical approaches and to move towards multi-scales understanding.

Chapter 1.

Literature Review

| | |
|---|----|
| <u>Chapter 1. Literature Review</u> | 12 |
| <u>I. Hydrogen – metal and hydrogen embrittlement</u> | 15 |
| <u>I.1 Hydrogen-metal interactions</u> | 15 |
| <u>I.2 Hydrogen embrittlement</u> | 15 |
| <u>I.2.1 Hydrogen - hydride</u> | 16 |
| <u>I.2.2 Hydrogen - decohesion</u> | 17 |
| <u>I.2.3 Hydrogen - dislocation</u> | 18 |
| <u>I.2.4 Hydrogen - vacancy</u> | 20 |
| <u>I.2.5 Hydrogen – defactant</u> | 21 |
| <u>II. Hydrogen in Ni single crystals</u> | 22 |
| <u>II.1 Solubility</u> | 23 |
| <u>II.2 Diffusivity</u> | 26 |
| <u>III. Grain boundaries in metals</u> | 30 |
| <u>III.1 Grain boundaries (GBs)</u> | 30 |
| <u>III.1.1 Geometry</u> | 30 |
| <u>III.1.2 Classifications of grain boundaries</u> | 31 |
| <u>III.2 Free volume of grain boundary</u> | 34 |
| <u>III.3 Grain boundary energy</u> | 35 |
| <u>III.4 Defects in grain boundary</u> | 40 |
| <u>IV. Hydrogen in GBs-Intergranular segregation and diffusion</u> | 44 |
| <u>IV.1 Grain boundary segregation</u> | 45 |
| <u>IV.1.1 Driving force of segregation</u> | 45 |
| <u>IV.1.2 Experiments of segregation in polycrystals</u> | 46 |
| <u>IV.1.3 Atomic approaches of segregation in GBs</u> | 48 |
| <u>IV.2 Grain boundary diffusion</u> | 53 |
| <u>IV.2.1 Grain boundary diffusion model</u> | 53 |
| <u>IV.2.2 Experiments of GB diffusion in polycrystals</u> | 57 |
| <u>IV.2.3 Atomic approaches of GB diffusion</u> | 58 |
| <u>V. Summary</u> | 61 |

Diffusion in solids is fundamental in the art and science of materials and thus a key point for solid-state physics, physical chemistry and metallurgy. Processes connected with diffusion pose some problems such as creep, corrosion, and embrittlement. Particularly, hydrogen diffusion is extremely fast in solids even at low temperature. *Figure 1.1* shows a comparison for H, O, and N in Nb and for C in Fe [Volk1975]. Moreover, hydrogen diffusion can be observed at low temperatures so that quantum effects in the diffusion of hydrogen can be expected. Fritz *et al.* [Fritz1961] found heat production below 1 K in Palladium, possibly resulting from a rearrangement of hydrogen atoms. The quenching experiments by Hanada [Hanada1973,1976] on hydrogen in Ta have shown hydrogen mobility at 11 K.

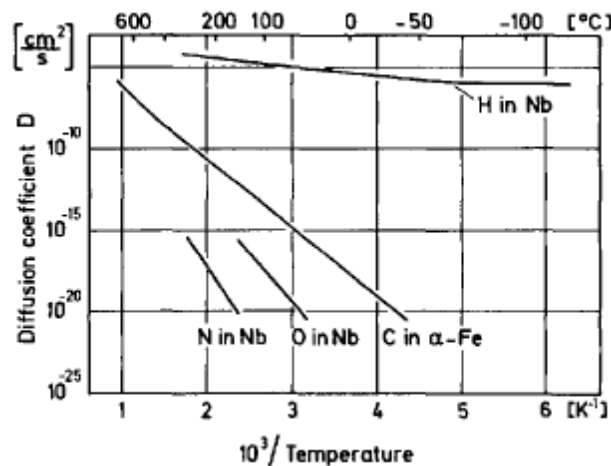


Figure 1.1 – Diffusion coefficients of H, N, and O in Nb, and C in Fe [Volk1975]

Getting a better understanding of hydrogen diffusion in solids is a challenge for scientists and engineers who design and build operating materials. Hydrogen embrittlement of metals has been and continues to be the subject of much work. HE is complex since all phenomena are linked altogether, and the HE mechanisms remain highly dependent on the microstructural defects and its evolution, it thus becomes important to know precisely the microstructural defects characteristics and their consequences on the embrittlement. HE mechanisms will be discussed with their corresponding defects in the crystal lattice, furthermore, we will compare the literature data of hydrogen in single/poly crystalline in order to understand the contributions of grain boundaries on the hydrogen transport, the effects of grain boundaries are eliminated using single crystals and the density of point defects can be kept to a minimum. Despite many achievements on the understanding of grain boundary and hydrogen-grain boundaries interactions, there is still a lot of phenomena cannot be fully explained. This part started thus a fundamental literature study on the nature of grain boundaries, and later hydrogen in different grain boundaries comparing between experimental and numerical studies at different scales in order to obtain a complete view of the whole phenomenon.

I. Hydrogen – metal and hydrogen embrittlement

I.1 Hydrogen-metal interactions

Hydrogen is the lightest and also the smallest element on the periodic table, the form H is the most abundant element in the universe (Oxygen is the most abundant element in the earth and hydrogen is the eighth), which always links with other atoms and ions and because of its small size with one electron and one proton, hydrogen has a high mobility in metals. This behavior is a concern in metallurgy as an embrittlement element for many metals, complicating the design of pipelines, storage tanks, etc. For the initial overview, only stable structural systems involving metal-solute hydrogen effects in the bulk, i.e. no hydrides, are considered.

In face-centered cubic (FCC) lattices, interstitial hydrogen generally prefers octahedral sites, while it is located on tetrahedral sites in body-centered cubic (BCC) and hexagonal close-packed (HCP) metals, at room temperature [Wipf1997]. Furthermore, the interstitial hydrogen modifies the local electronic structure of the metal atoms, especially because of its ability to transfer all or some of its electric charge to its close neighbors. This modification may decrease the interatomic cohesion and can result in a possible embrittling effect [Coudreuse2000]. In addition, considering the insertion of solutes in the interstitial sites can generate distortions in lattices, the generated stresses have an impact on the diffusion process due to modification of the chemical potential [Larche1982, Kirchheim1987, Zhang2000, Haftbaradaran2011, Li2017]. However, the real materials present different kind of defects (vacancies, dislocations, grain boundaries, etc.) which have strong influences on the hydrogen diffusion transport in metals. These defects could be diffusion paths or trapping sites. Due to the complexity of hydrogen in metals and the nature of the surrounding environment, HE phenomenon cannot be described by one single theory.

I.2 Hydrogen embrittlement

Most mechanisms of hydrogen embrittlement are directly linked to the microstructural defects and are classified with some major candidates advanced: Hydride induced embrittlement, hydrogen enhanced decohesion (HEDE), hydrogen enhanced localized plasticity (HELP), adsorption induced dislocation emission (AIDE) and hydrogen-vacancy interactions. *Figure 1.2* presents schematic diagrams for different HE mechanisms, the relative importance of these mechanisms for different fracture models, which depends on the material, microstructure/strength, and testing conditions.

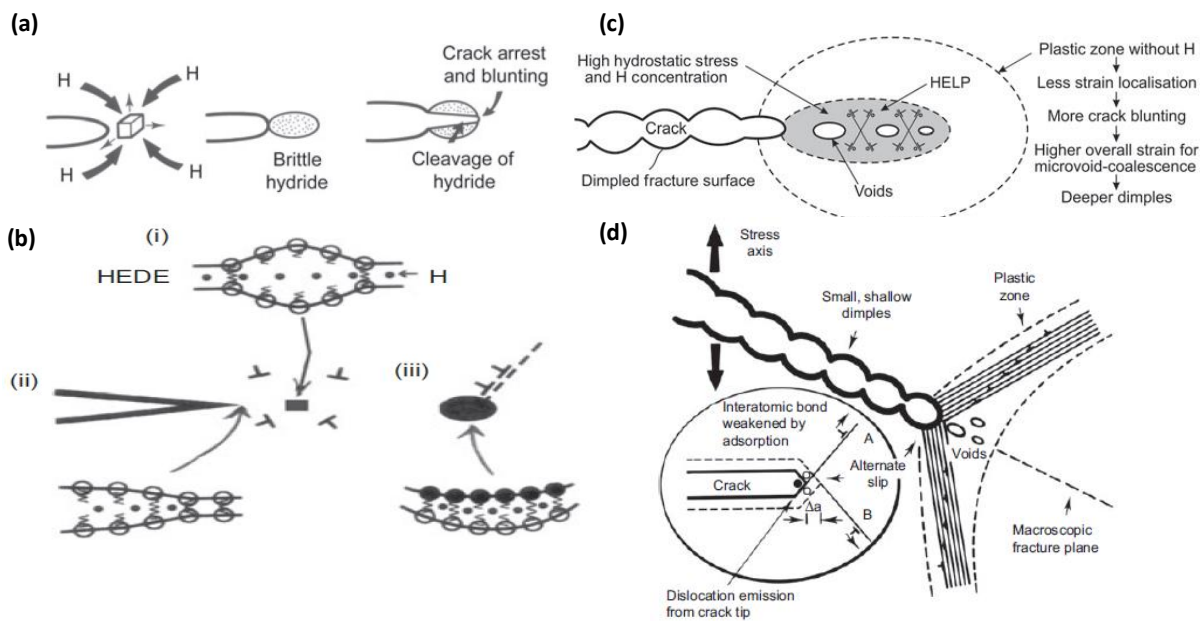


Figure 1.2 – Schematic diagrams illustrating HE mechanisms – (a) brittle hydride formed due to the high hydrogen concentration, (b) weakening of interatomic bonds by hydrogen, (c) presence of micro/nano void coalescence with plasticity localised and facilitated in regions of high hydrogen concentrations, (d) crack growth by alternate-slip from crack tips, facilitating coalescence of cracks with voids formed in the plastic zone ahead of cracks. [Lynch2012]

HE occurs the combinations of HE mechanisms and highlights the importance of microdefects, such as AIDE and HELP possibly acting conjointly to localize plasticity, additional strain localization could occur due to hydrogen-vacancy interactions. Vacancy effects probably play only a secondary role, although there has been a somewhat radical suggestion that HE may be primarily the result of a high concentration of vacancies ahead of cracks, due to hydrogen-induced reductions in the vacancy-formation energy, rather than hydrogen effects [Nagumo2004]. Vacancy agglomeration could lead to nano-void formation [Cuitino1996], and autocatalytic void-growth and coalescence might occur if the number or size of nano-voids reached a critical level. Vacancies could also facilitate dislocation climb and cross slip, and reduce strain hardening, thereby promoting strain localization, possibly in conjunction with hydrogen-induced slip localization due to AIDE or HELP. We will discuss separately these HE mechanisms with their related microdefects.

1.2.1 Hydrogen - hydride

The stress-induced hydride formation and cleavage mechanism are one of the well-established hydrogen embrittlement mechanisms with experimental and theoretical supports [Birnbaum1990, Vehoff1997]. The hydride is formed with oversaturation hydrogen content at the stress field, this phenomenon is often observed in materials as V, Nb, Ti and Zr [Koike1981, Matsui1990, Makenas1980; Robertson1998; Teter2001]. Tal-Gutelmacher and Eliezer [Tal-Gutelmacher 2004]

have studied the hydrogen interactions with titanium alloys in different hydride phases, *figure 1.3* shows that hydride accumulates at the high stress zone and the ultimate tensile strength decreases at high hydrogen concentration. In some particular cases, pure Ni with a relatively low hydrogen solubility could form the hydride $\text{NiH}_{0.68}$ using electrochemical method [Wayman1989, Tavares2002], this hydride is not stable at room temperature and at normal pressure, which could only exist for a period of a few tens of hours by the evolution of hydrogen.

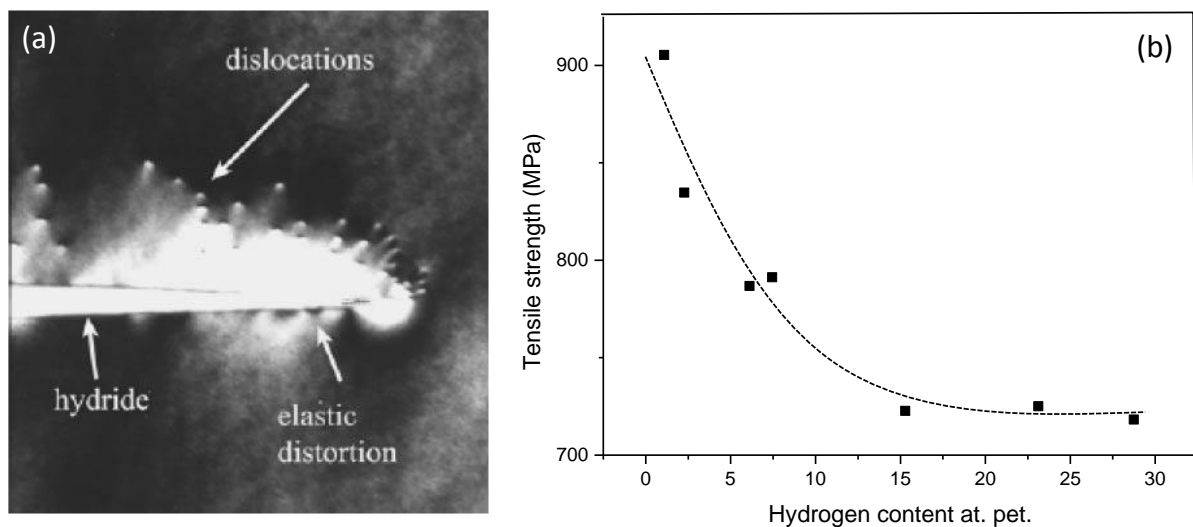


Figure 1.3 – (a) Surface of Ti-4%Al during tensile testing, (b) ultimate tensile strength as a function of hydrogen concentration in Ti-10V-2Fe-3Al alloy [Tal-Gutelmacher2004]

1.2.2 Hydrogen - decohesion

The HEDE mechanism is described by the hydrogen accumulation within the lattice and decreasing the cohesive bonding force between metal atoms. This concept was first proposed by Troiano [Troiano1960], and later developed in details [Wriedt1970]. Hydrogen accumulation is generated by the lattice dilation due to elastic hydrostatic stresses [Li1966], and trapping is also a potential mechanism for hydrogen segregation [Pressouyre1980]. The HEDE is a basic notion that hydrogen damage occurs in the crack tip fracture process zone when the local crack tip opening tensile stress exceeds the maximum local atomic cohesion strength, lowered by the presence of hydrogen [Oriani1972]. The crystallographic orientation influence on the HEDE mechanism has been reported by Lynch [Lynch1988] (*figure 1.4 (a)* and (*b*)), the appearance of fractures depended on the orientation of crystals but was the same in hydrogen and mercury environments for each orientation. And recently Carter *et al.* [Carter2004, 2010] has reported their works on the surface energy as a function of the hydrogen coverage for different elements by DFT calculations (*figure 1.4 (c)*), the plane (110) is more affected by the presence of hydrogen comparing to the plane (100) in Tungsten.

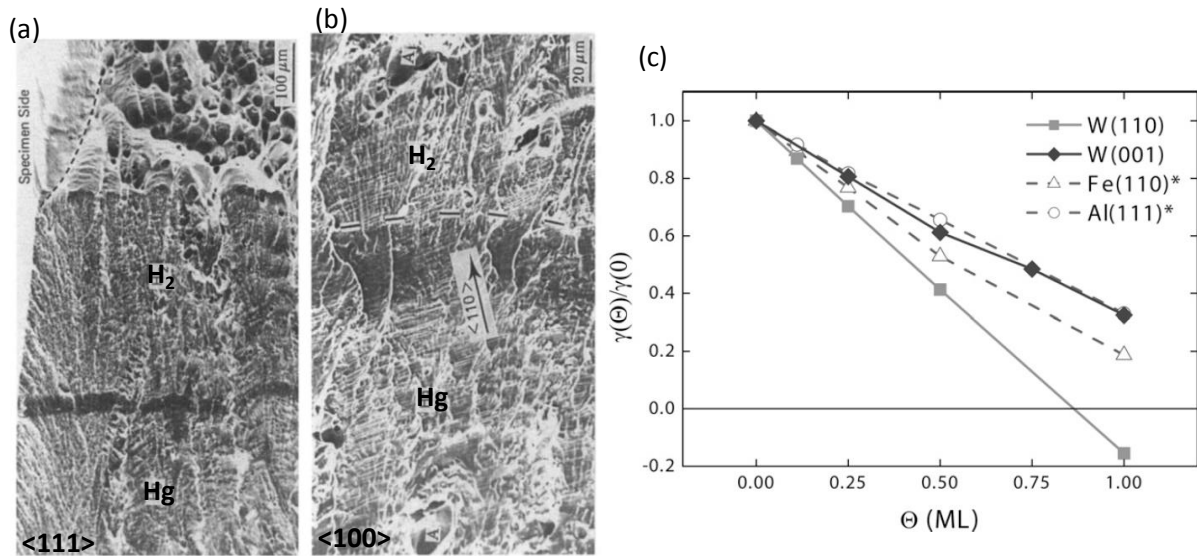


Figure 1.4 – SEM of fracture surface produced in a nickel single crystal orientation by rapid crack growth in liquid mercury and then in gaseous hydrogen at 20 °C. (a) Near the orientation <111>, (b) Near the orientation <100>, [Lynch1988] (c) Ideal fracture energies as a function of hydrogen coverage, at 1.0 ML coverage = one H per surface element for W, Fe and Al [Carter2010]

I.2.3 Hydrogen - dislocation

The HELP mechanism [Beachem1972] describes hydrogen-dislocation interactions with Adsorption-Induced Dislocation Emission (AIDE) theory. Hydrogen accumulates at the crack tip reduces the dislocation formation energy, the dislocation mobility is enhanced by the presence of hydrogen. Hydrogen stimulates dislocation processes that local plastic deformation could lead to the sub critical crack growth. The experimental evidence is often provided by TEM with an observation of an increasing number of dislocations and the initiation of dislocation motion (*figure 1.5*) [Robertson2001]. The role of hydrogen on plasticity has been formalized within the framework of the isotropic elasticity in continuous mechanics media, the hydrogen segregated at the elastic distortion field near the dislocations decreases the elastic interaction force (*figure 1.6*) [Sofronis1995, Delafosse2001].

The interaction of hydrogen with dislocations plays an important role in the phenomenon of hydrogen embrittlement due to the influence of these effects on plastic flow and hydrogen mobility. Dislocations cause distortion in the lattice, hydrogen tends to segregate to the hydrostatic stress fields, and therefore, dislocations are considered as strong trapping sites because of their strong hydrostatic stresses. The dislocation core with higher binding energy is an irreversible trapping site and the dislocation edge is considered as a reversible site [Taketomi2008]. As a result of the attractive interaction of dislocations, the mobility of dissolved hydrogen is substantially reduced.

As the opposite of the dislocation trapping effect, the acceleration of hydrogen transport is found during the deformation. This mechanism was first introduced by Bastien and Azou [Bastien1951], recently, Chene [Chene1999] and Frappart [Frappart2011, 2012] have studied the hydrogen transport in metals under the tensile. Chene *et al.* have reported that tritium radiation activity in a single crystal of nickel is sharply increasing in the plastic field due to mobile dislocations. The diffusion is faster in the plastic field than in the elastic field. High mobility of dislocations has an acceleration effect on the hydrogen diffusion. However, Frappart *et al.* have only found an increase of hydrogen concentration in martensitic steels, they confirmed that dislocations have a trapping effect that affects the hydrogen diffusivity by slowing it down, and they showed no contribution of mobile dislocations in the hydrogen transport. Hydrogen-dislocation interactions have thus still several factors to understand such as the deformation rate, the dislocation density and the microstructure of materials. Recently, Guedes *et al.* [Guedes2015] highlight that the mobile and stored dislocations influence the behavior of hydrogen in quenched and tempered martensitic steel. They give a strong evidence on the correlation between the evolution of the mobile dislocation density and the hydrogen diffusion flux.

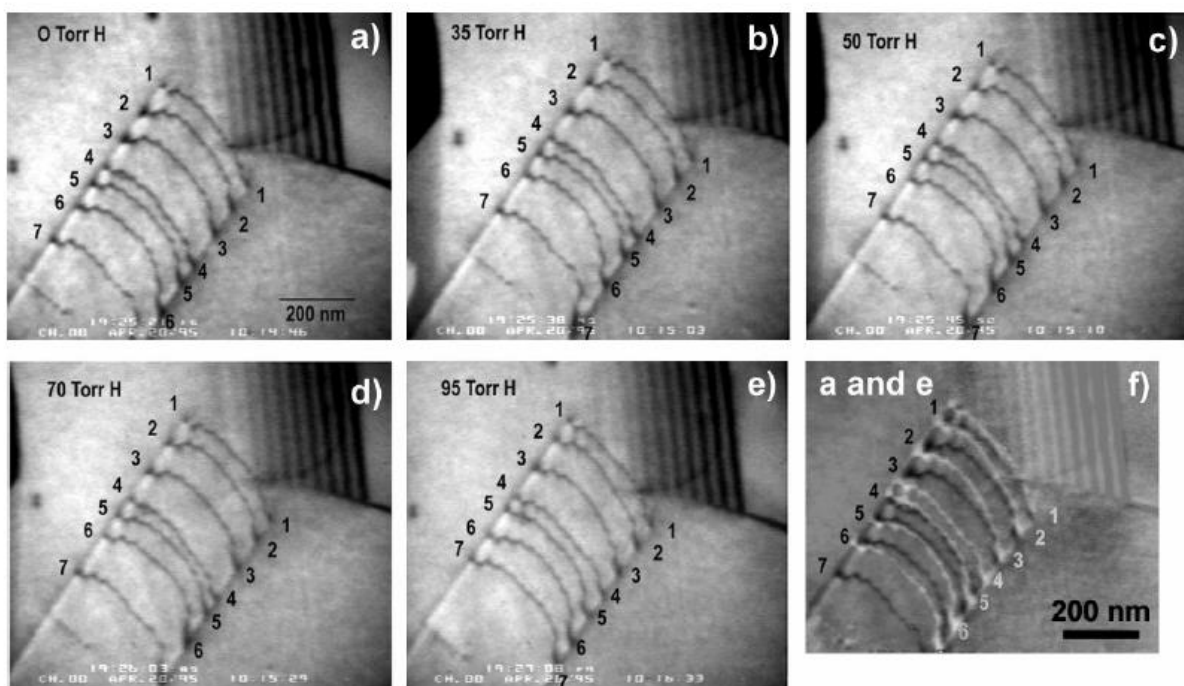


Figure 1.5 – The evolution of a stack of dislocations in an austenitic steel AISI 310 as a function of the partial pressure of gaseous hydrogen, the comparison shows a displacement of the dislocations relative to their initial position [Robertson2001]

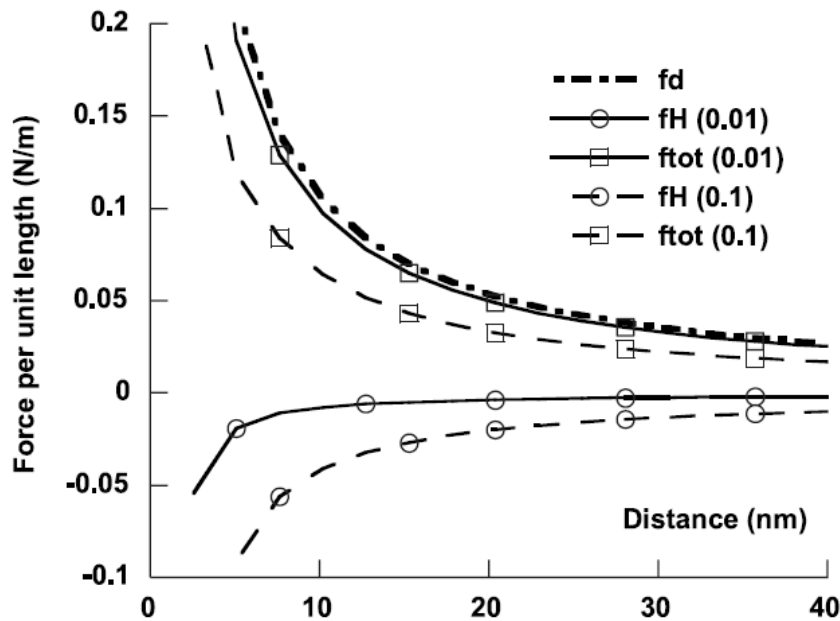


Figure 1.6 – Interaction forces between two coplanar dislocations, as a function of their separation distance and of the remote hydrogen concentration. Peach and Kohler force (fd), hydrogen component (fH) and total force ($ftot=fd+fH$) in the presence of hydrogen in mean concentration 0.01 and 0.1 [Delafosse2011].

1.2.4 Hydrogen - vacancy

The vacancy is an empty site as the simplest point defect in the lattice, hydrogen is strongly connected to vacancies in most metals and the interaction has been investigated using a combination of experimental and theoretical methods [Bockris2000, Mao2002, Tateyama2003]. The hydrogen-vacancy interactions highlight that vacancy formation (V-H clusters) enhanced by the presence of hydrogen, this phenomenon has been observed in many Metal-Hydrogen alloys [Fukai2005, Oudriss2012c]. This approach is based on the hydrogen ability to create superabundant vacancy (SAV) and to stabilize them. The multiplication of vacancies may lead to the formation of microcracks or microvoids [Nagumo 2004, Takai 2008]. Fukai *et al.* [Fukai2003] have pointed out that for nickel, the presence of hydrogen enhances vacancy formation. These observations are supported by the atomistic calculations of Nazarov *et al.* [Nazarov2012, 2014] for FCC metals and Metsue *et al.* [Metsue2016] for nickel single crystals, which highlight the fact that hydrogen decreases the energy of vacancy formation. Similar results for hydrogen in tungsten (*figure 1.7 (a)*) were investigated by Jin *et al.* [Jin2015] and (*figure 1.7 (b)*) Kato *et al.* [Kato2009], the works of Kato have reported the vacancy concentration as a function of the hydrogen concentration in tungsten, which turns out that the rapid increase of the vacancy concentration is associated with an increase in the average number of the hydrogen atoms trapped by the vacancy. It has been shown experimentally that the only presence of vacancies can be responsible for the loss of ductility in nickel alloys and iron [Takai2008].

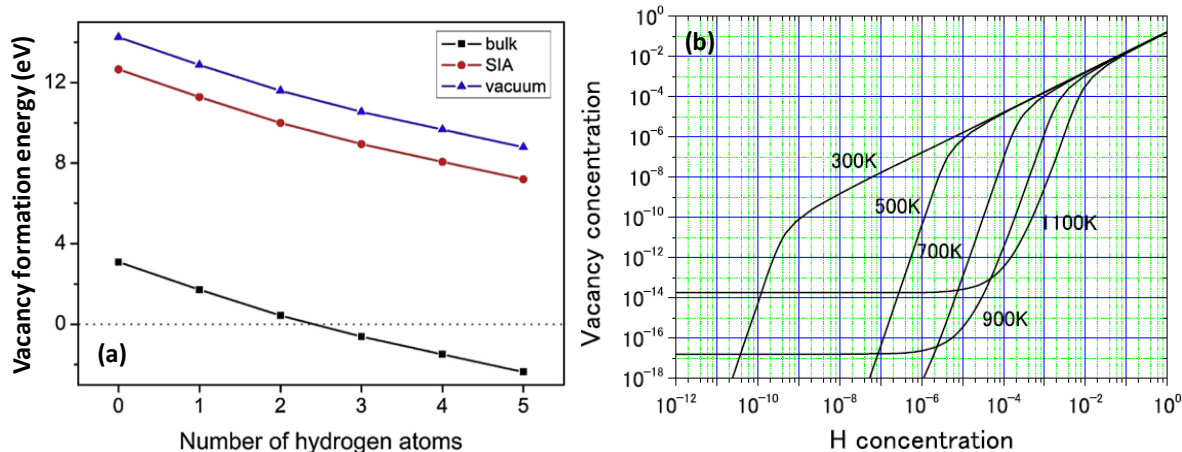


Figure 1.7 – (a) Vacancy formation energy as a function of a number of H atoms. The vacancy formation energies for the blue (triangle), red (dot) and black (square) lines correspond to three different reference energies, i.e., an isolated atom in the vacuum, a self-interstitial atom (SIA), and a bulk lattice atom, respectively. [Jin2015] (b) Vacancy concentration at thermal equilibrium as functions of hydrogen concentration at five temperatures for 300-1100K. [Kato2009].

The hydrogen trapping at vacancies as a major interaction has been pointed out by different studies [Besenbacher1990, Birnbaum1997, Fukai2003, Fukai2005, Liu2009, Metsue2014], hydrogen atoms originally at interstitial lattice positions, are trapped at vacancies in multiple numbers with rather high binding energies. It was impressed that numbers of hydrogen atoms or molecules can be trapped by a single vacancy, with a maximum six hydrogen atoms corresponding to the number of octahedral sites around a vacancy in either the FCC or the BCC lattice [Kaxiras2005, Connetable2014, Nazarov2014, Metsue2016]. Recent works on the hydrogen-metal system have pointed out that hydrogen can induce superabundant vacancies (SAV) formation, indicating that hydrogen promotes and stabilizes vacancies. Hickel and coworkers have reported the hydrogen trapping at vacancies may decrease H diffusion coefficients by several orders of magnitude [Hickel2014]. However, this effect mainly depends on the vacancy concentration which is relatively low at room temperature [Oudriss2012a].

1.2.5 Hydrogen – defactant

Recently, Kirchheim has proposed a common model for different types of HE that the hydrogen atoms segregating at defects with an excess Γ called defactants [Kirchheim2007a, Kirchheim2007b, Kirchheim2010], analogous to the action of surfactants with surfaces. From a thermodynamic point of view, it appears that the different approaches of HE are based on a decrease of the energy of formation or emission of defects (dislocations, vacancies, microcavities), the cohesion and surface energy, or the energy associated with the displacement of defects such as dislocations, with the presence of adsorbed hydrogen. Experimental support is given by the nano-indentation with the onset of plasticity in

extremely small volumes, the reduction in the cohesion and defect formation energy are responsible for hydrogen embrittlement [Barnoush2008, 2010]. This energy approach proposes a general formalism based on the Gibbs theory concerning the decrease of the surface energy γ by the adsorption of solutes, which is directly related to the solute concentration or the chemical potential μ as: $d\gamma = -\Gamma d\mu$. The evolution of the surface energy γ of a defect (grain boundary, dislocation, vacancy ...) can be represented with a solute type A (hydrogen) as shown in figure 1.8.

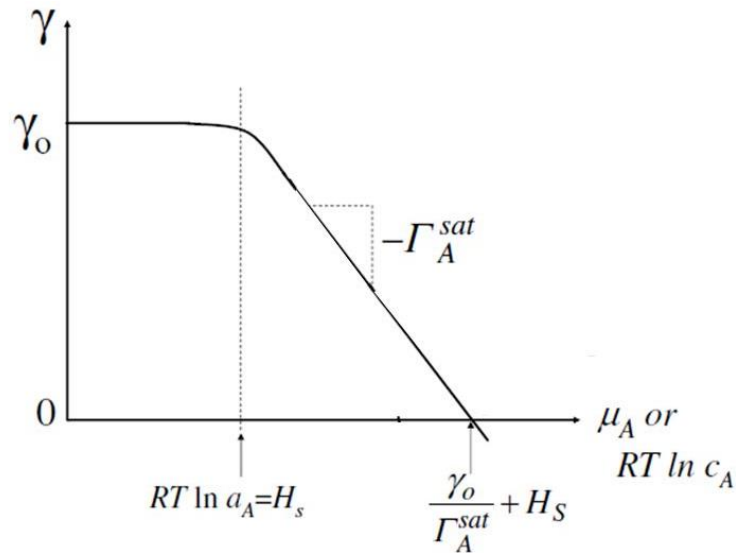


Figure 1.8 - Predicted variation of the surface energy of a defect as a function of the chemical potential μ_A , and activity a_A or concentration, C_A [Kirchheim2007a].

Actually, we can see that at low concentrations of solute A, the excess solute Γ_A is low, and the surface energy γ is little affected. However, Γ_A increases and reaches saturation for μ_A approaching or even exceeding the defect-solute interaction energy H_S . This causes a decrease in the surface energy of the defect γ and the importance of the solute concentration is clarified.

All HE mechanisms highlight not only the direct impact of hydrogen on materials but also its enhancement for hydride, dislocation, and vacancy. The interactions of hydrogen with lattice imperfections are dominant in determining of embrittlement process. The first step is then to understand the hydrogen's behavior in the perfect lattice, we keep thus the focus on the single crystals of nickel.

II. Hydrogen in Ni single crystals

A single crystal of metal is less influenced by defects than polycrystals, theoretical property values based on idealized atomic interactions may be attainable. A better understanding of factors such as crystallographic orientation and microstructure is helpful to study the influence of a specific defect.

The nickel – hydrogen system is an interesting binary model from a thermodynamic point of view. The absence of polymorphism have enabled both thermodynamic and kinetic data to be obtained in a large temperature range.

II.1 Solubility

Mclellan and coworkers [Stafford1974, Mclellan1984] have reported their works on the nickel-hydrogen system for a large temperature range using the equilibrate-quench-analyze technique. Since the solubility of hydrogen in nickel is limited, the thermodynamic properties of hydrogen in the solution are usually derived by plotting the logarithm of the hydrogen solubility in the metal at constant pressure versus reciprocal temperature:

$$\ln(\theta) = -\frac{\Delta\bar{H}}{R} \left(\frac{1}{T}\right) + \frac{\Delta S^{ex}}{R} + \ln(\sqrt{P_{H_2}}) \quad (\text{Eq.1.1})$$

Where θ is the atom ratio of hydrogen in metal, equation (Eq.1.1) assumed that the relative partial molar enthalpy $\Delta\bar{H}$ and the relative partial excess molar entropy ΔS^{ex} are independent of temperature, a linear relation would appear, $\Delta\bar{H}$ and ΔS^{ex} can thus be determined. Nickel single crystal at a relatively small temperature range seems to have a linear relation (*figure 1.9(a)*), however the plot, is curved for nickel poly crystal. This equation was later corrected taking into account the term $\theta T^{4/7}$ considering the partition function of the H₂ molecular [Stafford1974]:

$$\ln(\theta T^{4/7}) = -\frac{\Delta\bar{H} - \frac{1}{2}E_0^D}{R} \left(\frac{1}{T}\right) + \frac{\Delta S^{ex}}{R} + \ln(\sqrt{P_{H_2}} \lambda) \quad (\text{Eq.1.2})$$

Where λ is a known Planck constant, $-E_0^D$ is the dissociation energy per atom of the H molecule at 0 K.

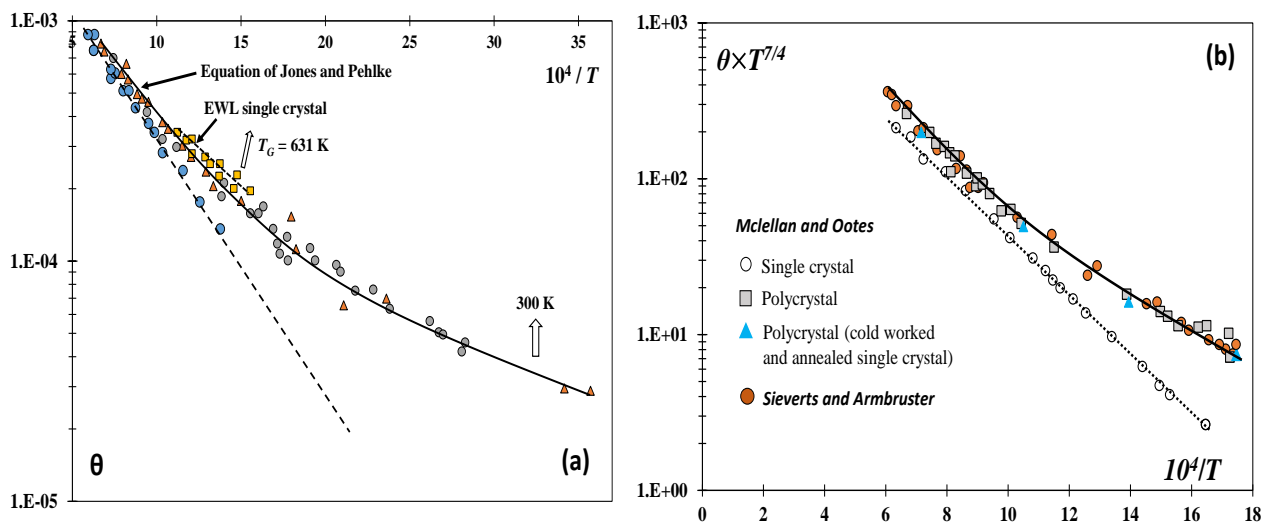


Figure 1.9– (a) Arrhenius plot of the solubility θ of hydrogen in nickel at atmospheric pressure against reciprocal temperature, dash line (-|-) is the single crystal data. [Mclellan1984], (b) Solubility of hydrogen in nickel, $\ln(\theta T^{4/7})$ against $1/T$ is plotted [Stafford1974]

The nonlinearity related to the temperature dependence of $\Delta\bar{H}$ and ΔS^{ex} is still found for nickel poly crystal, however, nickel single crystal shows a linear plot (*figure 1.9(b)*). The deviation of Arrhenius solubility plot is significant at the lowest temperature, despite single/poly crystals of nickel have a closer solubility of hydrogen at high temperature. This result highlights the role of hydrogen-defects interactions that are more pronounced at low temperatures.

A more complementary data collection of the hydrogen solubility in nickel has been done by Lekbir *et al.* [Lekbir2012]. *Figure 1.10* presents the hydrogen solubility as a function of $(1000/T)$, this representation is based on a general Sievert form with S_0 is a constant:

$$S = S_0 \sqrt{P_{H_2}} \exp\left(\frac{-\Delta H}{RT}\right) \quad (\text{Eq.1.3})$$

Atomic simulations have now the possibility to calculate an increasing number of materials properties as a complementary for the experiments. Particularly, atomic calculations can access materials data at some extreme conditions which could be unachievable for experimental techniques. Low amount of hydrogen in materials makes experimental measurements sensitive to structural defects, which is inevitable even for high purity materials.

The solubility of hydrogen in nickel single crystal has been studied by Metsue *et al.* [Metsue2016] (*figure 1.11*), the comparison with the experiments performed on single crystals shows that the solubility calculated with *ab initio* model is overestimated by a ~ 1.7 factor in the 650 K to 890 K temperature range. The agreement is found with the data at a higher temperature, authors emphasized that the electronic excitations lead to a marked deviation of the solubility at high temperature. The gap deviation between experiment data and *ab initio* calculations could be due to the effects of defects and the grain size of polycrystals.

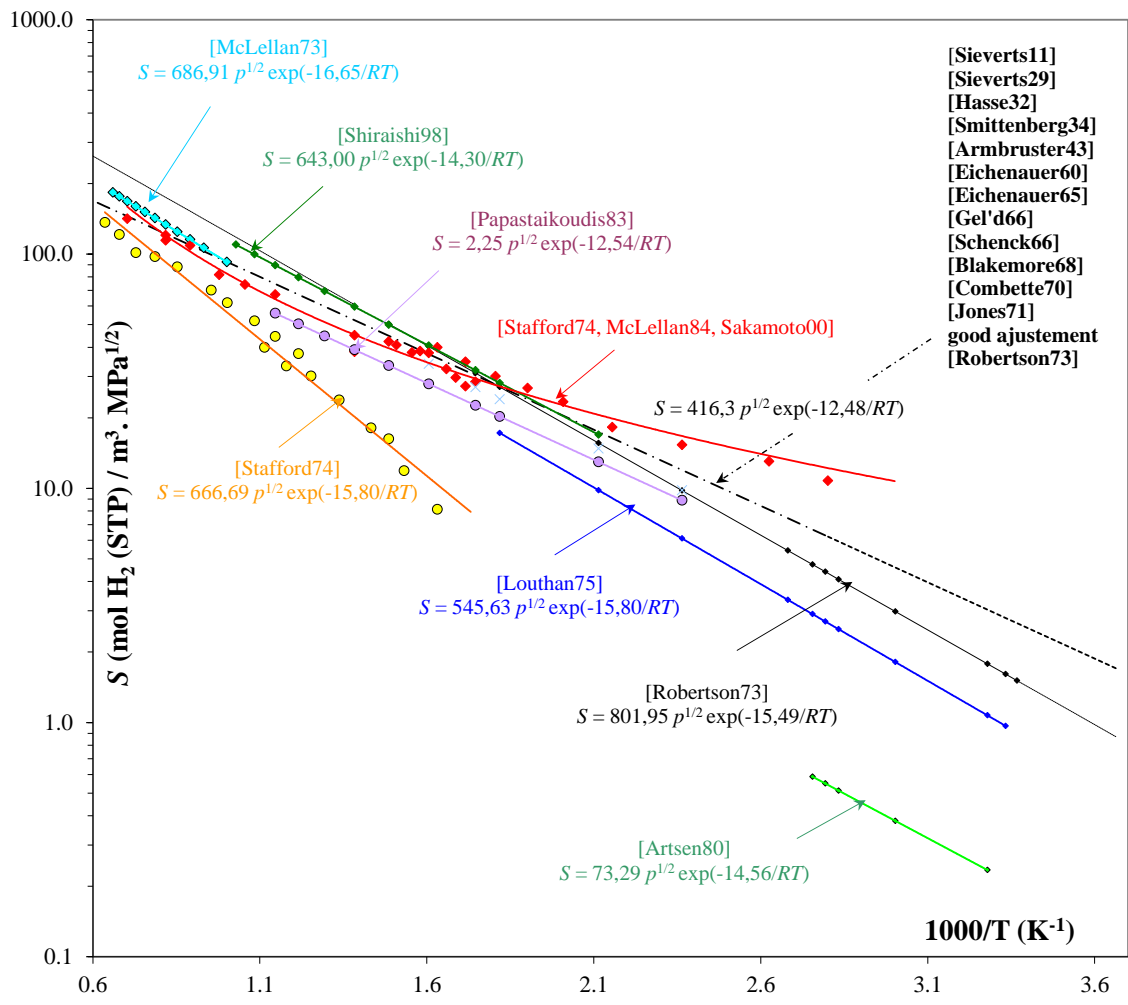


Figure 1.10– Compilation data of the solubility of hydrogen in nickel, S against 1000/T is plotted [Lekbir2012]

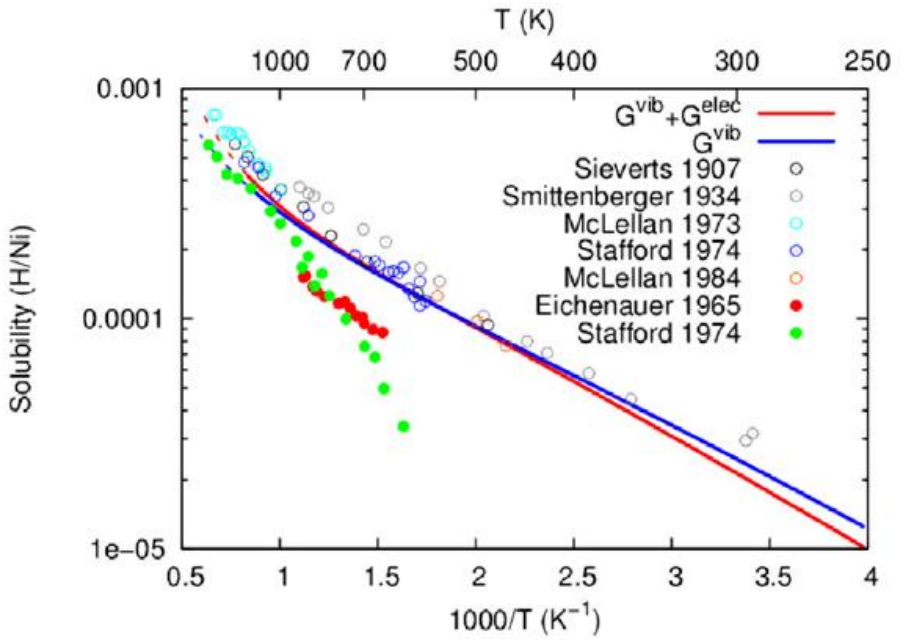


Figure 1.11– Solubility of hydrogen in nickel at atmospheric pressure, polycrystals Ni - unfilled circles, single crystals-filled circles and solid lines are simulations [Metsue2016]

There is little data of the nickel single crystals and most of the specimens should be the nickel polycrystals. In addition, there is a lack of information on these specimens about the structural defects since they play an important role on the hydrogen transport in solids, the solubility of hydrogen is thus strongly influenced by these defects. In order to clarify the influences of defects on the hydrogen transport in solids such as diffusion and trapping mechanisms, it is necessary to get more details on the structural defects (the defect density of vacancy, precipitate...and for polycrystals the grain boundary type, grain size...) of specimens for the future studies.

II.2 Diffusivity

Ebisuzaki and coworkers [Ebisuzaki1967] have investigated the hydrogen diffusion in a single crystal of nickel [100] at a temperature range (500K to 700K) using the gas permeation technique. Same specimens have been studied by Oudriss *et al.* [Oudriss2012c] using the electrochemical permeation at a temperature range (300K to 330K). The diffusivity of hydrogen in nickel (100) is obtained by the “breakthrough time” method is given in the *figure 1.12* and compared to nickel polycrystals with different grain sizes. At high temperature, similar diffusivities have been found both in single and polycrystals, however a dispersion appears at low temperature. This is an evidence that hydrogen diffusion is strongly influenced by grain boundaries at this temperature range, particularly the dispersion is more significant for small grain size grain boundaries.

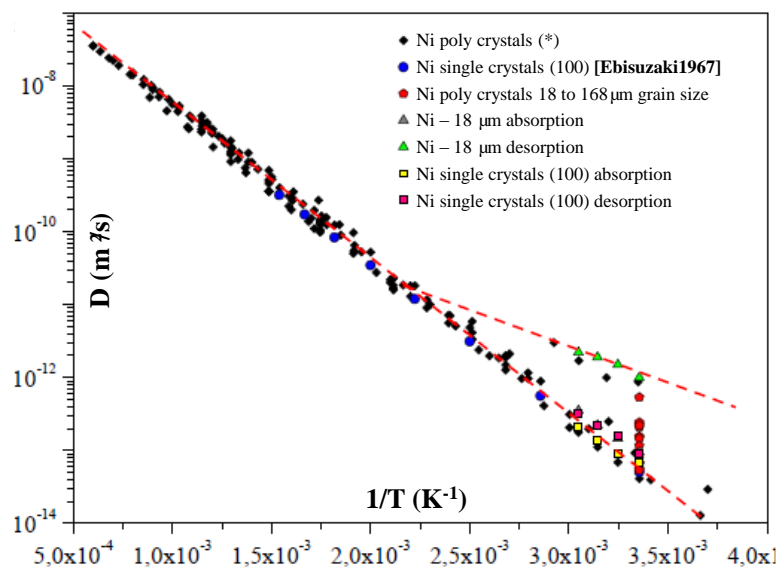


Figure 1.12 – Diffusion coefficients of hydrogen in nickel single crystal (100) and polycrystals, D against $1/T$ is plotted [Oudriss2012c]. (*) is data collected by works of [Robertson 1973; Louthan 1975; V äkl 1975; Bakker 1990; Chanfreau 1992; Arantes 1993; Altunoglu 1996]

A compilation of the hydrogen diffusivity data in nickel is given in *figure 1.13*, temperature dependence on diffusion is expressed in terms of an Arrhenius type relationship. Mathematically, the temperature dependence of diffusion is given as:

$$D = D_0 \exp\left(\frac{-\Delta E_D^{eff}}{RT}\right) \quad (\text{Eq.1.4})$$

Where D_0 is the pre-exponential factor and E_D^{eff} is the effective activation energy of diffusion. Here D is a homogeneous value, the difference between the lattice diffusion and the grain boundary diffusion is not presented. Furthermore, grain boundaries have the acceleration and the trapping impacts on the diffusion which is dependent on the temperature and the nature of grain boundaries. This is an interesting point to deepen our understanding of the diffusion process.

In addition, the work of Ebisuzaki *et al.* [**Ebisuzaki1967**] was the first work that reported the orientation of single crystals, Brass *et al.* [**Brass1996**] have reported their works on the hydrogen diffusion in nickel single crystals by electrochemical permeation technique at room temperature, the hydrogen diffusion coefficient D is different between orientations $\langle 110 \rangle$ and $\langle 100 \rangle$; they obtained values of $D_{\langle 110 \rangle} = 6.2 \times 10^{-14} \text{m}^2 \text{s}^{-1}$ and $D_{\langle 100 \rangle} = 5.6 \times 10^{-14} \text{m}^2 \text{s}^{-1}$. A similar fundamental finding from an atomic point of view was reported by Dederichs & Schroeder [**Dederichs1978**], who claimed that the anisotropy of the saddle-point configuration leads to an anisotropy diffusion in cubic crystals. The variable nature of these results led us to question the different metallurgical features which can induce anisotropic diffusivity of solutes in fcc solids with high crystallographic symmetry. These works give a motivation to investigate the influence of crystallographic orientation on the hydrogen diffusion process.

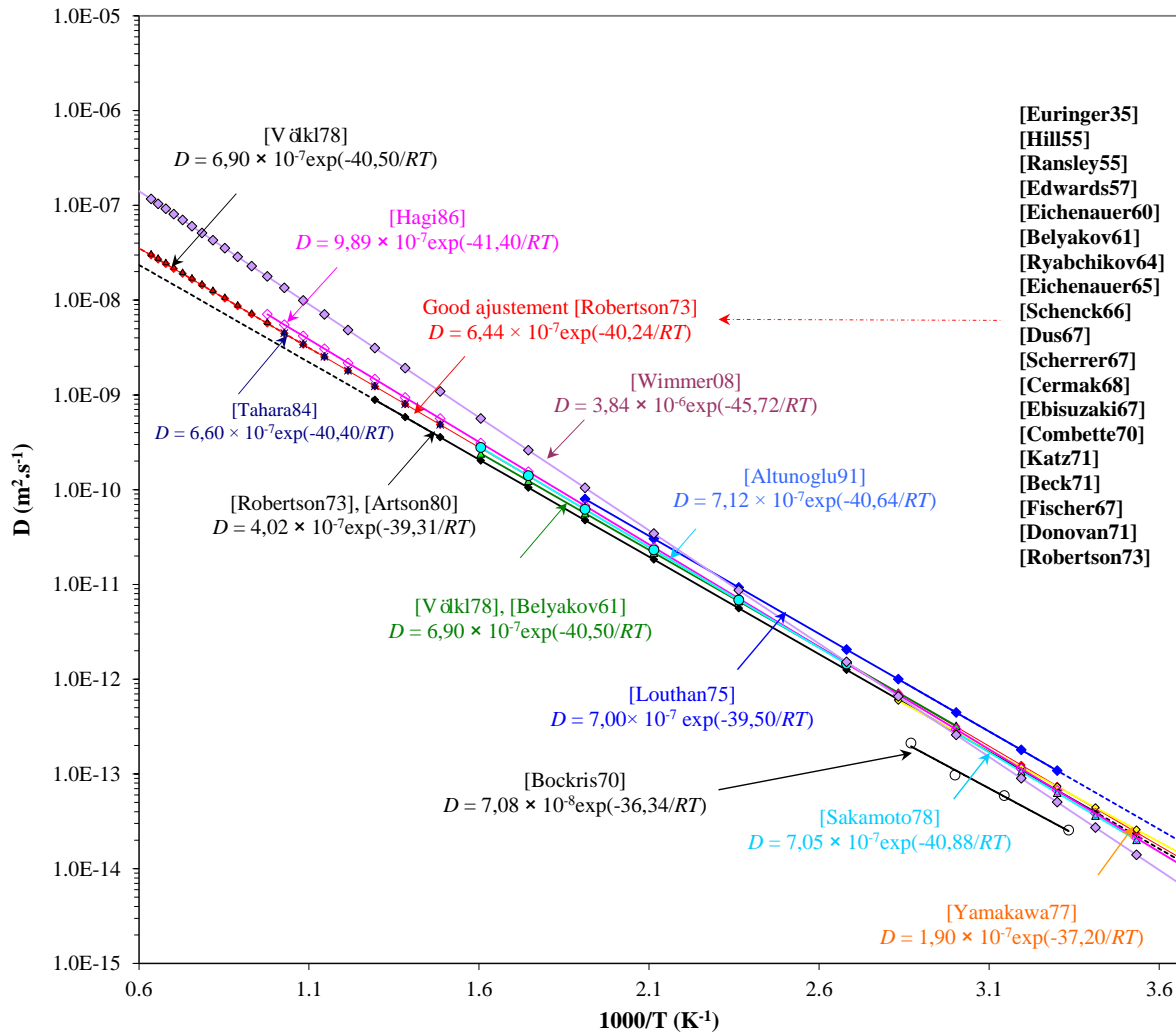


Figure 1.13– Compilation data of the diffusivity of hydrogen in nickel, D against $1000/T$ is plotted [Lekbir2012]

From a macroscopic point of view, hydrogen diffusion is assumed as a purely classic phenomenon described by an Arrhenius-like temperature dependence. Moreover, the hydrogen atom is the lightest chemical element, there is no doubt its diffusion is affected by quantum mechanics effects.

M.Toshihiko *et al.* [Toshihiko2008] have investigated the diffusion coefficients by Molecular dynamics (MD) with the embedded atom method (EAM) from 600K to 1000K. Similar results of ab initio calculations are given in works of Di Stefano *et al.* [Di Stefano2015] and Wimmer *et al.* [Wimmer2006] for a larger temperature range. All data are collected in figure 1.14, Arrhenius type relationship of the equation (Eq.1.4) is presented.

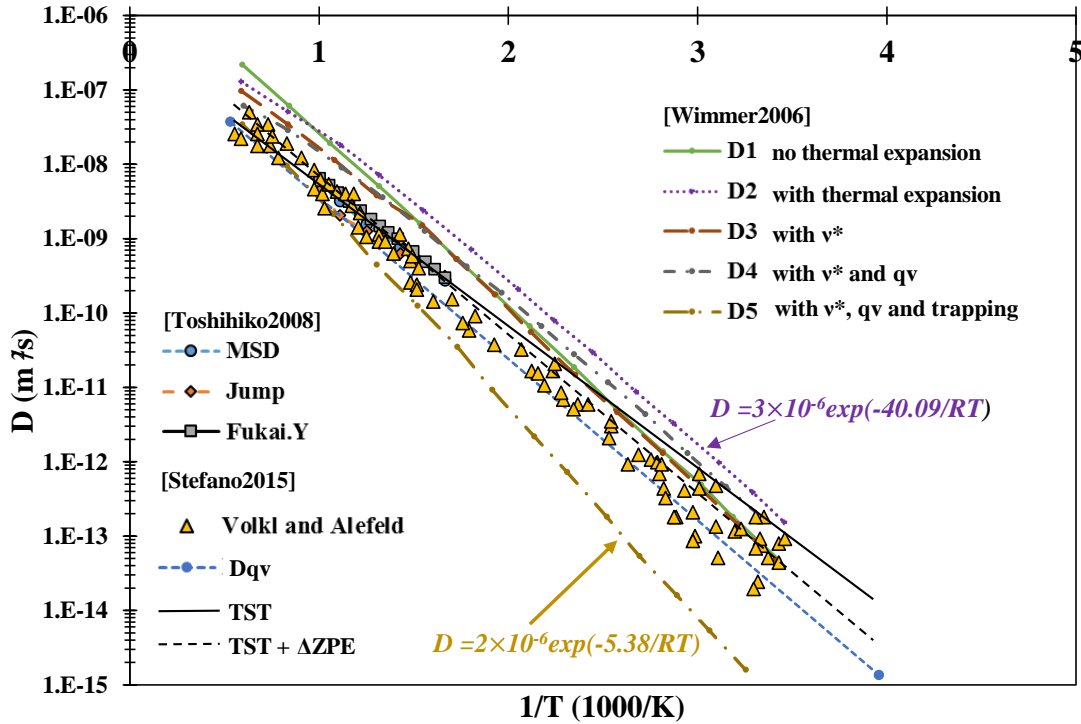


Figure 1.14– Diffusion coefficients against $1/T$ is plotted. Zero-point energy (ZPE), transition state theory (TST), mean square displacement (MSD), quantized vibration (qv), jump frequency (ν^*)

Table 1.1– Experimental data and atomic calculations of diffusion coefficients D in nickel single crystal.

| T (K) | Experiences D ($10^{-14}\text{m}^2\text{s}$) | Molecular Dynamics D ($10^{-14}\text{m}^2\text{s}$) | ab initio D ($10^{-14}\text{m}^2\text{s}$) |
|-------------|---|---|---|
| 300 | Ni (100) 5.6 [Brass1990] Ni (100) 5.1 [Ebisuzaki1967] Ni (110) 6.2 [Brass1990] | | Ni 4 [Wimmer2006] Ni 3.5 [DiSefano2015] |
| 600 | Ni (100) 1.7×10^4 [Ebisuzaki1967] | Ni 3×10^4 [Toshihiko2008] | Ni 3.5×10^4 [DiStefano2015] |
| 1000 | Ni (100) 4.23×10^5 [Ebisuzaki1967] | Ni 5×10^5 [Toshihiko2008] | Ni 4×10^5 [DiSefano2015] |

Atomic calculations are in good agreement with experimental data in nickel single crystal (*Table 1.1*), diffusion coefficients obtained by different methods have the same magnitude order. Most atomic simulations have implemented only one hydrogen atom in order to see the effect, the obtained results seem indicate that the diffusion is less influenced by the hydrogen-hydrogen interaction in the lattice.

However, hydrogen diffusion affected by the crystallographic orientation has been less considered in previous works.

III. Grain boundaries in metals

Hydrogen-grain boundary interaction is one of the key factors on the hydrogen diffusion process in metals, however the trapping and acceleration of diffusion effects with the presence of different kind of grain boundaries cannot be fully explained. Considering the complexity of grain boundaries structure, this part will focus on the nature of grain boundaries with two important indices, the free volume and the grain boundary energy. Moreover, grain boundary can be considered as a sink of microstructural defects, it is appreciated to concern also the microdefects-grain boundaries interactions. The intergranular diffusion and segregation of hydrogen will be discussed in the next section IV.

III.1 Grain boundaries (GBs)

Materials processing, properties and performance are strongly influenced by GB properties such as GB energy, mobility, sliding, segregation, cracking resistance, etc. Grains and their boundaries may have the most crucial influence on the HE, however, hydrogen-grain boundaries interactions are such elusive. One of the major reasons is that information on the boundary atomic configurations is incomplete and imprecise, and characters of the hydrogen cannot be quantitatively treated without such data. In addition, real boundaries in metals often involve other types of defects, and this can introduce the complication of the local environment. Studies on grain boundaries are difficult due to the large variability in their structure but also of their very fine scale which hampers the direct observation of their properties. Better determinations of boundary structures are thus in prospect with the advent of advanced computer modeling and a new generation of microscopy techniques with higher resolutions.

III.1.1 Geometry

The grain boundary is the interface between two neighboring grains, both sides display the same structure and the same composition. These two grains differ in mutual orientations and the grain boundary thus represents a transition region, where atoms are shifted from their regular positions in the crystal lattice. The characterization of these such complicated structures needs several parameters called *geometrical degrees of freedom* [Sutton1995, Priester2006]. From a macroscopic point of view, there are five degrees of freedom:

- 1 for the rotation angle θ between the two crystals
- 2 for the rotation axis $[uvw]$ defined by its direction cosines

- 2 for the orientation of the grain boundary plane defined by its normal n .

And there are four microscopic degrees of freedom:

- 3 for the translation of one crystal with respect to the other: the rigid body translation vector τ
- 1 for the vector d normal to the grain boundary plane that indicates the position of the plane along its normal.

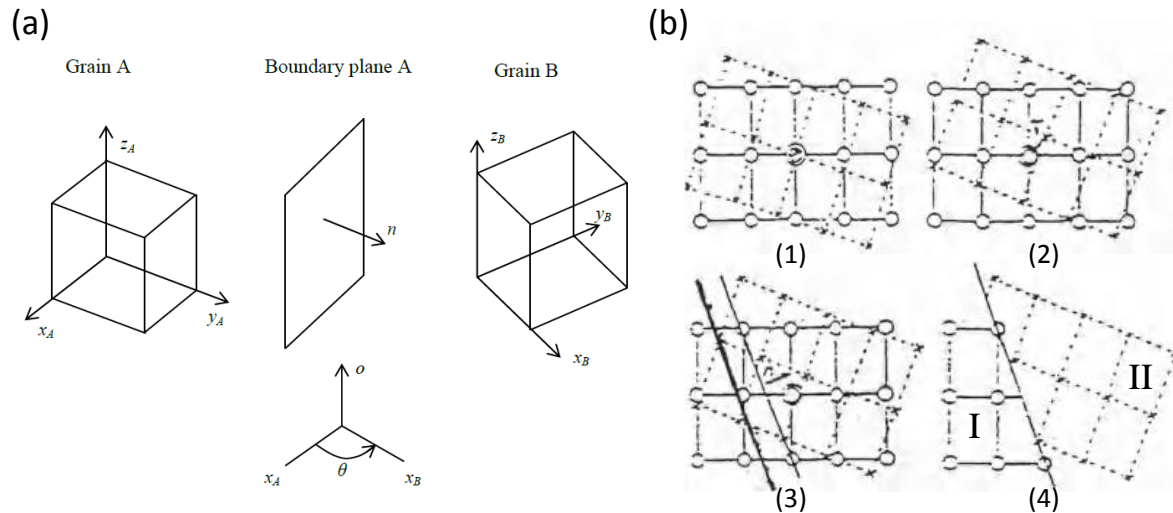


Figure 1.15 – (a) Macroscopic parameters that define a GB (b) Microscopic GB construction: **1** interpenetration of two misorientated crystals; **2** rigid body translation of one crystal with respect to the other; **3** introduction of a grain boundary plane (different positions are possible for the same orientation); **4** atoms of crystal I and crystal II are rejected on one side and on the other side, respectively [Priester2006]

Actually, the microscopic parameters resulting from relaxation processes are not independent of macroscopic parameters. Five macroscopic degrees of freedom constitute the thermodynamic variables that are sufficient to give a complete description of the GB. *Figure 1.15* presents five macroscopic parameters for GBs and the construction of a GB. The microscopic parameters are obtained after the GB energy minimization. These parameters are random for real GBs in polycrystals, however, a better control can be realized in bicrystals. Furthermore, for non-cubic structures, the description of GB may need more than five macroscopic parameters in an adequate coordinate system.

III.1.2 Classifications of grain boundaries

There exists an abundance different grain boundaries, therefore, establishing a categorization of the grain boundaries is necessary. *Table 1.2* summarizes the three most used classifications. However, none of them is a perfect classification, each has its limits for whole GB characters.

Based on the misorientation angle, two groups can be distinguished: *Low angle grain boundaries* (LAGBs) are those with a misorientation less than about 15 degrees for nickel, this angle varies from

10 to 15 degrees depending on the materials. These GBs are composed of an array of dislocations and their properties and structure are a function of the misorientation. *High angle grain boundaries* (HAGBs) have the misorientation angle greater than about 15 degrees, these GBs are normally found to be independent of the misorientation because individual dislocations are no more distinguishable and overlap each other. In this group, a new classification based on the coincidence site lattice (CSL) has been proposed.

Table 1.2– Classifications of grain boundaries

| | | |
|---------------------|---|--|
| Grain boundaries | Classification based on rotation angle θ | <ol style="list-style-type: none"> 1. Low angle : $\theta < 15^\circ$ 2. High angle : $\theta > 15^\circ$ |
| | Classification based on axis o | <ol style="list-style-type: none"> 1. Twist : o parallel to n 2. Tilt : o perpendicular to n 3. mixed |
| | Classification based on lattice for $\theta > 15^\circ$ | <ol style="list-style-type: none"> 1. Special – CSL : $\Sigma < 29$ 2. Random : $\Sigma > 29$ |

From a point of view the minimum Gibbs energy of the system, CSL concept is based on the assumption that the GB is more stable when coincidence of sites in both adjoining grains is high, because the number of bonds broken across the boundary is small [Lejcek2010]. The first model used for identification of special GBs was proposed by Kronberg and Wilson [Kronberg1949] and later by Randl [Randl1996]. The density of coincidence sites, or better, its reciprocal value Σ is an important parameter characterizing the CSL [Priester2013]. Choosing an elementary cell, the value of Σ can be expressed as:

$$\Sigma = \frac{\text{Coincidence unit cell volume}}{\text{Crystal primitive unit cell volume}}$$

CSL is a geometrical construction based the orientation rotation of the lattice (*figure 1.16*), lattices cannot actually overlap and atomic positions are not accounted for in CSLs. Due to the purely geometrical character of CSL, any small change of grain orientation from the singular GB results in a drastic change in Σ . A maximum angular deviation needs to be accepted for the boundary CSL [Grimmer1974], this maximum angular deviation θ_x is given as: $\theta_x = \theta_i / \Sigma^w$. θ_i is mostly accepted as 15 degrees which correspond to the limit of *LAGBs*, and all *LAGBs* are thus described as $\Sigma = 1$. The mostly adopted Brandon criterion w uses the value 1/2, while other authors proposed to use other values, for example Ishida and McLean the value of 1, Dechamps *et al.* the value of 2/3 and Palumbo *et al.* the value of 5/6. [Brandon1966, Ishida1973, Dechamps1987, Palumbo1990a].

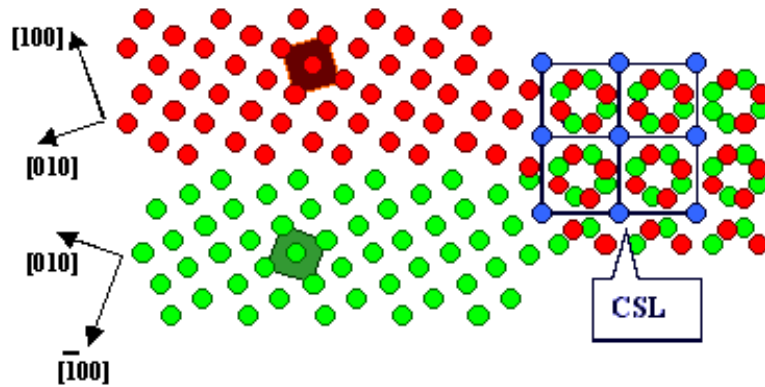


Figure 1.16 – CSL fitting for $\Sigma 5$ boundary [Online by Dr. Helmut Föll]

The boundaries with a low value of ($\Sigma < 29$) are called CSL or special boundaries, and boundaries with a high value of ($\Sigma > 29$) are named general or random boundaries. This classification is generally used in the field of engineering grain boundary (GBE). But the relationship between the crystallographic characteristics and the boundary properties is not still well established.

Another classification is based on the rotation axis o (figure 1.17), a grain boundary is denoted *twist* boundary if the rotation axis o is perpendicular to the boundary plane or *tilt* boundary if the rotation axis o within the boundary plane. Several tilt boundary planes have the mirror symmetry of two grains, these symmetrical grain boundaries have been often used as the simulation models and experimental samples due to this simplicity of construction. Furthermore, symmetrical tilt grain boundary may be transformed to a twist grain boundary with a 180° rotation angle around an axis normal to the boundary plan. This is an ambiguity of this classification. Other positions of the rotation axis with respect to the boundary plane lead to a *mixed tilt/twist* grain boundary.

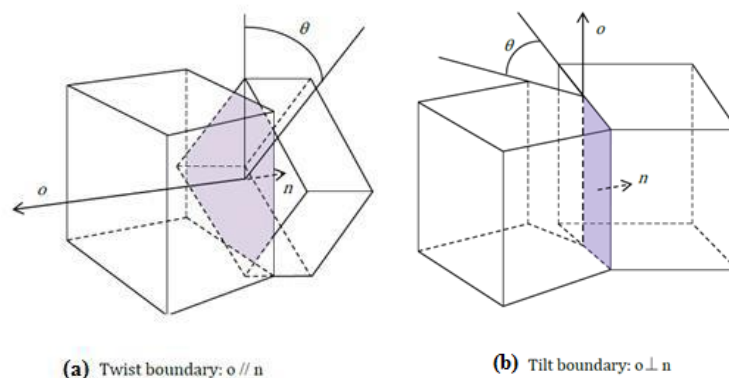


Figure 1.17 – (a) Twist grain boundary (b) Tilt grain boundary

III.2 Free volume of grain boundary

In the 1970s, the concept of a free volume associated with GBs started developing and applied it as a criterion for GB models [Aaron1972a, Aaron1972b]. For close-packed materials, a minimum grain boundary free volume V_F (Unit: volume/area) can be obtained for any given misorientation by subtracting the volume attributable to atoms arranged in perfect crystal from the volume of the same number of atoms in GB, the length unit for GB free volume is because of the 2D nature of GBs the length of interest is the expansion normal to the GB plane. The variation of V_F is roughly inverse to the coordination of atoms in the GB. The idea is that many properties associated with the presence of GB are directly affected by the atom density, Smoluchowski [Smoluchowski1952] has suggested that enhanced diffusion along GBs can be correlated with paths of reduced atomic density, both jump distance and attempt frequency might be expected to vary with atomic density. Several effects can be explained in terms of an amount of free volume is given in *Table 1.3*.

Table 1.3 – Phenomena associated with GB free volume [Aaron1972a]

| Some GB phenomena | | |
|---|--------------------------------|---------------------------------|
| Static | | Dynamic |
| Grain Boundary Melting | Grain Boundary Sliding, | Grain Boundary migration |
| Precipitation | Segregation behavior | |
| Fracture | Resistivity | Grain growth |
| Grooving | Energy | |
| Interaction | Diffusion | Internal friction |
| with solutes, vacancies, interstitials, dislocations, etc. | Corrosion | |

Free volume can give the first information of GB properties without the need for a detailed description of the GB structure, *figure 1.18(a)* compares free volume against misorientation angle for different symmetric tilt GBs, the periodic angle range appears because different symmetrical tilt axis has different rotation symmetry order. Free volume is high with a relative high misorientation angle. *Figure 1.18(b)* gives the details for the symmetric tilt GB (001) [001], this is a minimum free volume matching of GB. Free volume seems to have a linear relationship with the intergranular energy, this part will discuss later.

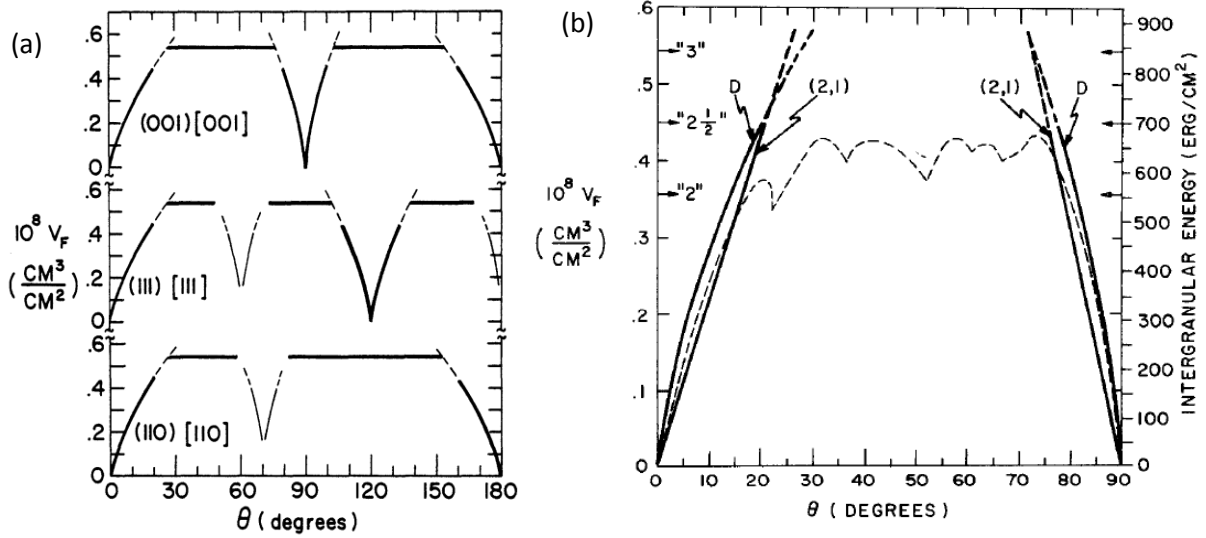


Figure 1.18 – (a) Comparison of free volume vs misorientation angle for different symmetric tilt GBs in FCC [Aaron1972a] (b) Free volume vs misorientation angle for symmetric tilt GB (001)[001] [Aaron1972b].

III.3 Grain boundary energy

Grain boundary energy is defined as the excess of free energy associated with the presence of GB, the perfect lattice is considered as the reference. Experimentally, grain boundary energy can be quantified as a constant between the increment in total system energy and the increment in the area. The GB energy is actually misfit between atoms across the boundary, the deviation of atom positions from the perfect lattice leads to a higher energy state [Online by A.D. Rollet]. For low angle GBs, Read and Shockley have proposed a method based on the dislocation structure [Read1950], no universal theory exists to describe the energy of high angle GBs. By choosing the two variables, temperature T and pressure P (the usual thermodynamic variables), the increase of the Gibbs enthalpy of a system calculating a GB is given by:

$$dG = -SdT + VdP + \sum_{i=1}^c \mu_i N_i + \gamma dA \quad (\text{Eq.1.5})$$

With N_i and μ_i are the quantity and the chemical potential of the constituent i ; C is the number of constituents, S the entropy of the system and V the volume. The free energy of the GB is defined as:

$$\gamma = \frac{\partial G}{\partial A_{T,P,N_i}} \quad (\text{Eq.1.6})$$

However, this interface of free energy is not the only function of the variables T and P , the GB is in a deformed state compared to the perfect crystals, its structure and thus its energy is a function of the

five macroscopic degrees of freedom. Finally, γ is a complex function that may be written as **[Priester2006]**:

$$\gamma = \gamma(T, P, \mu_i, \varepsilon_{ij}, \rho_1, \rho_2, \theta, n_1, n_2) \quad (\text{Eq.1.7})$$

With ε_{ij} the grain boundary deformations, ρ_1 and ρ_2 the direction cosines of the rotation axis, θ the rotation angle and n_1, n_2 the directions of the normal to the boundary plane in the two crystals. Other variations of the energy are beyond the classical thermodynamics; they result from the variations of the microscopic geometrical parameters and from local atomic relaxations. The investigation of the property correlations is complex since the geometrical structure involves macroscopic, microscopic and atomic aspects. Some atomic scale calculations based on embedded atom method (EAM) have investigated the relationship among GB energy, the misorientation angles and the Σ values, however, we cannot obtain a predictable correlation due to the anisotropy characters. Several atomic simulations suggest that GB energy is correlated with free volume at the interface. However, no simple way exists to predict the free volume based on the crystallographic type **[Wolf1990, Tschopp2007, Olmsted2009, Rohrer2015]**.

Actually, the misorientation angle with the GB energy is extremely crystallographic orientation dependent, generally distinguished by the GB rotation axis and their GB planes. By reporting on a 3D diagram the interfacial energy values calculated for different tilt or twist angles, D. Wolf **[Wolf1990]** draws by interpolation an energy surface of copper for the mixed grain boundaries (*figure 1.19*). The deep valleys on the 3D surface show the importance of the dense planes and of the neighboring orientations. This representation clearly highlights that twist boundary with $\theta = 180^\circ$ is identical to symmetrical $\langle 110 \rangle$ tilt boundaries. Then, the twist boundaries with $0^\circ < \theta < 180^\circ$ may be considered as pure twist or as mixed boundaries having two components: θ_{tilt} and θ_{twist} . Similar works on FCC structure have been reported by Olmsted *et al* **[Olmsted2009]** for nickel and Tschopp *et al* **[Tschopp2007]** for aluminum (*figure. 1.20 and 1.21*).

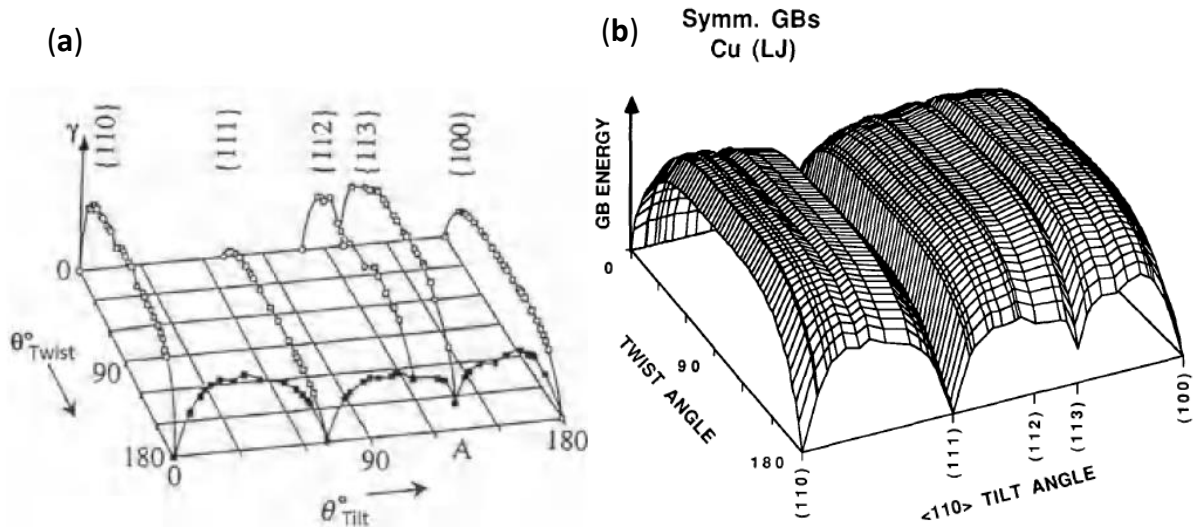


Figure 1.19 – (a) Calculated energies for grain boundaries with various tilt and/or twist angles. The curves represent the energy evolutions with θ_{twist} for five pure twist {110}, {111}, {112}, {113} and {100} copper boundaries. For $\theta_{twist} = 180^\circ$, the twist boundaries are identical to symmetrical tilt boundaries; (b) curved surface drawn by an interpolation of the curves given in (a) allowing to predict the energies of mixed boundaries [Wolf1990].

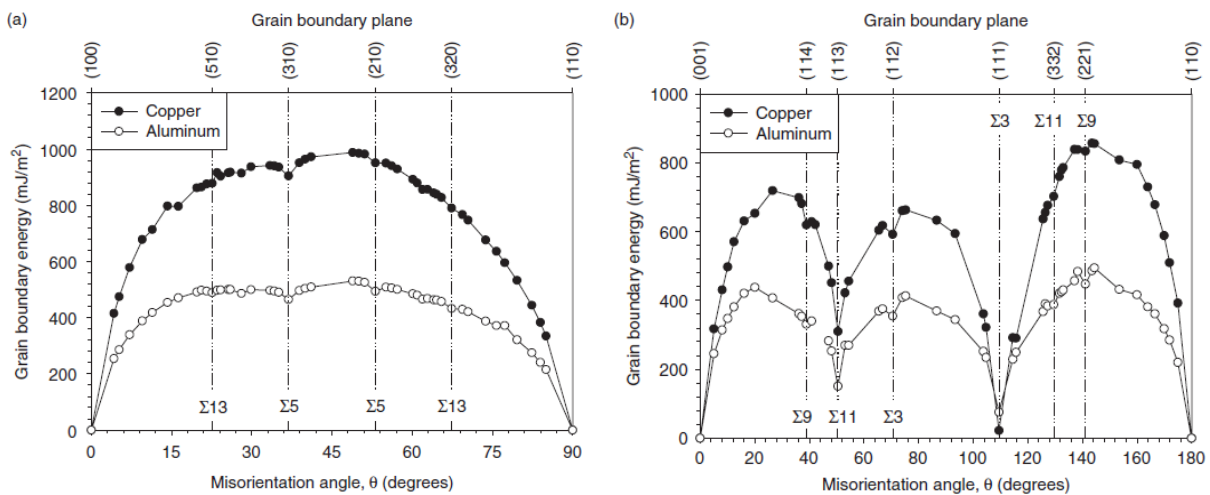


Figure 1.20 – Structure and energies of symmetric tilt grain boundaries with the (a) [100] and (b) [110] misorientation axes [Tschopp2007].

Note that the GB energy varies strongly with the misorientation angle for the <110> tilt axis, the two deep cusps are $\Sigma 11$ (113) $\theta=50.48^\circ$ STGB (Symmetric Tile GB) and the $\Sigma 3$ (111) $\theta=109.47^\circ$ CTB (Coherent Twin Boundary). For the <100> tilt axis, $\Sigma 5$ and $\Sigma 13$ boundaries have only minor cusps in the energy relationship. CTB boundary energy is lower in copper than in aluminum while the others GBs of copper have higher energy than aluminum. The results of nickel have clearly highlighted the importance of the GB planes on the determination of the GB energy, for the same misorientation angle, the GB energy may lay in a wide range, consequently, the misorientation angle alone is not sufficient to determine GB energy.

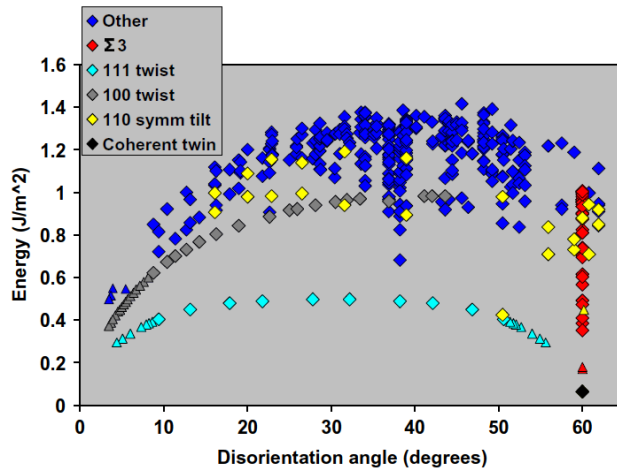


Figure 1.21 – The computed grain boundary energies for Ni plotted against the misorientation angle [Olmsted2009].

Historically, there has been a concept that the GB energy can be interpreted in terms of its Σ value, which is the inverse of the density of coincidence sites of the near grain lattices. The reasoning of this idea is that a small value of Σ (high density of coincident sites) suggests the lattices match together well and thus the GB energy would be lower. The GB energy in Ni and Fe are plotted as a function of Σ in the *figure 1.22*. Actually, there is no apparent trend of the energy with Σ with the exception of the low energy of the coherent twin boundary. In particular, $\Sigma 5$ and $\Sigma 9$ GBs have high energy configurations, which are the same energy levels as GBs with high Σ values. The other important observation is that there is a wide variation in GB energy for any given value of Σ . Recall that the Σ value derives from the relative orientation of the two neighboring grains, but does not depend on the orientation of the boundary plane. This large spread of the energy of boundaries with the same relative orientation again reflects the significant role that boundary plane orientation plays in GB energy.

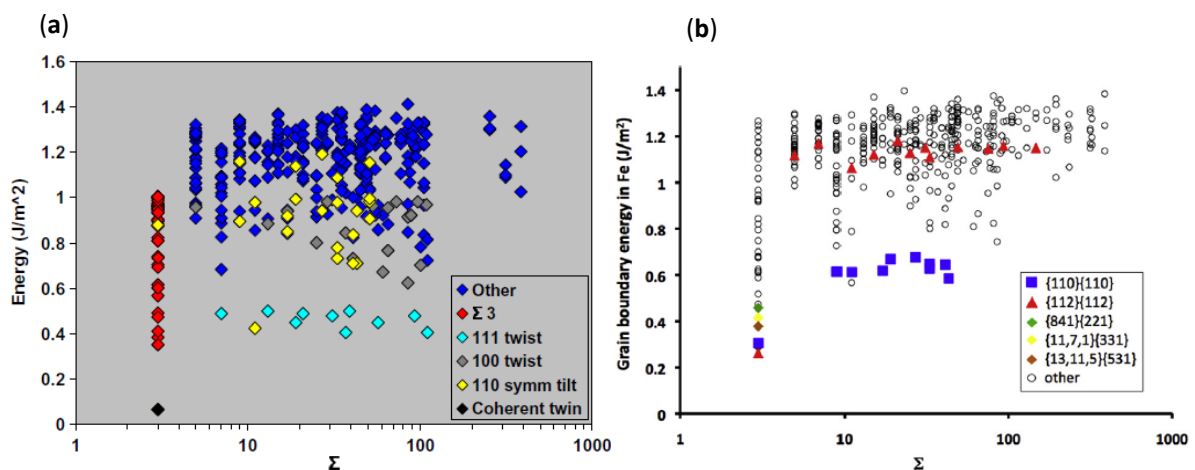


Figure 1.22 – The computed grain boundary energies for (a) Ni and (b) Fe plotted against Σ , the inverse density of coincident sites. [Olmsted2009] [Rohrer2015].

Another idea has been widely discussed is that the GB energy has a correlation with the GB expansion. The GB expansion is the excess of free volume per unit area of the GB, there is a rough correlation with the GB energy (*figure 1.23*). CTB has both a very low energy and very small expansion, the other boundaries lie in a region which trends upward in energy with increasing expansion. After all, while there is an overall trend of increasing boundary energy with increasing boundary expansion, there is substantial variation about that trend such that one could not reliably predict the boundary energy based on the expansion.

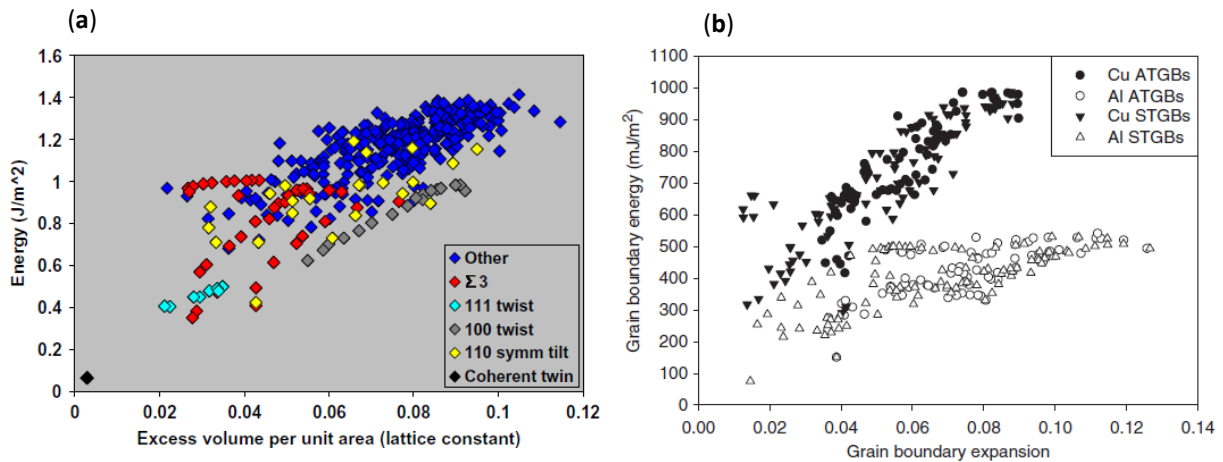


Figure 1.23 – The computed grain boundary energies for (a) Ni and (b) Cu/Al plotted against GB expansion. [Olmsted2009] [Tschopp2007]

D. Wolf [Wolf1990] has reported the investigation of the role of the local coordination at the interface (*figure 1.24*). This idea is based on the number of the broken nearest-neighbor bonds, the limitation is that only dislocation cores give rise to broken bonds, the elastic strain field is not concerned. A broken bonds description is therefore fully applicable for *HAGBs*.

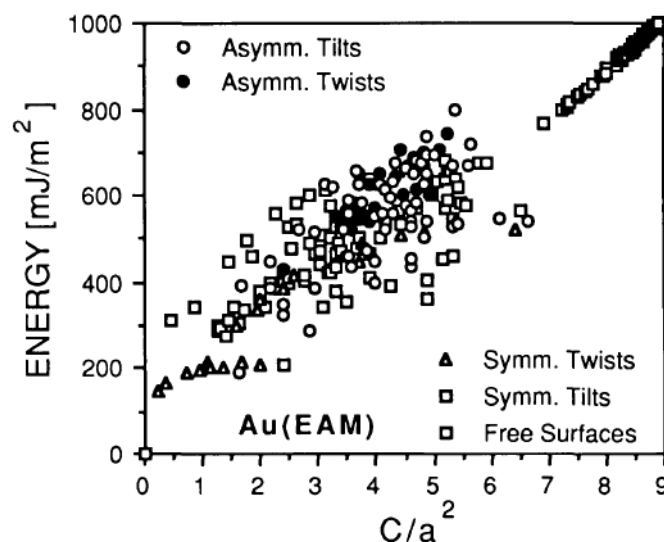


Figure 1.24 – The computed grain boundary energies against the number of broken nearest-neighbor bonds per unit area. [Wolf1990]

III.4 Defects in grain boundary

GB is a type of planar defects, not as the ideal GB model, at any temperature differing from 0 K, the real GB involves several defects such as impurities, precipitates, triple junctions, interstitials, vacancies and dislocations. These defects have often higher densities in GB than in the bulk. The interaction of defects with GBs in metals is a crucial subject and is still far from its complete understanding. Experimentally, it is difficult to directly reveal these defects owing to the low concentration of atoms in GB core.

The point defects in GBs play a key role in recovery, creep, radiation damage, and solutes transport phenomena [Sutton1995]. Suzuki *et al* [Suzuki2003] have studied interstitials and vacancies in Cu and Al GBs. Table 5 summarizes the vacancy and interstitial calculated formation energies by EAM, the vacancy formation energy is lower than the interstitial formation energy. The vacancy formation in Σ 3 nickel GBs has been studied by Hallil *et al* [Hallil2016]. Figure 1.25 gives the collected vacancy formation information in GBs.

Table 1.4 – Formation energies (eV) of vacancies and interstitials in Cu, Al and Ni. The experimental data are given in parentheses. [Suzuki2003][Hallil2016]

| Defects | Cu | Al | Ni |
|---------------------|--|--------------------------------------|---|
| Vacancy | 1.272 (1.27 ^a , 1.28 ^b) | 0.707 (0.68 ^c) | 1.59 (1.49 ^d , 1.55 ^e) |
| Interstitial | 3.066 (2.8-4.2 ^f) | 2.178 | |

a:[Siegel1978], b: [Balluffi1978], c:[Schaefer1987], d:[Johnson1965], e: [Matter1979], f: [Young1978]

Tschopp *et al.* [Tschopp2012] have reported their interesting results of a vacancy in α -Fe GBs (*figure 1.25* (e and f)), they particularly highlighted that vacancy-GB interactions are more pronounced for the high energy GBs since the vacancy formation energy is far lower. The vacancy binding energy is the difference between the vacancy created in GB and that created in the perfect bulk. The vacancy formation energy in the GB core is much lower than in the bulk, however, this energy is highly non-uniform within the GB core and extremely dependent on the GB structures.

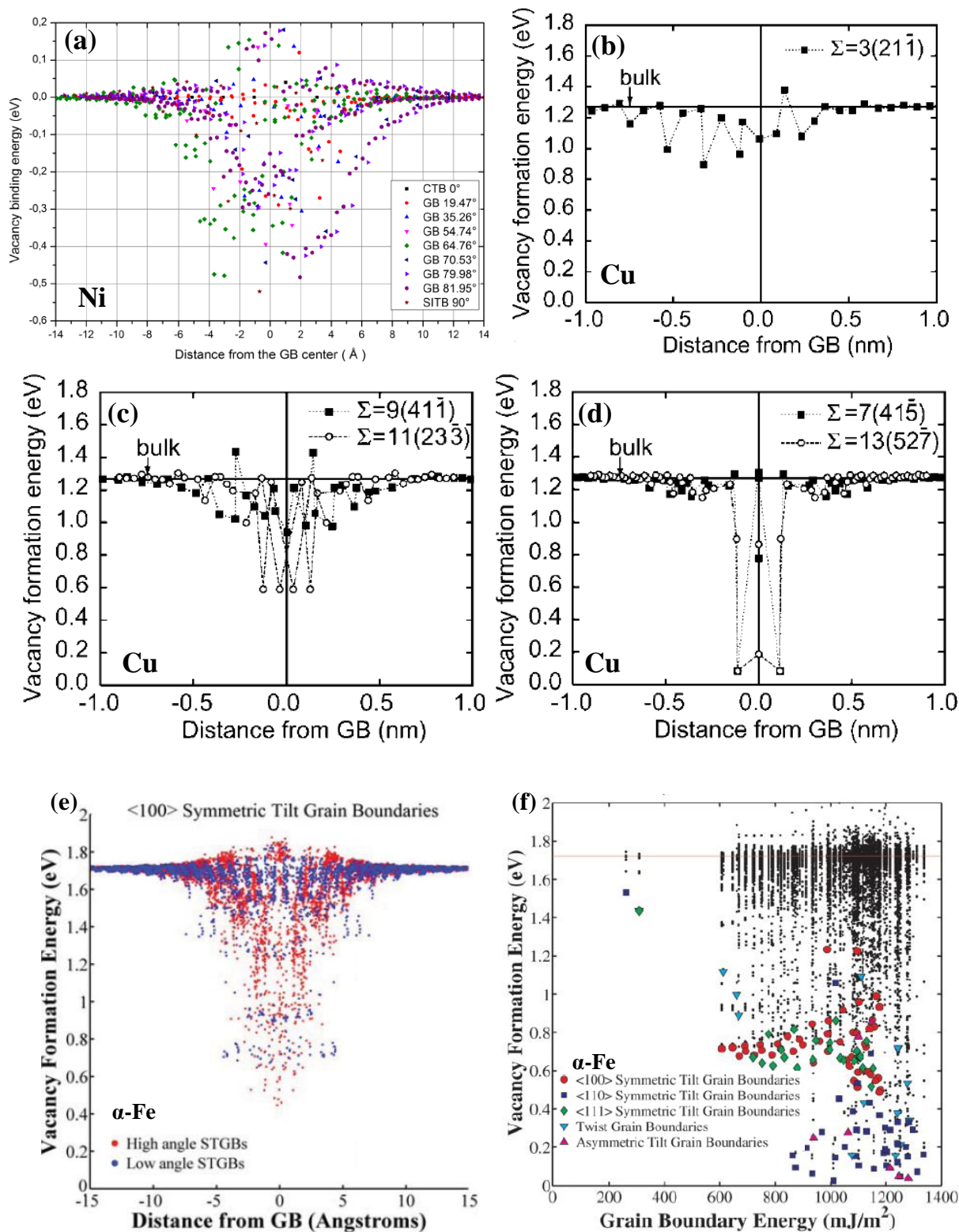


Figure 1.25 – (a) Vacancy binding energy as a function of the distance from the Ni Σ 3 GB core, (b) vacancy formation in Cu GB, (c) vacancy formation energy in [011] symmetrical tilt Cu GBs, (d) vacancy formation energy in [111] symmetrical tilt Cu GBs, (e) vacancy formation energies as a function of distance from the grain boundary for $\langle 100 \rangle$ symmetric tilt grain boundaries, (f) vacancy formation energies as a function of the grain boundary energy for all types symmetric tilt grain boundaries. [Suzuki2003] [Tschopp2012] [Hallil2016].

Figure 1.26 displays the vacancy formation energy versus the GB energy, for high energy GBs, the vacancy formation energy is dramatically lowered. Furthermore, interstitials are highly localized within the GB core since the interstitial formation energy in GB core is lower than in the bulk (figure 1.27). All these defects have strong interactions with higher energy GBs, since their formation energy is low in these GB core.

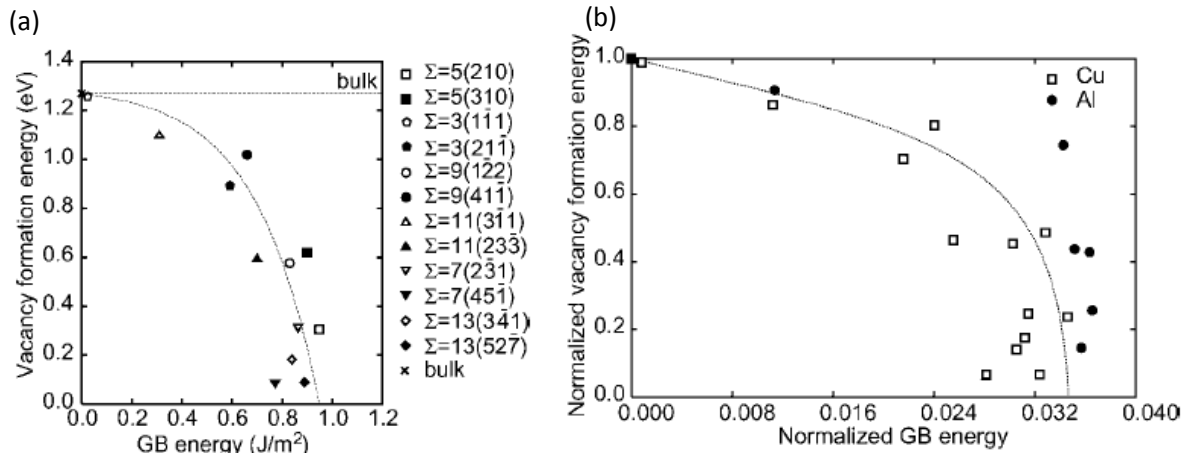


Figure 1.26 – (a) Vacancy formation energy as a function of the GB energy in Cu, (b) normalized vacancy formation energy against GB energy in Cu and Al [Suzuki2003].

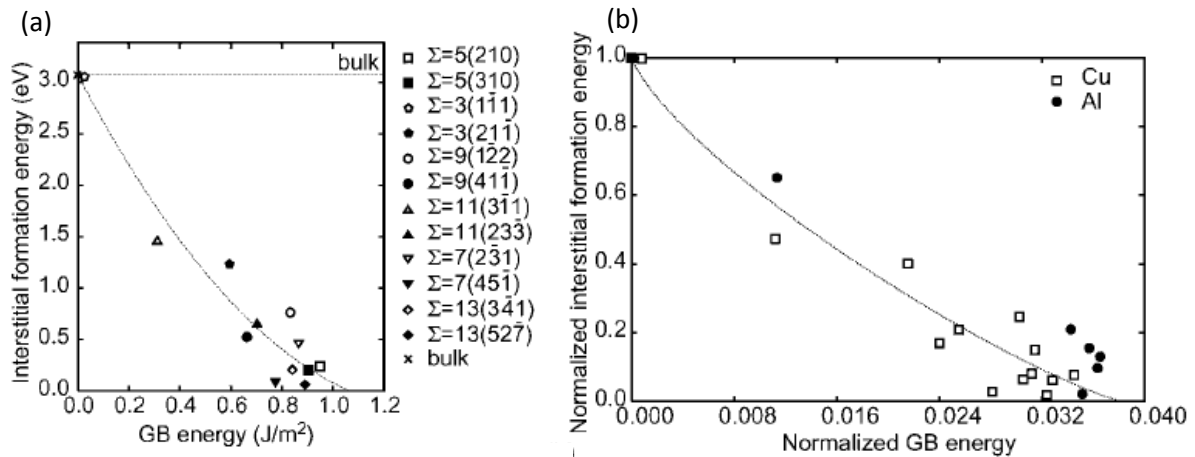


Figure 1.27 – (a) Interstitial formation energy as a function of the GB energy in Cu, (b) normalized interstitial formation energy against GB energy in Cu and Al [Suzuki2003].

When linear defect lattice dislocations interact with a grain boundary, isolated linear defects (in that sense that they are not arranged in periodic networks) are formed within the GB. These defects, called *extrinsic dislocations*, we distinguish *intrinsic dislocations* which are a part of GBs. Dislocations interactions with GBs play an important role in the strengthening of metallic systems, crack initiation, stress corrosion cracking, irradiation embrittlement, as well as embrittlement due to sergents such as hydrogen at GBs [Martin2012, Zhevnenko2011, Auger2011, Nam2009]. The origin of the extrinsic dislocation comes from the exterior of GB, most often from the adjacent crystals, the GBs play the

role of the sink for lattice dislocations; the extrinsic dislocation can also be considered as the faulted GB which means out of the equilibrium grain boundary structure, whatever the dislocation origin [Priester2013]. Figure 1.28 gives simple examples of extrinsic dislocations within GBs, the periodic arrangement is broken by the presence of extrinsic dislocation.

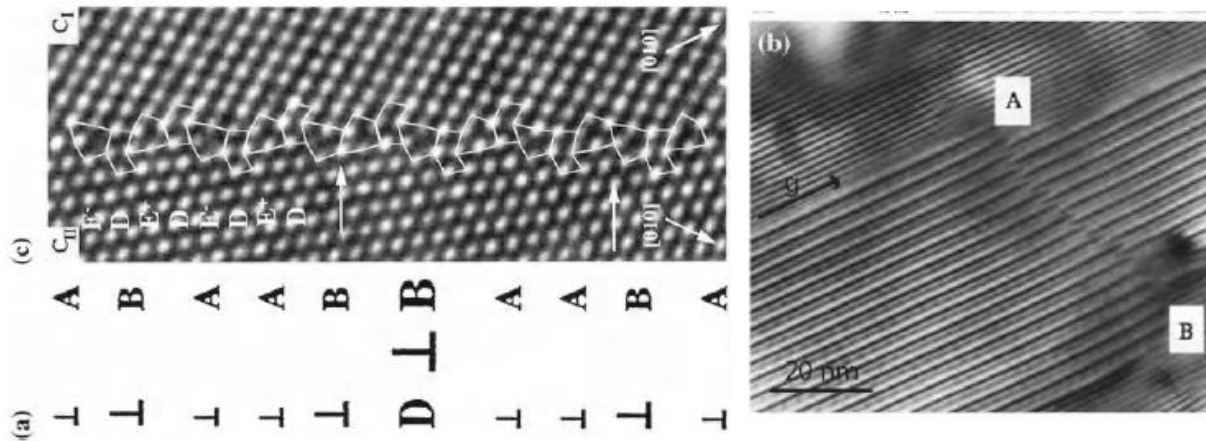


Figure 1.28 – (a) An extrinsic dislocation D introduces a break of periodicity in the GB structure described in terms of structural units A and B; (b) The extrinsic dislocation AB induces a displacement of the intrinsic dislocation network parallel to $g = \langle 110 \rangle$ in a low angle twist grain boundary in gold; (c) Atomic structure of a $\Sigma = 11 \{332\}$ tilt grain boundary in nickel: the period is constituted by two D units of the $\Sigma = 3 \{111\}$ boundary and two E units of the $\Sigma = 9 \{221\}$ boundary [Poulat2000, Priester2013].

Dislocations interact with GBs are more pronounced and are fundamental to the properties of polycrystalline materials, several phenomena need still a better understanding due to the complexity of GB structure such as the movement of a dislocation in and through a network of GB dislocations, the transmission of a crystal lattice dislocation across a GB and the absorption of dislocations by GBs. Dislocation slip transmission in FCC metals has been studied by Kurtz *et al.* [Kurtz2003] and Robertson *et al.* [Robertson2014]. An example of dislocations crossing twin boundary is shown in the figure 1.29 (a), where dislocations are trapped at in the twin boundary and intersect at boundary 2. No transmission occurred through this GB. This phenomenon highlights that dislocation interactions with GBs are dependent on the GB structure. Comparisons of different types GBs are given in the figure 1.29(b) and figure 1.29(c), the energy barrier of dislocation and the dislocation nucleation are correlated with the GB energy, GB with lower energy present stronger barriers to slip transmission and dislocation nucleation.

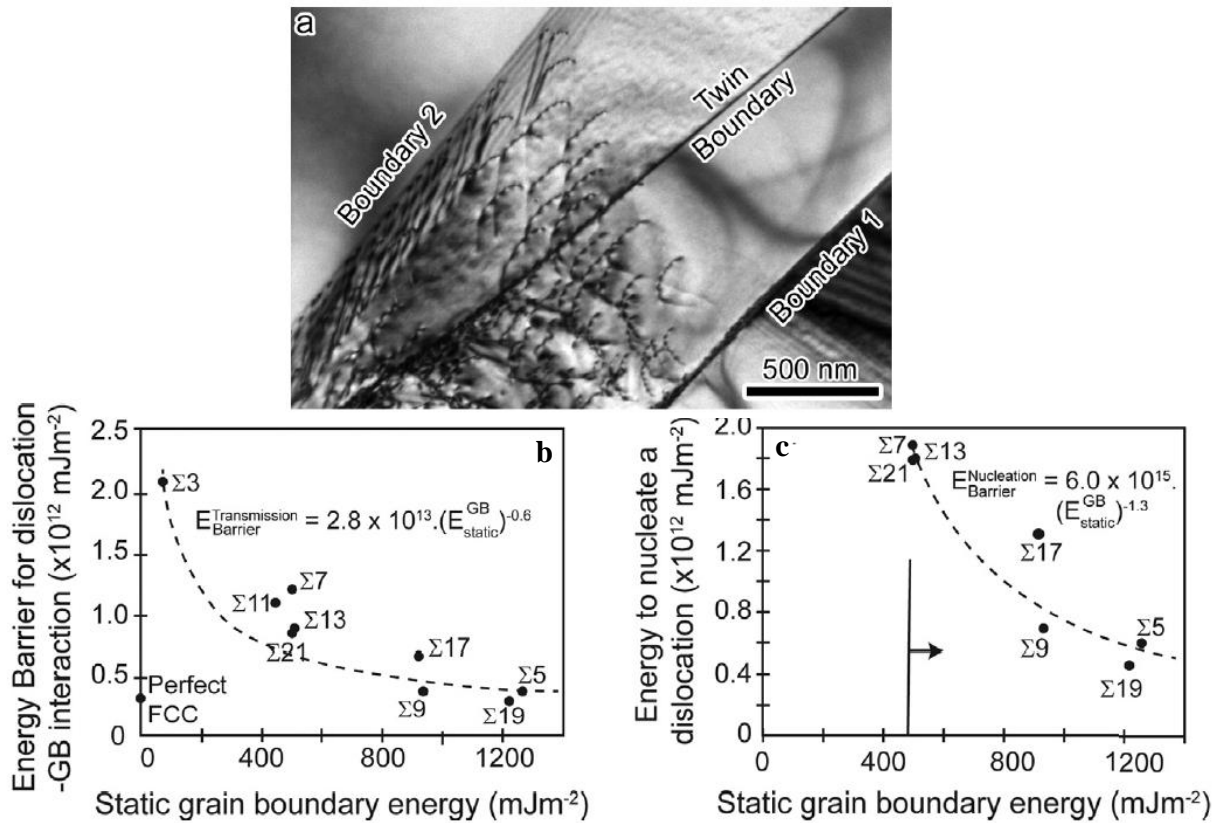


Figure 1.29 – (a) Bright-field electron micrograph showing screw dislocations interacting with a twin boundary in *a*-Ti, (b) energy barriers plotted against the static grain boundary energy for various types of coincident site lattice grain boundaries for slip penetration into the grain boundary and (c) slip nucleation from the grain boundary [Robertson2014].

IV. Hydrogen in GBs-Intergranular segregation and diffusion

Hydrogen has a strong tendency to segregate in, or interact with structural defects as dislocations and internal interfaces. This tendency affects the solid solubility and the mobility of hydrogen and consequently modifies the embrittlement process. Hydrogen segregation controls the properties of hydrogenated materials in many cases (hydrogen diffusion, hydrogen induced cracking, electrical properties in semiconductors, etc.) and more precisely their mechanical behavior (embrittlement itself). While segregation and diffusion of hydrogen at grain boundaries has been of great interest, the difficulty of hydrogen analysis has limited the number of studies carried out. The brief description of hydrogen - GB interactions is introduced with a focus on its relationship with GB diffusion and GB segregation.

IV.1 Grain boundary segregation

The interactions between point defects and linear or planar defects lead to a decrease of the total free energy of the system and a relaxation of the defects. Concerning grain boundaries, the segregation is complicated since real GBs involves other types of defects. For example, the segregation of hydrogen is enhanced by the presence of impurity such as Sulphur. However, Carbon gives an opposite behavior [Aucouturier1982]. Grain boundary segregation strongly modifies the grain boundary behaviors; the solute content in boundaries may be very high even though the elements are in a very small amount in the crystals.

With the assumption of an infinitely diluted solution, the segregation energy of a solute atom located at site i , E^{seg} , is given as

$$E_i^{seg} = E_i^{tot} - E_b^{tot} \quad (\text{Eq.1.8})$$

E_i^{tot} is the total energy of the relaxed system with a solute atom located at site i , E_b^{tot} is the total energy of the relaxed system with a solute atom located at a bulk site. A negative value of segregation indicated that the corresponding site is favourable to segregation.

IV.1.1 Driving force of segregation

Grain boundary segregation can be seen as a rejection of solute from crystals. Much of the effects thus are explained on the basis of the bulk solubility limits and controlled by two types of factors, steric and electronic. The energy of solute in GB is lower after the relaxation, at a fundamental level, all the effects come from an electronic origin; but it is convenient to separate the elastic from the electronic effects; most often the consideration of the first ones is sufficient to understand the interactions between solutes and grain boundaries and to obtain the segregation energies with a good accuracy. [Priester2013]

The energy of segregation is thus regarded as the sum of a “chemical” term due to the breaking of strong distortion of chemical bonds and an “elastic” term due to the deformation elastic energy [Lezzar2004].

$$E_i^{seg} = E_i^{chem} - E_i^{elas} \quad (\text{Eq.1.9})$$

The second term, E_i^{elas} , is related to the deformation elastic energy. It is the elastic energy gained by the system when a solute atom segregates from a bulk position to the interface. [Pines1940, Friedel1954, Maclean1957, Eshelby1956]

$$E_i^{elas} = \frac{24\pi B_i \mu_M r_i r_M (r_i - r_M)^2}{3B_i r_i + 4\mu_M r_M} \quad (\text{Eq.1.10})$$

B_i is the bulk modulus of the solute and μ_M the shear modulus of the solvent. Variables r_i and r_M have been defined as the atomic radius of the solute and the solvent, respectively. The interaction energy for the segregation equal to the elastic strain energy decrease resulting from the fact that an atom too large (or too small) for a crystal site finds a more adapted site in the grain boundary.

The elastic modulus effects are generally less pronounced than those linked to the size, the influences come from three different aspects. The first aspect is the difference between the solute and the matrix, an interaction is linked to the elastic energy stored in the inserted solute that depends on the GB stress field (dilatation + shear). The second aspect is the difference between the matrix and the GB, the GB is often considered as a soft medium compared to the bulk, the solute atom with corresponding strain energy decreases when this solute atom is located in GB. The final aspect is the difference between two crystals on each side of GB in an anisotropy medium. All three effects depend on the elasticity modulus and are a function of the grain size.

IV.1.2 Experiments of segregation in polycrystals

There is little available experimental data of the hydrogen segregation for well-defined GBs, because a well characterized GB is still an engineering challenge, especially the crystallographic orientation and the misorientation angle need be well controlled. Oudriss *et al.* [Oudriss 2012b] have reported that the GBs with low misorientation ($\Sigma 1$) and a category of “special” boundaries ($\Sigma 3 - \Sigma 29$) are usually preferential areas for hydrogen segregation. In fact, considering their ordered structure, this kind of boundary is accommodated by defects (dislocations, vacancies) that represent potential traps of hydrogen, which can affect the diffusion mechanisms.

The hydrogen distribution in nickel polycrystals has been studied by Osman Hoch *et al.* [Osman Hoch2016] using SEM-EBSD analysis and ToF-SIMS analysis. *Figure 1.30* gives an example of the hydrogen distribution following a scan line, four types of profiles can be obtained: a gap where instantaneous variation of hydrogen content is observed when we cross the GB, a constant profile where no significant modification of hydrogen content is related to both grains around GB, a break where the profile evolved crossing a GB and a gradient of hydrogen content for both sides of GB.

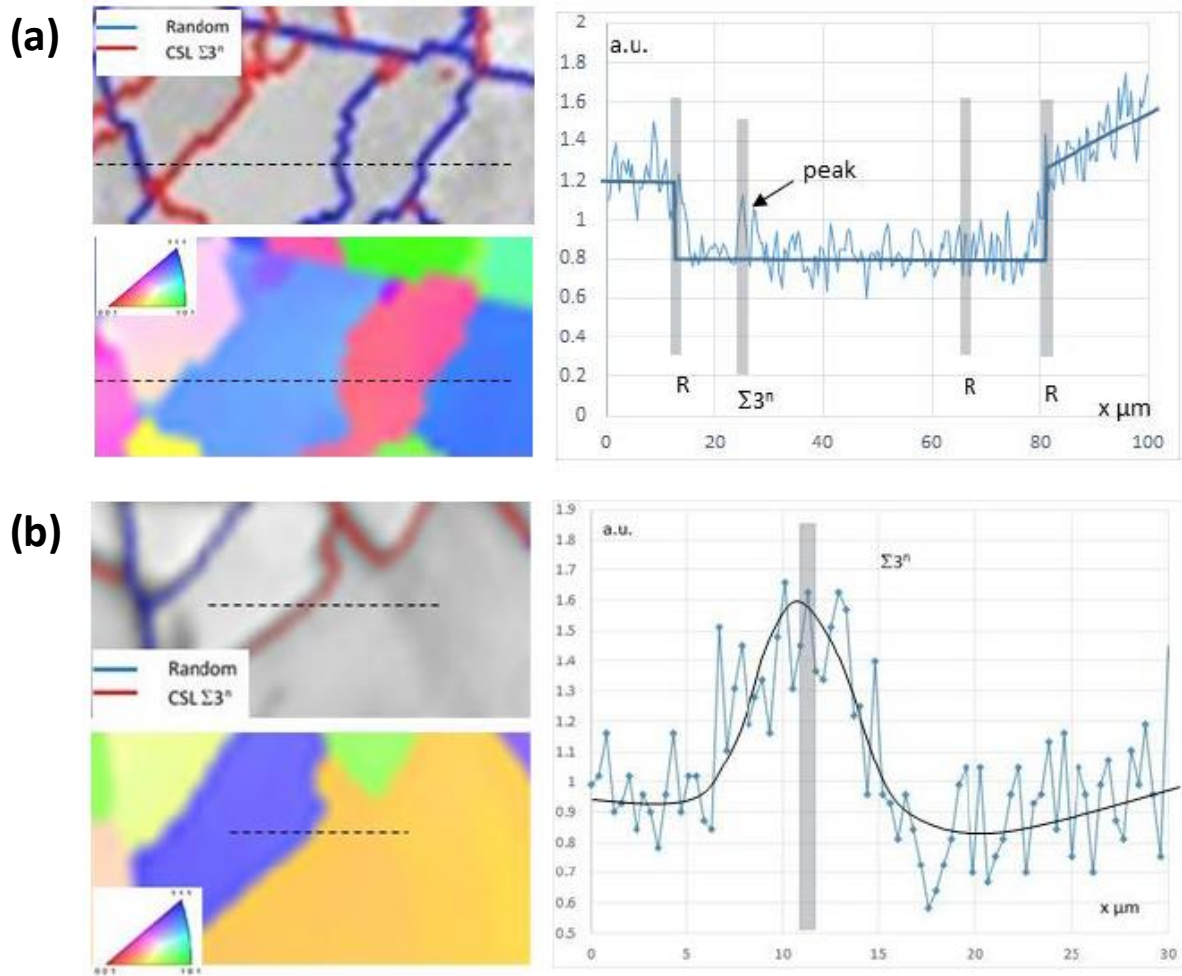


Figure 1.30– (a) Line profile position in EBSD scan, (b) Normalized ^1H signal intensity versus the position along the line. [Osman Hoch2016].

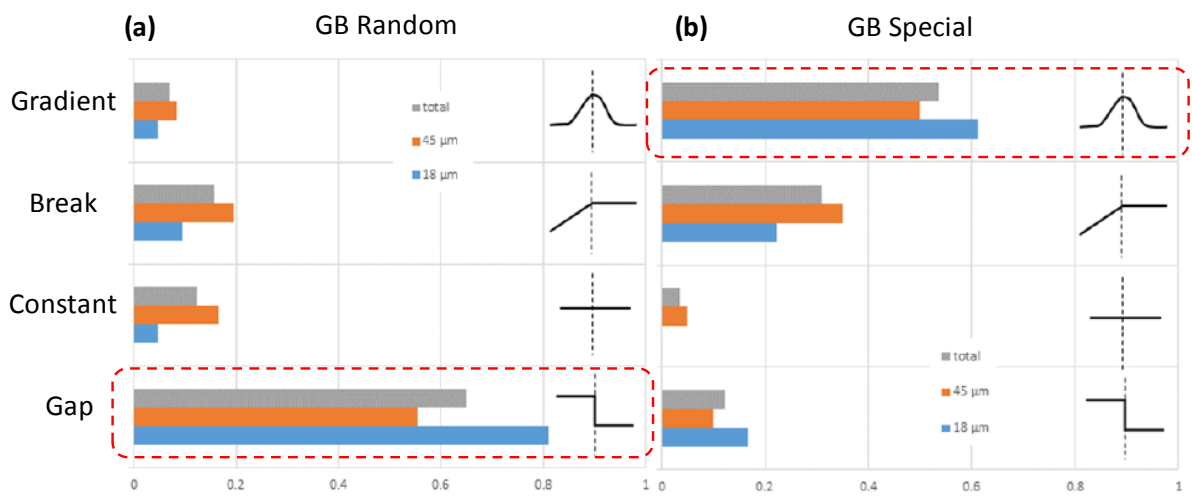


Figure 1.31 – (a) GB fraction for the type Random, the Gap profile is the major hydrogen distribution form (b) GB fraction for the type Special, the Gradient profile is the major hydrogen distribution form [Osman Hoch2016].

Figure 1.31 presents a statistical study of the hydrogen distributions in nickel polycrystals (Grain sizes are 45 and 18 μm), the results are presented for different GB fractions. Considering the hydrogen local profiles around GBs, two main situations were observed for hydrogen in relation with the GB category (Random or Special). A gap for hydrogen concentration was mainly detected near random boundaries. In opposite, a gradient of hydrogen was observed near most of the special boundaries which links directly to the hydrogen trapping. This result evidences the significant impact of GB character on the hydrogen distribution.

IV.1.3 Atomic approaches of segregation in GBs

Atomic simulations can construct GBs with good accuracy since the atoms arrangement can be controlled, and now we have opportunities to study some particular GBs. All GBs are more or less sensitive to solute segregation. Based on ab initio calculations, Matsumoto *et al.* [Matsumoto2011] have investigated the hydrogen-GBs interactions of $\langle 110 \rangle$ symmetrical tilt grain boundaries (STGBs) in bcc Fe under a gaseous hydrogen environment by using density functional theory, figure 1.32 shows that high-energy GBs have large gaps, and many hydrogen atoms are captured at these spaces. Thus, GBs with higher GB energy are more influenced by hydrogen.

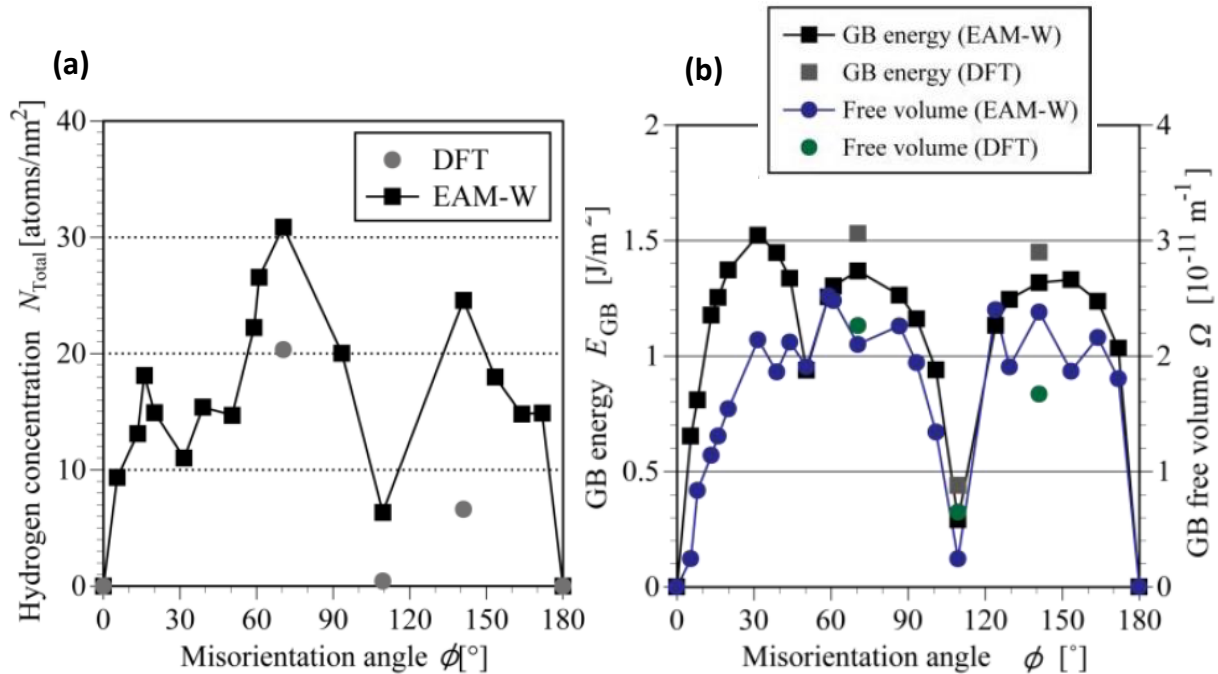


Figure 1.32 – (a) Hydrogen concentration at $\langle 110 \rangle$ axis STGB under gaseous hydrogen environment (300 K, 70 MPa), (b) Dependence of GB energy and GB free volume on the misorientation angle of $\langle 110 \rangle$ axis STGB [Matsumoto2011].

Du *et al.* [Du2011] have studied the interaction of H interstitials with grain boundaries in α - and γ -Fe, this investigation have compared the hydrogen segregation in 4 different GBs, such as $\Sigma 3\langle 110\rangle\{112\}$ bcc and $\Sigma 3\langle 110\rangle\{111\}$ fcc Fe GBs as representatives for dense and the $\Sigma 5\langle 001\rangle\{310\}$ bcc and $\Sigma 11\langle 110\rangle\{113\}$ fcc Fe GBs as examples for more open interface structures. ab initio calculations show that even in the case of simple GBs many different situations occur: $\Sigma 3$ and $\Sigma 5$ GBs in bcc Fe trap hydrogen and slow down hydrogen diffusion while, in fcc Fe, the $\Sigma 3$ GB repels hydrogen and the $\Sigma 11$ traps hydrogen and offers an easy diffusion path parallel to the GB plane. The corresponding high local concentration does not act as a seed for a local hydride, as the case for Ni. Similar results have been reported by Chen *et al.* [Chen2016] in polycrystalline Ni, their calculations suggest that the hydrogen binding at the interstitial site in GB layer is found to be less favorable as compared to the bulk octahedral site for all the coverages considered, in contrary to oxygen, which prefers interstitial sites at the GB layer. Thus, the hydrogen atoms prefer to be in the bulk as compared to the $\Sigma 3$ (111) CTB suggesting that the presence of $\Sigma 3$ (111) CTBs renders high resistance to hydrogen segregation. The local geometric structure for the hydrogen segregation positions are given in *figure 1.33(a)*, most interstitial sites resemble slightly distorted tetrahedral/octahedral sites as in bcc/fcc iron, respectively. Similar works are reported by Song *et al.* [Song2016] in fcc metals (*figure 1.33(b)*), they give five principal types of polyhedrons are involved: i.e., tetrahedron (TET), octahedron (OCT), pentagonal bipyramid (PBP), cap trigonal prism (CTP), and bitetrahedron (BTE).

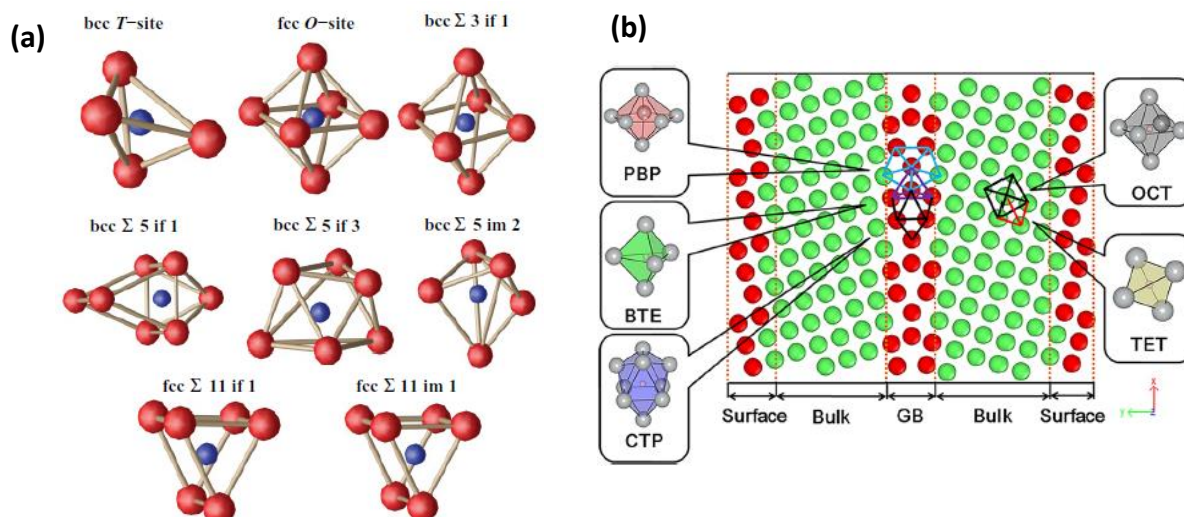


Figure 1.33 – (a) Local coordination of interstitial sites, if: interface, im: intermediate, (b) Schematic illustration of a polyhedron in representative $\Sigma 5\{130\}\langle 100\rangle$ GB and bulk lattice. The gray ball in the distinguished polyhedron represents the host Ni atom, and the small pink ball in the center is the hydrogen atom. [Du2011][Song2016].

Shen *et al.* [shen2014] have investigated the hydrogen segregation in $\Sigma 9\{2\ 2\ 1\}[1\ 1\ 0]$ symmetric tilt grain boundary in Al. They report approximate hydrogen segregation energy maps for the two most

stable structures in *figure 1.34*. Black and white balls represent two $\{2\ 2\ 0\}$ planes. The small balls represent stable interstitial positions for isolated hydrogen atoms. The “E” structural units are underlined, as well as a CSL unit cell. The core of the E structural unit offers a large density of trap sites, with energies of the order of -0.3 eV/at, including non-negligible zero-point energy (ZPE) corrections. In the case of the mirror symmetrical structure (GB2), the ‘twin’ like units are found to be unstable upon hydrogen segregation. Hydrogen triggers local distortions to transform GB2 into GB1. This gives an interesting mechanism where interfaces of slightly higher energy than the optimum have more flexibility to rearrange and offer favorable local environments for hydrogen.

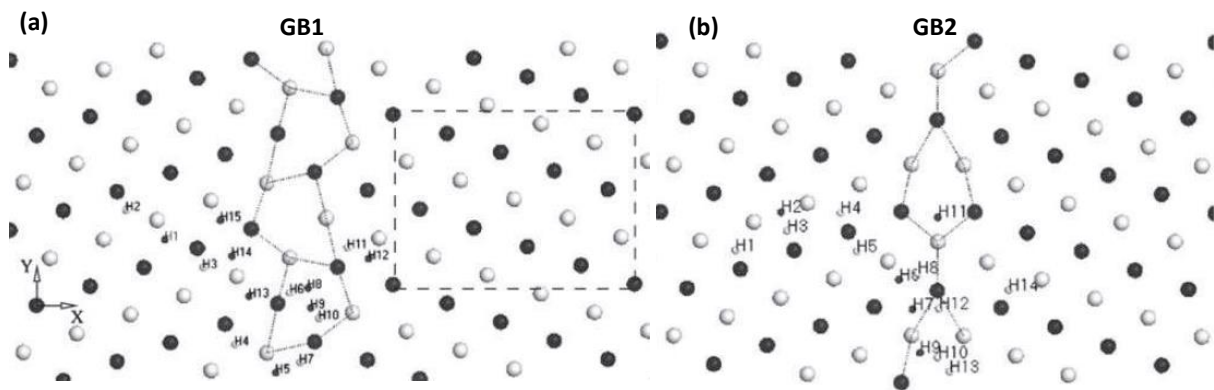


Figure 1.34 – (a) Atomic structure of the symmetric grain boundary (GB1) after relaxation with DFT. (b) ‘Mirror symmetric’ (GB2) atomic structure [Shen2014].

Based on MD/MC simulations, larger systems can be investigated. Moody *et al.* [Moody1991] have studied the equilibrium segregation of hydrogen in tilt $\Sigma 9\{2\ 2\ 1\}[1\ 1\ 0]$ grain boundary in nickel. Hydrogen concentration is enhanced at this GB, *figure 1.35(a)*, (b) show that hydrogen first occupies the high energy polyhedral sites along the grain boundary, after that hydrogen then occupies the lower energy dilated octahedral sites near the grain boundary until all sites are occupied. A second major finding is that the tilt boundary concentration increases as chemical potential increases until all sites are occupied as shown in *figure 1.35(c)*. The simulations also indicate that insignificant changes in grain boundary structure occur as trap site occupancy increases. This indicates that there is a limit to any effect that hydrogen-induced dilation has on hydrogen concentration in the boundary region. However, the existing prediction that hydrogen induces significant lattice rearrangements in the boundary region raises questions as to the roles of hydrogen-defects and GBs-defects interactions.

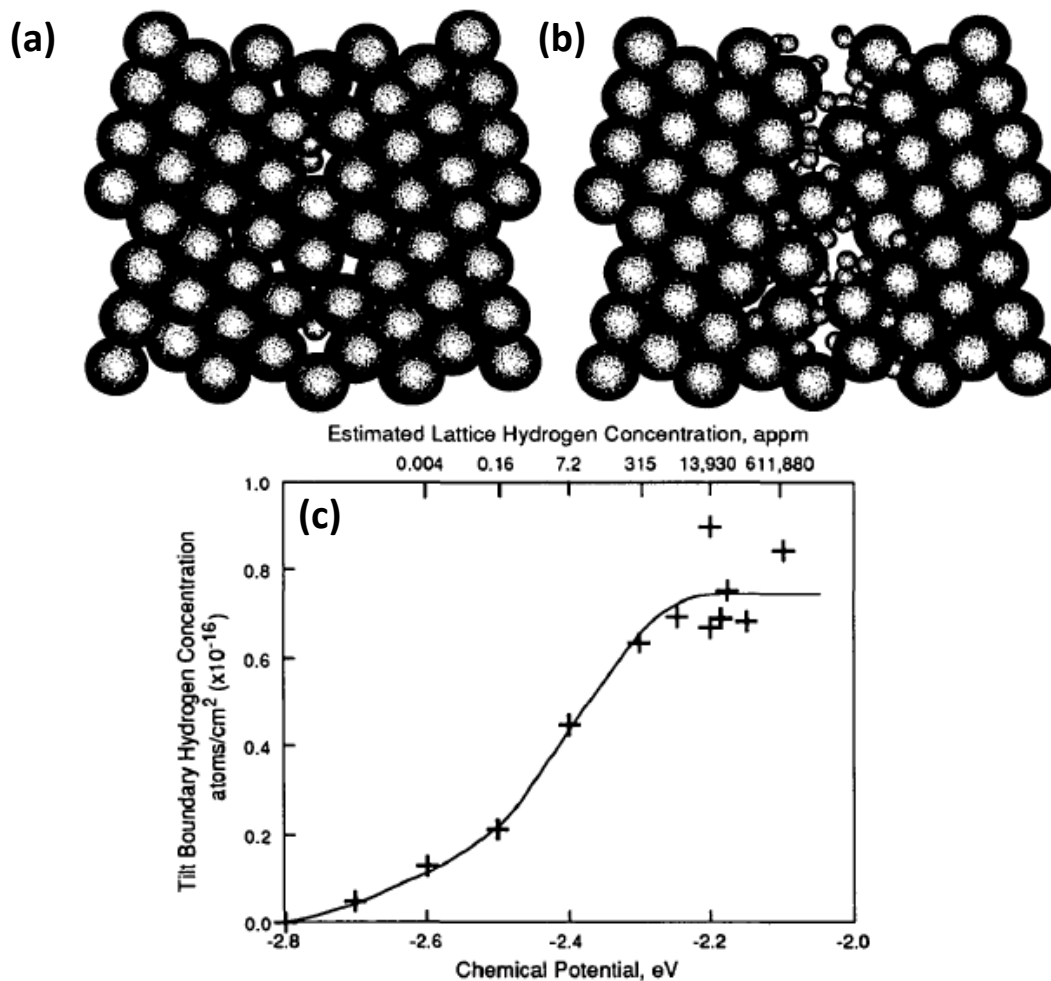


Figure 1.35 – (a) hydrogen first occupies the high energy polyhedral defect sites and then (b) fills all trap sites at high hydrogen concentrations, (c) The tilt boundary concentration increases as chemical potential increases until all sites are saturated. [Moody1991].

Solanki *et al.* [Solanki2012] have reported their results for pure α -Fe with a single H atom at an interstitial and vacancy site, and two H atoms at an interstitial and vacancy site for each of the $\langle 100 \rangle$, $\langle 110 \rangle$, and $\langle 111 \rangle$ symmetric tilt grain boundary (STGB) systems. Simulation results show that the GB system has a smaller effect than the type of hydrogen defect configuration (interstitial H, H-vacancy, interstitial 2H, and 2H-vacancy). The segregation energy of hydrogen configurations as a function of distance is comparable between symmetric tilt GB systems in *figure 1.36*. The highest segregation energy is 2H at the interstitial site, this implies that there is a large binding energy associated with two interstitial H atoms in the GB. However, segregation is more stable at vacancy site for 1H.

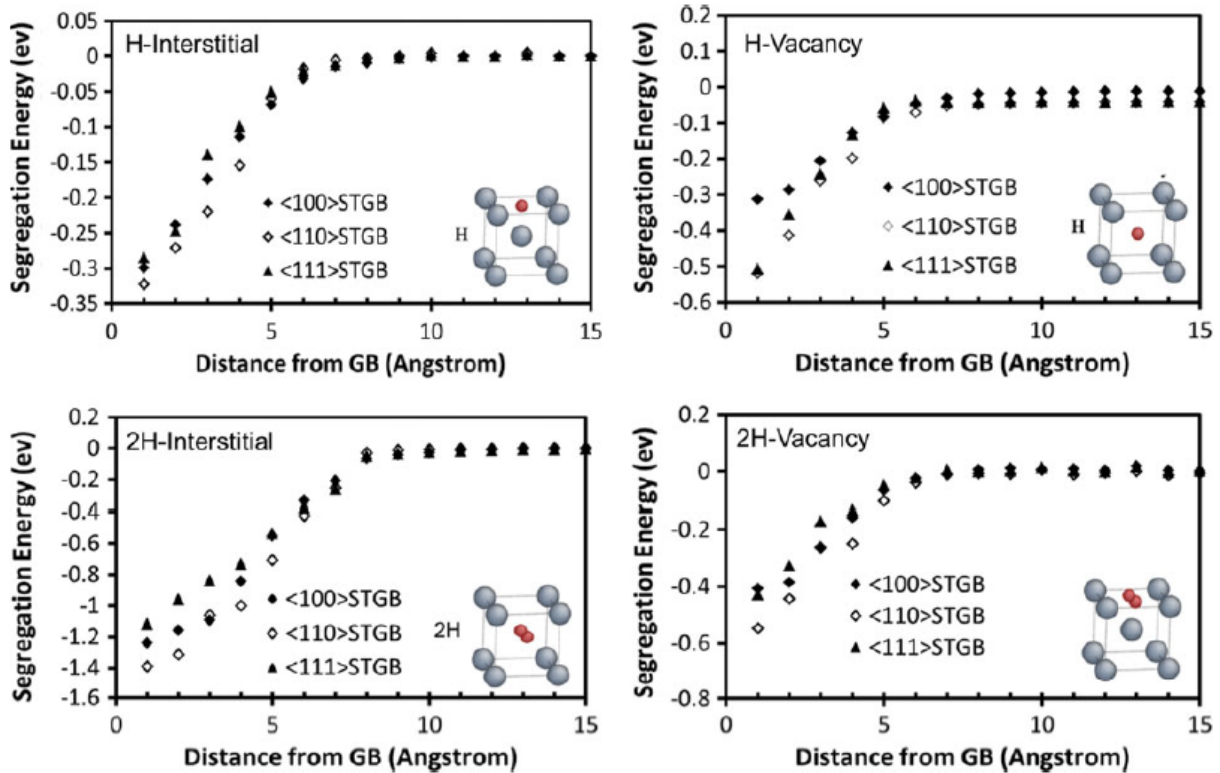


Figure 1.36 – The mean H segregation energy as a function of the GB distance, tilt system type and different H configurations. The type of GB system has a smaller effect than the type of H configuration. Also, the GB has a characteristic hydrogen segregation length scale that is 5 to 8 Å [Solanki2012].

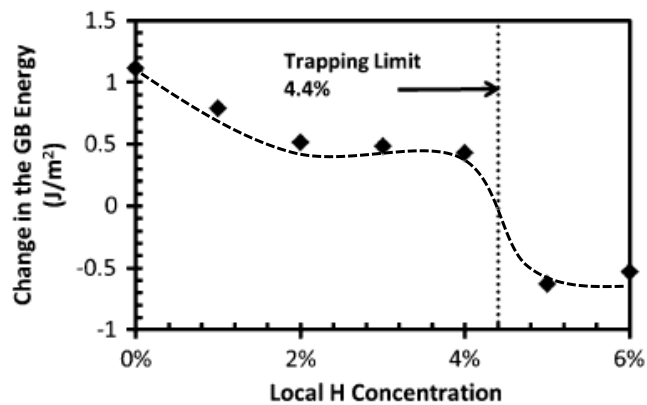


Figure 1.37 – Calculated GB segregation energy as a function of local hydrogen concentrations for the Σ 53(720) $\theta = 31.89$ deg STGB with [Solanki2012].

Another finding is that there is a strong correlation between the GB character and the trapping limit (saturation limit) for hydrogen. In *figure 1.37*, as the change in grain boundary energy approaches zero, there is no significant energy to be gained from further trapping hydrogen atoms at the boundary, this transition demarcates the trapping limit of hydrogen for this particular boundary. The local H trapping limit for the Σ 53 (720) $\theta = 31.89$ deg STGB was found to be 4.4 % (~23 H atoms), which results in decohesion of the Fe GB by hydrogen in a cleavage manner. A higher trapping limit GB is Σ 17(410) $\theta = 28.07$ deg STGB which can achieve to 7%.

Recently, J.O'Brien and M.Foilles [J.O'Brien2016] have studied the hydrogen segregation in inclined $\Sigma 3\langle 110 \rangle$ nickel GBs using the hybrid MC/MD and an analytic segregation model. The degree of segregation of hydrogen to inclined twin grain boundaries is provided in *figure 1.38* at saturated values of 30, 2000 and 3000 appm at 300, 500 and 600 K, respectively. The maximum concentration of hydrogen occurs at the boundary at the inclination with the highest enthalpy, $\Phi = 70.53^\circ$.

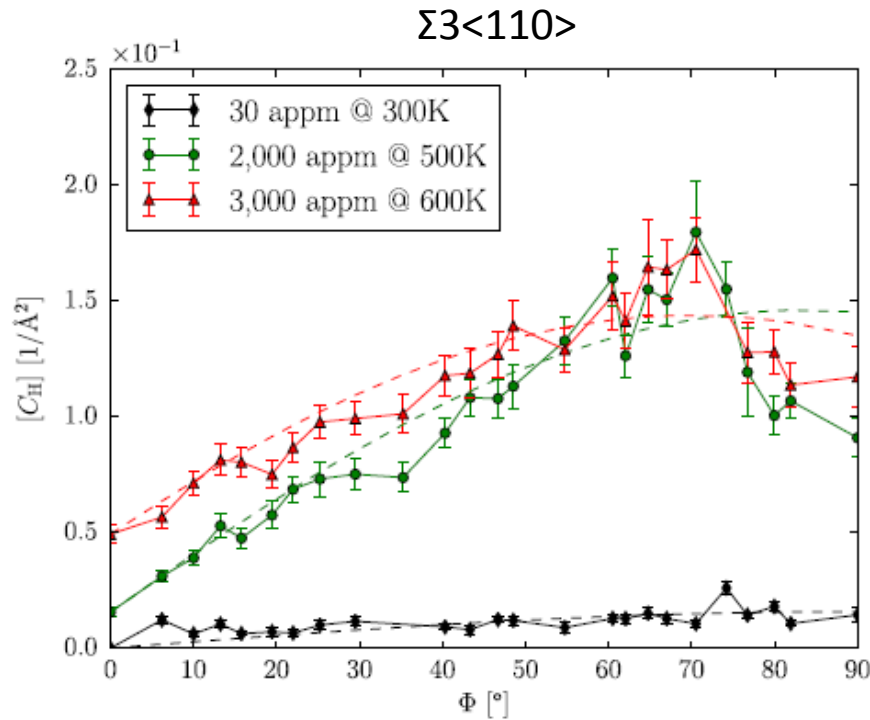


Figure 1.38 – The excess hydrogen concentration as a function of the inclination angles for different temperatures [J.O'Brien2016].

Actually this result gives also a correlation between the hydrogen segregation and the GBs energy since previous results show that the GB energy increase with the inclination angle for the nickel GB $\Sigma 3\langle 110 \rangle$. The hydrogen segregation phenomenon is more pronounced for high energy GBs which may be explained by the high excess volume for these GBs.

IV.2 Grain boundary diffusion

IV.2.1 Grain boundary diffusion model

The description of grain boundary diffusion is usually based on the classical model first proposed by Fisher [Fisher1951, Mehrer2007, Lejcek2010]. The GB is represented by a semi-infinite, uniform, and isotopic slab embedded in an isotropic crystal perpendicular to its surface, the GB diffusivity D_{gb} is different from lattice diffusivity D (*figure 1.39*). The diffusion occurs in two ways (a) via the volume diffusion into the grains and (b) via the grain boundary diffusion along the interfaces. It is

usually considered that the GB diffusion is much higher than the lattice diffusion ($D_{gb} > D$). The atoms moving along the grain boundary may either continue in the grain boundary diffusion or diffuse perpendicularly to the interface into the grain regions adjacent to the boundary. The total concentration of the diffuser in the specimen is the result of two contributions: a concentration c_g , established either directly by in-diffusion from the source or by leaking out from the grain boundary and the concentration inside the grain boundary, c_{gb} .

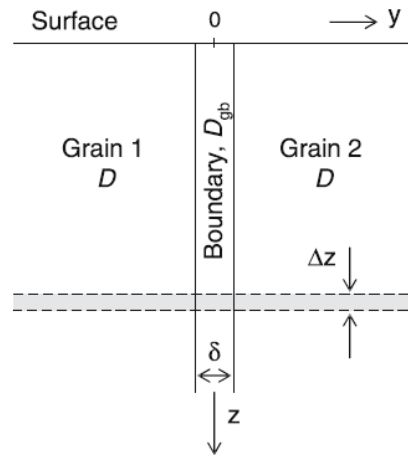


Figure 1.39 – Fisher’s model of an isolated grain boundary. D : lattice diffusivity, D_{gb} : diffusivity in the grain boundary, δ : grain boundary width [Mehrer2007].

Mathematically, this diffusion problem can be described by applying Fick’s second law to diffusion inside the grains and inside the grain boundary slab. Multiscale transitions are conducted using FEM approaches in the framework of diffusion in polycrystalline microstructures. Hydrogen diffusion in the membrane has been studied by Bouhattate *et al.* [Bouhattate2011], and later Legrand *et al.* have pushed this investigation to the polycrystalline aggregates with the homogenization method [Legrand2013]. The impacts of oxide layer and the hydrogen trapping on the diffusion process have been investigated, the diffusion was impeded by hydrogen trapping only when the trap density and the trap binding energy were high enough. If one of them was low, there were no observed effects of trapping. However, with strong trapping, a slowdown of hydrogen diffusion which led to an underestimation of the hydrogen diffusion coefficient and an overestimation of the effective subsurface concentration. Moreover, Osman Hoch *et al.* [Osman Hoch2015] have investigated the GB (Random and Special) diffusion considering the influences of GB topology and connectivity on the hydrogen effective diffusivity. The results highlighted the important effects of the microstructural constraints on the GB connectivity, and the fractions of triples junctions of different type are a more accurate indicator of the GB connectivity than the fractions of Random (or Special boundaries). Recently, the effects of stress state and hydrogen trapping on the diffusion process have been considered in the works of Ilin *et al.* [Ilin2015] and Charles *et al.* [Charles2017].

A general model is that the GB plane as a symmetry plane of the GB, the concentration field depends on the variables y and z , and the boundary conditions are then:

$$C_g\left(\pm\frac{\delta}{2}, z, t\right) = C_{gb}\left(\pm\frac{\delta}{2}, z, t\right) \quad (\text{Eq.1.11})$$

And at the interface between the grain and the grain boundary:

$$D\left(\frac{\partial C_g(y, z, t)}{\partial y}\right)_{|y|=\delta/2} = D_{gb}\left(\frac{\partial C_{gb}(y, z, t)}{\partial y}\right)_{|y|=\delta/2} \quad (\text{Eq.1.12})$$

Since the grain boundary width is very small ($\delta \approx 0.5$ nm) and $D_{gb} \gg D$, one can simplify the problem [Mishin1995] and arrive at the following equations:

$$\frac{\partial C}{\partial t} = D\nabla^2 C \quad (\text{Eq.1.13})$$

$$\frac{\partial C_g}{\partial t} = D\left(\frac{\partial^2 C_g}{\partial y^2} + \frac{\partial^2 C_g}{\partial z^2}\right) \quad \text{for } |y| \geq \delta/2 \quad (\text{Eq.1.14})$$

$$\frac{\partial C_{gb}}{\partial t} = D_{gb}\frac{\partial^2 C_{gb}}{\partial y^2} + \frac{2D}{\delta}\frac{\partial C_g}{\partial y} \quad \text{for } |y| < \delta/2 \quad (\text{Eq.1.15})$$

The equation (Eq.1.14) represents direct diffusion from the source into the lattice. In the equation (Eq.1.15), the first term on the right-hand side represents the concentration change due to diffusion in the grain boundary. The second term describes the concentration change due to leakage of the diffusing species through the ‘walls’ of the grain-boundary slab into the grains. The exact solutions of Fisher model have been developed by Whipple [Whipple1954] and Suzuoka [Suzuoka1964].

The GB segregation can be taken into account by introducing the segregation factor s , the relationship is written as [Gibbs1966]:

$$sC_g\left(\pm\frac{\delta}{2}, z, t\right) = C_{gb}\left(\pm\frac{\delta}{2}, z, t\right) \quad (\text{Eq.1.16})$$

The solute atoms in the GB maintain local thermodynamic equilibrium with the solute atoms in the lattice adjacent to the interfaces, the segregation is considered in local equilibrium at any depth z . The segregation factor is a function of temperature only and not a function of concentration, and have a significant influence on the diffusion process. Based on Fisher model, Harrison [Harrison1961] has proposed three regimes of GB diffusion which depend on the relative magnitudes of the lattice diffusivity and the GB diffusivity (*figure 1.40*). Each regime prevails in a certain domain of annealing

temperatures, annealing times, grain sizes, lattice and GB parameters. The knowledge of the diffusion regimes is important for designing diffusion experiments and for the interpretation of their results. This is because the shape of the diffusion profile depends on the dominating kinetic regime. Moreover, different GB diffusion parameters can be extracted in the various diffusion regimes, which therefore must be identified in dependable studies.

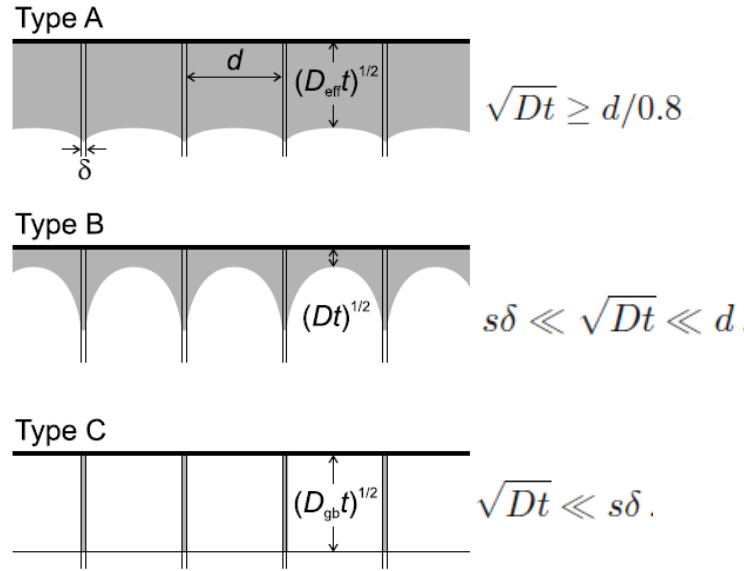


Figure 1.40 – Illustration of type A, B, and C diffusion regimes in a polycrystal according to Harrison’s classification; d is the grain size and δ is the GB width [Mehrer2007].

The type A is often observed at high temperature, or/and in materials with small grain size. The diffusion is almost planar with a penetration depth proportional to \sqrt{t} . On the macroscopic scale, the system can be approximated by a homogenized equivalent system with an effective diffusion coefficient D_{eff} .

$$D_{eff} = sgD_{gb} + (1 - sg)D \quad (\text{Eq.1.17})$$

$$g = \frac{q\delta}{d} \quad (\text{Eq.1.18})$$

Where q is a numerical factor depending on the grain shape. For example, $q = 1$ for parallel grain boundaries and $q = 3$ for cubic grains. Actually, the activation enthalpy of D is larger than that of D_{gb} , the enhancement due to grain boundaries becomes weaker with increasing temperature. Usually, at sufficiently high temperatures the effective diffusivity in coarse-grain polycrystals approaches the lattice diffusivity.

In the kinetic regime B, atoms diffuse faster along the GBs than inside the grains and the diffusion from adjacent GBs into the crystal do not overlap. The regime B is the most appropriate to the

experimental diffusion measurements because it happens for a wide range of annealing temperatures. For solute diffusion, the B regime diffusion profile character is described by the triple product, $P = s\delta D_{gb}$,

Type C kinetics corresponds to conditions where lattice diffusion is practically ‘frozen in’. Then, diffusion takes place along GBs only, without any essential leakage into adjacent grains. This situation can be matched in diffusion anneals at sufficiently low temperatures and/or for very short diffusion times. The GB diffusivity D_{gb} can be determined if type C kinetics profiles are measured, since grain boundary width, δ , can be approximated by a constant value $\delta = 0.5$ nm, the segregation factor is then obtained.

IV.2.2 Experiments of GB diffusion in polycrystals

The influence of GBs on the diffusion process of hydrogen in materials is still a controversial topic. The acceleration of hydrogen diffusion along GBs has been reported in several studies [**Ladna 1987**, **Louthan1975**, **Tseng1988**, **Harris1991**, **Brass1995**, **Oudriss2012b**], the idea is that GBs present short circuits paths due to their high free volume and high dislocation density compared to single crystals (*figure 1.41(a)*). Ladna and Birnbaum [**Ladna1987**] have investigated the effect of the grain boundary structure on the hydrogen distribution in nickel bicrystals and have shown the dependence of hydrogen diffusion on the nature of grain boundaries. They observed enhanced diffusion across the GB only along high energy GB ($\Sigma 9$ - $\langle 110 \rangle$) but not along lower energy symmetric tilt GB ($\Sigma 11$ - $\langle 110 \rangle$), however it is not sufficient to correlate the diffusion process with the GB energy since GB characters are anisotropic. T. Mutschele and R. Kirchheim [**Mutschele1987**] have highlighted the influence of hydrogen concentration on the GB diffusion process. The effective diffusion coefficient is dependent on the hydrogen concentration, being lower than the single-crystalline value at low H-contents due to the GB segregation and vice-versa for higher contents (*figure 1.41(b)*).

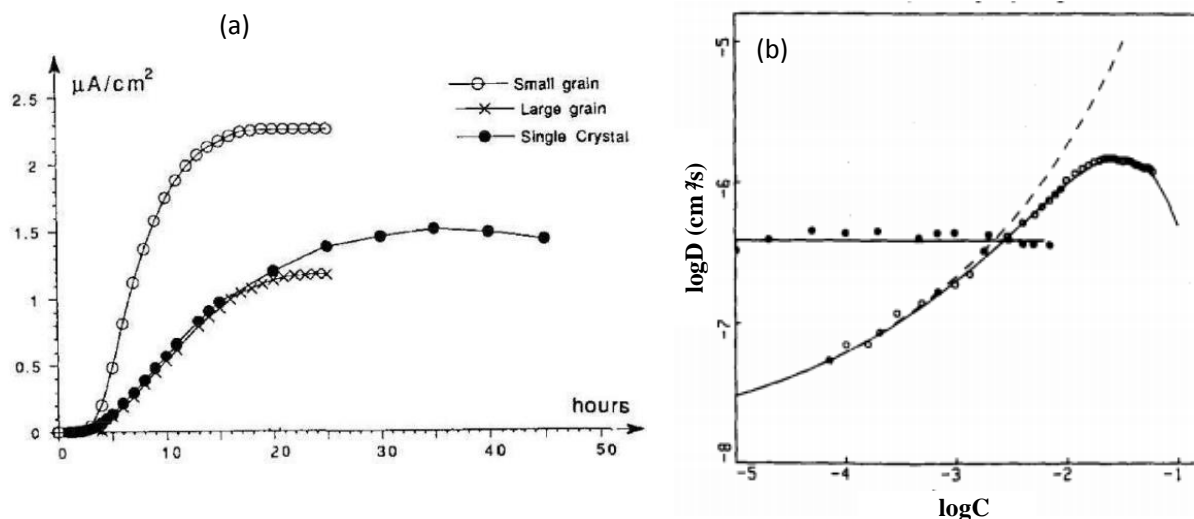


Figure 1.41 – (a) Hydrogen diffusion in nickel polycrystals with different grain sizes at 300K (b) Diffusion coefficient of hydrogen at 293K as a function of concentration in single-crystalline Pd (closed circles) nano-crystalline Pd (open circles). [Brass1995, Mutschele1987].

The above conclusion was challenged by the work of Yao and Cahoon [Yao1991]. They have shown that GBs in nickel represent areas privileged to the segregation of hydrogen but not diffusion short circuits. Similar results were confirmed by studies on aluminum [Ichimura1991] and on ferritic steel [Yazdipour2012]. This opposite observation could be due to the low hydrogen contents or the exact configurations of GB in polycrystals are not clear. Oudriss *et al.* [Oudriss2012b] have conducted experiment investigations performed on polycrystalline nickel, with a large number of membranes with different grain size. In this study, it has been shown that Random boundaries with a high value of $\Sigma > 29$ are high diffusivity paths.

As mentioned previously, real GBs have different defects which could explain the controversial interpretations of the GB contribution to the hydrogen effective diffusivity. Furthermore, GBs are not isolated in materials, GB network effects [Watanabe1994] on the transport process have their significant contribution.

IV.2.3 Atomic approaches of GB diffusion

Atomic approaches give complementary information in the GB diffusion, since we can now study key factors in the GB diffusion mechanisms separately such as GB structure, vacancy, interstitial, etc. Molecular Dynamics (MD), Monte Carlo (MC) and Density Function Theory (DFT) atomic methods are widely used for both understanding and calculating the GB diffusion.

Suzuki *et al* [Suzuki2003] have reported that the anisotropy of GB diffusion depends on the GB structure and the diffusion in the direction parallel to the tilt axis can be faster or slower than in the

direction perpendicular to it. Pedersen *et al.* [Pedersen2009] has investigated the effect of the grain-boundary structure on the hydrogen diffusion mechanism and the hydrogen diffusion rate in aluminum, using KMC method. It was found that the hydrogen diffusion is slightly increased in the twist boundary parallel to the diffusion, due mainly to the configuration. It was observed that twist+tilt boundaries reduce the hydrogen diffusion, because of the trapping effects.

Di Stefano *et al.* [Di Stefano2015] have compared the hydrogen diffusion in nickel bicrystals using the first-principles with nudged-elastic band method (NEB), GB $\Sigma 3\langle 110 \rangle\{111\}$ could act as a barrier for the diffusion process, the segregation energy in this GB is closed to the bulk. GB $\Sigma 5\langle 100 \rangle\{210\}$ has a short circuit path along the GB, the diffusing hydrogen atoms can easily reach the favorable segregation sites inside the GB cavities, but the escape rates are much lower due to significantly higher migration barriers for the reverse jumps (*figure 1.42*). As a result, the $\Sigma 5\langle 100 \rangle\{210\}$ GB can also behave as a barrier for hydrogen diffusion, not because of higher migration barriers but due to the effective trapping.

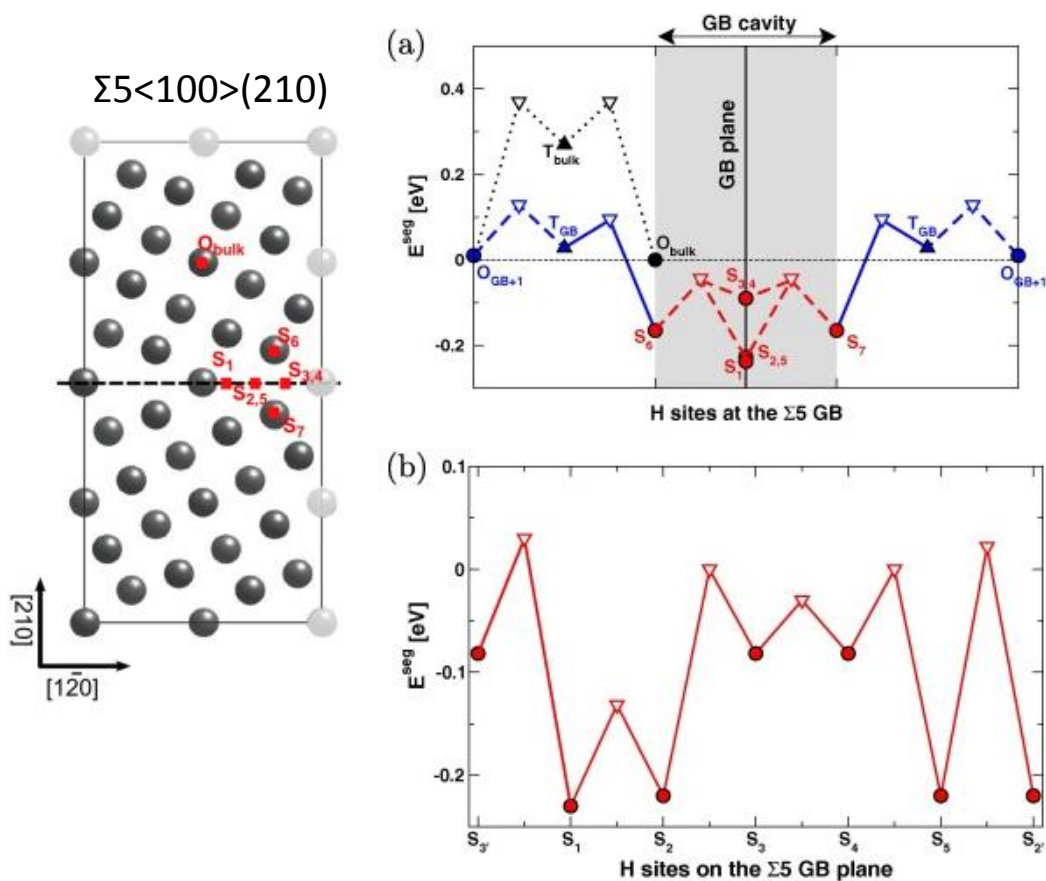


Figure 1.42 – Segregation energies for metastable H sites (full symbols) and associated transition states (empty symbols) for H migration across (a) and along (b) the $\Sigma 5$ GB [Di Stefano2015].

DFT studies on GBs in α - and γ - Fe have been reported by Du *et al.* [Du2011]. Within the close-packed, low energy $\Sigma 3$ grain boundaries, the available interstitial sites are very similar to the

tetrahedral and octahedral sites in the corresponding bulk structures. At the interface, different interstitial sites are available, leading to an attraction of hydrogen within the bcc $\Sigma 3\langle 110\rangle\{112\}$ structure and a repulsion from the fcc $\Sigma 3\langle 110\rangle\{111\}$ grain boundary. Within the open grain boundary structures, $\Sigma 5\langle 001\rangle\{310\}$ bcc and $\Sigma 11\langle 110\rangle\{113\}$ fcc, various different interstitial sites are available, generally providing favorable binding sites for H atoms, which implies that hydrogen is trapped at the grain boundary (figure 1.43 (a)). However, they found that none of the investigated grain boundaries provide a fast diffusion channel for H atoms in the dilute limit, the diffusion paths with energy barriers (≈ 0.25 eV for $\Sigma 5\langle 001\rangle\{310\}$ in bcc Fe and 0.7 eV for $\Sigma 11\langle 110\rangle\{113\}$ in fcc Fe (figure 1.43 (b)) comparable to the bulk values (≈ 0.1 eV in bcc and 0.6 eV in fcc Fe).

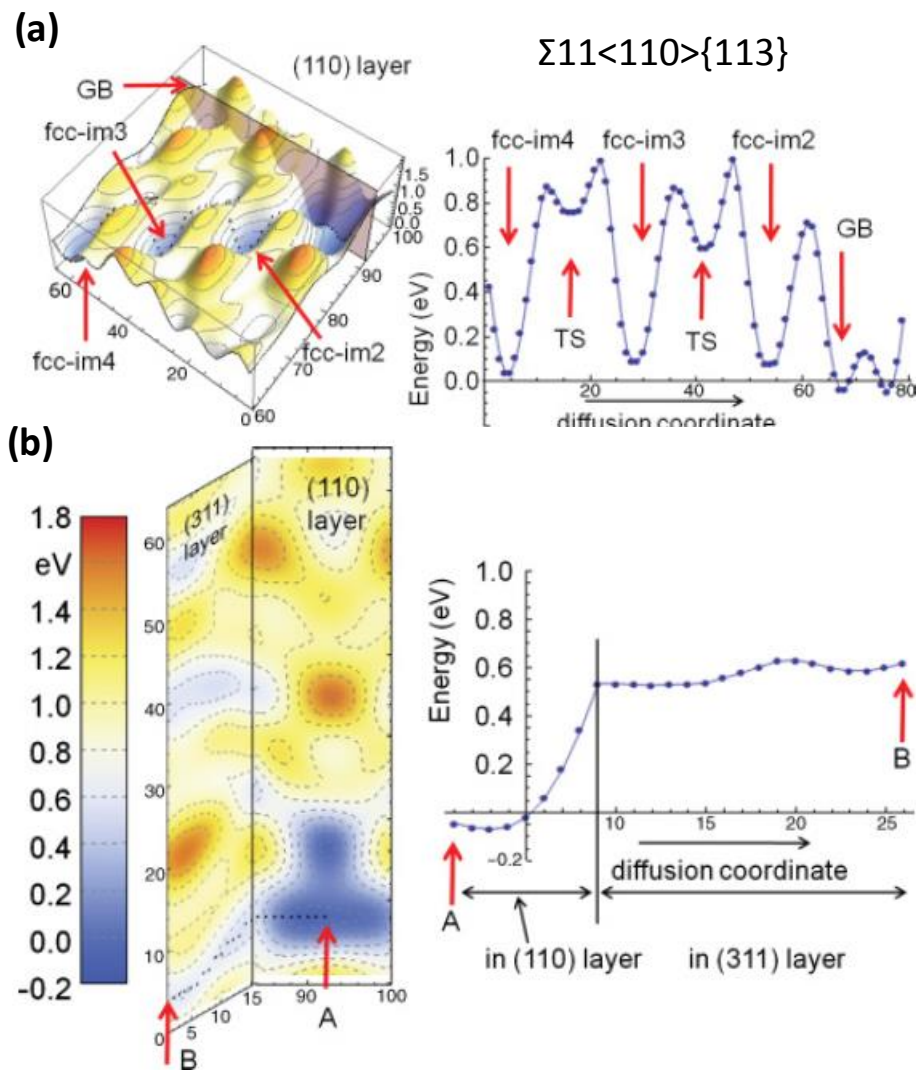


Figure 1.43 – (a) Diffusion for an H interstitial perpendicular to GB in fcc iron. The pathway lies within the part of the (110) plane indicated. The overall barrier for H to escape from the interface region is computed to be 1.1 eV, (b) Diffusion pathway for an H interstitial close to the GB in fcc iron. After a displacement within the (110) plane out of the center of the grain boundary (point A), the displayed motion occurs in the [110] direction [within the (113) plane parallel and perpendicular to the (110) plane. The overall barrier for this pathway is 0.7 eV. [Du2011].

Generally, only one atom of hydrogen in the atomic simulation model and only a few properties of GBs can be compared, however, a real polycrystalline have a heterogeneous ensemble of GBs with different structures, defects and properties. Thus the experimental diffusion measurements on polycrystalline materials are affected by the whole ensemble of GBs and it is therefore more complex to understand the real contribution of different grain boundaries to the effective diffusivity in the materials. It is worthwhile to study the hydrogen behavior with GBs well characterized such as in a bi crystal system, a better understanding can be achieved by comparing to the atomic approach of hydrogen interactions with the same theoretical GBs.

V. Summary

In this chapter, we give a review of the literature on the behavior of hydrogen in metals, the important roles of defects such as hydride, vacancy, dislocation on the HE mechanisms have been discussed. The early stage of HE corresponds directly to the hydrogen transport in materials, we summarized the hydrogen diffusion in single and poly crystalline nickel concerning the hydrogen diffusivity and solubility, the influences of the crystallographic orientation and the texture on the diffusion process have been highlighted.

The nature of GBs cannot give a complementary classification for all types of GBs, however the free volume and the GB energy can be considered as two important indices for GBs behaviors. Microdefects such vacancy and dislocation are more active in the GB core than in the crystal lattice, hydrogen – GBs interactions are complex since other types of defects intervene at the same time and their contribution to the macroscopic and microscopic hydrogen transport is not fully understood and can lead to some controversial effects. Atomic calculations suggest that hydrogen – GBs interactions and defects – GBs interactions are more pronounced for high energy GBs, additionally, the defects are formed easier with the presence of hydrogen. There is still a lack of complete understanding of the whole phenomena.

In order to get a better understanding of the impacts of these defects separately, it is necessary to start our investigation with single crystals since the microstructure defects can be well controlled. The influence of different GBs on the hydrogen diffusion process will be carried out in the bi crystal system using experimental and numerical approaches, although a bi crystal is able to distinguish different GBs, the effects of other defects cannot be totally eliminated due to the production process and the hydrogen charging conditions.

Chapter 2.

Materials and methods

| | |
|---|----|
| <u>Chapter 2. Materials and methods</u> | 62 |
| <u>I. Materials and metallurgical characterization</u> | 64 |
| <u>I.1 Nickel single crystals</u> | 64 |
| <u>I.2 Nickel bi crystals</u> | 65 |
| <u>II. Experimental and numerical methods</u> | 67 |
| <u>II.1 Experimental approaches</u> | 67 |
| <u>II.1.1 Hydrogen charging – thermal desorption spectroscopy (TDS)</u> | 67 |
| <u>II.1.2 Electrochemical permeation (EP)</u> | 70 |
| <u>II.2 Numerical approaches</u> | 74 |
| <u>II.2.1 Finite element method (FEM)</u> | 74 |
| <u>II.2.1.1 2D hydrogen transport models</u> | 76 |
| <u>II.2.1.2 3D hydrogen transport models</u> | 77 |
| <u>II.2.2 Atomic Simulation</u> | 79 |
| <u>III. Overview</u> | 84 |

This part is intended to present the materials of this study as well as the experimental and numerical methods. For each one of these methods, it will be introduced the main principles as well as the utilization in the framework. *Figure 2.0* gives a brief description of materials and methods applied in our study, nickel single/bi crystals were first characterized by Electron Back Scatter Diffraction (SEM-EBSD) and Transmission Electron Microscopy (TEM). Hydrogen transport in these materials was then studied by Electrochemical Permeation (EP) and Thermal Desorption Spectroscopy (TDS), these two methods access information of the hydrogen diffusion and solubility which gives the inspiration for the numerical approaches. FEM has been used to study the macroscopic diffusion process and MD is able to investigate the segregation and diffusion at the atomic scale. TEM was also used to study the influence of the hydrogen on the microstructure of nickel materials.

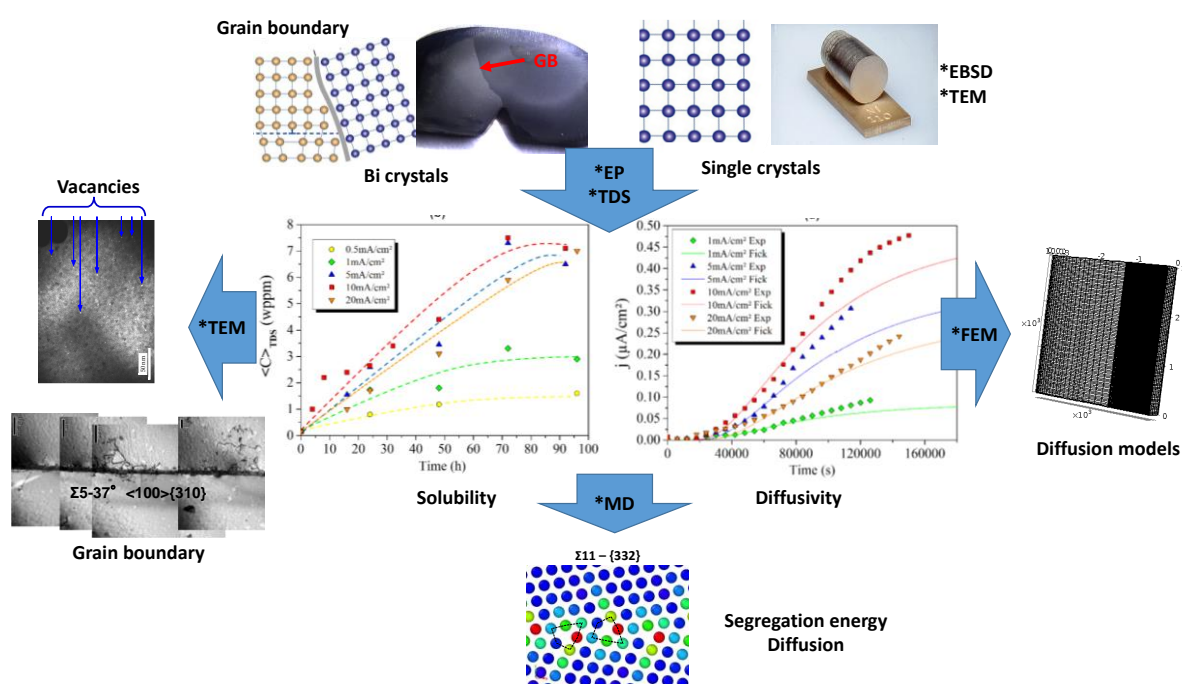


Figure 2.0 – A brief description of the experimental and numerical methods applied in our study.

I. Materials and metallurgical characterization

I.1 Nickel single crystals

Nickel single crystals (99.999% purity) with three different crystallographic orientations [001], [110] and [111] were provided by Goodfellow. Samples are cylindrical with an 18 mm diameter for nickel [001] and 11mm for nickel [110] / [111], they were obtained by Bridgman-Stockbarger method with

an accuracy of $\pm 3^\circ$ and the dislocation density was less than 10^{12} m^{-2} , the chemical compositions are given in (Table 2.1). Each orientation was then characterized by EBSD with instruments EDAX / TSL IOM coupled to SEM FEI Quanta 200 FEG-ESEM. A fourth more complicated orientation was obtained by cutting a sample nickel [001] following an angular deviation of approximately 15° . After a characterization using EBSD, the corresponding crystallographic orientation was [219] (figure 2.1).

Table 2.1- Chemical compositions presented by weight for nickel single crystals.

| Elements | Co | Cr | Cu | Fe | Mg | Mn | Si | Ti | C | S |
|----------|----|----|----|----|----|----|----|----|----|----|
| wppm | 8 | 8 | 10 | 10 | 10 | 10 | 8 | 10 | 10 | 10 |

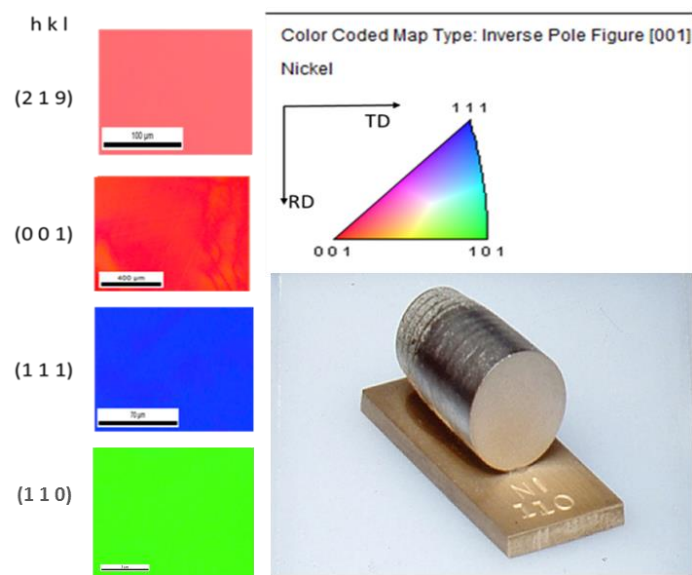


Figure 2.1 – EBSD scanning for crystallographic orientations [001], [219], [110] and [111]. An example of nickel [110] illustrated, the normal is the crystallographic orientation which is perpendicular to the surface plane of samples.

EBSD is widely used in recent years, because it has many advantages, including a simple surface preparation [Feaugas2003, Sahal2006] with electropolishing (Appendix 2.1), fast data acquisition and it gives enough metallurgical parameters such as the size of grains, site coincidence lattice for grain boundaries, phases identification, textures...

I.2 Nickel bi crystals

Nickel bi-crystals were made in Laboratory (provided by L.Priester and Mine St-Etienne School), the material for solidification was electrolytic Incomond nickel which was remelted under vacuum. The bi-crystals were grown from a seed in an argon atmosphere using the horizontal boat method (Chalmers method) of a final length of 14.4cm at a rate of about 3mm per hour. The impurity contents

are given in (Table 2.2), although low, the sulfur content could be enough to promote intergranular segregation. All samples were then carried out a desulfurization heat treatment at 550 °C for 10 hours in flowing hydrogen (the hydrogen content will be discussed in Chapter 3) [Juhás1994, Duparc2000, Poulat2000]. After the microscopy characterization, four bi-crystals (*figure 2.2*) were selected to continue experimental tests:

$\Sigma 11-50^\circ \text{ } ^\circ 30 \langle 110 \rangle \{311\}$, $\Sigma 11-129^\circ \text{ } ^\circ 30 \langle 110 \rangle \{332\}$, $\Sigma 3-70^\circ \text{ } ^\circ 30 \langle 110 \rangle \{111\}$ and $\Sigma 5-37^\circ \text{ } ^\circ \langle 100 \rangle \{310\}$.

Table 2.2- Chemical compositions (in weight percent) in nickel after different steps of bi crystals preparation [Juhás1994]

| Samples | Ni, Co | Fe | Others | C | S | P | O |
|----------|--------|------|---------|--------|--------|--------|-------|
| Initial | 99.95 | 0.01 | <0.01 | | | | |
| Remelted | | | | 0.005 | 0.001 | <0.001 | 0.001 |
| Grown | | | 0.05 Mo | 0.0015 | 0.0003 | | |

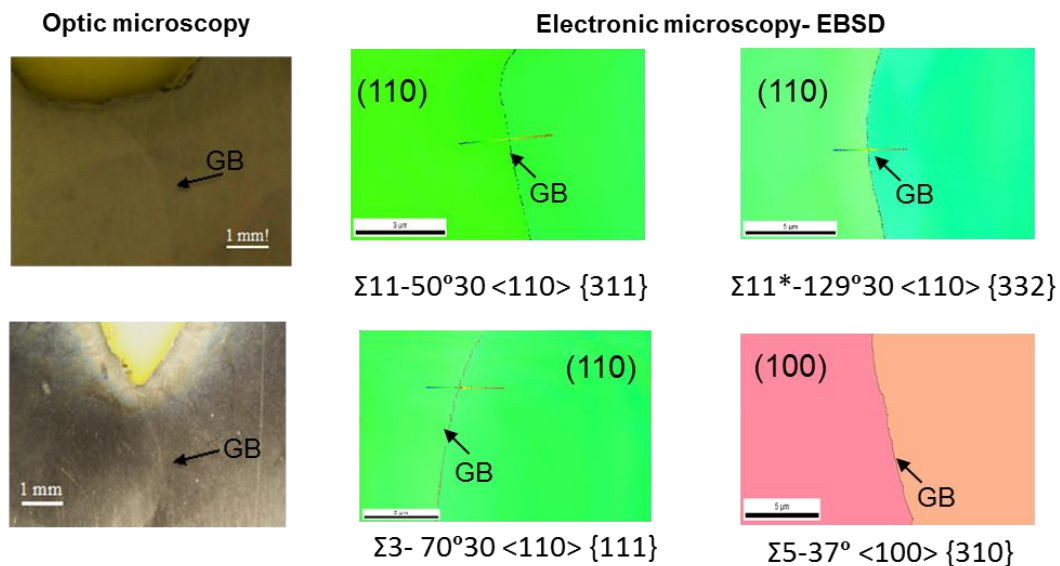
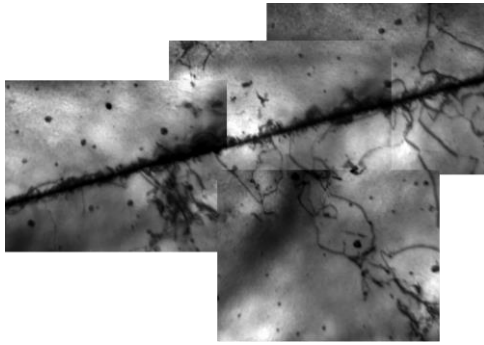


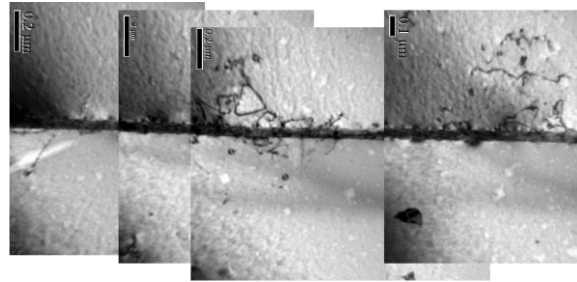
Figure 2.2 – Grain boundary in bi-crystal is visible using the optic microscopy, and EBSD scanning is to identify the site coincidence lattice (Σ) for nickel bi-crystals $\Sigma 11-50^\circ \text{ } ^\circ 30 \langle 110 \rangle \{311\}$, $\Sigma 11-129^\circ \text{ } ^\circ 30 \langle 110 \rangle \{332\}$, $\Sigma 3-70^\circ \text{ } ^\circ 30 \langle 110 \rangle \{111\}$ and $\Sigma 5-37^\circ \text{ } ^\circ \langle 100 \rangle \{310\}$.

After a chemical etching (50 mL HNO_3 + 25 mL CH_3COOH + 25 mL H_2O), grain boundaries (GBs) are visible by optic microscopy. EBSD gives information about the grain orientation and the site coincidence lattice. In order to obtain local information and compare GBs by experimental/numerical methods. We have investigated GBs using the transmission electron microscopy (TEM), TEM scanning images are given in *figure 2.3*, and a GB in reality presents several dislocations around the interface due to the fabrication process. The description of TEM and the sample preparation are given in Appendix 2.2.

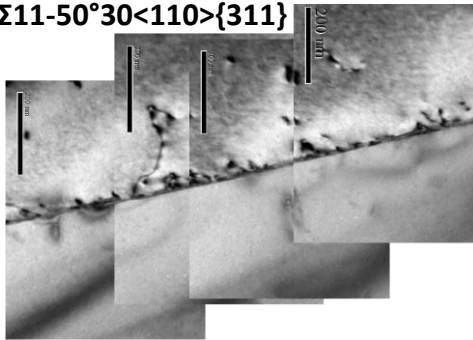
$\Sigma 3\text{-}70^\circ 30\langle 110\rangle\{111\}$



$\Sigma 5\text{-}37^\circ 30\langle 100\rangle\{310\}$



$\Sigma 11\text{-}50^\circ 30\langle 110\rangle\{311\}$



$\Sigma 11\text{-}129^\circ 30\langle 110\rangle\{332\}$

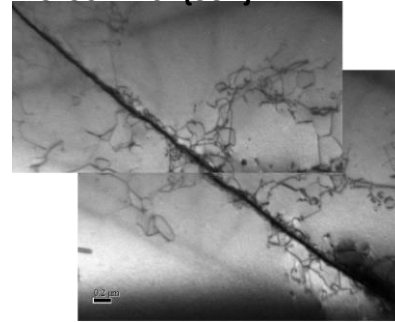


Figure 2.3—TEM scanning for grain boundaries $\Sigma 3\text{-}70^\circ 30\langle 110\rangle\{111\}$, $\Sigma 5\text{-}37^\circ 30\langle 100\rangle\{310\}$, $\Sigma 11\text{-}50^\circ 30\langle 110\rangle\{311\}$ and $\Sigma 11\text{-}129^\circ 30\langle 110\rangle\{332\}$.

II. Experimental and numerical methods

II.1 Experimental approaches

II.1.1 Hydrogen charging – thermal desorption spectroscopy (TDS)

Hydrogen charging in nickel samples was realized by an electrochemical method at 25°C . The charging devices are shown in *figure 2.4*. The working electrode coated with resin was the nickel sample for charging, the working area was about to 0.3 cm^2 . The surface for the charging side was prepared by the mechanical polishing until 4000 SiC. Previous work [Lekbir2012] did prove that electrolytic polishing as well as diamond polishing paste have little influence (less than 1%) on the following experimental tests. According to previous studies [Ebisuzaki1967, Brass1990, Brass1996, Oudriss2012a], hydrogen diffusion in nickel is relatively low (the order of magnitude for the diffusion coefficient is around $10^{-14}\text{ m}^2/\text{s}$), the thickness of the samples was fixed at 330 ± 20 microns in order to have a detectable hydrogen concentration (hydrogen concentration should be high enough for TDS) and a reasonable charging time until the steady state (less than 5 days). The sample was

installed in a thermostated cell with an electrolytic solution NaOH 0.1M, and then a predetermined current density according to the polarization curve (*figure 2.5*) was applied to the sample by using a potentiostat. The hydrogen generated on the surface would penetrate the sample according to the process described in the context of the HER (hydrogen evolution reaction) and HAR (hydrogen absorption reaction). The reaction mechanisms are generally formulated into four stages [Marcus2011]:

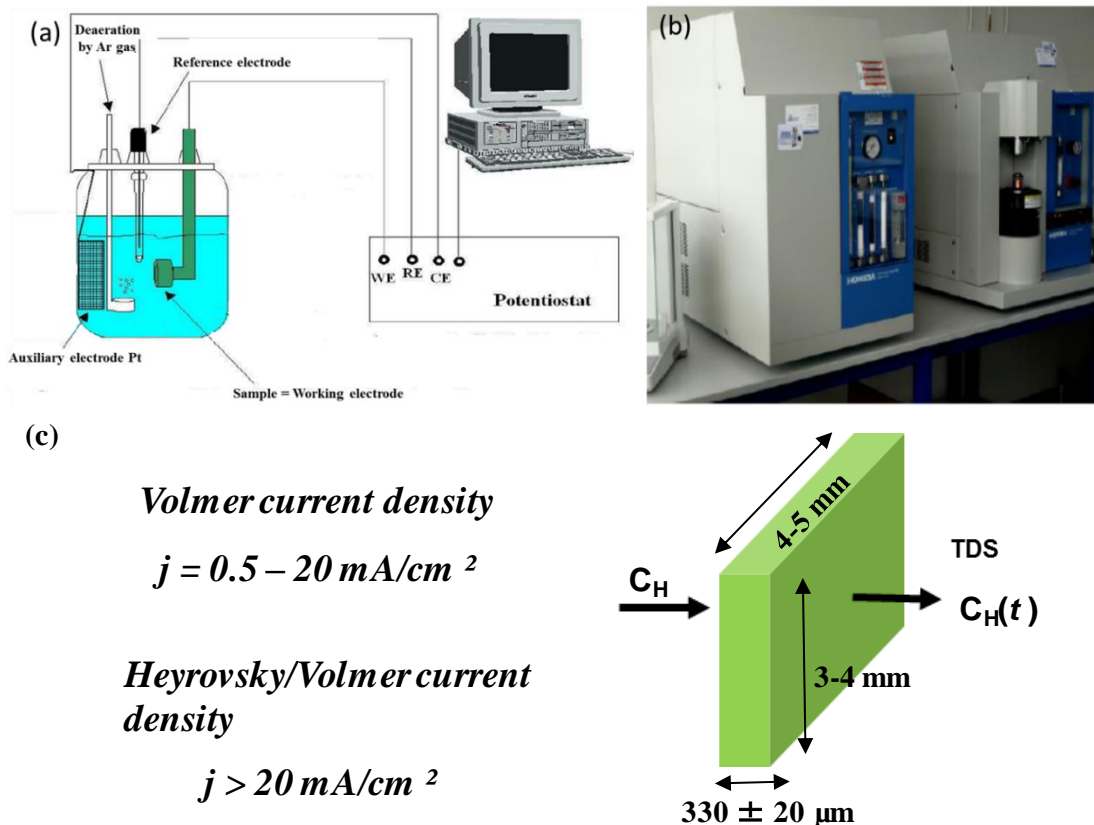
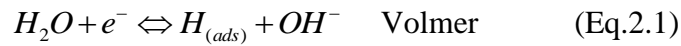


Figure 2.4 – (a) Hydrogen charging setup, (b) TDS instruments - Jobin Yvon Horiba EMGA-621W, (c) hydrogen charging conditions.

The quantity of hydrogen charged in the sample was then measured by TDS (Thermal desorption spectroscopy - Jobin Yvon Horiba EMGA-621W). Briefly, the technique consists in a non-isothermic

study of desorption kinetics. The sample, previously charged with hydrogen, is continuously heated following a predefined temperature profile (a linear ramp) up to 2000 °C while the quantity of gas desorbed from the sample is recorded. The plot of the flow of gas desorbed as a function of temperature is a TDS spectrum. TDS spectra are usually composed of many desorption peaks, each of them can be associated with a different kinetic process (*figure 2.6*). The main goal of a TDS experiment is to identify the rate limiting step and to determine the kinetic parameters associated with the process. In our study, two different analytical procedures were used: the first procedure ‘Total fusion’ of quantifying the total amount of hydrogen charged, the sample was heated instantaneously to 2000 °C and maintained at this temperature for 75 seconds; and the second procedure ‘Ramp’ that allowed identifying different states of hydrogen with associated energy, the sample was heated to 2000 °C with different temperature ramp rates (60, 130, 230 and 500 °C/min) to desorb the different states of hydrogen (diffusible in lattice, trapped reversibly and trapped irreversibly).

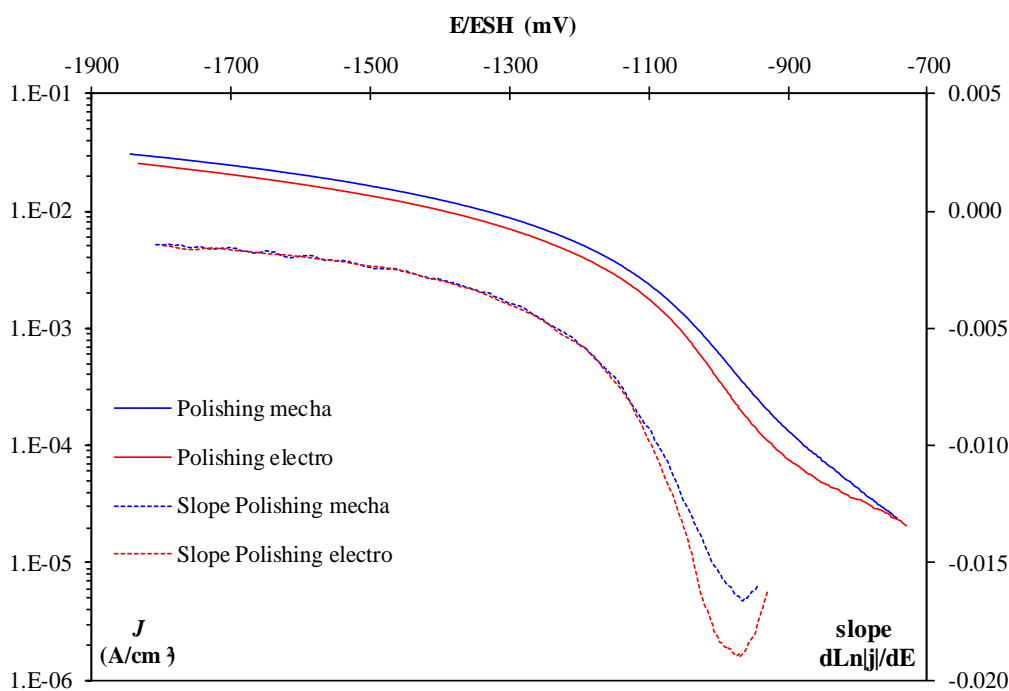


Figure 2.5 – Two cathodic polarization curves at 300 K (Blue: mechanical polishing, Red: electrochemical polishing) for nickel sample in 0.1M NaOH (pH~13), and the slope of the polarization curve.

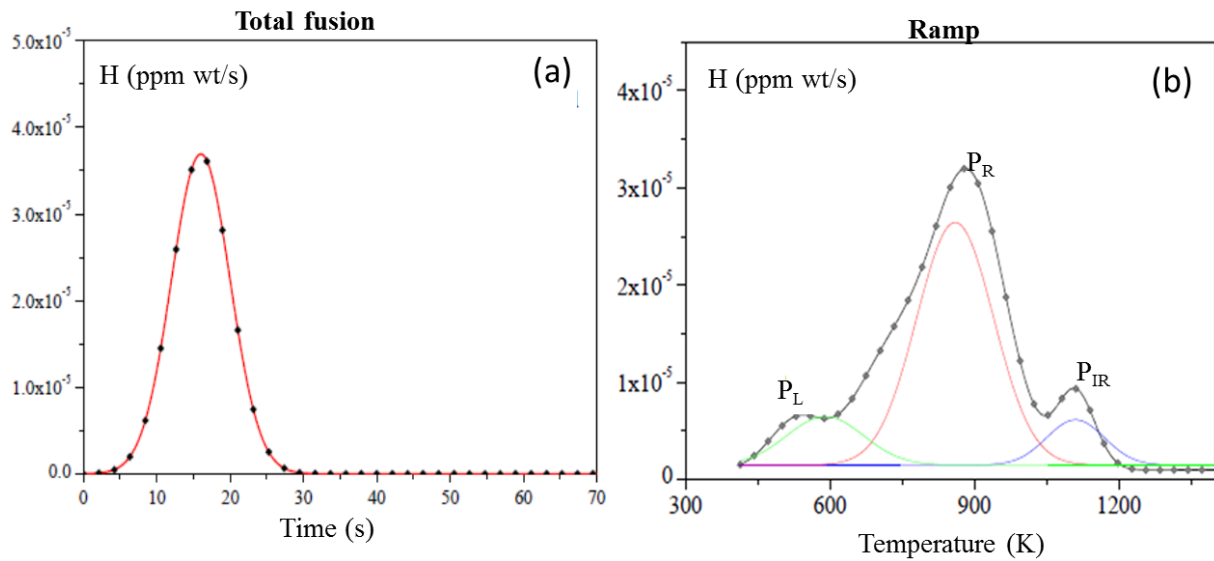


Figure 2.6 – Nickel 18 μm poly crystals - (a) Spectra of total fusion is to determine the whole amount of hydrogen charged, (b) Spectra of the ramp is to identify different states of hydrogen with ramp rate of 230 $^{\circ}\text{C}/\text{min}$, P_L present the peak lattice, P_R present the peak reversible and P_{IR} is the peak irreversible. [Oudriss2012c]

II.1.2 Electrochemical permeation (EP)

The electrochemical permeation (EP) method is one of the main technique used to detect the mechanisms of diffusion and trapping of hydrogen in different microstructures. This technique was initially introduced by Devanathan and Stachurski [Devanathan1962] and has been widely developed and used later in several works [Tanabe1986, Arantes1993, Brass1995, Doyle1995, Altunoglu1996, Zakroczymski2006, Addach2009]. The test allows to follow the kinetics of absorption and desorption of hydrogen, and to detect different parameters such as diffusion coefficients (apparent) and hydrogen concentrations. EP is well developed in our laboratory, and several studies have been achieved by using this technique, on martensitic steels [Frappart2011] and polycrystalline nickel [Oudriss2012b].

As shown in *figure 2.7*, the EP technique is composed of two cells separated by a membrane with an exposed surface in contact with the electrolytic solution. The detection side (exit side) of EP was maintained with a constant anodic open circuit potential of $0/E_{\text{OCP}}$ in 0.1M NaOH (pH~13). The charging side (entry side) of EP was galvanostatically polarized at a constant cathodic charging current density in 0.1M NaOH (pH~13), the current density was defined according to the polarization curve (*figure 2.5*). The temperature was maintained at 25 $^{\circ}\text{C}$ and both solutions are continuously deaerated by argon gas at 1.4 bar. Before the permeation test, both surfaces of the sample were prepared by the mechanical polishing up to grade 4000 SiC, the final thickness of the sample was about to $200 \pm 20 \mu\text{m}$.

The experimental procedure consists of two steps: the first step is hydrogen charging to the steady state (j_{∞}), followed by the desorption step by intercepting the charging conditions. During the first step, the NaOH 0.1M solution was deaerated more than 70 minutes in the detection cell, the open circuit potential evolution (E_{OCP}) was measured during 15-16 hours up to its stabilization. E_{OCP} is then applied on the exit side of the sample using a potentiostat and the current density was recorded during 1-2 hours. The residual current density on the exit side before the hydrogen charging was about a few nA/cm². Then, the deaerated 0.1 M NaOH solution was introduced into the charging cell and a cathodic current density of a few mA/cm² was applied. The hydrogen passing through the membrane was detected in the detection cell, and the curve recorded corresponds to the permeation-charging curve of hydrogen (figure 2.8). When the steady (j_{∞}) state was reached, the charging step was stopped and the NaOH solution was then removed. Then the desorption process started, the registered curve corresponded to the hydrogen desorption on the exit side of the sample.

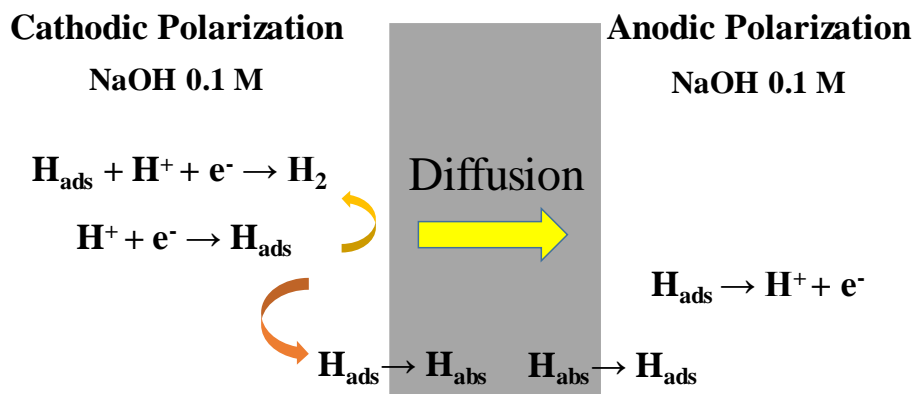
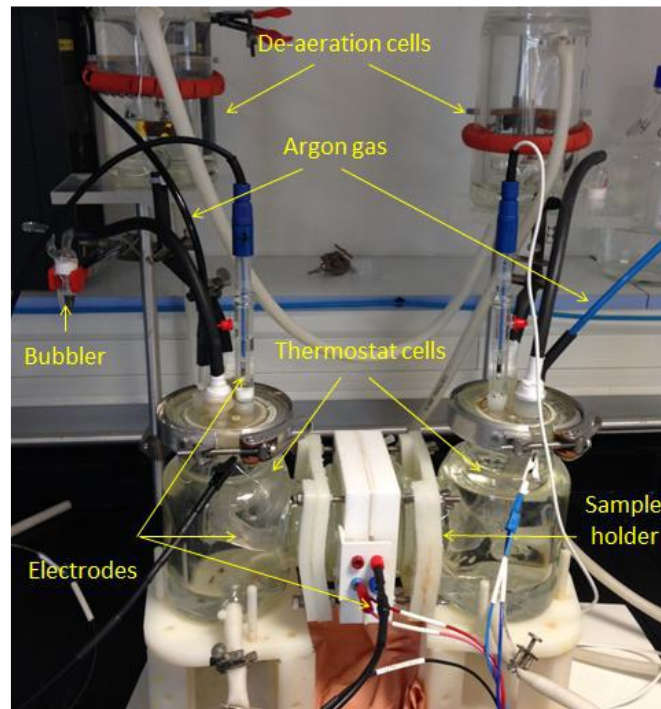


Figure 2.7– Experimental setup for EP test, the whole process of hydrogen permeation is dominated by the transfer of adsorption hydrogen (Volmer reaction) to absorption hydrogen.

Experimental conditions for hydrogen diffusion in nickel are given in *Table 2.3*, the working surface was selected according to the sample size, and however, the smaller surface size might sometimes have the containment problem blocking the hydrogen diffusion when an unsuitable current density was applied, furthermore, the diffusion is dominated by the Volmer reaction, our study framework is then limited to a small range of current density.

Table 2.3- Experimental conditions of electrochemical permeation for hydrogen diffusion in nickel

| Materials | Nickel |
|---|-----------------------------|
| Thickness (μm) | 220 \pm 20 |
| Surface state | Polishing 4000 SiC |
| Temperature ($^{\circ}\text{C}$) | 25 |
| Working surface (cm^2) | 0.785 or 0.385 |
| Charging side | |
| Potentiostat | PGP 201 VoltaLab |
| Courant density applied (mA/cm^2) | 20, 10, 5 and 1 |
| Operation mode | Floating |
| Detection side | |
| Potentiostat | SP300 / VSP VoltaLab |
| Potential applied (mV) | 0 vs Open circuit potential |
| Operation mode | Grounded |

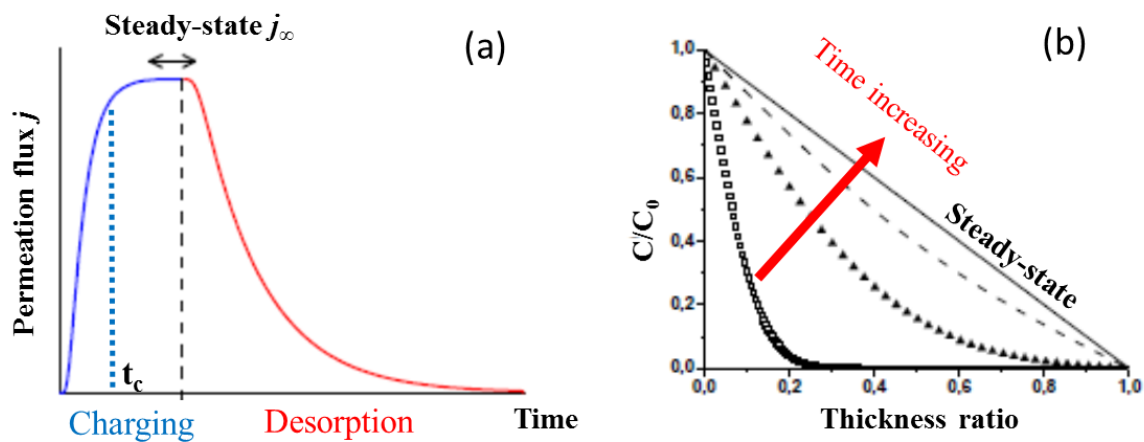


Figure 2.8 – (a) Electrochemical permeation curve for the charging and the desorption steps, t_c is the characteristic time. (b) Evolution of the hydrogen concentration profiles as a function of charging time, assuming that the hydrogen concentration at the subsurface C_0 is constant.

The diffusion coefficient of hydrogen in the material was calculated using the flux curve. However, this diffusion coefficient was called ‘apparent’ because it was affected by of all phenomena such as hydrogen trapping, surface state evolution, microstructures, self-stress, vacancy formation, etc. For a given temperature, the diffusion coefficient was considered as a constant. The apparent diffusion coefficient D_{app} is calculated by determining the characteristic time t_c on the flux curve with equation (Eq.2.5)

$$D_{app} = \frac{e^2}{M \times t_c} \quad (\text{Eq.2.5})$$

Where e is the sample thickness, t_c the characteristic time, and M a constant factor depending on the selected characteristic time, the time that required to reach a given percentage of the steady-state flux. Three values are the most used in the literature 63%, 10% and 1%. The intersection between the tangent to the flux curve and the time axis gives the other time, t_{tg} , called ‘breakthrough-time’ [Boes1976, Pyun1989, Arantes1993, Doyle1995]. However, we chose to note this time as t_{tg} since in the literature the time for 10% is sometimes referred as “breakthrough-time” [Frappart2011, Oudriss2012b, Legrand2013]. The time for 63% is called ‘time-lag’ [Devanathan1962, Boes1976, Yao1991b, Luppo1998], based on a mathematical model developed by Daynes [Daynes1920]. The M values are collected in Table 2.4

Table 2.4- M values according to different percentages of steady state flux.

| Percentage of j_∞ | Characteristic time | M value |
|--------------------------|---------------------|------------------|
| 1% | $t_{1\%}$ | 6 |
| 10% | $t_{10\%}$ | 15.12 or 15.3 |
| 63% | $t_{63\%}$ | 25 |
| Tangent | t_{tg} | 15.3 or $2\pi^2$ |

We have also used the analytical solution of Fick’s laws to fit the experimental curve by assuming that the hydrogen concentration at the subsurface is constant [McBreen1966, Boes1976], the flux is calculated with equations (Eq.2.6 and Eq.2.7)

$$j = j_\infty \frac{2}{\sqrt{\pi\tau}} \exp\left(\frac{-1}{4\tau}\right) \quad \text{with} \quad \tau = \frac{D_{app}t}{e^2} < 0.3 \quad (\text{Eq.2.6})$$

$$j = j_\infty (1 - 2\exp(-\pi^2\tau)) \quad \text{with} \quad \tau = \frac{D_{app}t}{e^2} > 0.3 \quad (\text{Eq.2.7})$$

The concentration gradient is supposed to be constant when the steady state is reached. The subsurface hydrogen concentration is then calculated with equation (Eq.2.8) [Frappart2011]:

$$C_0 = \frac{j_\infty \times e}{D_{app}} \quad (\text{Eq.2.8})$$

Fick’s second law allows us to predict the evolution of the hydrogen concentration at any point and at any time of the whole thickness during the diffusion process. The solution of Fick’s law for a homogenous medium and electrochemical permeation conditions is given by equation (Eq.2.9):

$$C(x,t) = C_0 \left(1 - \frac{x}{e}\right) + \frac{2C_0}{\pi} \sum_{n=1}^{\infty} \frac{1}{n} \sin\left(\frac{n\pi x}{e}\right) \exp\left(-\frac{n^2 \pi^2 D_{app} t}{e^2}\right) \quad (\text{Eq.2.9})$$

For the case of the steady state, equation (Eq.2.5) becomes a linear equation (Eq.2.10):

$$C(x,t) = C_0 \left(1 - \frac{x}{e}\right) \quad (\text{Eq.2.10})$$

The subsurface hydrogen concentration C_0 is a value obtained from the apparent diffusion coefficient D_{app} , because the analytical Fick's model has just considered a simple diffusion process with constant parameters. Other phenomena are neglected in this calculation such as hydrogen trapping, surface states, microstructures, self-stress, vacancy formation, etc. The value C_0 was validated by comparing with the TDS results with the pre-charged samples.

II.2 Numerical approaches

II.2.1 Finite element method (FEM)

The basic idea of the numerical method for a differential equation is to find an approximation solution or to obtain a discrete problem by using a computer. The finite element method is a very powerful and flexible numerical approach for solving partial differential equations. Its flexibility means that it can be used to solve complicated equations in domains whose geometries range from a simple polygon or polyhedron such as a square or a cube to more complex shapes with curved boundaries, for some complicated cases, the mesh may need a software to be dealt with. It is necessary to transform the differential equation into a more suitable form, the so called weak form is a discrete mathematical algorithm. Generally, the quality of discretization should be verified by the existence of a solution, the stability, the convergence and of course the error estimated between a discrete solution and the initial problem.

In our case, the hydrogen diffusion phenomena were studied by using FEM software Comsol Multiphysics © associated to the computing code Matlab. The transport of diluted species interface provided by Comsol Multiphysics was used to solve the hydrogen transport in the membrane. This module provides a predefined modeling environment for studying the evolution of chemical species transported by diffusion and convection. As most of the multiphase simulations, the transport phenomenon of chemical species is governed by partial differential equations (PDE). The PDE equation is implemented in Comsol Multiphysics as a weak form PDE. This consists in transforming

the PDE into an integral form, which is less strict than the PDE and more practical with the FEM. By default, the diffusion of the transport of diluted species interface is established by Fick's law (Eq.2.11)

$$\frac{dC}{dt} + D \frac{d^2 \mathcal{C}}{dx^2} = R \quad (\text{Eq.2.11})$$

Where C is this concentration, t the time, x the coordinate, D the diffusion coefficient and R the constant. A discrete mathematical algorithm works well for finding an approximate solution of this partial differential equation by using the weak form proposed by Comsol Multiphysics.

The general form PDE was also used in order to study the non-Fickian diffusion (Eq.2.12).

$$d \frac{dC}{dt} + e \frac{d^2 \mathcal{C}}{dt^2} + \nabla \cdot R = f \quad (\text{Eq.2.12})$$

Here C is this concentration, t the time, d the damping or mass coefficient is 1, e the mass coefficient is 0, R the conservative flux and f the source term.

After defining the boundary conditions of the problem and the geometry meshing, the model is ready to be solved. To do that, Comsol Multiphysics first proceeds to the spatial discretization, using the FEM. This means that any arbitrary function defined in the geometry is approximated by a set of local functions referred to as shape functions, the so called nodes. The FEM discretization is based on a particular choice of the shape functions. These functions are defined using polynomials on each element of the mesh. They are associated with the nodes of the elements and must verify some properties such as to be continuous and non-zero only on the elements containing their attachment node. The FEM discretization results in a system of equations that, once resolved, give an approximation of the exact solution of the PDE. Comsol Multiphysics assembles the system of equations to be solved in a matrix. The size of this matrix determines the number of degrees of freedom (DOFs) of the model.

To solve the linear system of equations, Comsol Multiphysics chooses by default the optimized solver, depending on the physics, space dimensions and the type of study. There are two types of solvers available in Comsol Multiphysics: iterative solvers and direct solvers. The main advantage of iterative solvers is the memory use, which is low compared to others methods. Direct methods generally offer a very good robustness but their computation cost and memory usage can be high. In this work, the default direct solver was used, namely MUMPS (Multifractal massively parallel sparse direct solver).

II.2.1.1 2D hydrogen transport models

Two principal models were established for studying hydrogen diffusion in nickel samples. The first charging model presented hydrogen across the sample is described as a two-dimensional system of which the boundary conditions and parameters are respectively given in *figure 2.9* and *Table 2.5*. The constant concentration $C_0 = 2 \times S_{max}$ was imposed at the entry side, where S_{max} corresponds to the maximum solubility obtained by experimental tests. At the exit side, we have compared two situations: 1. hydrogen cross the membrane and then accumulate at the exit side (the flux is zero); 2. concentration at the exit side is zero ($C_s = 0$), hydrogen cross the membrane and then can get out of the membrane. In a first step, the two situations were simulated in order to find the model with best fitting to the experimental situation. The diffusion is considered to be one-dimensional along the x-axis with a concentration gradient following a simple Fick's law.

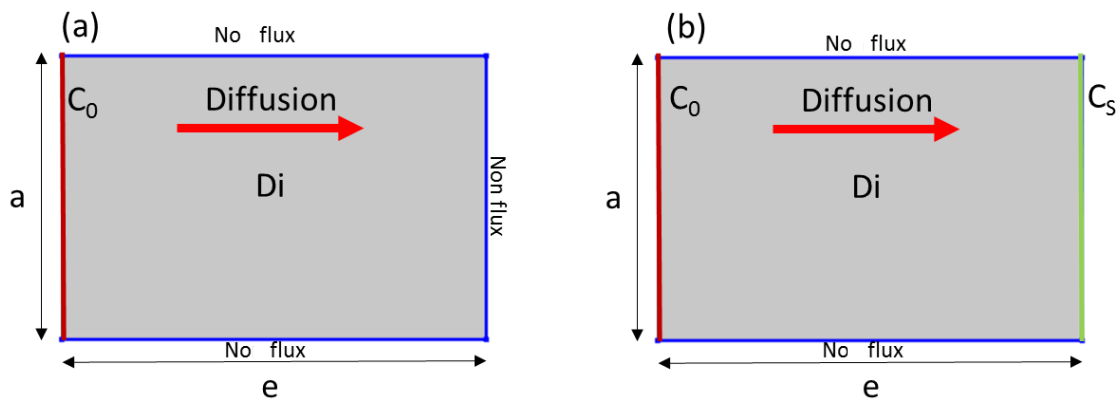


Figure 2.9 – Boundary conditions for the 2D charging models: (a) hydrogen remains in the membrane, (b) hydrogen can get out of the membrane

Table 2.5- 2D charging model parameters.

| Nom | Value | Unity | Description |
|--------|---------------------|---------------------------------|-----------------------------|
| D_i | $i = 1, 2, 3 \dots$ | $10^{-14} \text{ m}^2/\text{s}$ | Diffusion coefficient |
| e | 330 | μm | Thickness |
| a | $2/3e$ | μm | Height |
| c | 1.34 | mol/m^3 | Initial concentration |
| C_0 | $2S_{max}$ | mol/m^3 | Concentration at entry side |
| C_s | 0 | mol/m^3 | Concentration at exit side |
| $stat$ | *Step (t) | s^{-1} | 1st point of diffusion |

*Step(t) : a function increase from 0 to C_0 during 0.000001s

Simulations can reproduce the experimental results when the numerical model is well established, similar models were well studied in previous works in the scale transition [Legrand2013] and in the diffusion in the heterogeneous medium [Osman Hoch2015].

The second desorption model has simulated the desorption process after the hydrogen charging to the steady state. A linear distribution of concentration was imposed in the membrane, the value

corresponded to the maximum solubility of hydrogen in the nickel sample which was given by experimental test, the linear profile was defined by the function Ramp(x) (figure 2.10), the boundary condition is given in Table 2.6. Both exit sides of the membrane were imposed zero concentration $C_s = 0$, hydrogen was evacuated from two sides.

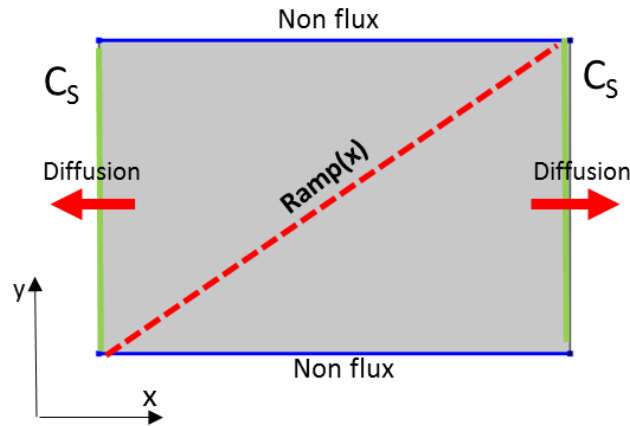


Figure 2.10 – Boundary conditions for the 2D desorption model.

Table 2.6- 2D desorption model parameters.

| Name | Value | Unity | Description |
|----------------------|---------------------|---------------------------------|----------------------------|
| Di | $i = 1, 2, 3 \dots$ | $10^{-14} \text{ m}^2/\text{s}$ | Diffusion coefficient |
| e | 330 | μm | Thickness |
| a | $2/3e$ | μm | Height |
| C₀ | $2S_{\text{max}}$ | mol/m^3 | Hydrogen concentration |
| C_s | 0 | mol/m^3 | Concentration at exit side |
| Rm | *Ramp(x) | m^{-1} | Initial concentration |

*Ramp(x): a function increase linearly from 0 to C_0 following the x-axis.

II.2.1.2 3D hydrogen transport models

3D models were also studied in order to get the scale effects on the diffusion process and the hydrogen transport in bi-crystals. Two different boundary conditions have been compared as shown in figure 2.11, and GB mesh is illustrated in figure 2.12.

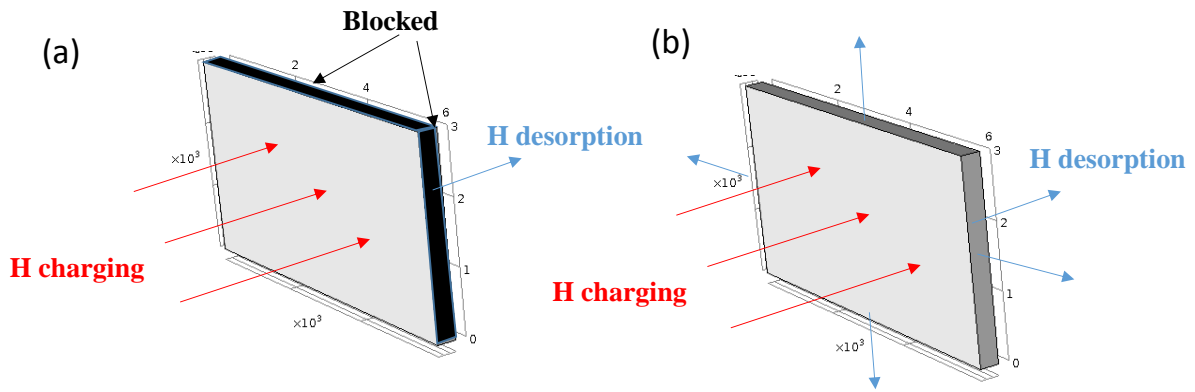


Figure 2.11 – Boundary conditions for the 3D models – (a) Hydrogen entry at one surface and exit at the other opposite surface, (b) Hydrogen entry at one surface and exit at all others surfaces.

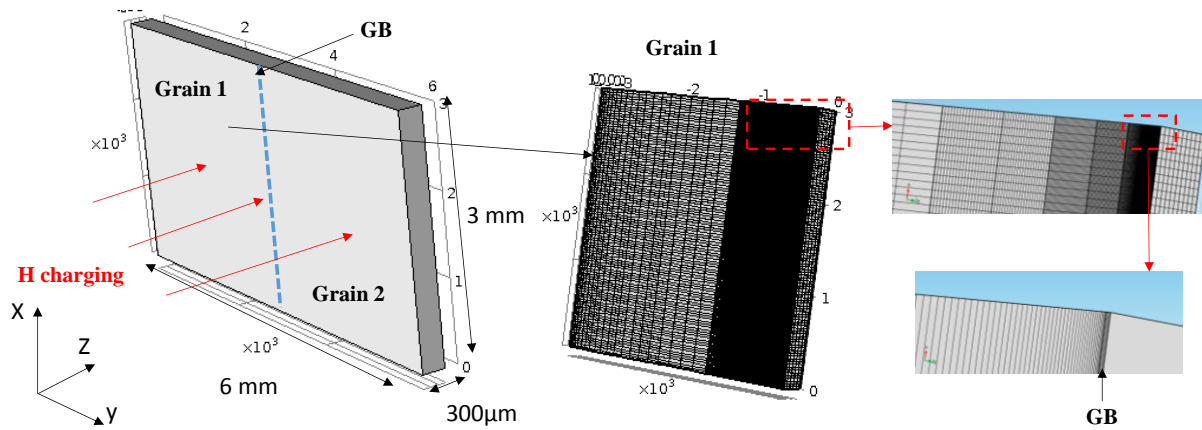


Figure 2.12 – Schematic illustration of bi crystal 3D model.

Table 2.7- 3D hydrogen charging model parameters.

| Nom | Value | Unity | Description |
|----------------------|--|---------------------------------|--------------------------------------|
| *Dg | $\begin{pmatrix} D_{xx} & D_{xy} & D_{xz} \\ D_{yx} & D_{yy} & D_{yz} \\ D_{zx} & D_{zy} & D_{zz} \end{pmatrix}$ | $10^{-14}\ \text{m}^2/\text{s}$ | Grain diffusion coefficient |
| *Dgb | $\begin{pmatrix} D_{xx} & 0 & 0 \\ 0 & D_{yy} & 0 \\ 0 & 0 & D_{zz} \end{pmatrix}$ | $10^{-14}\ \text{m}^2/\text{s}$ | Grain boundary diffusion coefficient |
| z | 300 | μm | Thickness |
| x | 3 | mm | Height |
| yg | 3 | mm | Grain size |
| ygb | 1 | μm | Grain boundary size |
| C₀ | 130 | mol/m^3 | Hydrogen concentration |
| C_s | 0 | mol/m^3 | Concentration at exit side |
| S | *S(y) | Pa | Stress function |

*S(y): a function following the y-axis, stress is the maximum at the GB and the minimum at two borders; *Dg: the apparent diffusion tensor for single crystal (see in Chapter III), this tensor will be rotated with the corresponding GB (see in Chapter IV), *Dgb: the value of this diffusion tensor is based on our molecular dynamics calculation with NEB method (see in Chapter IV).

The coefficient form PDE (Eq.2.13) equation was applied to simulate the hydrogen diffusion under stress gradient.

$$d \frac{dC}{dt} + e \frac{d^2 C}{dt^2} + \nabla \cdot (-c \nabla C - \alpha C + \gamma) + \beta \cdot \nabla C + aC = f \quad (\text{Eq.2.13})$$

Where C is the hydrogen concentration, t the time, $d=1$ is the damping or mass coefficient, $e=0$ the mass coefficient, c the diffusion coefficient, α is the conservative flux convection coefficient, $\beta=0$ is the convection coefficient, $\gamma=0$ is the conservative flux source, $a=0$ is the adsorption coefficient and $f=0$ is the source term. The transport equations for GB and G are given in (Eq.2.14 and Eq.2.15).

$$\frac{dC}{dt} + \nabla \cdot (-\overline{\overline{D}}_g \nabla C + \frac{\overline{\overline{D}}_g V_H \nabla \overline{\overline{\sigma}}_H}{RT} C) = 0 \quad (\text{Eq.2.14})$$

$$\frac{dC}{dt} + \nabla \cdot (-\overline{\overline{D}}_{gb} \nabla C + \frac{\overline{\overline{D}}_{gb} V_H \nabla \overline{\overline{\sigma}}_H}{RT} C) = 0 \quad (\text{Eq.2.15})$$

Where $\alpha = -\overline{\overline{D}}_i V_H \nabla \overline{\overline{S}} / RT$ with $\overline{\overline{D}}_i = \overline{\overline{D}}_{gb}$ or $\overline{\overline{D}}_g$ and $\nabla = \left[\frac{d}{dx}, \frac{d}{dy}, \frac{d}{dz} \right]$. V_H is the partial molar volume, R the gas constant and T the temperature, $\overline{\overline{\sigma}}_H$ is the hydrostatic stress.

II.2.2 Atomic Simulation

The past decade has seen rapid progress in the design, manufacturing, and theoretical research at micro and nanometers length scales with an increase in computing capacity. While advances continue to be made in fabrication techniques and material characterization, there is a definite lag in theoretical approaches that can successfully predict how these things will behave. As the limits of classical and continuum theories are reached, some phenomena that may be insignificant at larger length and time scales can become dominant. Actually, in many cases only a basic and qualitative understanding of the observed behavior exists with the hypothesis. One of the major parts of this lack of knowledge is due to the difficulty in solving the Schrodinger equation exactly for anything more than one hydrogen atom, and particularly the enormous computational resources required to solve it with a system of a few hundred atoms.

By ignoring the electrons and atomic level's description using fitted potential, the computational requirement is greatly reduced. Larger systems (tens and hundreds of thousands of atoms) can be investigated with molecular dynamics (MD) simulations, Monte Carlo methods and coarser approaches. In this study, the investigation was carried out using code LAMMPS (Large-scale Atomic/Molecular Massively Parallel Simulator) for MD simulations at 0 K, or more precisely, molecular statics (MS). LAMMPS is a classical open source molecular dynamics code and is

distributed by Sandia National Laboratories, a US Department of Energy laboratory. It can be used to model atoms or, more generically, as a parallel particle simulator at the atomic, meso, or continuum scale. LAMMPS can run on single processors or in parallel using message-passing techniques and a spatial-decomposition of the simulation domain. The code is designed to be easily modified or extended with new functionality.

The MD method calculates physical movements of atoms and then obtains the desired properties. A simple description of the MD algorithm is given in the *figure. 2.13*, the MD simulation generally starts with giving the atoms initial positions, and in some cases with the initial velocities or other attributes of atoms. The key point is that a proper force field should be given to defining the forces between the atoms, potential energy and the accelerations obtained from the new forces. The trajectories of atoms or molecules can be determined by alternatively calculating force with solving Newton's equations of motion. In the fields of physics, chemistry and materials sciences, some types of potentials are widely used such as empirical and semi-empirical potentials, pair potentials versus many-body potentials, polarizable potentials and so on.

The Lennard-jones potential is a simple mathematical model that is widely used the materials sciences. This potential approximates the interaction between a pair of neutral atoms or molecules based on their distance of separation. It is worth mentioning that the 12-6 Lennard-Jones model is not the most faithful representation of the potential energy surface, but rather its use is widespread due to its computational expediency. The expression is given in (Eq.2.16)

$$E_{LJ} = 4\varepsilon \left[\left(\frac{\sigma}{r} \right)^{12} - \left(\frac{\sigma}{r} \right)^6 \right] \quad (\text{Eq.2.16})$$

Where ε is the depth of the potential well and a measure of how strongly the two particles attract each other, σ is the finite distance at which the interparticle potential is zero, r is the distance between the particles. Despite the existence of more accurate potentials, the L-J potential is extensively applied in computer simulations due to its computational simplicity.

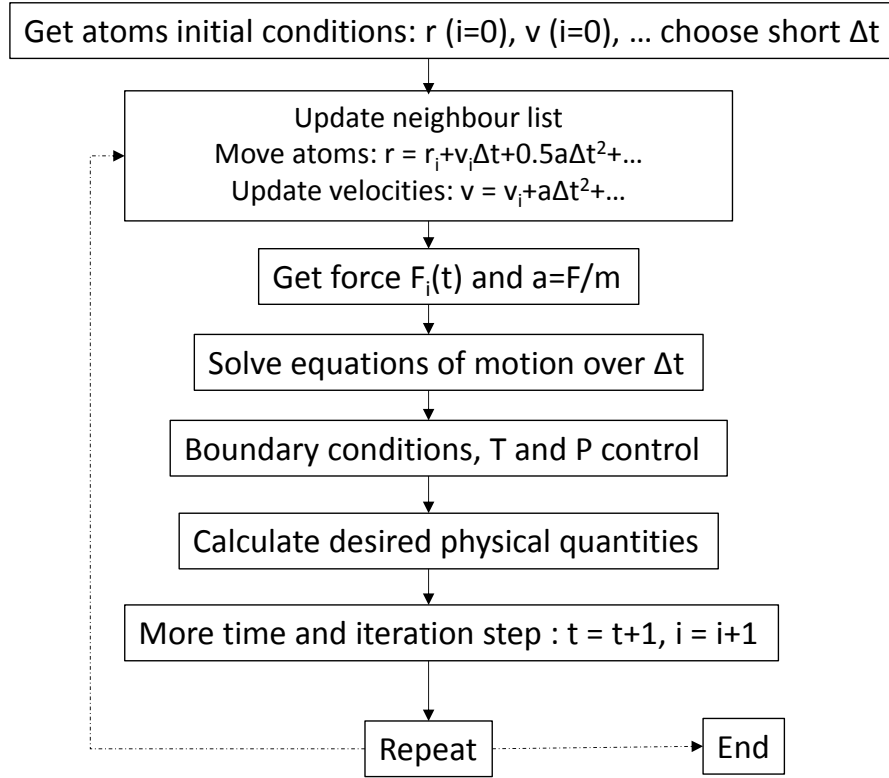


Figure 2.13 – A simplified description of the molecular dynamics simulation algorithm

In this study, the relaxed configuration of atoms is found using the minimization of the total energy with an appropriate interatomic potential at 0 K and 0 Pa. For the H-Ni system, the interatomic potential was established by embedded-atom method (EAM) [Angelo1995]. The EAM is a semi-empirical and many-atom potential for computing the total energy of a metallic system. In this method, the energy is determined by embedding an atom into the local electron density of its neighbor. With the EAM, the materials community has investigated many problems of interest: point defects, melting, alloying, grain boundary structure and energy, dislocations, segregation, fracture, surface structure, and epitaxial growth. In general, most of the EAM calculations have been carried out in close connection with experimental work. The energy of atom i in the EAM method is given by the following equation:

$$E_i = F_\alpha \left(\sum_{i \neq j} \rho_\beta(r_{ij}) \right) + \frac{1}{2} \sum_{i \neq j} \phi_\beta(r_{ij}) \quad (\text{Eq.2.17})$$

Where F is the embedding energy function, ρ is the partial electron density contribution, r_{ij} denotes the distance between atom i and j , ϕ is the pair potential, α and β are the element types of atom i and j . A potential can be very complicated. For example, in chemistry and biology it is usually referred to as a force field and may be defined at many levels of physical accuracy. The potential energy is a function that describes the atomic positions ($3N$) of all the atoms in a system and the nature of this

function can be very complicated, there is no analytical solution to the equations of motion. Generally, we define a cut-off region r_{cut} (interaction cell region) to simplify the calculations, numerous numerical algorithms [Plimpton1995] (*Verlet*, *Leap-frog*, *Velocity Verlet* and *Beeman's*) have been developed for integrating the equations of motion, in reality, much more complicated versions of the algorithm are applied, including two steps (predictor and corrector) in solving the equations of motion and many additional steps such as temperature and pressure control. The choice of algorithms is based on (i) its numerical stability for large time steps, (ii) its simplicity, and (iii) modest memory requirements.

In order to use the EAM, empirical expressions must be developed for the pair energy term and the electron density. As proposed by Chen and coworkers [Chen1989, Chen1990, Angelo1995] the form of the pair energy term is given by:

$$\varphi(r) = C_1 [\exp(-C_2(r - C_3)) - 2\exp(C_2(r - C_3))] f_{cut}(r) \quad (\text{Eq.2.18})$$

Here c_1 , c_2 , and c_3 , are parameters determined by the fitting procedure. The term $f_{cut}(r)$ is a function that forces the pair potential smoothly to zero beyond a certain distance r_{cut} . The form chosen for the cut-off function is:

$$f_{cut}(r) = \exp\left(\frac{1}{r - r_{cut}}\right) \quad (\text{Eq.2.19})$$

This form for the cut-off function is simple to implement numerically and is infinitely differentiable so that it lends itself to numerical calculations. The value of the cut-off distance, r_{cut} , as a parameter in the fitting procedure that was adjusted to provide the best match between the calculations and experiments (3.0047 Å in our study). The form chosen for the electron density was again the form proposed by Chen and coworkers [Chen1989, Chen1990] and is given by:

$$\rho(r) = C_4 r^6 [\exp(-C_5 r + 2^9 \exp(-2C_5 r))] f_{cut}(r) \quad (\text{Eq.2.20})$$

Here, c_5 is a parameter that is determined by the fitting procedure. The parameter c_4 does not affect the properties of a pure material. It can be shown that any variation in the density can be offset by a corresponding transformation in the embedding energy [Daw1993]. This parameter is important since it allows for scaling the relative electron densities in an alloy system. In the study of Angelo [Angelo1995], it was fixed at the value one for nickel.

For grain boundaries in a bi-crystal system, the construction of grain boundary is to find the most optimal configuration, an example of simulation cell for the grain boundary $\Sigma 5$ -36 $\langle 87 \rangle_{\langle 100 \rangle} \{310\}$ is illustrated in *figure 2.14*. θ is the misorientation angle between two identical nickel crystals around the symmetric tilt axis along the grain boundary plane.

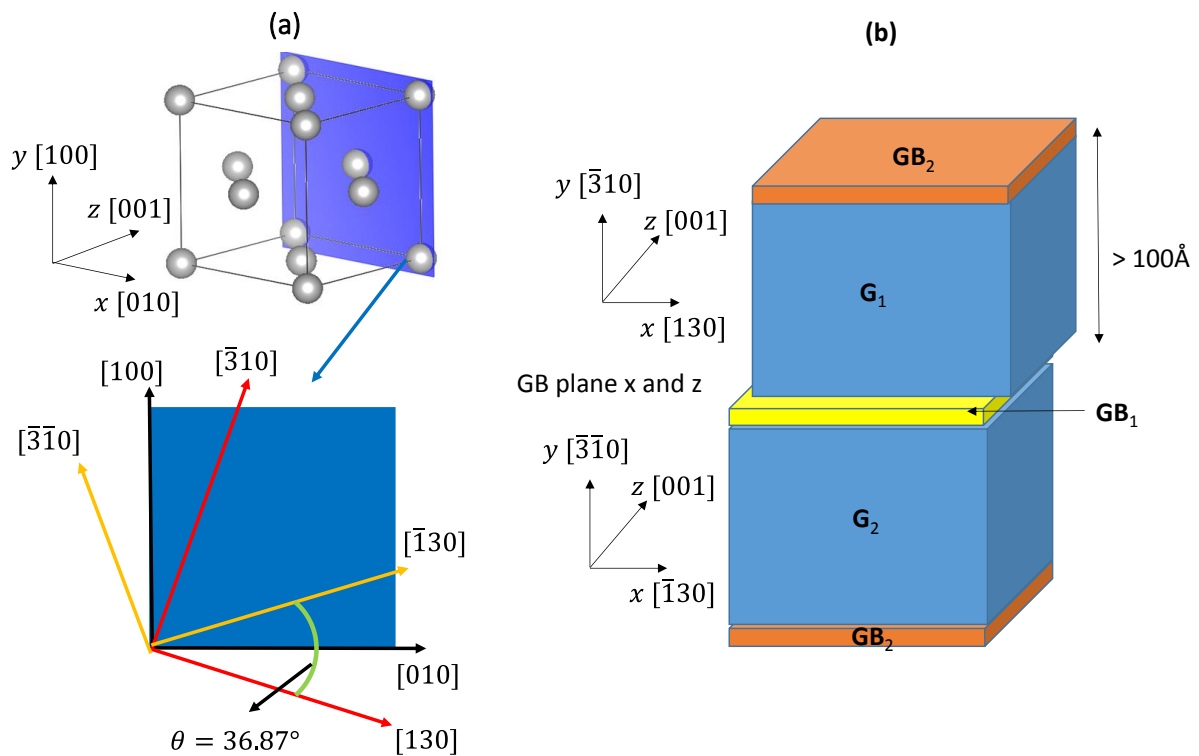


Figure 2.14 – (a) GB $\Sigma 5\text{-}36 \text{ } \langle 001 \rangle \{310\}$ plane for nickel. (b) Schematic of a bi crystal simulation cell.

The direction along the GB plane is designated by the tilt z-axis [001] in the simulation cell and common for both grains. Each GB simulation cell contains two-grain lattices which are characterized by two distinct crystallographic orientations in x and y directions. The GB simulation cells are considered in 3D periodic boundary conditions, this representation provides an existence of two GBs in each simulation cell: one in the middle of the simulation cell and on another counting for a mirror image in the bound parts of the simulation cell. The separation distance between each GB is chosen to be large enough so that there will be no energetic interaction between two GB interfaces. Several grain boundaries configurations have been treated in order to determine the most stable microstructure GB interface. A rigid body translation parallel to the GB plane has been applied following x and z-axis, all translational vectors are in a primitive cell of the displacement shift complete (DSC) lattice [Priester2013] and the lattice spacing in the planar directions of each grain is kept constant. The translation of one grain relative to another yields a re-arrangement of atoms at the GB plane. After testing hundreds of configurations, the configuration with the minimum energy of grain boundary is obtained and the excess volume could be calculated using Voronoi tessellation method implemented in LAMMPS code.

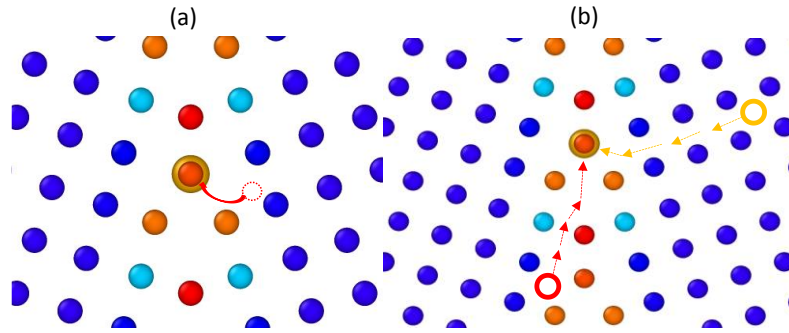


Figure 2.15 – (a) Segregation site of the hydrogen atom from the initial position. (b) An example of minimum energy path of diffusion.

Since the GB structure is well defined, we can insert an atom of hydrogen into the GB. The initial position of hydrogen is near to an atom of nickel, after the energy minimization, the hydrogen atom will find its stable position *figure 2.15 (a)* using atomic simulation analysis software OVITO (OVITO is an open source scientific visualization and analysis software for atomic simulation data developed by Alexander Stukowski at Darmstadt University of Technology, Germany). The stable hydrogen position is a segregation site, we have studied several segregation sites to get a better understanding of the GB – H system.

After determining several stable segregation sites in the core region, we are interested in the diffusion paths (*figure. 2.15 (b)*) among these different segregation sites using nudged elastic band method (NEB). This method is used for finding saddle points and minimum energy paths (MEP) between the known initial and final states. Transition states of diffusion paths (referred to as images) find the lowest energy possible while maintaining equal spacing to neighboring images. To enable the transition geometry and energy to be accurately obtained from the NEB method, once the images have converged sufficiently to the MEP the image at the highest energy point is allowed to climb uphill along the MEP until it reaches the transition state. We have investigated the MEP and the energy barrier between the most stable segregation positions and the highest Voronoi volume positions (the volume occupied by the hydrogen atom) using LAMMPS code with NEB package.

III. Overview

In order to study the impact of intergranular nature on the hydrogen transport in nickel, several single crystals and bi-crystals have been studied by EBSD and TEM. These tests have identified the main metallurgical factors likely to influence the diffusion and segregation of hydrogen, in particular the crystallographic orientation and the initial microstructure state such as the distribution of dislocations.

The diffusivity and solubility of hydrogen were then studied using electrochemical permeation and TDS, the experimental results show clearly the effects of metallurgical factors on the hydrogen transport process. In order to investigate the impacts of these metallurgical factors separately, TEM has been used to study the microstructure with the presence of hydrogen and difference diffusion models have been established by FEM to reproduce the experiment. These diffusion models give a macroscopic point of view on the key parameters of the hydrogen diffusion process such as the scale effect and the stress state. At the atomic scale, the hydrogen diffusion and segregation in nickel GBs have been studied by EAM-MD, this method allowed us to get local results and particularly to study different grain boundaries. The results of nickel single crystals and bi-crystals will be presented in Chapter III and IV, respectively.

Chapter 3.

Impact of crystallographic orientation on the hydrogen transport

| | |
|---|-----|
| <u>Chapter 3. Impact of crystallographic orientation on the hydrogen transport</u> | 86 |
| <u>Chapter 3a. Hydrogen charging in nickel</u> | 88 |
| <u>I. Identification of the hydrogen charging conditions</u> | 88 |
| <u>I.1 Electrochemical kinetic model</u> | 89 |
| <u>I.1.1 Steady state</u> | 91 |
| <u>I.1.2 Thermodynamics</u> | 96 |
| <u>II. Equivalence conversion: Over potential – fugacity</u> | 99 |
| <u>Chapter 3b. Hydrogen in nickel single crystals</u> | 105 |
| <u>I. Hydrogen segregation and diffusion in Ni <001></u> | 105 |
| <u>I.1 Hydrogen solubility in nickel <001></u> | 105 |
| <u>I.2 Hydrogen diffusivity in nickel <001></u> | 110 |
| <u>II. Orientations <100>, <110>, <219> and <111></u> | 111 |
| <u>II.1 Anisotropic diffusion</u> | 111 |
| <u>II.2 Influence of self-stress on the diffusion process</u> | 113 |
| <u>II.2.1 Description of diffusion in the solids</u> | 114 |
| <u>II.2.1.1 Volume variation with the presence of a solute</u> | 115 |
| <u>II.2.1.2 Atomic and volume expansion</u> | 116 |
| <u>II.2.1.3 Strain state near of the solute</u> | 117 |
| <u>II.2.1.4 Hydrogen flux and the apparent diffusion coefficient</u> | 118 |
| <u>II.2.1.5 In a solid with anisotropic elasticity properties</u> | 119 |
| <u>II.2.2 Confrontation of the thermodynamic approach with experimental data</u> | 122 |
| <u>III. Conclusions</u> | 131 |

This chapter is intended to provide insight into the hydrogen transport in single crystalline nickel, the diffusion and segregation of hydrogen have been studied in different crystallographic orientations using two experimental techniques: electrochemical permeation (PE) and thermal desorption spectroscopy (TDS). A first study deals with the hydrogen charging conditions for nickel, the kinetics of hydrogen evolution at the surface has been analyzed in the alkaline solution at room temperature, the objective is to identify the working current density range for the hydrogen charging by the electrochemical way. A conversion model of the equivalent hydrogen pressure has been discussed and compared with the atomistic calculations.

In the second part, we first present the results of the diffusion and segregation of hydrogen in nickel $\langle 001 \rangle$, the diffusion process has been studied using finite elements method (FEM). And later, we will focus on the anisotropic diffusion with different crystallographic orientations, a first approximation is described using the classical Fick's laws and an apparent diffusion tensor. Within a thermodynamic framework, the diffusion equation can be derived from Fick's laws with an apparent diffusion coefficient which contains an added solute content. This added term is due to the elastic strain field associated with the insertion of solute atoms. For nickel crystals, the dependence of crystallographic orientation arises from the elastic anisotropy. Additionally, our results elucidate the discrepancies between the thermodynamic model and experimental observations of the effect of the solute concentration on the diffusion process. Moreover, this result highlights the importance of the impact of hydrogen on vacancy formation and the subsequent consequences on the anisotropy of the apparent diffusion coefficient.

Chapter 3a. Hydrogen charging in nickel

I. Identification of the hydrogen charging conditions

Hydrogen entry into metals has two different sources from environment: (i) hydrogen gas and (ii) hydrogen corrosion. Corrosion can involve hydrogen in the cathodic partial reaction. In order to define an equivalence between cathodic and gaseous charging conditions, we start from the kinetic and thermodynamic formalisms of the Hydrogen Evolution Reaction (HER) and Hydrogen Absorption Reaction (HAR) reactions. The objective is to formalize the link between the conditions of cathodic charging (Overpotential, hydrogen flux, surface coverage) and the equivalent pressure (Fugacity) of dihydrogen. Theoretically, the same amount of hydrogen can be charged into a metal through the different charging methods if the right charging parameters are chosen. The gaseous charging and electrolytic charging are thus equivalent.

I.1 Electrochemical kinetic model

The hydrogen evolution at the surface and the behavior in bulk can be considered as thermodynamics formalisms of HER and HAR. At the surface, the direct absorption mechanism is that protons are reduced directly to form the subsurface absorbed hydrogen. The *figure 3.0* summarizes the processes of HAR and HER mechanisms at the surface.

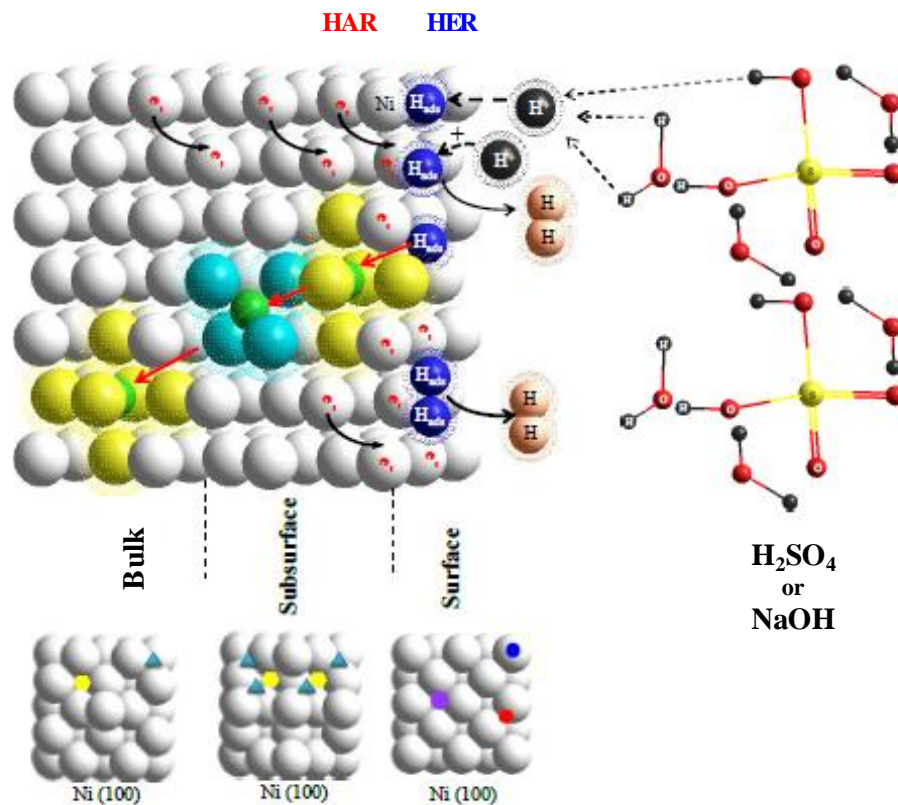
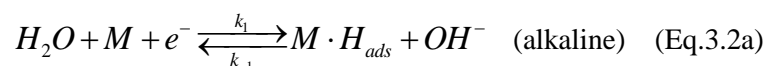
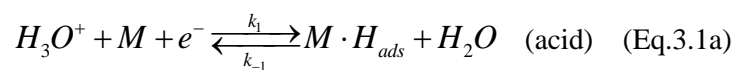


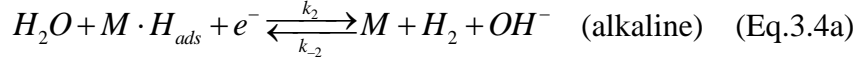
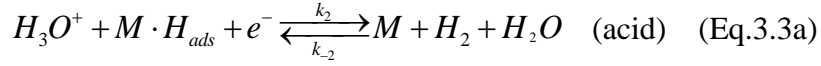
Figure 3.0 - The global mechanism of the evolution reaction of hydrogen on the surface of undeformed single crystal nickel (100) [Lekbir 2012]

According to the indirect absorption mechanisms, the HER proceeds through the following steps [Lasia1995, Sepa2001, Gabrielli2006]:

Volmer reaction



Heyrovsky reaction (electrochemical recombination)



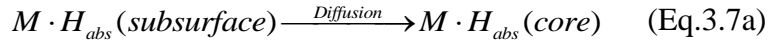
Tafel reaction (chemical recombination)



$M \cdot H_{ads}$ is a hydrogen atom adsorbed on the metal surface, hydrogen molecular can be formed and then can desorb from the sample surface. Hydrogen can enter into the metal through HAR [Lasia2006]:



The absorption is in the subsurface layer from the interface, $M_{subsurface}$ and $M_{surface}$ are the empty subsurface and surface sites, the subsequent diffusion into the bulk is:



Assuming each step of HER is elementary and controlled by charge transfers, and there is no concentration polarization. The reaction rates according to the Langmuir adsorption isotherm are [Lasia2002/06, Gabrielli2006]:

$$v_1 = k_1(1-\theta) - k_{-1}\theta \quad (\text{Eq.3.8a})$$

$$v_2 = k_2\theta - k_{-2}(1-\theta) \quad (\text{Eq.3.9a})$$

$$v_3 = k_3\theta^2 - k_{-3}(1-\theta)^2 \quad (\text{Eq.3.10a})$$

$$v_4 = k_4\theta(1-X_0) - k_{-4}(1-\theta)X_0 \quad (\text{Eq.3.11a})$$

Where θ is the surface coverage by adsorbed hydrogen. $X_0 = C_{H,0}/C_{H,max}$ is the dimensionless ratio of concentration of the subsurface hydrogen (at $x = 0$) to its saturation concentration. k_i are the forward reaction constants (k_{-i} are the backward reaction constants) in alkaline solution:

$$k_1 = k_1^0 c(H_2O) \exp(-\beta_1 FE / RT) \quad (\text{Eq.3.12a})$$

$$k_{-1} = k_{-1}^0 c(OH^-) \exp((1 - \beta_1)FE / RT) \quad (\text{Eq.3.13a})$$

$$k_2 = k_2^0 c(H_2O) \exp(-\beta_2 FE / RT) \quad (\text{Eq.3.14a})$$

$$k_{-2} = k_{-2}^0 c(OH^-) \exp((1 - \beta_2)FE / RT) \quad (\text{Eq.3.15a})$$

$$k_4 = k_4^0 \quad (\text{Eq.3.16a})$$

β_i is the reaction symmetry coefficient. k_i^0 is the standard rate constant. The electron transfer with the Faradic current density involving HAR and HER can be given as:

$$r_0 = \frac{-j}{F} = v_1 + v_2 \quad (\text{Eq.3.17a})$$

$$r_1 = \frac{q}{F} \frac{d\theta}{dt} = v_1 - v_2 - v_3 - v_4 \quad (\text{Eq.3.18a})$$

In the metal, as trapping is not considered, the diffusion process is supposed to follow the classic Fick's laws ($X = C_H / C_{H,max}$):

$$\frac{dX}{dt} = D_{app} \frac{\partial^2 X}{\partial x^2} \quad (\text{Eq.3.19a})$$

$$J(x) = -D_{app} \times C_{H,max} \frac{\partial^2 X}{\partial x^2} \quad (\text{Eq.3.20a})$$

The hydrogen flux at the electrode surface gives the boundary condition at $x = 0$:

$$J(x=0) = v_4 \quad (\text{Eq.3.21a})$$

I.1.1 Steady state

At the steady state, we considered that the surface coverage dose not evaluate with the time, the kinetic parameters could be identified as well as the flux – potential relationship at this step. We have thus

$\frac{d\theta}{dt} = 0$ and $\frac{dX(x)}{dt} = 0, \forall x$, consequently:

$$\frac{\partial^2 X(x)}{\partial x^2} = 0, J(x) = J(0) = v_4 \text{ and } X(x) = -\frac{J(0)}{C_{H,max} D_{app}} x + X(0)$$

In the first case of an infinitely long solid $X(d)=0$, d is the solid thickness and is long enough.

$$X(0) = \frac{J(0)}{D_{app} \times C_{H,max}} d = \frac{v_4}{D_{app} \times C_{H,max}} d \quad (\text{Eq.3.22a})$$

$$v_4 = \frac{X(0)D_{app}C_{H,max}}{d} \ll v_1, v_2, v_3 \quad (\text{Eq.3.23a})$$

The surface kinetics do not depend on the hydrogen activities in the sample, thus v_4 is not considered here and we could give the expressions of the coverage rate assuming negligible inverse reactions ($k_{-1} = k_{-2} = k_{-3} = 0$):

$$r_1 = \frac{q}{F} \frac{d\theta}{dt} = 0 = v_1 - v_2 - v_3 - v_4 \quad (\text{Eq.3.24a})$$

$$0 = k_1(1-\theta) - k_2\theta - k_3\theta^2 \quad (\text{Eq.3.25a})$$

$$\theta = \frac{-(k_1 + k_2) + \sqrt{(k_1 + k_2)^2 + 4k_1k_3}}{2k_3} \quad (\text{Eq.3.26a})$$

And the current density takes then the following form:

$$r_0 = \frac{-j}{F} = v_1 + v_2 = k_1(1-\theta) + k_2\theta \quad (\text{Eq.3.27a})$$

$$-j = -F(k_1(1-\theta) + k_2\theta) \quad (\text{Eq.3.28a})$$

In an alkaline solution of 0.1 M NaOH at room temperature, we have realized the cathodic polarization for nickel single crystals with different crystallographic orientations. The modelization (Mod) of experimental data using equation (Eq.3.26a, Eq.3.28a) allows us to identify reaction rates for the different steps (*figure. 3.1*), all values are given in *table 3.1*.

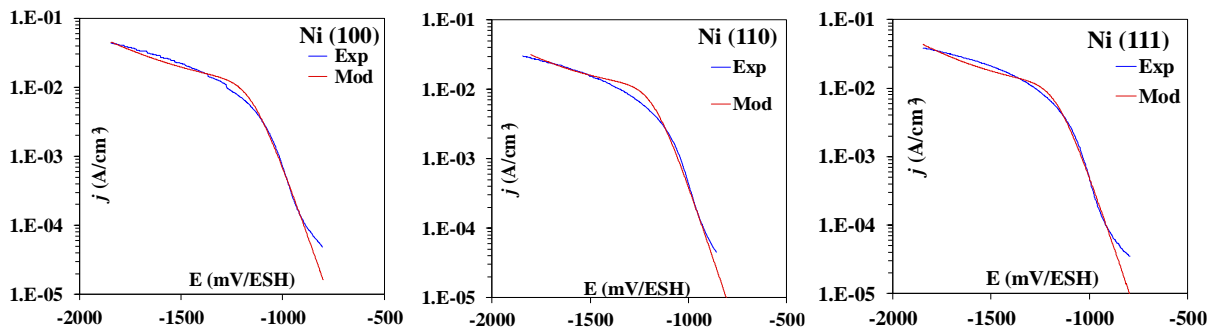


Figure 3.1 – Polarization curves for nickel (100), (110) and (111) single crystals.

Table 3.1 Reaction constants for different steps in 0.1 M NaOH at 300 K.

| | (100) | (110) | (111) |
|---|-------------------|-------------------|---------------------|
| k^0_1 ($\text{m}\times\text{s}^{-1}$) | 5×10^{-5} | 3×10^{-5} | 3.8×10^{-5} |
| k^0_2 ($\text{m}\times\text{s}^{-1}$) | 2×10^3 | 7×10^2 | 9×10^2 |
| k^0_3 ($\text{m}\times\text{s}^{-1}$) | 5×10^{-8} | 5×10^{-8} | 5×10^{-8} |
| b_1 (mV^{-1}) | -0.021 | -0.021 | -0.021 |
| b_2 (mV^{-1}) | -0.0037 | -0.0041 | -0.0041 |

* $b_i = -F\beta_i/RT$

The reaction rates at the surface are similar for different crystallographic orientations. The surface coverage is presented in the *figure 3.2*, the difference of surface coverage among these three orientations is less than 8%, and we can consider that the hydrogen evolution at the surface is the same.

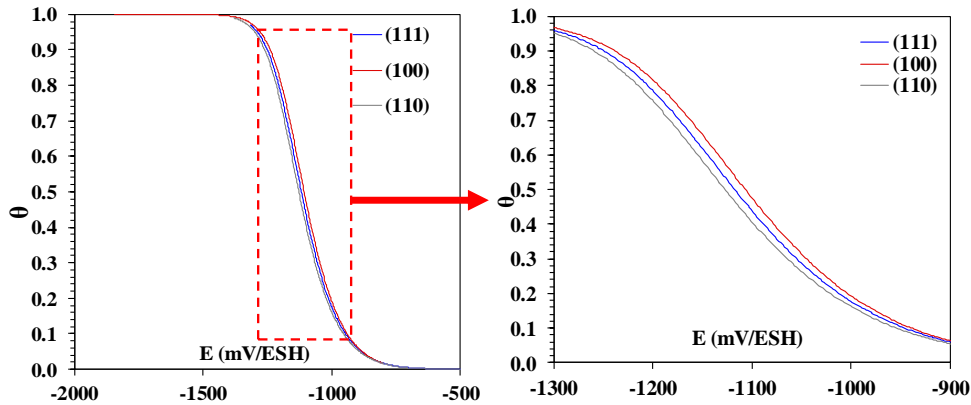


Figure 3.2 – Surface coverage for nickel (100), (110) and (111) single crystals

Figure 3.3 compares the hydrogen evolution reaction rates for Volmer, Heyrovsky and Tafel steps, the cathodic polarization at the nickel surface in an alkaline solution indicates that the mechanism involves discharging from a water molecule followed by rapid chemical recombination at low currents. This result indicates that the hydrogen evolution for our experimental conditions is dictated by Volmer-Tafel mechanism and has been confirmed by works of Devanathan [Devanathan1960] and Scully [Scully2017].

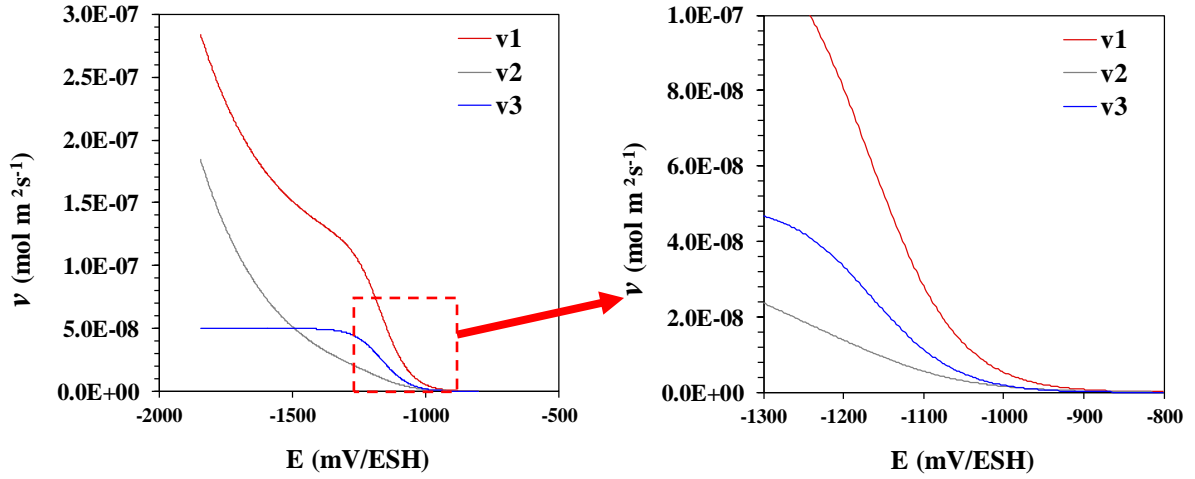


Figure 3.3 – Reaction rates as a function of the applied potential for different hydrogen evolution steps.
(v1=Volmer, v2=Heyrovsky and v3=Tafel)

In the second case of a finite solid, $J(x=0)=v_4$ is not zero and has to be taken into account in the calculation with $X(d) = 0$ at the output side, at low hydrogen concentration ($C_H \ll C_{H,max}$ and $\theta \ll 1$), we can get then :

$$v_4 = k_4\theta - k_{-4}X_0 = J(0) = J \quad (\text{Eq.3.29a})$$

$$r_1 = 0 = k_1(1-\theta) - k_2\theta - k_3\theta^2 - k_4\theta + k_{-4}X_0 \quad (\text{Eq.3.30a})$$

The surface coverage is then:

$$\theta = \frac{-(k_1 + k_2) + \sqrt{(k_1 + k_2)^2 - 4k_3J + 4k_1k_3}}{2k_3} \quad (\text{Eq.3.31a})$$

We then want to find the link with the current density and the hydrogen flux, knowing that $X_0 = Jd/D_{app}C_{H,max}$ and $J = v_4 = k_4\theta - k_{-4}X_0$. The hydrogen flux is then:

$$J = k_4\theta + k_{-4} \frac{Jd}{D_{app}C_{H,max}} \quad (\text{Eq.3.32a})$$

$$J = \frac{k_4}{1 + k_{-4} \frac{d}{D_{app}C_{H,max}}} \theta = K\theta \quad (\text{Eq.3.33a})$$

$K=k_4$ if the inverse reaction is not considered and we have $j=-F(v_1+v_2)$ and $r_1=0=v_1-v_2-v_3-v_4$, the new expression is then:

$$J = K\theta = v_4 = -2v_2 - v_3 - j / F \quad (\text{Eq.3.34a})$$

$$0 = -k_2\theta - k_3\theta^2 - j / F - K\theta \quad (\text{Eq.3.35a})$$

$$\theta = \frac{-(K + 2k_2) + \sqrt{(K + 2k_2)^2 - 4k_3j / F}}{2k_3} \quad (\text{Eq.3.36a})$$

$$J = K \frac{-(K + 2k_2) + \sqrt{(K + 2k_2)^2 - 4k_3j / F}}{2k_3} \quad (\text{Eq.3.37a})$$

For low surface coverage and V-T mechanism, assuming that $k_2/K \ll 1$:

$$J = \frac{K^2}{2k_3} \left(\sqrt{1 - \frac{4k_3}{K^2} \frac{j}{F}} - 1 \right) \quad (\text{Eq.3.38a})$$

In order to simplify the equation (Eq.3.38a), we assumed that $\frac{4k_3}{K^2} \frac{j}{F} \gg 1$, this hypothesis will be verified later when the constant K is identified. The hydrogen flux as a function of the current density is then:

$$J = \frac{K}{\sqrt{k_3F}} \sqrt{-j} \quad (\text{Eq.3.39a})$$

Figure 3.4 presents the curve of equation (Eq.3.39a) based on the experimental data of EP and TDS, the constant K can be calculated using the Volmer slope ($y=3 \times 10^{-9}x + 1 \times 10^{-9}$).

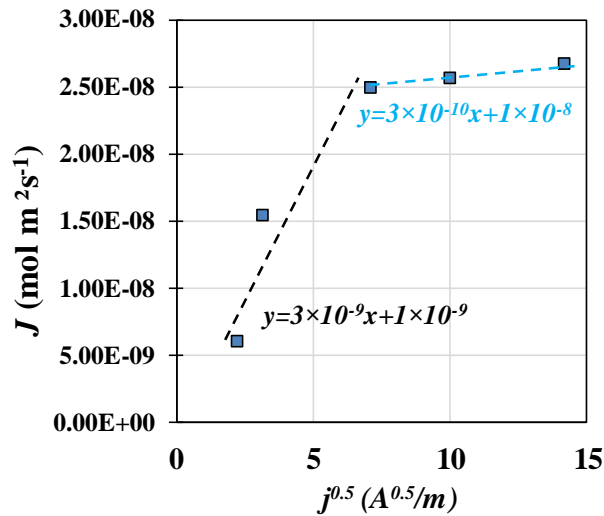


Figure 3.4 – The hydrogen flux J as a function of $j^{0.5}$, the Volmer slope equals to $3 \times 10^{-9} = K/\sqrt{k_3F}$.

We consider here that the first Volmer slope is available to identify the reaction constant. The current density increases with the hydrogen flux towards a saturation due to the increase of the Tafel and Heyrovsky reactions. The production of the diffusible hydrogen is thus slowed down even when we increase the current density. The constant K is found to be equals to 2.7×10^{-10} and the hypothesis for the simplification of equation (Eq.3.39a) is verified.

Since the diffusion process is dominated by the Volmer reaction, we consider now only the Volmer step with $-j/F=v_1$:

$$J = \frac{K}{\sqrt{k_3}} \sqrt{v_1} \quad (\text{Eq.3.40a})$$

$$J = \frac{K}{\sqrt{k_3}} \sqrt{k_1^0 c(H_2O)(1-\theta) \exp(b_1 E)} \quad (\text{Eq.3.41a})$$

$$J = \frac{K}{\sqrt{k_3}} \sqrt{k_1^0 c(H_2O)(1-\theta) \sqrt{\exp(-b_1 E)}} = K' \sqrt{\exp(b_1 E)} \quad (\text{Eq.3.42a})$$

$$\ln(J) = \ln(K') \frac{b_1 E}{2} \quad (\text{Eq.3.43a})$$

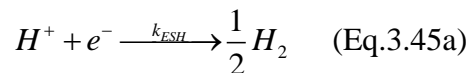
These expressions will be discussed later in the part II of conversion model of equivalent pressure.

I.1.2 Thermodynamics

This step is to establish the relationship between the surface conditions (the surface coverage, overpotential) and the fugacity. Considering the system of two electrodes (the working electrode = metal, the hydrogen reversible electrode), we can get the Volmer reaction (T=constant, P=constant):



The reaction at the hydrogen standard electrode is:



The thermodynamic equilibrium of two reactions is then:

$$\mu_M^0 + \mu_{H^+} + \mu_{e^-}^M = \mu_{MH} \quad (\text{Eq.3.46a})$$

$$\mu_{H^+} + \mu_e^{M'} = \frac{1}{2} \mu_{H_2} \quad (\text{Eq.3.47a})$$

(Eq.46a) - (Eq.47a) is:

$$\mu_e^M - \mu_e^{M'} = \mu_{MH} - \mu_M^0 - \frac{1}{2} \mu_{H_2} \quad (\text{Eq.3.48a})$$

μ_M^0 is the metal chemical potential, μ_{H^+} is the proton chemical potential in the solution, μ_e^M is the chemical potential of electron at the side of metal M (working electrode), μ_{MH} is the chemical potential of the adsorbed hydrogen, $\mu_e^{M'}$ is the chemical potential of electron at the side of M' (reference) and μ_{H_2} is the chemical potential of H_2 gas.

The difference of potential between the working electrode and the reference electrode is:

$$\eta = \phi_M - \phi_{M'} \quad (\text{Eq.3.49a})$$

And

$$\mu_e^M - \mu_e^{M'} = -\eta F \quad (\text{Eq.3.50a})$$

The chemical potential of H_2 gas can be written as a function of fugacity f_{H_2} :

$$\mu_{H_2} = \mu_{H_2}^0 + RT \ln(f_{H_2}) \quad (\text{Eq.3.51a})$$

$$\mu_{MH} = \mu_{MH}^0 + RT \ln\left(\frac{\theta}{1-\theta}\right) \quad (\text{Eq.3.52a})$$

$\mu_{H_2}^0$ is the chemical potential of H_2 gas at 0 K and 1 atm, and we can obtain the equation (Eq.3.48a) by (Eq.3.52a)-(Eq.3.51a):

$$-\eta F = \mu_{MH}^0 + RT \ln\left(\frac{\theta}{1-\theta}\right) - \mu_M^0 - \frac{1}{2} \mu_{H_2}^0 - \frac{1}{2} RT \ln(f_{H_2}) \quad (\text{Eq.3.53a})$$

With $\Delta G_{ads}^0 = \mu_{MH}^0 - \mu_M^0 - \frac{1}{2} \mu_{H_2}^0$,

$$-\eta F = \Delta G_{ads}^0 + RT \ln\left(\frac{\theta}{1-\theta}\right) - \frac{1}{2} RT \ln(f_{H_2}) \quad (\text{Eq.3.54a})$$

$$f_{H_2}^{\frac{1}{2}} = \left(\frac{\theta}{1-\theta}\right) \exp\left(\frac{\eta F}{RT} + \frac{\Delta G_{ads}^0}{RT}\right) \quad (\text{Eq.3.55a})$$

At equilibrium state with $\eta=0$, we can get:

$$\left(\frac{\theta}{1-\theta}\right) = f_{H_2}^{\frac{1}{2}} \exp\left(\frac{-\Delta G_{ads}^0}{RT}\right) \quad (\text{Eq.3.56a})$$

θ_R is the surface coverage when $f_{H_2} = 1$ atm, we have then :

$$\left(\frac{\theta_R}{1-\theta_R}\right) = \exp\left(\frac{-\Delta G_{ads}^0}{RT}\right) \quad (\text{Eq.3.57a})$$

The combination of (Eq.3.56a) and (Eq.3.57a) gives:

$$\left(\frac{\theta}{1-\theta}\right) = \left(\frac{\theta_R}{1-\theta_R}\right) f_{H_2}^{\frac{1}{2}} = \theta_0 f_{H_2}^{\frac{1}{2}} \quad (\text{Eq.3.58a})$$

It is possible now to get the link with the potential taking into account only the Volmer step with $-j = Fv_1$:

$$-\frac{j}{F} = k_1^0 c(H_2O)(1-\theta) \exp(-\beta_1 FE / RT) - k_{-1}^0 c(OH^-)\theta \exp(-\alpha_1 FE / RT) \quad (\text{Eq.3.59a})$$

We assume here the symmetry coefficients β_1 and α_1 are different, and for $j=0$ the expression is then:

$$\frac{\theta}{1-\theta} = \frac{k_1^0 c(H_2O)}{k_{-1}^0 c(OH^-)} \exp\left(\frac{-(\beta_1 - \alpha_1)FE}{RT}\right) \quad (\text{Eq.3.60a})$$

The same development for θ_R when $f_{H_2} = 1$ atm gives:

$$\theta_0 = \frac{\theta_R}{1-\theta_R} = \frac{k_1^0 c(H_2O)}{k_{-1}^0 c(OH^-)} \exp\left(\frac{-(\beta_1 - \alpha_1)FE_0}{RT}\right) \quad (\text{Eq.3.61a})$$

(Eq.3.60a)/(Eq.3.61a) is then:

$$\frac{\theta}{1-\theta} = \theta_0 \exp\left(\frac{-(\beta_1 - \alpha_1)F(E - E_0)}{RT}\right) \quad (\text{Eq.3.62a})$$

The combination of (Eq.3.58a) and (Eq.3.62a) is simplified as:

$$f_{H_2} = \exp\left(\frac{-2(\beta_1 - \alpha_1)F\eta}{RT}\right) \quad (\text{Eq.3.63a})$$

The expression (Eq.3.63a) gives the relationship between the fugacity and the overpotential, similar results have been reported by different works [Bockris1970, Atrens1980, Liu2014].

II. Equivalence conversion: Over potential – fugacity

Based on the equations (Eq.3.42a), (Eq.3.43a), (Eq.3.62a) and (Eq.3.63a), we can establish the relationship among the hydrogen flux, the potential and the fugacity. We rewrite the equations (Eq.3.42a) and (Eq.3.63a) as:

$$J = K' \exp\left(\frac{b_1 E}{2}\right) = K' \exp\left(-\frac{\frac{1}{2} \beta_1 F E}{RT}\right) \quad (\text{Eq.3.64a})$$

$$\sqrt{f_{H_2}} = \exp\left(\frac{-(\beta_1 - \alpha_1) F (E - E_0)}{RT}\right) \quad (\text{Eq.3.65a})$$

$$\exp\left(\frac{-(\beta_1 - \alpha_1) F E_0}{RT}\right) \sqrt{f_{H_2}} = A_0 \sqrt{f_{H_2}} = \exp\left(\frac{-(\beta_1 - \alpha_1) F E}{RT}\right) \quad (\text{Eq.3.66a})$$

(Eq.3.64a)/(Eq.3.66a) gives

$$J = K' A_0 \exp\left(\frac{\left(\frac{1}{2} \beta_1 - \alpha_1\right) F E}{RT}\right) \sqrt{f_{H_2}} \quad (\text{Eq.3.67a})$$

The electrochemical conditions for the hydrogen permeation can be translated into an equivalent pressure in the Volmer potential range. The similar results have been reported in the works of Atrons and Bockris [**Bockris1970**, **Atrons1980**] with a simplified equivalence model for the charging conditions based on the Volmer-Tafel mechanism. The constraints which must be satisfied for equivalence of charging conditions follow from simple thermodynamic and kinetic considerations.

In the gas phase permeation studies, $f_{H_2}^g$ is the fugacity of hydrogen entry at the specimen surface. It fixes the surface concentration of hydrogen by Sieverts Law. The solution of the diffusion equations for the steady-state permeation current resulting from a given driving force (fugacity), yields to:

$$J_\infty^g = \frac{2FA_s DK_s}{V_0 L} \sqrt{f_{H_2}^g} \quad (\text{Eq.3.68a})$$

J_∞^g is the current at the steady state, F the Faraday constant, A_s the surface area, D the diffusion coefficient, K_s the solubility constant, V_0 the molar volume and L the thickness. If it is assumed that the surface concentration of hydrogen established by electrolytic charging is equivalent and can be described by Sievert's Law, then

$$J_{\infty}^e = \frac{2FA_sDK_S}{V_0L} \sqrt{f_{H_2}^e} \quad (\text{Eq.3.69a})$$

The thermodynamic expression which relates $f_{H_2}^e$ to the electrolytic charging condition is:

$$f_{H_2}^e = \exp(F\eta / ZRT) \quad (\text{Eq.3.70a})$$

η is the over potential, R the perfect gas constant, T the temperature and Z is given in (Eq.3.71a):

$$Z = -\frac{F}{2RT} \frac{\partial \eta}{\partial \ln(J_{\infty}^e)} \quad (\text{Eq.3.71a})$$

If, in the respective studies, J_{∞}^e can be measured as a function of η using EP/TDS, then Z may be determined empirically from the $\eta - \ln(J_{\infty}^e)$ relation. The calculation was based on the experimental data from a current density range (0.5 mA/cm² - 20 mA/cm²). The relationship between the overpotential and the hydrogen flux at the steady state is given in *figure 3.5*. Two slopes correspond to different adsorption reactions, following the same line of thought, diffusible hydrogen is produced by the Volmer reaction which indicates that only the first slope is taken into account in the calculation, Z is then calculated and equals to 2.655. This value is in good agreement with the collected data by Bockris and Atrens. [Bockris1970, Atrens1980].

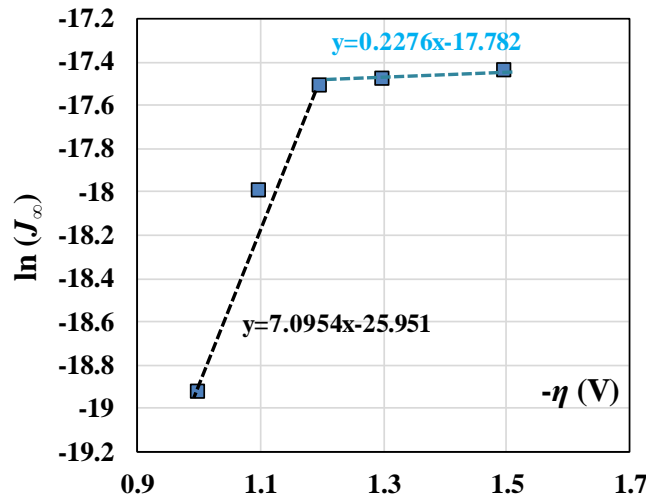


Figure 3.5 – $\ln(J_{\infty}^e)$ as a function of η , the Volmer slop equals to 7.0954.

Since fugacity was obtained using equations (Eq.3.70a) and (Eq.3.71a), we are now able to calculate the real pressure of the hydrogen gas using the Van der Waals constants. [Hand book chemistry and physics 75th Edition]

$$(P + n^2a / V^2)(V - nb) = nRT \quad (\text{Eq.3.72a})$$

n is the amount of substance, a, b are constants related to critique T_c, P_c . For hydrogen gas, $a = 27R^2T_c^2/64P_c = 0.2453 \text{ bar L}^2/\text{mol}^2$ and $b = RT_c/8P_c = 0.02651 \text{ L/mol}$. a and b are neglected in the case of perfect gas $f = P$. From an equation starts for a reel gas based on the Van der Waals equations, we simplify the relationship between f and P as:

$$\frac{f}{P} \approx 1 + \frac{P}{RT} \left(b - \frac{a}{RT} \right) \quad (\text{Eq.3.73a})$$

$$A = \left(b - \frac{a}{RT} \right) / RT \quad (\text{Eq.3.74a})$$

$A = 6.7 \times 10^{-19}$ when $T = 300 \text{ K}$ and $f = P + P^2A$

$$P = \frac{\sqrt{1 + 4Af} - 1}{2A} \quad (\text{Eq.3.75a})$$

The fugacity as a function of the overpotential is given in *figure 3.6 (a)*, hydrogen charging can be realized for a fugacity above 25 atm at room temperature. Fugacity as a function of the gas pressure is presented in the *figure 3.6(b)*, the linearity disappears for a gas pressure higher than 400 atm.

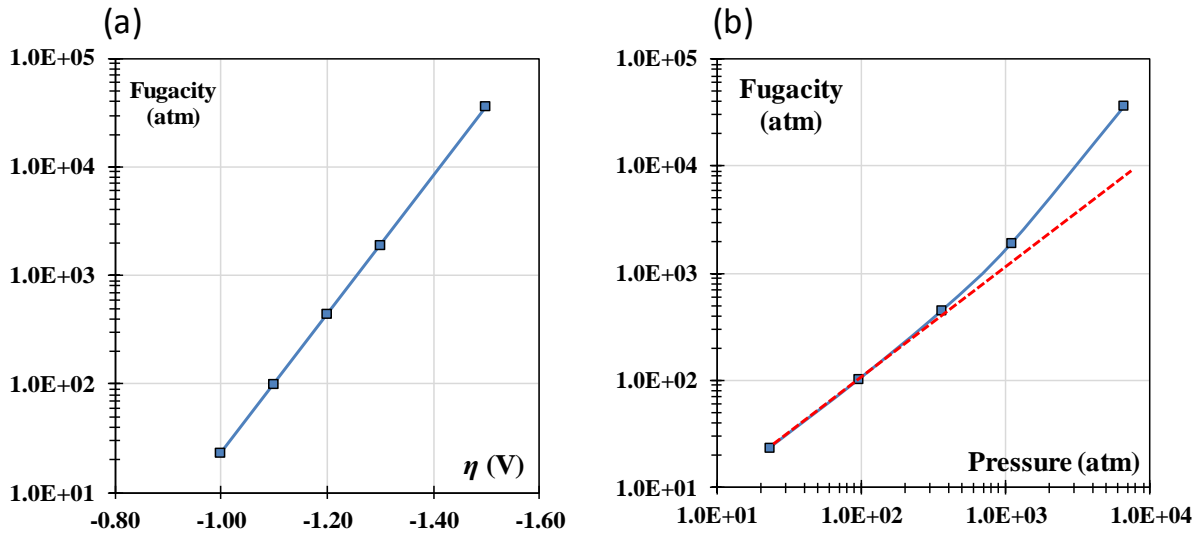
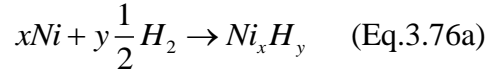


Figure 3.6 – (a) Fugacity vs overpotential. (b) Fugacity vs gas pressure according to equation (Eq.3.73a).

Figure 3.7 gives a comparison between the equivalence overpotential-fugacity model and the DFT calculations. Experimental data provides the relationship between the overpotential and the hydrogen solubility, an equivalent fugacity for the same hydrogen solubility is calculated by the conversion model.

DFT calculations were carried out at finite temperature. The free energy ($\forall T$) is calculated based on the vibration free energy and the electronic excitation. The reaction of hydrogen in nickel is:



At equilibrium, the chemical potential relationship is then:

$$x\mu(Ni) + y\frac{1}{2}\mu(H_2) = \mu(Ni_xH_y) \quad (\text{Eq.3.77a})$$

Here, we considered H_2 is the case of the perfect gas at the pressure P to the standard pressure $P_0 = 10^5$ Pa where the chemical potential of the H_2 molecule is written as:

$$\mu_{H_2}^g(P, T) = \mu_{H_2}^0(T) + k_B T \ln\left(\frac{P}{P_0}\right) \quad (\text{Eq.3.78a})$$

$\mu_{H_2}^0(T)$ is the standard chemical potential obtained by the partition function for all degrees of freedom (Vibration, translation and rotation) [Landau1980, Metsue2016] including the dissociation energy of the molecule E_D (4.26 eV within Zero point motion energy contribution) and its vibration free energy at the frequency ν_{H_2} (132.1 THz) :

$$\mu_{H_2}^0(T) = -E_D + k_B T \ln\left(1 - \exp\left(-\frac{h\nu_{H_2}}{k_B T}\right)\right) + k_B T \ln\left(\frac{P}{P_0(T)}\right) \quad (\text{Eq.3.79a})$$

With $P_0(T) = \frac{(2\pi M k_B T)^{\frac{3}{2}} k_B T}{h^3} \times \frac{8\pi^2 I_r k_B T}{h^2}$, the first part corresponds to the translation with M the mass of the H_2 molecule (2.016 g/mol) and the second rotation part with I_r the moment of inertia (4.68×10^{-48} kg/m²).

The solution Gibbs free energy can be obtained as (table 3.2):

$$G^{sol}(P, T) = H^{sol}(P, T) - TS^{sol}(P, T) - \frac{1}{2}\mu_{H_2}^g(P, T) \quad (\text{Eq.3.80a})$$

With the enthalpy and the corrected entropy:

$$H^{sol}(P, T) = E^{sol}(V, T) + T\alpha(P, T)K_T(P, T)V^{relax}(P, T)$$

$$S^{sol}(P, T) = S^{sol}(V, T) + \alpha(P, T)K_T(P, T)V^{relax}(P, T)$$

Where $\alpha(P, T)$, $K_T(P, T)$ and $V^{relax}(P, T)$ are the thermal expansion coefficient, the isothermal bulk modulus and the relaxation volume of the crystal, respectively. All parameters are taken from the previous study in [Metsue2014]. The partial solution energy $E^{sol}(V, T)$ and entropy $S^{sol}(V, T)$ at constant volume for the incorporation of H in the perfect crystal are given by the difference between the total energy and the total entropy of the H-bearing supercell and the bulk Ni:

$$E^{sol}(V, T) = E_{Ni+H}^{tot}(V, T) - E_{bulk}^{tot}(V, T)$$

$$S^{sol}(V, T) = S_{Ni+H}^{tot}(V, T) - S_{bulk}^{tot}(V, T)$$

The concentration of hydrogen in nickel is then:

$$C_H = \exp\left(\frac{-G^{sol}}{k_B T}\right) = \exp\left(\frac{-(H^{sol} - TS^{sol} - \frac{1}{2}\mu_{H_2}^0 - \frac{1}{2}k_B T \ln(\frac{P}{P_0}))}{k_B T}\right) = \exp\left(\frac{-G^0}{k_B T} + \frac{1}{2} \ln\left(\frac{P}{P_0}\right)\right)$$

(Eq.3.81a)

$$C_H = \sqrt{\frac{P}{P_0}} \exp\left(\frac{-G^0}{k_B T}\right) \quad (\text{Eq.3.82a})$$

Table 3.2 – The solution Gibbs free energy at 300 K for the insertion of hydrogen atom in an octahedral site.

| P_{H_2} (Pa) | G^{sol} (eV) | C_H (wppm) |
|----------------|----------------|--------------|
| 10^5 | 0.28 | 0.38 |
| 10^6 | 0.25 | 1.19 |
| 10^7 | 0.22 | 3.76 |
| 10^8 | 0.19 | 11.87 |

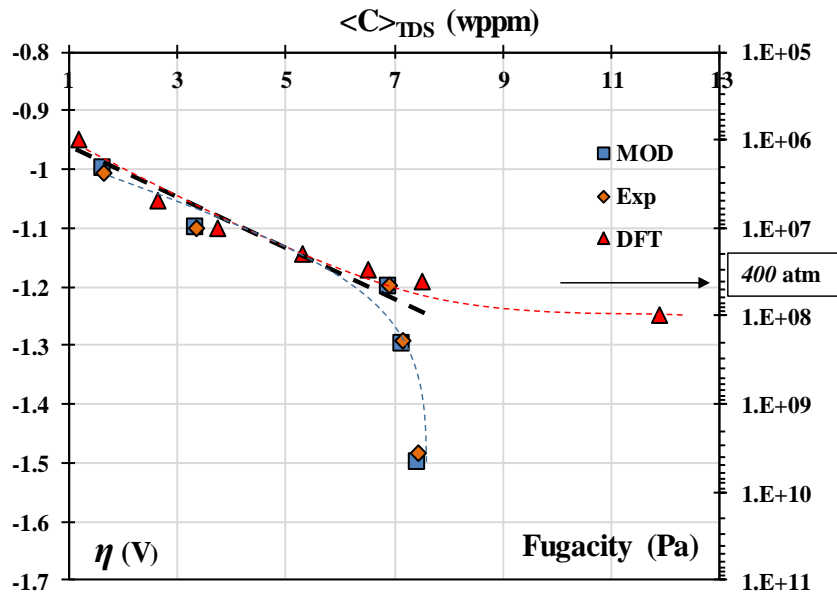


Figure 3.7 – Hydrogen solubility vs fugacity/overpotential. Exp: experimental data of EP/TDS, overpotential vs solubility; Mod: fugacity obtained by the conversion model vs solubility; DFT: fugacity vs solubility.

DFT calculations are in good agreement with this equivalence conversion model for a fugacity lower than 400 atm or an overpotential lower than about -1.2 V (this overpotential corresponds to a current density of -5 mA/cm²). Apart from this fugacity range, results of DFT start to lose the agreement with the equivalent fugacity due the limit of the case of the perfect gas. However, their values are still very close towards 1000 atm.

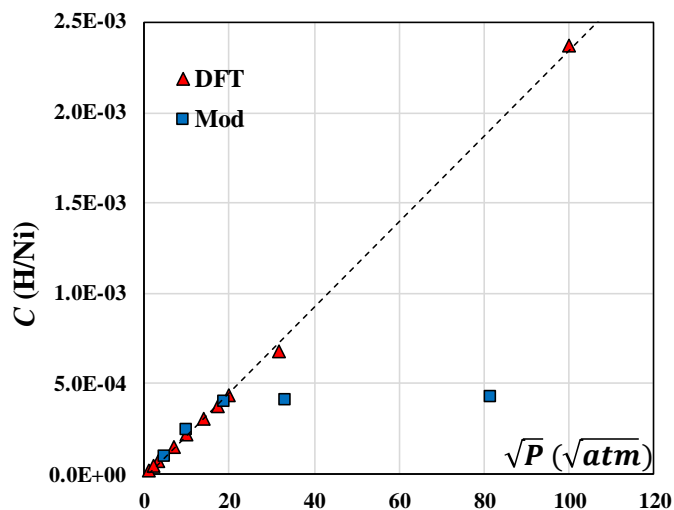


Figure 3.8 –Hydrogen solubility as a function of \sqrt{P} .

Figure 3.8 presents the relationship between the hydrogen solubility and the gas pressure, not like a linear relationship for the case of the perfect gas in DFT calculations, the deviation of Sievert's law in conversion model is due to the limit of hydrogen charging by the electrochemical way (dominated by the Volmer reaction), the overpotential range is from -1 V to -1.2 V.

Chapter 3b. Hydrogen in nickel single crystals

I. Hydrogen segregation and diffusion in Ni <001>

The hydrogen diffusion in nickel single crystal <001> has been studied by EP (electrochemical permeation) and TDS (Thermal desorption spectroscopy), in this part we explore the behavior of hydrogen in the nickel single crystal <001> with the influence of charging time and the charging current density on the hydrogen solubility and on the hydrogen diffusivity. The hydrogen solubility was determined for various charging conditions by TDS total fusion method at 2000 °C. The evolution of hydrogen solubility versus time for a given charging condition was modeled by Fick's law with FEM to evaluate the apparent diffusion coefficient. Thus for different electrochemical charging conditions, we have accessed the maximum solubility and the diffusion coefficient at room temperature.

I.1 Hydrogen solubility in nickel <001>

At room temperature, the solubility of hydrogen in the single crystal nickel <001> increases as a function of charging time towards the saturation. The maximum solubility of hydrogen was usually reached after 70 hours charging time for a thickness of around 300 μm . The hydrogen solubility as a function of charging time for five charging conditions is given in *figure 3.9*. We noted that when the charging current density increased with the solubility. It could reach a maximum value of about 7.5 wppm for current densities between 0.5 and 20 mA/cm². For a current density higher than 20 mA/cm², the hydrogen solubility measured in nickel decreases with the increase of the current density. This situation is illustrated in *figure 3.10* for 24 hours charging time with different charging current densities between 0.5 and 100 mA/cm². It corresponds to the competition between the adsorption mechanism (Volmer reaction) and the recombination (Heyrovsky/Tafel reactions). The Heyrovsky/Tafel reactions lead to the generation of hydrogen bubbles at the surface which reduces the activity of the surface.

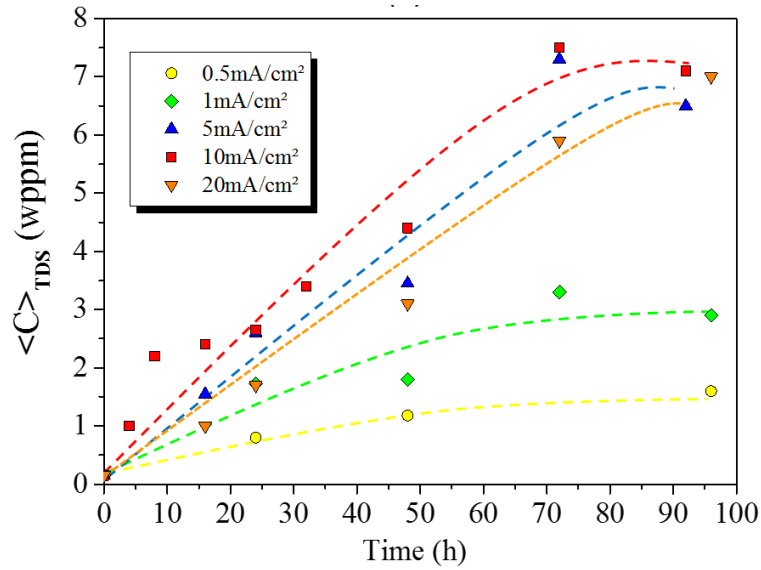


Figure 3.9 – The average hydrogen concentration in nickel <001> detected by TDS as a function of the charging time for current densities 0.5 mA/cm², 1 mA/cm², 5 mA/cm², 10 mA/cm² and 20 mA/cm²

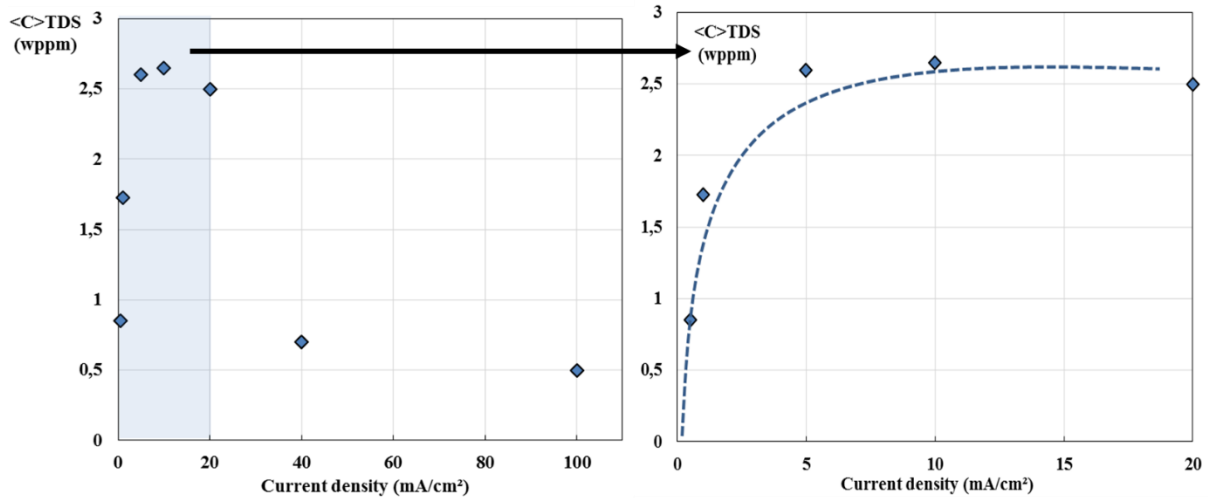


Figure 3.10 – The average hydrogen concentration in nickel sample detected by TDS as a function of current density for 24 hours charging.

To access the apparent hydrogen diffusion coefficient and the lost hydrogen concentration associated with the transfer step between the charging cell and the TDS instruments, we used FEM Comsol Multiphysics with a simple 2D geometry and the diffusion process is based on Fick's laws. At first, two conditions are simulated in order to find the model with the better fitting to the experimental data. Diffusion is considered to be one-dimensional along the membrane thickness with the driving force (a concentration gradient). Hydrogen diffuses from a high concentration area to a low concentration area, the concentration profiles as a function of the charging time and is given in *figure 3.11*. The solubility of hydrogen is the average hydrogen concentration of the whole thickness L and is calculated by the equation (Eq.3.1b):

$$S(t) = \frac{1}{L} \int_0^{x=L} c dx \quad (\text{Eq.3.1b})$$

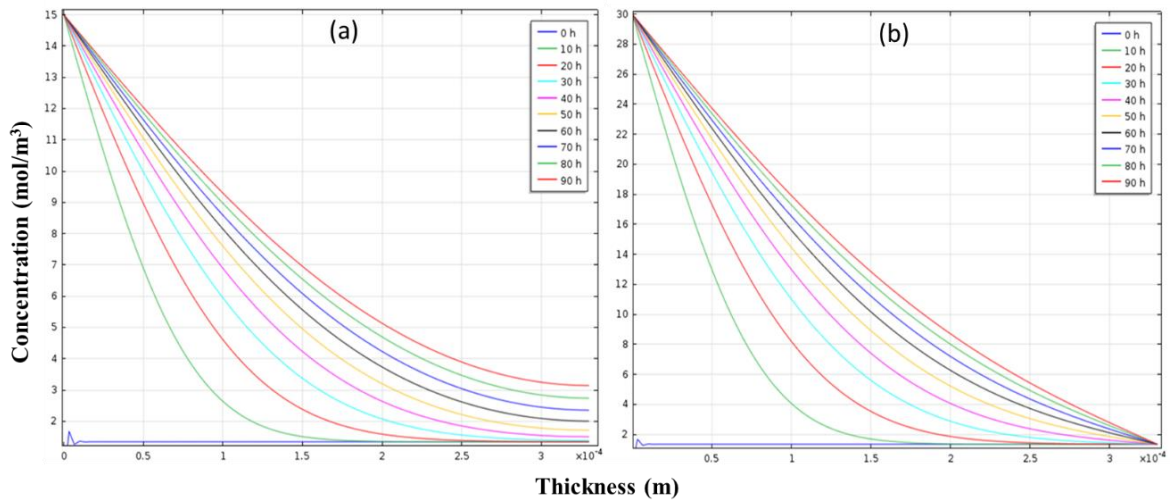


Figure 3.11 – Hydrogen concentration profiles as a function of sample thickness with diffusion time increase, (a) the exit side blocked – no flux, (b) the exit side opened – $C_s = 0$

The hydrogen solubility was compared between the experimental data and FEM model (*figure 3.12*), The model with the open exit side (zero hydrogen concentration at this side $C_s = 0$) is suitable to fit our experimental data, that means that the hydrogen charging process is the same as the hydrogen permeation process, in other words the diffusible hydrogen crosses the sample and then gets out of the exit side. This model was later applied to calculate the apparent diffusion coefficient with different charging conditions.

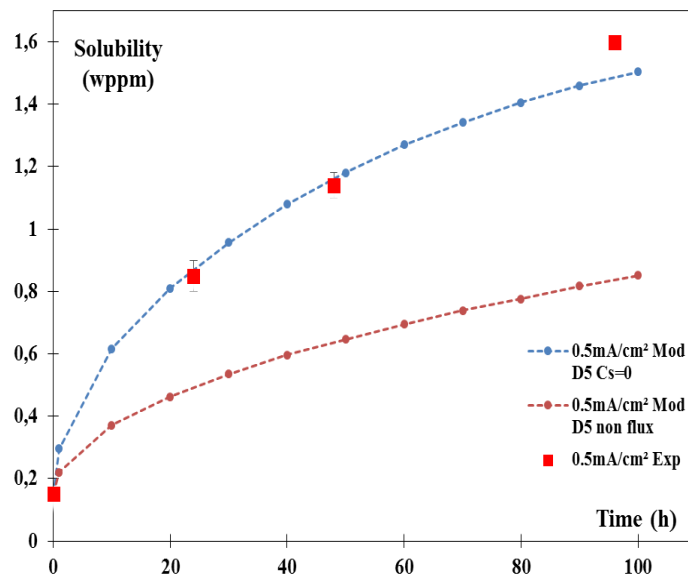


Figure 3.12 – Red points are experimental data with hydrogen charging at 0.5 mA/cm^2 ; D5 means the diffusion coefficient is $5 \times 10^{-14} \text{ m}^2/\text{s}$.

The hydrogen concentration C_0 at entry side was modified according to the maximum solubility as a function of the applied charging current density, five charging conditions were simulated by Fick's model with different diffusion coefficients D_i ($i = 1, 2, 3 \dots [10^{-14} \text{ m}^2\text{s}]$). The simulation results are presented in *figures 3.13* compared with experimental data, each charging condition illustrated with three different diffusion coefficients.

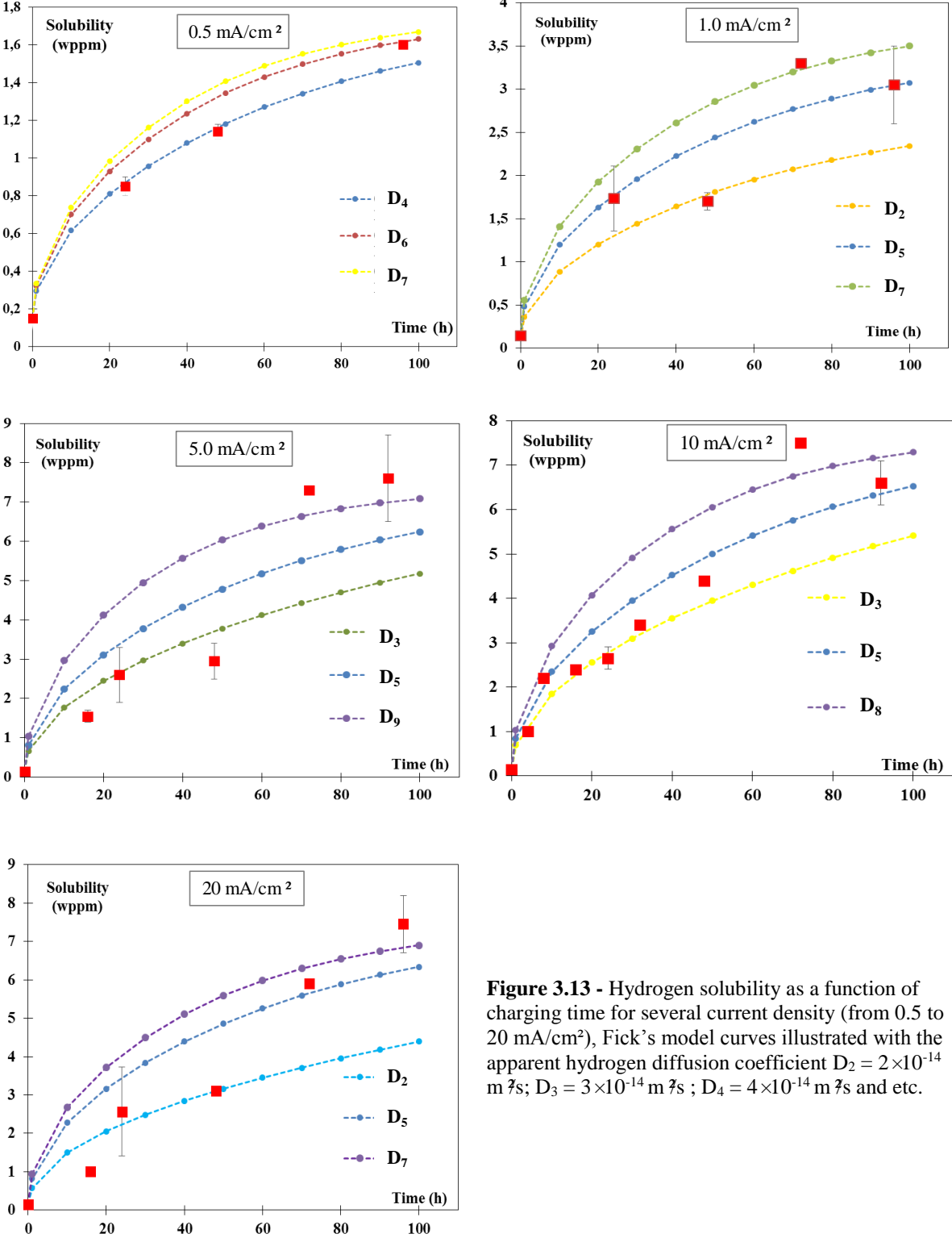


Figure 3.13 - Hydrogen solubility as a function of charging time for several current density (from 0.5 to 20 mA/cm²), Fick's model curves illustrated with the apparent hydrogen diffusion coefficient $D_2 = 2 \times 10^{-14} \text{ m}^2\text{s}$; $D_3 = 3 \times 10^{-14} \text{ m}^2\text{s}$; $D_4 = 4 \times 10^{-14} \text{ m}^2\text{s}$ and etc.

The experimental data and the Fick's model data are collected in *Table 3.3*. The maximum hydrogen solubility corresponds to the hydrogen charging up to the saturation. The apparent hydrogen diffusion coefficient for each charging in the current density range (0.5 to 20 mA/cm²) is from 2 to 11 × 10⁻¹⁴ m² s depending on the hydrogen solubility (More details will be discussed in the part *II.2 Influence of self-stress on the diffusion process*). The average value of apparent diffusion coefficient is about 4.5 to 6 × 10⁻¹⁴ m² s in single crystal nickel <001> at room temperature and will be compared with EP (Electrochemical permeation) data in next paragraph.

Table 3.3- The maximum solubility values and the apparent hydrogen diffusion coefficient for single crystal nickel <001> at room temperature.

| Current density (mA/cm ²) | Corresponding potential From the beginning to the end of charging (V/ESH) | Maximum solubility (wppm) | Diffusion coefficient with charging time increase (10 ⁻¹⁴ m ² s) |
|---------------------------------------|---|---------------------------|--|
| 0.5 | 0.95 to 1.05 | 1.6 | 3 to 6 |
| 1 | 1.05 to 1.1 | 3.05 ± 0.45 | 2 to 8 |
| 5 | 1.1 to 1.25 | 7.1 ± 1.1 | 2 to 10 |
| 10 | 1.3 to 1.6 | 7.5 ± 0.5 | 3 to 11 |
| 20 | 1.5 to 1.7 | 7.45 ± 0.75 | 3 to 8 |

During the transfer step between the hydrogen charging cell and the thermal heating in TDS, a part of the hydrogen could be lost. To assess the experimental error on the evaluation of the hydrogen solubility, the hydrogen desorption was simulated after a saturation charging. The desorption time was estimated about 10 min, the amount of hydrogen in the sample during the desorption as a function of time could be calculated as above by integrating the concentration profiles (*figure 3.14*) along the thickness. The difference between the two curves (red surface in figure 3.14) is the lost hydrogen during the transfer step, the quantity was estimated about 0.24 wppm for a charging at 10 mA/cm² and about 0.06 wppm for a charging at 0.5 mA/cm². The experimental uncertainty is insignificant by comparing with the maximum hydrogen solubility (less than 4%).

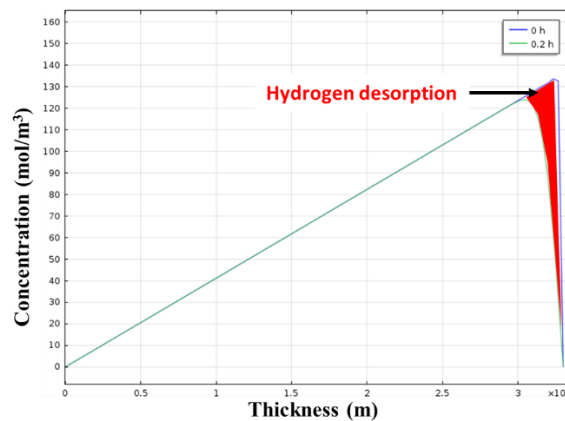


Figure 3.14 – Hydrogen concentration profiles as a function of the thickness with a desorption time of 10 min.

I.2 Hydrogen diffusivity in nickel <001>

The hydrogen diffusivity in nickel <001> was measured by EP (Electrochemical permeation), the characteristic time methods and the model with Fick's law were used to estimate the apparent diffusion coefficient. The hydrogen flux as a function of charging time is given in *figure 3.15*, the same result was found as the hydrogen solubility with different charging conditions, the hydrogen diffusion decreases for a current density higher than 20mA/cm² at room temperature, 10 mA/cm² was the most powerful charging condition. The EP results showed that hydrogen flux was higher than that calculated by Fick's laws. The experimental results suggested an acceleration of the diffusion since the diffusion coefficient is considered constant in Fick's model.

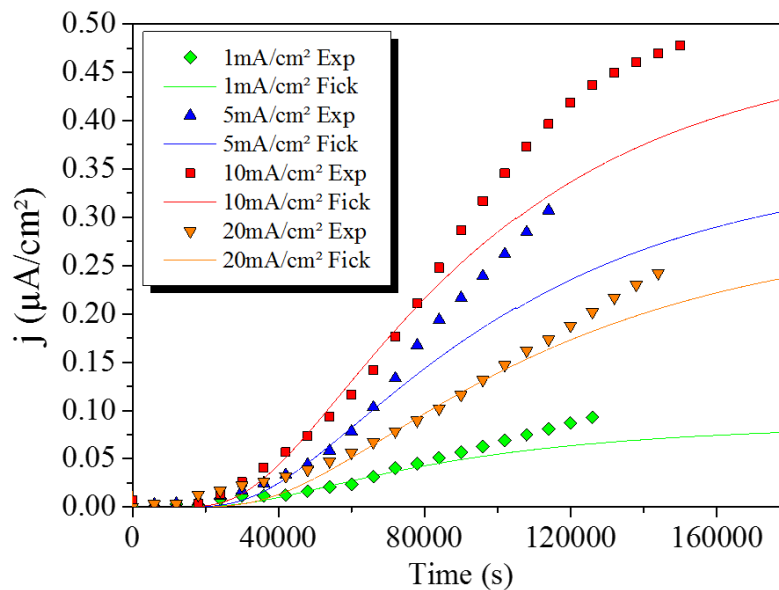


Figure 3.15 – Evolution of the current density proportional to the hydrogen flux j as a function of time with different charging conditions (cathodic current densities) for nickel single crystal <100>. Exp: experimental data; Fick: curves calculated using Fick's law with a constant apparent diffusion coefficient D_{app} .

The analytical calculation could access the maximum hydrogen solubility and the apparent diffusion coefficient, the values are given in *Table 3.4* which is a good agreement with the results of TDS. These data will be later used to establish a model for the equilibrium pressure for nickel <001>.

Table 3.4- The maximum solubility and the apparent hydrogen diffusion coefficients for single crystal nickel <001> at room temperature.

| Current density (mA/cm ²) | Corresponding potential From the beginning to the end of charging (V/ESH) | Maximum solubility (wppm) | Diffusion coefficient (10 ⁻¹⁴ m ² /s) |
|---------------------------------------|---|---------------------------|---|
| 1 | 1.0 to 1.25 | 0.65±0.1 | 8.1±0.5 |
| 5 | 1.28 to 1.4 | 6.15±0.9 | 7.1±1.1 |
| 10 | 1.45 to 1.6 | 7.75±0.47 | 6.9±0.3 |
| 20 | 1.65 to 1.75 | 6.45±0.82 | 5.7±0.7 |

Both analyses of EP and TDS show an increase in hydrogen diffusivity with hydrogen concentration. A need for a realistic interpretation of the experiments motivated the development of a thermodynamic approach that is introduced in the next section.

II. Orientations $\langle 100 \rangle$, $\langle 110 \rangle$, $\langle 219 \rangle$ and $\langle 111 \rangle$

II.1 Anisotropic diffusion

Based on a number of EP experiments performed at room temperature, hydrogen diffusivity along different crystallographic orientations was determined. A charging current density of 5 mA/cm² was selected for a reliable testing environment to take into account the sample dimension for the sealing and the experimental containment issues, and in order to respect the Volmer process (a predominance of adsorption kinetics). The hydrogen diffusion flux as a function of charging time is given in *figure 3.16* for several crystallographic orientations: $\langle 100 \rangle$, $\langle 110 \rangle$, $\langle 219 \rangle$ and $\langle 111 \rangle$. A significant effect of crystallographic orientation on hydrogen diffusivity was observed. Hydrogen diffusion was fastest along the $\langle 111 \rangle$ orientation and slowest along the $\langle 100 \rangle$ orientation. Using Fick's laws, the apparent diffusion coefficients were determined for each orientation and could be ranked as follows: $D\langle 111 \rangle > D\langle 110 \rangle > D\langle 219 \rangle > D\langle 100 \rangle$. The results obtained were used to determinate an anisotropic diffusion tensor in the cubic coordinate system which respected the symmetries of the fcc structure. Since nickel has an fcc structure and possesses high degrees of symmetry, the use of a simplification meant that only two index orientations, $\langle 100 \rangle$ and $\langle 110 \rangle$, were necessary to identify the diffusion tensor. Consequently, the $\langle 219 \rangle$ and $\langle 111 \rangle$ orientations were used to verify the tensor. *Table 3.5* shows the values of the apparent hydrogen diffusion coefficients for all crystallographic orientations obtained by the analysis of charging curves.

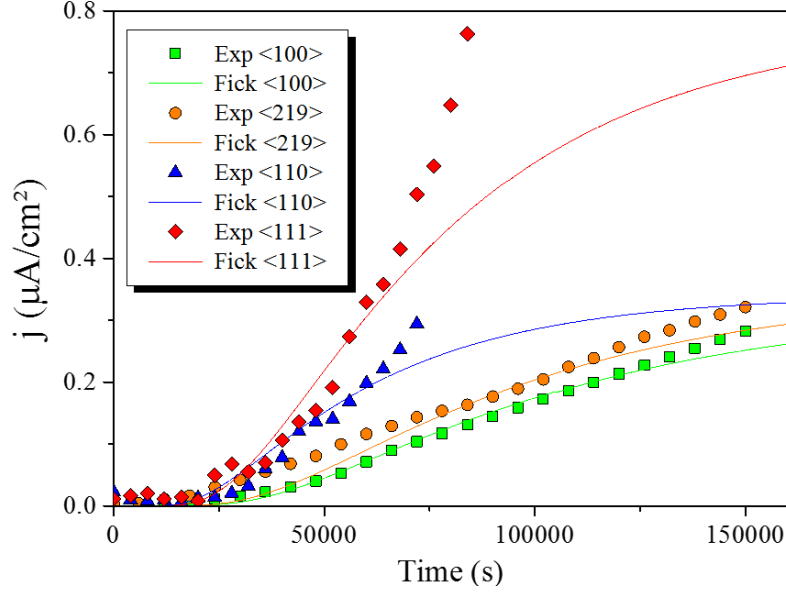


Figure 3.16 –Hydrogen flux as a function of charging time for different orientations and a charging cathodic current density of 5 mA/cm². Exp(hkl): experimental data; Fick(hkl): curves calculated using Fick's law with a constant apparent diffusion coefficient D_{app} .

Table 3.5- The apparent hydrogen diffusion coefficient for single crystals nickel <100>, <011>, <219> and <111> at room temperature.

| Orientations | Diffusion coefficient (10 ⁻¹⁴ m ² /s) | Standard deviation (10 ⁻¹⁴ m ² /s) |
|--------------|--|---|
| <100> | 7.1 | 1.1 |
| <219> | 9.3 | 1.3 |
| <110> | 11.2 | 1.2 |
| <111> | 17.5 | 2 |

The data of *table 3.5* allow us to establish a tensor formalism in three dimensions, the object is to describe the anisotropy of diffusion which could assess the diffusion coefficient of hydrogen regardless of the crystallographic orientation. To identify the anisotropic diffusion tensor, the reference axis is considered in a crystallographic system ([100], [010], and [001]). The diffusion simplified tensor (*Appendix 3.1*) is written (Eq.3.2b):

$$\bar{\bar{D}} = \begin{pmatrix} D_{11} & D_{12} & D_{13} \\ D_{21} & D_{22} & D_{32} \\ D_{31} & D_{32} & D_{33} \end{pmatrix} = \begin{pmatrix} 6 & 5 & 5 \\ 5 & 6 & 5 \\ 5 & 5 & 6 \end{pmatrix} \times (10^{-14} \text{ m}^2/\text{s}) \quad (\text{Eq.3.2b})$$

The hydrogen diffusion coefficient D_n for any orientation \vec{n}_{hkl} of the crystal could be expressed by (Eq.3.3b):

$$D_n = \vec{n}_{hkl}^T \bar{\bar{D}} \vec{n}_{hkl} = \begin{bmatrix} h \\ k \\ l \end{bmatrix}^T \begin{pmatrix} D_{11} & D_{12} & D_{13} \\ D_{21} & D_{22} & D_{32} \\ D_{31} & D_{32} & D_{33} \end{pmatrix} \begin{bmatrix} h \\ k \\ l \end{bmatrix} \quad (\text{Eq.3.3b})$$

The diffusion coefficients calculated by the diffusion tensor has a good agreement with experimental results (*figure 3.17*). For the case of FCC nickel, we can now predict the apparent hydrogen diffusion coefficient regardless of the crystallographic orientation, numerical values are presented in *figure 3.18* in the inverse pole figure.

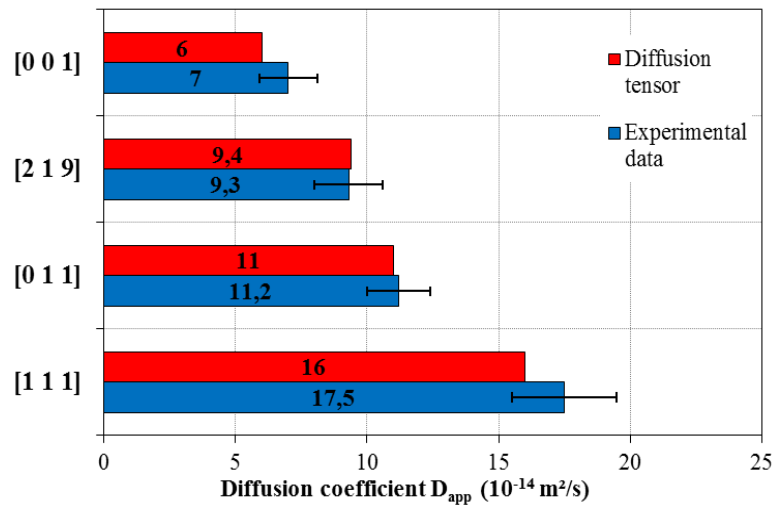


Figure 3.17 – The apparent diffusion coefficient calculated by the diffusion tensor and the experimental data

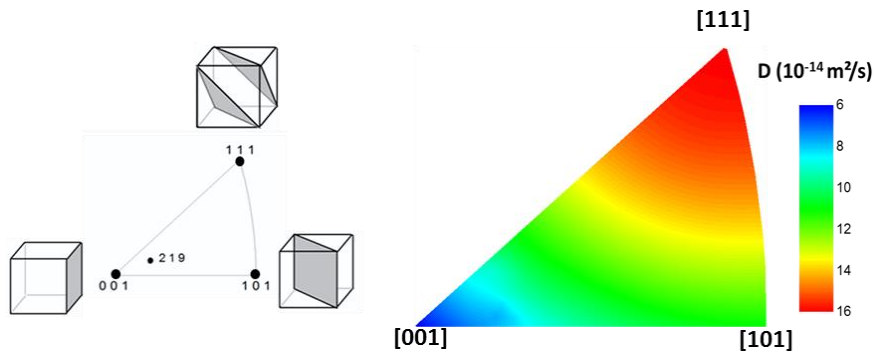


Figure 3.18– Iso-values of diffusion coefficients are represented in a standard triangle

II.2 Influence of self-stress on the diffusion process

In the literature, diffusion anisotropy has generally been studied in low symmetry crystals [Crank1975, Mehrer2007, Agarwal2016], but there remains a controversy concerning more symmetric crystallographic structures [Brass1990, Sosnowska1971]. In this part, our experimental data demonstrated firstly that hydrogen diffusivity increases with hydrogen content, and secondly that an anisotropy of diffusion is observed in high symmetry fcc nickel single crystals. In the present discussion, we would emphasize that the origin of this behavior lies in the elastic interactions of the solute and the crystallographic structure. Hydrogen incorporation into the interstitial sites of nickel

crystals causes an elastic expansion. Thus, a stress is induced by the presence of hydrogen atoms in the elastic solid. Stress, and more generally mechanical fields, are one of the common factors that determine the component of the chemical potential. Therefore, in the present situation, the stress induced or self-stress, resulting from hydrogen incorporation, will affect the transport of the solute in metals as a result of a modification of the stress gradient [Li1978, Larche1982, Larche1988, Oriani1993, Zhang2000]. The solution provided by classical Fick's diffusion equations characterizes hydrogen concentration as a linear variation through the solid at the steady state; we showed here that the stress induced by the incorporation of hydrogen atoms into interstitial sites led to a solution of the diffusion equations that deviated from Fick's solution. In particular, this stress accelerated the hydrogen diffusion and led to an anisotropic diffusion associated with the anisotropy of elastic coefficients in nickel.

II.2.1 Description of diffusion in the solids

In the context of a phenomenological description of the diffusion, respecting the thermodynamics of irreversible processes, the mobility of the solute is described by assuming a linear relationship between the flux and the driving force. In this case the relationship is expressed by the following equation (Eq.3.4b):

$$\bar{J} = -\bar{L} \cdot \nabla \mu \quad (\text{Eq.3.4b})$$

$\nabla \mu$ represents the gradient of the chemical potential for the solute and \bar{L} the tensor of transport coefficients [Kreuzer1981, Philibert1991, Allnatt1993, Mehrer2007]. In the particular case of the diffusion of an interstitial element in a crystal lattice, \bar{L} could be expressed in the term of a diffusion tensor \bar{D} and a concentration of solute C_H :

$$\bar{L} = \frac{\bar{D} C_H}{k_B T} \quad (\text{Eq.3.5b})$$

k_B is the Boltzmann constant and T the temperature. For the face-centered cubic lattice FCC, the symmetries lead to an isotropic diffusion tensor \bar{D} without being affected by the transport tensor \bar{L} . In fact, the gradient of the chemical potential could lead to an anisotropic behavior in terms of flux. In an isotherm state, the gradient of the chemical potential is considered as function of the stress $\bar{\sigma}$ and the hydrogen concentration C_H [Larche1982, Kirchheim1987]:

$$\mu_H(C_H, \bar{\sigma}) = \mu_0(C_{H0}, 0) + k_B T \ln\left(\frac{C_H}{1-C_H}\right) - \Omega_a \sigma_{ij} \varepsilon_{ij}^s + \Omega_a \left(\frac{1}{2} S_{ijkl} \sigma_{ij} \sigma_{kl} + \frac{1}{2} \frac{\partial S_{ijkl}}{\partial C_H} \sigma_{ij} \sigma_{kl}\right) \quad (\text{Eq.3.6b})$$

Ω_a is the atomic volume, C_{H0} the corresponding standard state concentration, σ_{ij} the stress tensor, S_{ijkl} the compliance tensor (the inverse of the stiffness tensor C_{ijkl}) and ε_{ij}^s the strain tensor associated with the insertion of a solute in the crystal lattice. The subscripts i, j, k, l = 1, 2, 3, refer to Cartesian coordinates, and repeated indices in the same term imply summation over 1, 2, and 3. In this expression (Eq.3.6b), the first term corresponds to the standard state with the absence of stress, the second is the solute distribution entropy, the third term is the elastic strain energy associated with the insertion of a solute, and the fourth term is the mechanical energy input into the system and the solute concentration sufficient to modify the compliance tensor S_{ijkl} . In the absence of external stress, the stress state only depends on the elastic strain from the insertion of a solute in the crystal lattice. Considering it as a negligible contribution, we get a simplified form of the chemical potential (Eq.3.7b):

$$\mu_H = \mu_0 + k_B T \ln\left(\frac{C_H}{1-C_H}\right) - \Omega_a \sigma_{ij} \varepsilon_{ij}^s \quad (\text{Eq.3.7b})$$

It is now necessary to define the volume variation, the associated deformation and then to express the resulting stress.

II.2.1.1 Volume variation with the presence of a solute

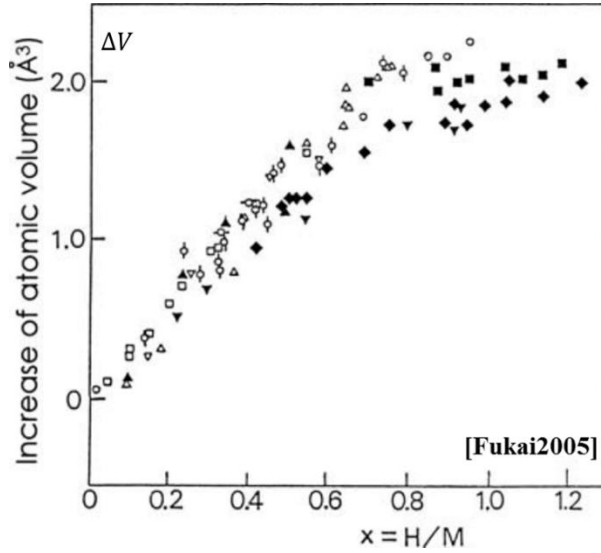
In the case of hydrogen, numerous authors have pointed out a linear relationship between the variable volume ΔV and the hydrogen concentration $x = n_H/n_M$ (n_H is the number of hydrogen atoms and n_M is the number of solid atoms). *Figure 3.19* illustrates this relationship for different metals and alloys [Fukai2005b]. The volume variation is then expressed as follows (Eq.3.8b):

$$\Delta V = \bar{V}_H \frac{V}{\Omega} x = n_H \bar{V}_H \quad (\text{Eq.3.8b})$$

Where $V = n_M \times \Omega$ the volume of solid and Ω is the atomic volume ($\text{m}^3/\text{at.}$). The partial volume of hydrogen \bar{V}_H ($\text{m}^3/\text{at.}$) is a measure of the volume variation by hydrogen insertion into the interstitial site. Thus the relative volume variation is given by (Eq.3.9b):

$$\frac{\Delta V}{V} = \frac{\bar{V}_H}{\Omega} x \quad (\text{Eq.3.9b})$$

According to a compilation of experimental data proposed by Fukai, \bar{V}_H is of the order of $2 \times 10^{-3} \pm 10^{-3} \text{ nm}^3/\text{at.}$ The experimental data gives $2.1 \times 10^{-3} \text{ nm}^3/\text{at.}$ [McLellan1973] and $2 \times 10^{-3} \text{ nm}^3/\text{at}$ [Fukai2005b] for nickel, while DFT based on the atomistic calculations give $2.3 \times 10^{-3} \text{ nm}^3/\text{at}$ [Nazarov2014] and $2.2 \times 10^{-3} \text{ nm}^3/\text{at}$ [Metsue2014].



○: Pd, ×: Pd-Cu, +: Pd-Ag, □: Pd-Au, ▽: Pd-Ir, △: Pd-Pt, ▲: Cu-Ni [4.29]; ■: Ni, ◆: Ni-Fe, ▼: Fe-Ni-Mn

Figure 3.19 – Volume increase due to H in FCC metals and alloys.

II.2.1.2 Atomic and volume expansion

The expansion ε_s associates with the insertion of a hydrogen atom is given by $\varepsilon_s = \frac{\bar{V}_H}{\Omega_a}$, the strain tensor is: $\varepsilon_{ij}^s = \frac{1}{3}\varepsilon_s\delta_{ij}$. When considering a given volume $V = n_M\Omega$, the volume expansion ε_H is directly proportional to the concentration $\Delta C_H = C_H - C_0$, C_0 refers to an initial homogeneous distribution of solute and $C_H = n_H/V$ (at./m³):

$$\varepsilon_H \frac{\Delta V}{V} = \bar{V}_H \Delta C_H \quad (\text{Eq.3.10b})$$

The hydrostatic strain tensor is then expressed as: $\varepsilon_{ij}^H = \frac{1}{3}\varepsilon_H\delta_{ij} = H_{ij} \cdot \Delta C_H$, or for some authors $\varepsilon_{ij}^H = \eta \Delta C_H \delta_{ij}$, where η is the expansion coefficient. We obtain $H_{ij} = \frac{\bar{V}_H}{3} \delta_{ij}$ and $\eta = \frac{\bar{V}_H}{3}$. Here need pay attention to the used units to define the hydrogen concentration. In this study, we used $C_H = n_H/V$ (at./m³) and the conversion as follow : C_H (wppm) = 0.017 × C_H (at./m³) and C_H (mol./m³) = 8.9 × C_H (wppm).

II.2.1.3 Strain state near the solute

The strain of a volume Ω near of the solute $\varepsilon_{ij}^{\Omega}$ is the sum of a component associated with the composition variation ε_{ij}^H and a component resulting from the stress applied by the crystal lattice on the volume $\varepsilon_{ij}^{el} = S_{ijkl}\sigma_{kl}^H$ (the superposition principle) *figure 3.20*:

$$\varepsilon_{ij}^{\Omega} = \varepsilon_{ij}^H + S_{ijkl}\sigma_{kl}^H \quad (\text{Eq.3.11b})$$

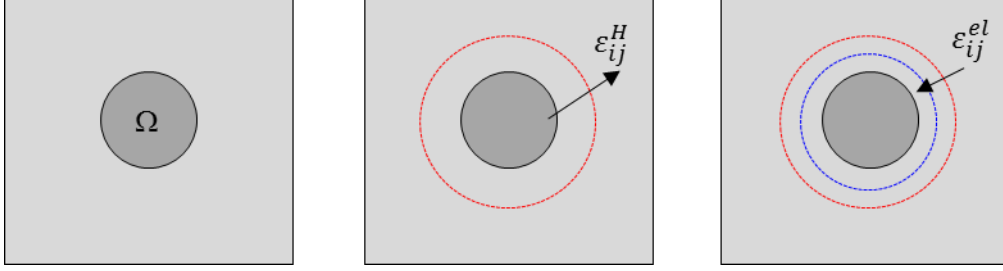


Figure 3.20 – Schematic of the superposition principle applied to an isotropic expansion in an elastic solid.

The stress in the volume is then:

$$\sigma_{ij}^{\Omega} = C_{ijkl}(\varepsilon_{ij}^{\Omega} - \varepsilon_{kl}^H) \quad (\text{Eq.3.12b})$$

There is a direct relationship between the tensor $\varepsilon_{ij}^{\Omega}$ and ε_{ij}^H : $\varepsilon_{ij}^{\Omega} = S_{ijkl}^I \varepsilon_{kl}^H$, where S_{ijkl}^I is Eshelby's tensor [Eshelby1957, Mura1987]. In the case of an isotropic elastic solid and the description of the solute as a dimensionally stable sphere, we could obtain $S_{1111}^I = S_{2222}^I = S_{3333}^I = \frac{7-5\nu}{15(1-\nu)}$ and $S_{1122}^I = S_{2233}^I = S_{3311}^I = S_{1133}^I = S_{2211}^I = S_{3322}^I = \frac{5\nu-1}{15(1-\nu)}$ (Appendix 3.2). The strain is expressed as:

$\varepsilon_{11}^{\Omega} = \varepsilon_{22}^{\Omega} = \varepsilon_{33}^{\Omega} = \left[\frac{1+\nu}{9(1-\nu)} \right] \varepsilon_H$. With the equations $C_{11kl} = 3\lambda + 2\mu = \frac{E}{1-2\nu}$ and $\varepsilon_{ij}^H = \frac{1}{3} \varepsilon_H \delta_{ij}$, the stress in (Eq.3.11b) could then be written as:

$$\sigma_{11}^{\Omega} = \sigma_{22}^{\Omega} = \sigma_{33}^{\Omega} = \frac{-2E}{9(1-\nu)} \varepsilon_H \quad (\text{Eq.3.13b})$$

The hydrostatic stress as:

$$\sigma_m^{\Omega} = \frac{-2E}{9(1-\nu)} \varepsilon_H \quad (\text{Eq.3.14b})$$

Without the external stress, we could obtain:

$$\Omega_a \sigma_{ij}^s \varepsilon_{ij}^s = \Omega_a \sigma_m^{\Omega} \delta_{ij} \left(\frac{1}{3} \varepsilon_s \delta_{ij} \right) = \Omega_a \sigma_m^{\Omega} \frac{\bar{V}_H}{\Omega_a} = \frac{-2E}{9(1-\nu)} \varepsilon_H \bar{V}_H = \frac{-2E}{9(1-\nu)} \bar{V}_H^2 \Delta C_H \quad (\text{Eq.3.15b})$$

The chemical potential could be reduced to:

$$\mu_H = \mu_0 + k_B T \ln\left(\frac{C_H}{1-C_H}\right) + \frac{2E}{9(1-\nu)} \bar{V}_H^2 \Delta C_H \quad (\text{Eq.3.16b})$$

The similar results have been pointed out by different authors [Li1978, Oriani1993, Larche1988, Zhang2000, Yang2005] on the equilibrium condition of $\sigma_{ij}n_j = 0$, typically setting to a free surface (\bar{n} is the normal of the surface), this condition is applied to the interface between the volume Ω and the rest of the solid.

II.2.1.4 Hydrogen flux and the apparent diffusion coefficient

In the case of isotropic diffusion, the combination of equations (Eq.3.5b), (Eq.3.6b) and (Eq.3.16b) gives a relationship between the hydrogen flux and the apparent diffusion coefficient:

$$\bar{J} = \bar{L} \nabla \mu = \bar{L} \frac{\partial \mu}{\partial C_H} \nabla C_H = -D \left[1 + \beta \bar{V}_H^2 \frac{C_H}{k_B T} \right] \nabla C_H = -D_{app} \nabla C_H \quad (\text{Eq.3.17b})$$

Where $D_{app} = D \left[1 + \beta (\bar{V}_H)^2 \frac{C_H}{k_B T} \right]$ and $\beta = \frac{2E}{9(1-\nu)}$, for the case of nickel at room temperature, the apparent diffusion coefficient is reduced as:

$$D_{app} = D(1 + 2.35 \times 10^{-4} C_H) \quad (\text{Eq.3.18b})$$

Here Young's module $E = 205$ GPa, the Poisson ratio $\nu=0.3$, the partial volume $\bar{V}_H = 3 \times 10^{-6}$ m³/mol, the Boltzmann's constant $k_B = 1.38 \times 10^{-23}$ m² kg s⁻² K⁻¹, the Avogadro number 6.022×10^{23} mol⁻¹. For a hydrogen concentration of 10 wppm, the relative variation of the diffusion coefficient is about 2% (figure 3.21).

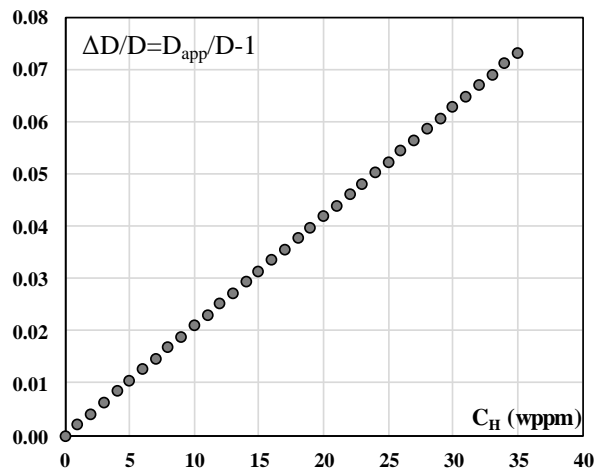


Figure 3.21 – The relative variation of the diffusion coefficient as function of the hydrogen concentration

II.2.1.5 In a solid with anisotropic elasticity properties

Considering the problem of a solute incorporation into a crystal lattice is reduced to a spherical inclusion in a homogeneous medium with anisotropic elasticity properties. The strain induced by the increase of solute concentration ΔC is expressed as the form: $\varepsilon_{lm}^H = \frac{1}{3}\varepsilon_H\delta_{lm} = L_{lm}\Delta C_H$ with $L_{lm} = \eta\delta_{lm}$ and $\eta = \frac{\bar{V}_H}{3}$. The resulting stress is written as:

$$\sigma_{ij} = C_{ijlm}(\varepsilon_{lm} - L_{lm}\Delta C_H) \quad (\text{Eq.3.19b})$$

$\Delta C_H = C_H - C_H^0$, where C_H^0 is the initial uniform hydrogen distribution. The equilibrium equation is:

$$\sigma_{ij}n_j = 0 \quad (\text{Eq.3.20b})$$

Here n_j is the coordinates of the normal to the surface (or the diffusion direction) expressed with the crystallographic reference [hkl]. In order to solve this equation and to deduce the stress state as a function of the hydrogen concentration, we assumed a linear dependence of the displacement $\bar{u}(\bar{r})$ which depends on the concentration ΔC_H , where \bar{r} is the position vector.

$$\Delta C_H = C_k \exp(-i\bar{k} \cdot \bar{r}) \quad (\text{Eq.3.21b})$$

$$\bar{\mu}(\bar{r}) = i\bar{A}_k C_k \exp(-i\bar{k} \cdot \bar{r}) \quad (\text{Eq.3.22b})$$

Where $\bar{k} = k\bar{n}$, \bar{A}_k is an unknown vector. The strain could be written as (Eq.3.23b):

$$\varepsilon_{lm} = \frac{1}{2}\left(\frac{\partial u_l}{\partial x_m} + \frac{\partial u_m}{\partial x_l}\right) = \frac{1}{2}k(n_m A_{kl} + n_l A_{km})C_k \exp(-i\bar{k} \cdot \bar{r}) = \frac{1}{2}k(n_m A_{kl} + n_l A_{km})\Delta C_H \quad (\text{Eq.3.23b})$$

Combining equations (Eq.3.19b) and (Eq.3.23b) leads to an expression for the stress tensor as a function of the solute concentration (Eq.3.24b):

$$\sigma_{ij} = C_{ijlm}\left(\frac{1}{2}k(n_m A_{kl} + n_l A_{km}) - L_{lm}\right)\Delta C_H \quad (\text{Eq.3.24b})$$

The equilibrium equation is then:

$$C_{ijlm}\left(\frac{1}{2}k(n_m A_{kl} + n_l A_{km}) - L_{lm}\right)n_j = 0 \quad (\text{Eq.3.25b})$$

$$(C_{ijlm}n_i n_j)kA_m = C_{ijlm}L_{lm}n_j = 0 \quad (\text{Eq.3.26b})$$

The solution of this equation gives us the expressions of A_i [Krivoglaz1983] (Appendix 3.3):

$$kA_i = \eta X_i, i \in \{1, 2, 3\} \quad (\text{Eq.3.27b})$$

Where:

$$X_1 = \frac{1}{1+a} \left(\frac{C_{11} + 2C_{12}}{C_{11}} \right) (1 - \gamma n_2^2) (1 - \gamma n_3^2) n_1$$

$$X_2 = \frac{1}{1+a} \left(\frac{C_{11} + 2C_{12}}{C_{11}} \right) (1 - \gamma n_1^2) (1 - \gamma n_3^2) n_2$$

$$X_3 = \frac{1}{1+a} \left(\frac{C_{11} + 2C_{12}}{C_{11}} \right) (1 - \gamma n_2^2) (1 - \gamma n_1^2) n_3$$

And

$$a = -\gamma\varphi(n_1^2 n_2^2 + n_3^2 n_2^2 + n_1^2 n_3^2) + \gamma^2 \psi n_1^2 n_2^2 n_3^2$$

$$\gamma = \frac{-C_{11} + C_{12} + 2C_{44}}{C_{44}}$$

$$\varphi = \frac{C_{11} + C_{12}}{C_{11}}$$

$$\psi = \frac{C_{11} + 2C_{12} + C_{44}}{C_{11}}$$

The strain tensor ε_{lm} is expressed as:

$$\varepsilon_{lm} = \frac{1}{2} k (n_m A_l + n_l A_m) \Delta C_H = \frac{1}{2} \eta \Delta C_H (n_m X_l + n_l X_m) \quad (\text{Eq.3.28b})$$

The resulting stress is deduced from the equations (Eq.3.24b) and (Eq.3.28b):

$$\sigma_{ij} = C_{ijlm} \left(\frac{1}{2} (n_m X_l + n_l X_m) - \delta_{lm} \right) \eta \Delta C_H \quad (\text{Eq.3.29b})$$

The energy associated with this elastic strain is then given as:

$$\Omega_a \sigma_{ij} \varepsilon_{ij}^S = \Omega_a (C_{ijlm} \left(\frac{1}{2} (n_m X_l + n_l X_m) - \delta_{lm} \right) \frac{\bar{V}_H}{3} \Delta C_H) \left(\frac{\bar{V}_H}{3\Omega_a} \delta_{ij} \right) = \frac{Y}{9} \bar{V}_H^2 \Delta C_H \quad (\text{Eq.3.30b})$$

Where, $Y = C_{ijlm} \left(\frac{1}{2} (n_m X_l + n_l X_m) - \delta_{lm} \right) \delta_{ij}$

Y is first published by Larché *et al.* [**Larche1982**] (Appendix 3.4):

$$Y = -(C_{11} + 2C_{12}) \left\{ 3 - \frac{(C_{11} + 2C_{12}) \left[1 - 2\gamma (n_1^2 n_2^2 + n_1^2 n_3^2 + n_2^2 n_3^2) + 3\gamma^2 n_1^2 n_2^2 n_3^2 \right]}{C_{11}(1 + \alpha)} \right\} \quad (\text{Eq.3.31b})$$

The chemical potential takes the following form:

$$\mu_H = \mu_0 + k_B T \ln \left(\frac{C_H}{1 - C_H} \right) + \frac{Y}{9} \bar{V}_H^2 \Delta C_H \quad (\text{Eq.3.32b})$$

In the case of isotropic elasticity, we obtain expression (Eq.3.15b) with $Y = -\frac{2E}{(1-\nu)}$. The hydrogen flux as a function of the apparent diffusion coefficient is expressed as:

$$\bar{J} = \bar{L} \nabla \mu = \bar{L} \frac{\partial \mu}{\partial C_H} \nabla C_H = -D \left[1 + \frac{Y}{9} \bar{V}_H^2 \frac{C_H}{k_B T} \right] \nabla C_H = -D_{app} \nabla C_H \quad (\text{Eq.3.33b})$$

Where, $D_{app} = D \left[1 + \beta (\bar{V}_H)^2 \frac{C_H}{k_B T} \right]$ and $\beta = \frac{Y}{9}$

We determined the variation of Y as a function of the crystallographic orientation, the orientation is the normal \bar{n} [hkl]. In the case of nickel, C_{11} , C_{12} and C_{44} are respectively equal to 250 GPa, 150 GPa and 120 GPa [**Ledbetter1973**]. *Figure 3.21* shows the evolution of Y in an inverse pole figure of the structure fcc. We get a value of 768 GPa for the orientation [111] and 440 GPa for the orientation [001]. This difference will have a direct impact on the apparent diffusion coefficient if the partial molar volume and the hydrogen concentration are high enough and at a relatively low temperature.

The apparent diffusion coefficient is simplified as: $D_{app} = D \left[1 + 1.2 \times 10^{-13} \left(\frac{Y}{T} \right) C_H \right]$ with $\bar{V}_H = 3 \times 10^{-6} \text{ m}^3/\text{mol}$, $k_B = 1.38 \times 10^{-23} \text{ m}^2 \text{ kg s}^{-2} \text{ K}^{-1}$ and $N_A = 6.022 \times 10^{23} \text{ mol}^{-1}$. At 300 K and with a hydrogen concentration of 10 wppm (90 mol/m³), we obtain a relative variation of the diffusion coefficient of 3% for the orientation [111] and 1.5% for the orientation [001], the relative variation as function of the hydrogen content is given in *figure 3.22*.

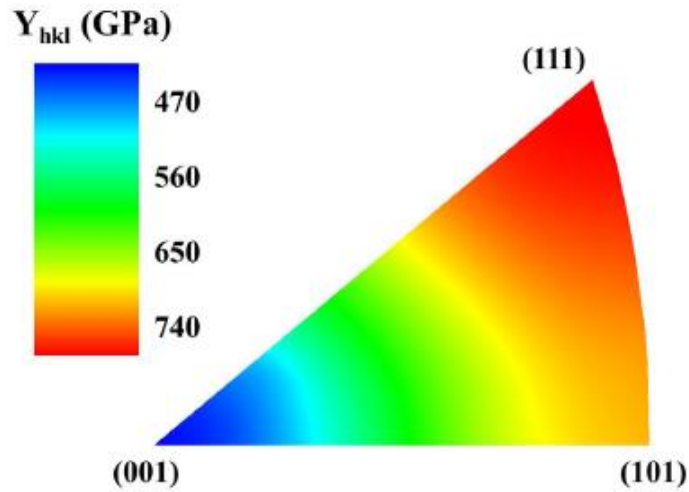


Figure 3.21 – Iso-value of Y on the standard triangle, the inverse pole figure is obtained by the stereographic projection of crystal directions.

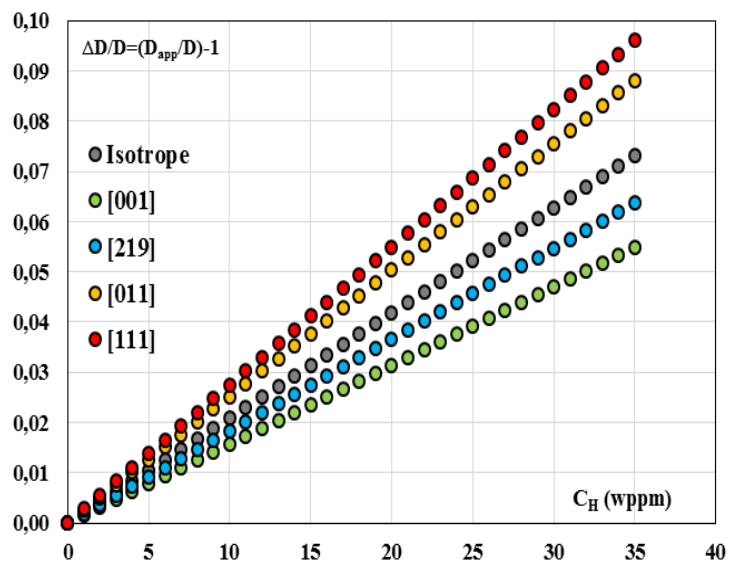


Figure 3.22 – The relative variation of diffusion coefficient as a function of hydrogen content

This approach clearly shows the impact of the anisotropy of elastic nature on the apparent diffusion coefficient. It is now appropriated to measure the impact on the experimental data.

II.2.2 Confrontation of the thermodynamic approach with experimental data

In the context of experimental approaches, we have deduced an apparent diffusion tensor. This anisotropic tensor comes from the identification of four orientations for D_{app} : $\langle 100 \rangle$, $\langle 110 \rangle$, $\langle 111 \rangle$ and $\langle 219 \rangle$. It is then possible to confront $D_{app}(hkl)$ to $Y(hkl)$ (figure 3.23), a linear relationship that takes the form as (Eq.3.34b):

$$D_{app}(hkl) = D + D\bar{V}_H^2 \frac{C_H}{9RT} Y_{hkl} = D + aY_{hkl} \quad (\text{Eq.3.34b})$$

With $a = D(\bar{V}_H)^2 \frac{C_H}{9RT}$ and C_H unit is mol/m³. The intercept gives us directly the diffusion coefficient D without the contribution of self-stress and the slope provides access to the partial molar volume \bar{V}_H assuming C_H equal to the average value in the sample. We get $D = 3.5 \times 10^{-14}$ m²/s and $\bar{V}_H = 40 \times 10^{-6}$ m³/mol. This diffusion coefficient is very close to the results determined by the atomistic calculations DFT. Indeed at 300 K, Metsue *et al.* [Metsue2014] reported a value of 3×10^{-14} m²/s and Wimmer *et al.* [Wimmer2006] 4×10^{-14} m²/s.

According to a compilation of experimental data proposed by Fukai [Fukai2005a], \bar{V}_H is of the order of $1.8 \pm 0.7 \times 10^{-6}$ m³/mol, while DFT based on atomistic calculations gave 1.39×10^{-6} m³/mol in Nazarov *et al.* [Nazarov2014] and 1.32×10^{-6} m³/mol in Metsue *et al.* [Metsue2016]. For a hydrogen concentration of 7 wppm, we determined that the apparent partial molar volume \bar{V} at about 40×10^{-6} m³/mol inferred from equation (Eq.3.34b) is much higher than the theoretical value of about $1.8 \pm 0.7 \times 10^{-6}$ m³/mol. Thus, the elastic strain associated with the incorporation of hydrogen atoms into the crystal lattice is not sufficient to explain the experimental observations. An alternative explanation for this approach would need to take into consideration the involvement of crystalline defects that may cause stress fields.

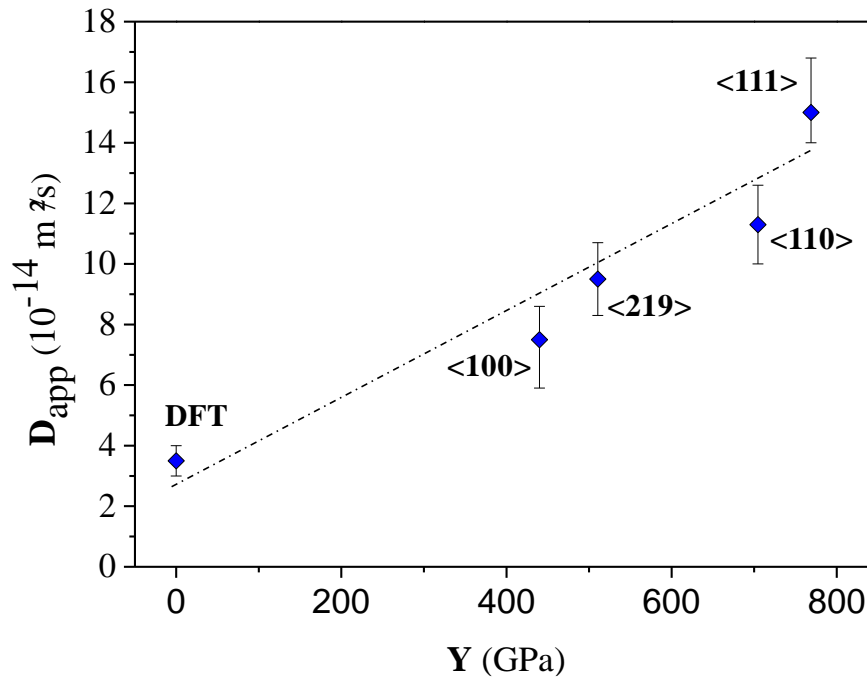


Figure 3.23 – The apparent diffusion coefficient D_{app} as a function of Y for a hydrogen concentration of 7 wppm. The slope of the linear relation between Y and D_{app} was used to determine the apparent partial molar volume using equation (Eq.3.34b).

The density of dislocations and vacancies are very low in the initial state in the single crystals and therefore cannot be an interpretation of our observations elements. However, Fukai *et al.* [Fukai2007] and Oudriss *et al.* [Oudriss2012a] have pointed out that in the case of nickel, the presence of hydrogen leads to the formation of vacancies. These results were supported by the atomistic calculations Nazarov *et al.* [Nazarov2012, 2014] and Metsue *et al.* [Metsue2016]. Thus it seems worthwhile to reconsider the previous approach by taking into account this time the stress field associated with the vacancies, or a cluster of vacancies. The chemical potential takes the new form as (Eq.3.35b).

The density of dislocations and vacancies is very low at the initial state of nickel single crystals and therefore cannot account for the discrepancies in our results. However, Fukai *et al.* [Fukai2007] and more recently Oudriss *et al.* [Oudriss2012a] have pointed out that for nickel, the presence of hydrogen enhances vacancy formation. These observations are supported by the atomistic calculations of Nazarov *et al.* [Nazarov2012, 2014] and Metsue *et al.* [Metsue2014], which highlight the fact that hydrogen decreases the energy of vacancy formation. Thus it seems worthwhile reconsidering the previous approach by taking into account the stress field associated with vacancies, or clusters of vacancies. According to the pioneering work of Eshelby [Eshelby1954], based on the isotropic elastic continuum approach, the elastic field induced by point defects is expressed as a displacement caused by a center of dilatation corrected by a component termed the constrained displacement field [Mishin2001]. For a monovacancy or a spherical cluster of vacancies, the isotropic elastic displacement can be used to evaluate a negative dilatation volume \bar{V}_V . Based on the hypothesis of an additive contribution of the n_v vacancies of a cluster, the volume dilatation can be deduced as a function of the expansion volume of a monovacancy. Additionally, atomistic calculations confirm the additive properties of the elastic field of vacancies for bivacancies [Yoshioki1976]. Thus if we reconsider the previous approach by taking into account the elastic distortion associated with a cluster of vacancies, the chemical potential introduced in equation (Eq.3.32b) takes the following form:

$$\mu_H = \mu_0 + k_B T \ln\left(\frac{C_H}{1-C_H}\right) + \frac{Y}{9} (n_v \bar{V}_V)^2 \Delta C_V \quad (\text{Eq.3.35b})$$

ΔC_V is the excess of vacancies induced by the addition of hydrogen, and the value of the partial molar volume of vacancy [Metsue2016] \bar{V}_V is $-2.25 \times 10^{-6} \text{ m}^3/\text{mol}$. In accordance with the neglected direct impact of the solute that was highlighted previously, in this equation we do not take into consideration the contribution of the term which depends on \bar{V}_H .

In quite similar thermodynamic conditions ($j = 20 \text{ mA/cm}^2$ and $T=300\text{K}$), Oudriss *et al.* [Oudriss 2012a] have described a linear relationship between vacancy and hydrogen concentration: $\Delta C_V = k \Delta C_H$ with $k = 0.15$. Equation (Eq.3.35b) then takes the form:

$$\mu_H = \mu_0 + k_B T \ln\left(\frac{C_H}{1-C_H}\right) + k \frac{Y}{9} (n_v \bar{V}_v)^2 \Delta C_H \quad (\text{Eq.3.36b})$$

The apparent diffusion coefficient is then:

$$D_{app}(hkl) = D + Dk(n_v \bar{V}_v)^2 \frac{C_H}{9RT} Y_{hkl} = D + aY_{hkl} \quad (\text{Eq.3.37b})$$

Where $a = Dk[n_v \bar{V}_v]^2 \frac{C_H}{9RT}$.

The apparent partial molar volume of $40 \times 10^{-6} \text{ m}^3/\text{mol}$ can now be considered to be $\bar{V} = \sqrt{k} n_v \bar{V}_v$ as suggested by equation (Eq.3.37b); we deduced that a cluster (radius $\approx 5\text{nm}$) of around forty vacancies is necessary to reach the apparent value. *Figure 3.24* illustrates that the deviation is particularly significant if the hydrogen concentration is high enough. On the other hand, the comparison between the *figure 3.22* and the *figure 3.24* points out that the impact of the induced stress on the apparent diffusion coefficient is just significant since the existence of vacancy clusters is considered.

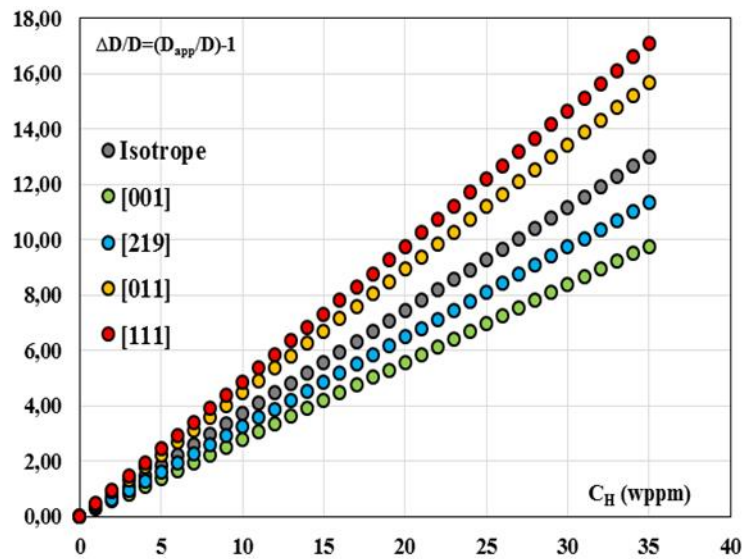


Figure 3.24 – The relative variation of the apparent diffusion coefficient as a function of hydrogen content with the contribution of vacancy clusters

The identification of the apparent diffusion coefficient has been previously obtained based on Fick's law. Considering the influence of the hydrogen concentration now, the solubility versus charging time obtained for the orientation [001] with different charging current densities is given in *figure 3.25*, it is possible to represent D_{app} as a function of the average hydrogen concentration $\langle C \rangle_{TDS}$ in the membrane. We get an almost linear trend between D_{app} and C_H described in the equation (Eq.3.38b).

$$D_{app} = D + D\bar{V}_H^{-2} \frac{Y}{9RT} \langle C \rangle = D + b \langle C \rangle \quad (\text{Eq.3.38b})$$

Where $b = D(\bar{V}_H)^{-2} \frac{Y}{9RT}$

Knowing that $Y_{[001]} = 440$ GPa, and we deduced a value of the apparent partial molar volume $\bar{V}_H = 40 \times 10^{-6}$ m³/mol. This value of \bar{V}_H is in good fit with different orientations for a constant hydrogen content. Similarly, the value of D is the intercept of the curve is close to 3.5×10^{-14} m²/s, this value was previously obtained by [Lekbir2012].

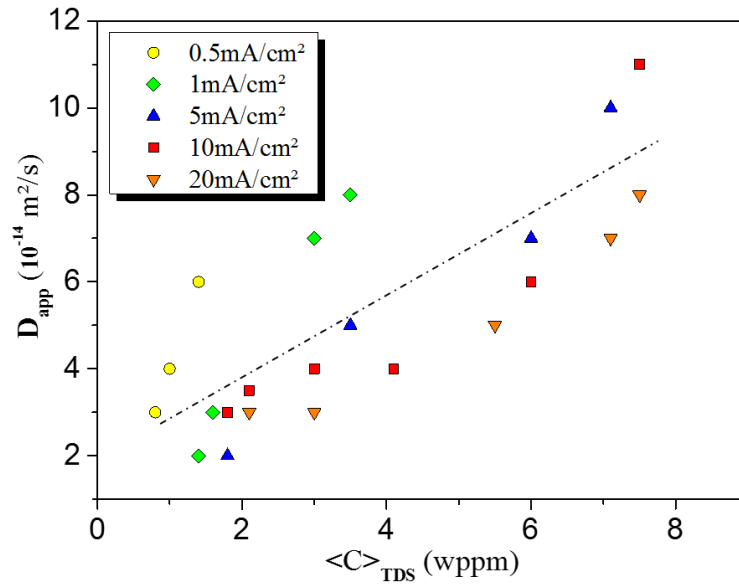


Figure 3.25 – The apparent diffusion coefficient as a function of the average hydrogen content in the membrane, the hydrogen solubility was measured by the total fusion TDS, D_{app} was obtained by the simulation with a sample of 300 μm and the orientation [001]. The model used was a Fick's equation, D_{app} was adjusted each time to fit the experimental hydrogen content by finite element method.

Note that the previous approach was based on an average value of the hydrogen content in the membrane. In order to validate the analysis, we later simulated the electrochemical permeation through samples of 200 μm using a modified Fick's model, the key point was to take into account the hydrogen concentration gradient:

$$J = -D_{app} \nabla C \quad \text{and} \quad \frac{dC}{dt} + \nabla J = 0 \quad (\text{Eq.3.39b})$$

$$D_{app} = -D \left(1 + \frac{Y}{9} \bar{V}_H^{-2} \frac{C_H}{k_B T} \right) \quad (\text{Eq.3.40b})$$

These two equations were implemented in Comsol Multiphysics to describe the variation of hydrogen flux in the membrane for the orientation [001] with different current densities (0.5 to 20 mA/cm²), and

for four different orientations [001], [011], [111] and [219] with a current density of 5 mA/cm². For simplification reasons of the calculation, this model assumed that the hydrogen concentration at the entry side C_0 is constant and the apparent partial molar volume \bar{V}_H is constant. This approach provided access to the distribution of hydrogen in the membrane (figure 3.26) and thus to measure the deviation from the Fick's law which leads to a linear distribution at the steady state. On the other hand, we could determine the apparent diffusion coefficient D_{app} with characteristic time methods $t_b = 1\%$, 10% , 63% and 100% of J_{max} . Figure 3.27 shows the evolution of the apparent diffusion coefficient D_{app} as a function of the average hydrogen concentration in the membrane. For a value of \bar{V}_H equals to 40×10^{-6} m³/mol, the result calculated (Eq.3.40b) is close to the experimental data. Knowing that the theoretical value of \bar{V}_H is 3×10^{-6} m³/mol, this means that there needs around forty vacancies to explain the apparent value of \bar{V}_H .

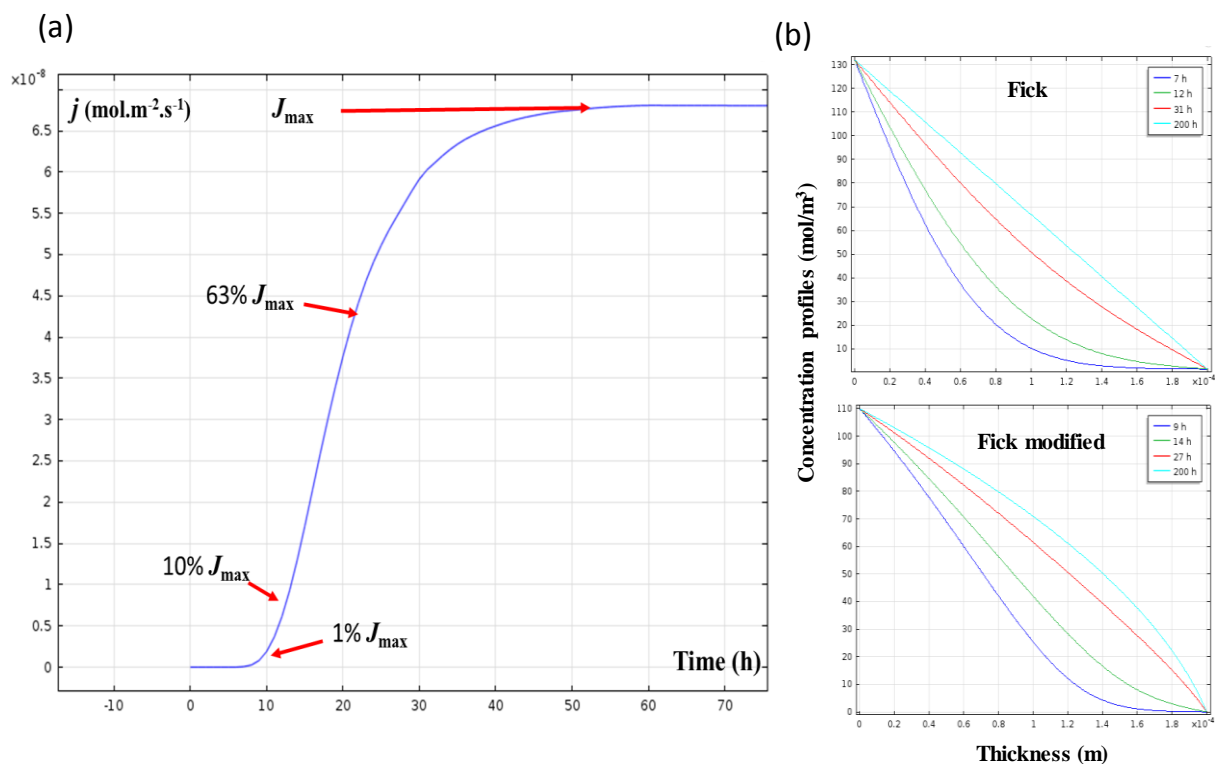


Figure 3.26– (a) The hydrogen flux of the exit side as a function of the diffusion time, (b) Concentration profiles in the membrane with different characteristic time t_b for the case of Fick's model and the case of modified Fick's model (Self-stress) vs membrane thicknesses.

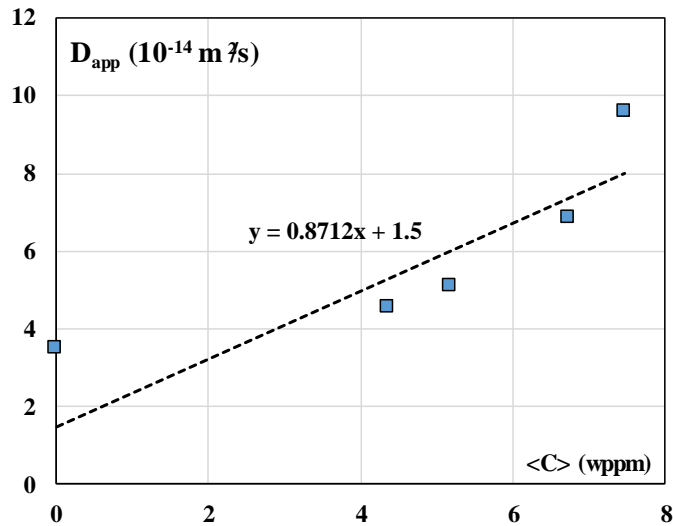


Figure 3.27 – The apparent diffusion coefficient as a function of the average hydrogen content in the membrane, results calculated for the orientation [001] with the modified Fick’s model

Figure 3.28 shows the results calculated by the modified Fick’s model (Self-stress effect) for different orientations ([001], [011], [111] and [219]) taking into account the variation of the pseudo modulus Y as a function of the crystallographic orientation. The calculated curves are in good agreement with the experimental curves of EP, the estimated error is given in the figure 3.29. The self-stress effect can explain the anisotropic diffusion with vacancies formed during the diffusion.

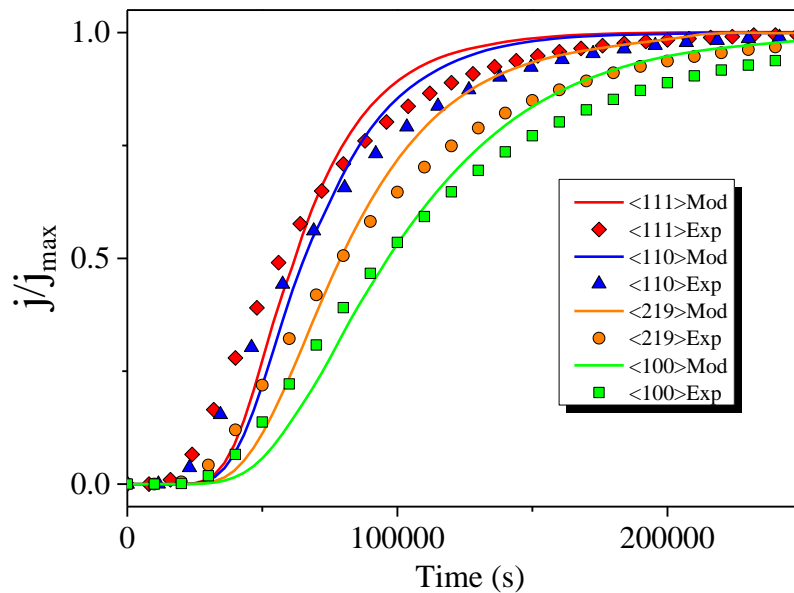


Figure 3.28 – The hydrogen flux at the exit side as a function of the diffusion time, Ni [hkl]-Mod : results calculated for four orientations with $Y_{[001]}=440$ GPa, $Y_{[110]}=705$ GPa, $Y_{[111]}=768$ GPa, $Y_{[219]}=511$ GPa and $\bar{V}_H=40 \times 10^{-6}$ m³/mol ; Ni [hkl]-Exp : experimental data

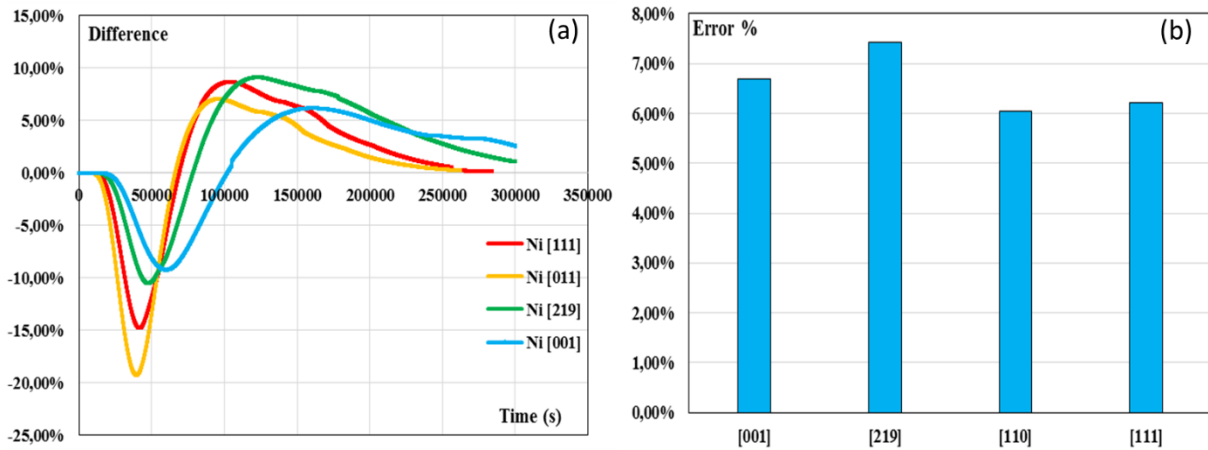


Figure 3.29 – (a) Difference $\frac{j_{Mod}-j_{Exp}}{j_{Max}}$ between the calculated curves and the experimental curves (b) The average error compared to the experimente.

In order to compare the calculated curves with the experimental curves, the average errors are calculated for four different orientations (Eq.3.41b) between the modified Fick's model and the experimental data, there is an approximately 6.5% error.

$$Error\% = \frac{\int |j_{Exp} - j_{Mod}| dt}{\int |j_{Exp}| dt} \% \quad (Eq.3.41b)$$

Fick's laws consider simply that the apparent diffusion coefficient D_{app} is a constant during the diffusion process under the isothermal conditions, *figure 3.30* compares the results calculated by the Fick's model and by the modified Fick's model for the diffusion of hydrogen in nickel [001] with different charging current densities. The influence of self-stress on the diffusion process is clearly shown as the calculated curves by the modified Fick's model have a better fit to the experimental curves than the classical Fick's model. The difference between the model of Fick and the modified Fick's model is about maximum 15%.

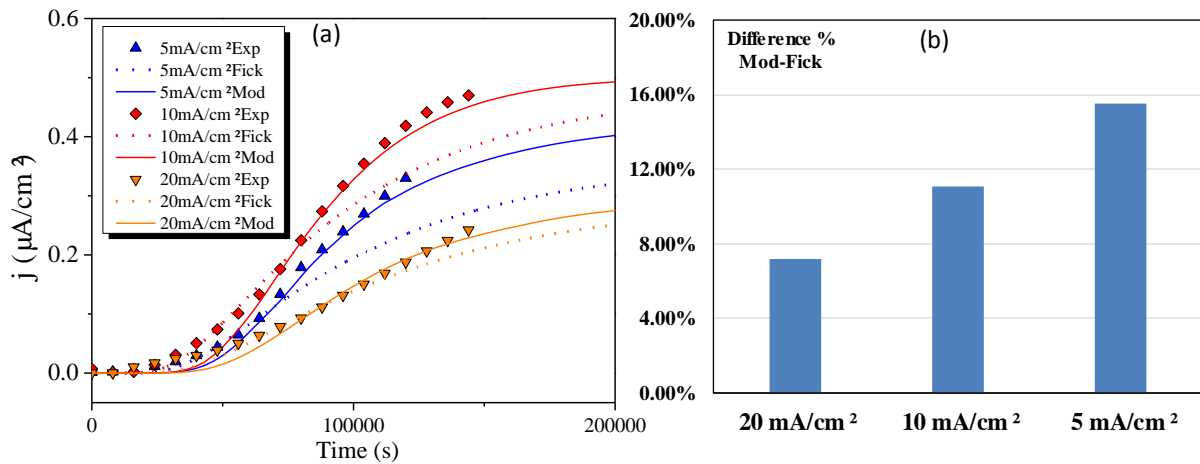


Figure 3.30 – (a) The hydrogen flux at the exit face for Ni [001] as a function of the diffusion time, Mod: results calculated with $Y_{[001]} = 440\text{GPa}$, $\bar{V}_H = 40 \times 10^{-6} \text{ m}^3/\text{mol}$ and C_0 varies with the charging current density; Exp: experimental results; Fick: results calculated by Fick's model with a constant D_{app} . (b) Difference % = $\frac{\int |j_{Mod} - j_{Fick}| dt}{\int |j_{Mod}| dt} \%$ between the curves of the classic Fick's model and the modified Fick's model.

The apparent diffusion coefficient is a function of the hydrogen concentration (Eq.3.40b). The hydrogen concentration affects the diffusion anisotropy as shown in *figure 3.31*, higher concentrations have more influence on the anisotropy of the diffusion process.

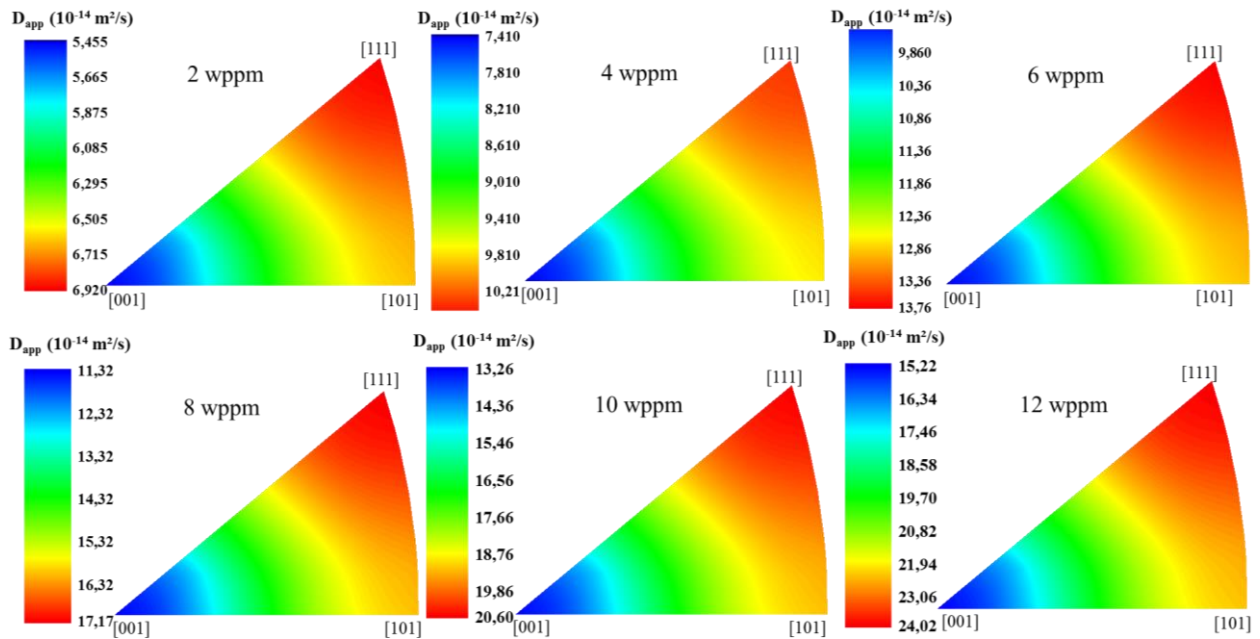


Figure 3.31 – Iso-values of the apparent diffusion coefficients are shown in the inverse pole figures for different hydrogen contents.

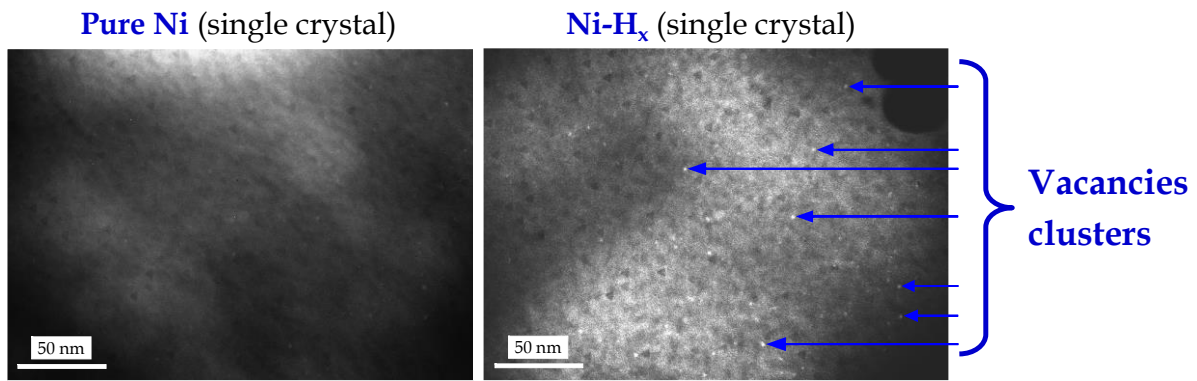


Figure 3.32 – TEM scan for nickel single crystals with/without hydrogen charging, vacancies clusters are illustrated after hydrogen charging.

To conclude, the analysis of coupling stress state/solubility in a thermodynamic framework has shown the importance of the stress state induced by the presence of the solute on the diffusion. Two major effects emerge:

- The apparent diffusion coefficient is a function of the concentration of hydrogen,
- Self-stress is the origin of the anisotropy of hydrogen diffusion in nickel, which is also a function of the concentration of hydrogen.

In both cases, it is not a direct effect of the hydrogen concentration that is highlighted but an induced effect associated with the formation of vacancy clusters during the diffusion of hydrogen (*figure 3.32*).

III. Conclusions

In this chapter, we presented the first studies on the nickel single crystals using experimental and numerical approaches. The reactions of hydrogen at the nickel surface in the alkaline solution are shown that dominated by the Volmer-Tafel mechanism at room temperature with the identification of kinetic constants. In addition, we have identified also the available charging current density range and their equivalent fugacity/ real gas pressure using a conversion model with a thermodynamic approach, in other words an equivalence in the Volmer field.

The hydrogen transport in nickel has been studied first using the classic Fick's laws to obtain the apparent diffusion coefficient and compared the calculated hydrogen solubility with experimental data. Within a thermodynamic framework, we have demonstrated that the diffusion can be derived from Fick's laws considering the influences of the solute concentration and the self-stress state. The anisotropic diffusion in nickel single crystals on different crystallographic orientations arises from the

elastic anisotropy due to the elastic strain field associated with the insertion of solute atoms. This analytical calculation indicates that the anisotropy is actually an anisotropic diffusion acceleration if the solute concentration is high enough, however the hydrogen concentration alone is not able to influence this anisotropic behavior.

We consider thus the impact of hydrogen on the vacancy formation in nickel, the clusters of vacancies are actually the key factor on the anisotropic diffusion in nickel single crystals. Since the solute concentration, the stress state and hydrogen induced vacancy formation are highlighted by their importance on the diffusion process in nickel, we will question these points in the future studies on the nickel GBs.

Chapter 4.

Role of grain boundary character on the hydrogen segregation and diffusion

| | |
|---|-----|
| <u>Chapter 4. Role of grain boundary character on the hydrogen segregation and diffusion</u> | 133 |
| <u>I. Grain boundaries structure</u> | 136 |
| <u>II. Hydrogen segregation states</u> | 140 |
| <u>II.1 Segregation energy</u> | 140 |
| <u>II.2 Stress states and hydrogen segregation</u> | 146 |
| <u>II.3 Segregation concentration</u> | 150 |
| <u>III. Hydrogen diffusion in GBs –atomic approach</u> | 155 |
| <u>IV. Experimental approaches</u> | 161 |
| <u>IV. 1 Hydrogen - twin boundaries in nickel polycrystals</u> | 162 |
| <u>IV. 2 Hydrogen - GBs in nickel bi crystals</u> | 164 |
| <u>IV. 3 FEM approaches</u> | 167 |
| <u>IV. 3.1 Pure diffusion</u> | 167 |
| <u>IV. 3.2 Stress near GB</u> | 171 |
| <u>V. Summary</u> | 177 |

In the present part, hydrogen/grain-boundaries interactions are studied for the different nickel bi-crystal systems described in chapter 2. Four configurations have been considered and defined in term of coincidence site lattice (Σ): $\Sigma_{11-50^\circ 48} \langle 110 \rangle \{311\}$, $\Sigma_{11-129^\circ 52} \langle 110 \rangle \{332\}$, $\Sigma_{3-70^\circ 53} \langle 110 \rangle \{111\}$ and $\Sigma_{5-36^\circ 86} \langle 100 \rangle \{310\}$. The representation of GBs is simplified in *table. 4.0* by using symbols. The influence of the GBs character on the hydrogen diffusion and segregation has been approached using complementary methods based on the experimental and numerical methods at different scales.

Table 4.0- Nickel bi-crystals details

| Nickel bi-crystals symbols | Details |
|---|--|
| S11 or $\Sigma_{11} \langle 110 \rangle \{311\}$ | $\Sigma_{11-50^\circ 48} \langle 110 \rangle \{311\}$ |
| S11* or $\Sigma_{11^*} \langle 110 \rangle \{332\}$ | $\Sigma_{11-129^\circ 52} \langle 110 \rangle \{332\}$ |
| S3 or $\Sigma_3 \langle 110 \rangle \{111\}$ | $\Sigma_{3-70^\circ 53} \langle 110 \rangle \{111\}$ |
| S5 or $\Sigma_5 \langle 100 \rangle \{310\}$ | $\Sigma_{5-36^\circ 86} \langle 100 \rangle \{310\}$ |

First we describe the different structures of GBs in relation with their excess volume and GB energy using atomic scale calculations. The GB energy calculation model [Wolf1991] based on the inclination angle will be discussed by comparing the atomic calculation results.

In a second part, we question the hydrogen-GBs interactions particularly the hydrogen segregation and diffusion at the atomic scale. The hydrogen atom's behavior is extremely dependent on the locale GB structure. Indeed, the high excess volume GBs have significant influence on the hydrogen diffusion and segregation. Therefore, the segregation sites for hydrogen atom in the GB core are reviewed according to their geometry and energy and the fast diffusion paths and trapping sites in the GBs is discussed.

Finally, the use of our experimental protocol combining the hydrogen charging with the thermal desorption spectroscopy (TDS) enabled experimental observations which highlight that divers types of GBs have their different influence on the hydrogen transport process. Also, FEM models were developed considering the anisotropic fast GB diffusion and the stress state near a GB. Besides, the impacts of microdefects in the experimental bi crystal samples such as vacancies and dislocations are questioned.

I. Grain boundaries structure

The first atomic simulation of the structural properties of GBs is focused on the symmetric and asymmetric $\Sigma 3$ $\langle 110 \rangle$ tilt grain boundaries. This work has been initiated during the post-doctoral position of A.Hallil [Hallil2016] for one type of GB and extended with his support to the all investigated GBs in the present study. The GB structures have been investigated in terms of global GB metrics such as the GB energy and the excess free volume. The GB energy is computed as the difference between the total energy of the relaxed GB atoms and the bulk energy in the whole system in GB plane. For a number of atoms N_{at} in the calculation, the grain boundary energy E_{GB} is given as:

$$E_{GB} = \frac{1}{2}(E_{GB}^{Ni}(N_{at}) - E_{Bulk}^{Ni}(N_{at})) / A_0 \quad (\text{Eq.4.1})$$

Where $E_{GB}^{Ni}(N_{at})$ is the total energy of the relaxed GB, $E_{Bulk}^{Ni}(N_{at})$ is the total bulk energy, A_0 is the area of the GB plane. ΔV_{GB} the excess volume of a GB can be accessed with:

$$\Delta V_{GB} = \frac{1}{2}(V_{GB}^{Tot}(N_{at}) - V_{Bulk}^{Tot}(N_{at})) / A_0 \quad (\text{Eq.4.2})$$

Where $V_{GB}^{Tot}(N_{at})$ is the volume of GB, $V_{Bulk}^{Tot}(N_{at})$ is the volume of bulk. The GB properties are treated by the notion of the plane inclination angle between the two symmetric tilt grain boundaries: the coherent twin boundary (CTB) and the symmetric incoherent twin boundary (SITB) configurations (figure.4.1).

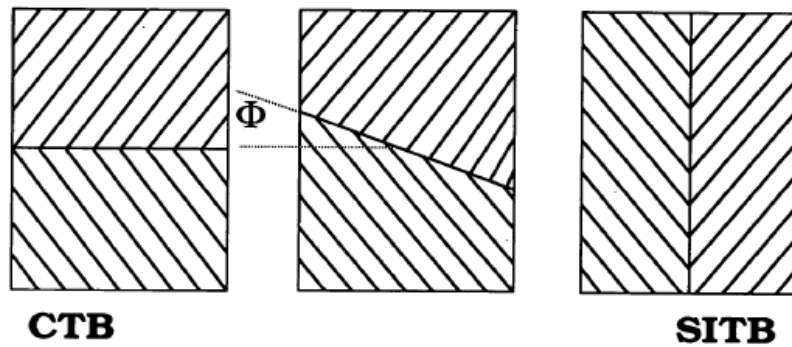


Figure 4.1 – Definition of the inclination angle Φ as the rotation angle of the boundary plane around the $\langle 110 \rangle$ tilt axis, $\Phi = 0^\circ$ refers to the CTB and $\Phi = 90^\circ$ refers to the SITB [Wolf1991]

The energy and excess volume for nine different Ni $\Sigma 3$ $\langle 110 \rangle$ GBs are compared in table 4.1. The GB energies of the nine Ni $\Sigma 3$ GB configurations are illustrated in figure 4.2 as a function of the inclination angle. The grain boundary energies and excess volumes depend strongly on the inclination angle Φ of the boundary plane. There is a good agreement between the GB energies computed and

calculated in this work despite a slight deviation concerning the magnitude of the values. This deviation is essentially ascribed to the difference in the simulation methodologies between the two studies. Olmsted and coworkers [Olmsted2009] used a Foiles-Hoyt [Foiles2001] Ni EAM potential with a simulation cell consisting of one GB with two free surfaces in the direction normal to the boundary plane. In our case, the GB energy calculations rely on 3D periodic simulation cells using the Angelo-Baskes EAM potential [Anglo1995]. GB energy trends as a function of the inclination angle is given in (Eq.4.3) in agreement with Wolf *et al.* [Wolf1991]:

$$E_{GB}(\Phi) = E_{CTB} \cos(\Phi) + E_{STB} \sin(\Phi) \quad (\text{Eq.4.3})$$

As illustrated in *table 4.1*, we observed an increase of the excess volume with the increase of GB energy. Additionally the GBs structural configurations and their energy profile given in *figure 4.3* highlight the variability of the states in one grain-boundary. Consequently, the interaction of hydrogen with GB need to be considered in term of local state.

Table 4.1. Energy (E_{GB}), excess volume (ΔV_{GB}) and geometric considerations including grain normal ((hkl)₁/(hkl)₂) for each inclination angle (Φ) of all the nine GBs investigated in this study. [Halli2016]

| $\Sigma 3$ (hkl) ₁ /(hkl) ₂ | Φ (deg°) | E_{GB} (mJ/m ²) | ΔV_{GB} (Å ³) |
|---|---------------|-------------------------------|-----------------------------------|
| (111 $\bar{1}$) ₁ /(111) ₂ | 0 | 50 | 0.01206 |
| (552 $\bar{2}$) ₁ /(112) ₂ | 19.47 | 362 | 0.04323 |
| (110) ₁ /(114) ₂ | 35.26 | 547 | 0.06006 |
| (221) ₁ /(001) ₂ | 54.74 | 723 | 0.07639 |
| (554) ₁ /(118 $\bar{8}$) ₂ | 64.76 | 779 | 0.08211 |
| (111) ₁ /(115 $\bar{5}$) ₂ | 70.53 | 797 | 0.08448 |
| (557) ₁ /(113 $\bar{3}$) ₂ | 79.98 | 801 | 0.08781 |
| (223) ₁ /(441 $\bar{1}$) ₂ | 81.95 | 800 | 0.08781 |
| (112) ₁ /(112 $\bar{2}$) ₂ | 90 | 806 | 0.08199 |

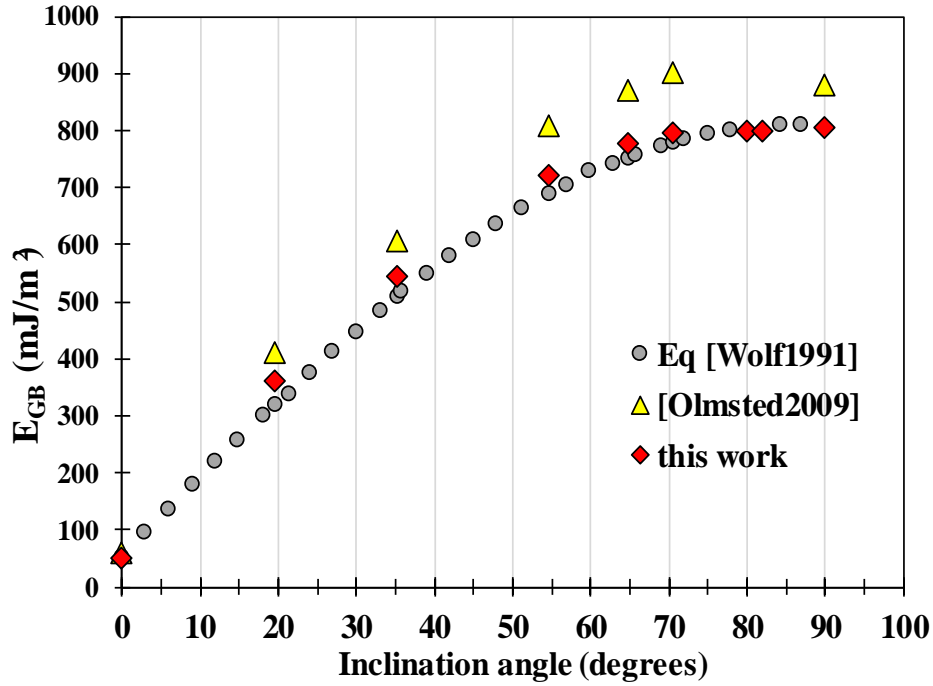


Figure 4.2 - Grain boundary energy as a function of the inclination angle Φ in Ni $\Sigma 3$ GBs [Hallil2016]. Yellow points are data of Olmsted *et al.* [Olmsted2009], Red points are calculated from (Eq. 4.3) [Wolf1991].

In a second step, my work has focused on the construction a number of some modeled bi-crystals with the objective to compare them with our experimental data. Four different bi-crystals ($\Sigma 11-50$ ${}_{48}\langle 110 \rangle \{311\}$, $\Sigma 11-129$ ${}_{52}\langle 110 \rangle \{332\}$, $\Sigma 3-70$ ${}_{53}\langle 110 \rangle \{111\}$ and $\Sigma 5-36$ ${}_{86}\langle 100 \rangle \{310\}$), has been considered. The results allow us to associate the discussion on the diffusion and segregation phenomena to the GB characters (the excess volume, GB energy, geometry, segregation position, local stresses, diffusion paths, etc.). GBs configurations are given in *figure 4.4* with the relationship of the GB energy as a function of the excess volume.

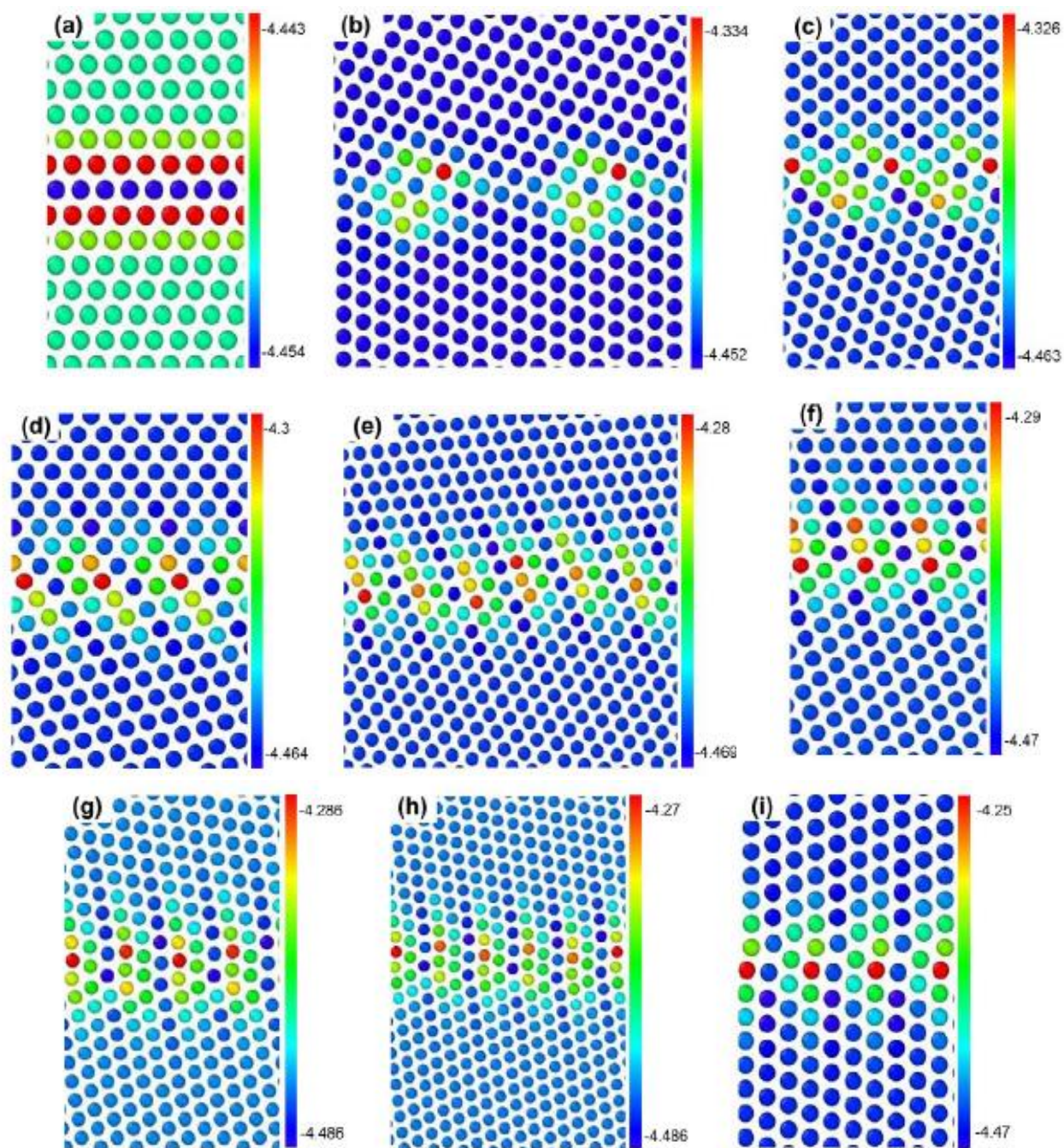


Figure 4.3 – Energetic profile (eV) of atoms in the Ni $\Sigma 3$ relaxed GB structures, viewed along the $[1\ 1\ 0]$ direction: (a) $\Sigma 3\ \Phi = 0^\circ$ CTB (b) $\Sigma 3\ \Phi = 19.47^\circ$ (c) $\Sigma 3\ \Phi = 35.26^\circ$ (d) $\Sigma 3\ \Phi = 54.74^\circ$ (e) $\Sigma 3\ \Phi = 64.76^\circ$ (f) $\Sigma 3\ \Phi = 70.53^\circ$ (g) $\Sigma 3\ \Phi = 79.98^\circ$ (h) $\Sigma 3\ \Phi = 81.95^\circ$ (i) $\Sigma 3\ \Phi = 90^\circ$ SITB.

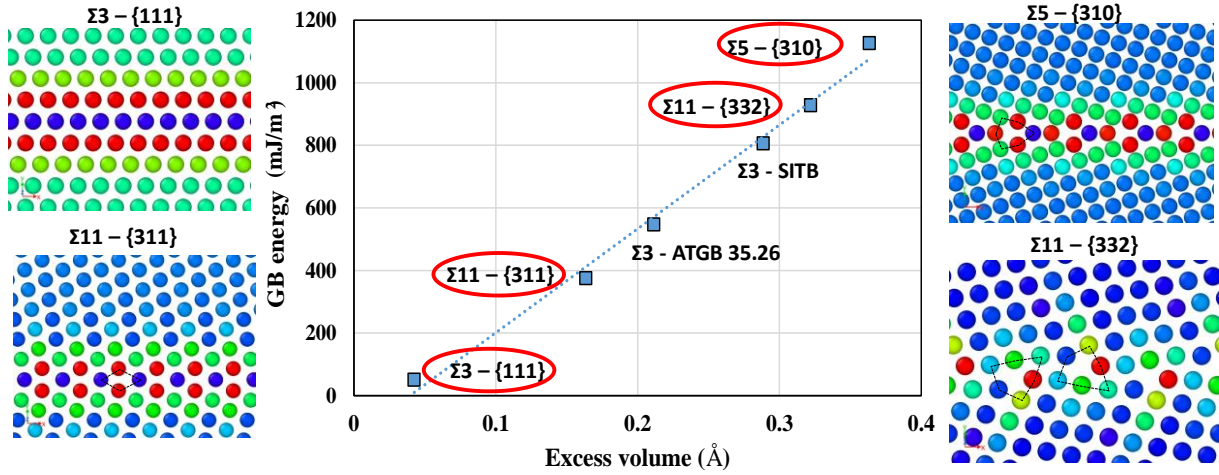


Figure 4.4 – The GB energy vs the excess volume for different GBs, GBs surrounded with red circle are given their GB plane configurations. $\Sigma 3$ configurations are illustrated in figure 4.3.

The GB energy is quite a linear function of the excess volume for different GBs, while the coincidence site lattice Σ (CSL) gives no information on the GB character, and the same Σ (CSL) family GBs can have very different GB energies and excess volumes. The GBs with lower energy have a more compact GB plane configuration. Thus, the next step now is to question the impact of these structural configurations on the segregation and diffusion path of hydrogen.

II. Hydrogen segregation states

II.1 Segregation energy

Since the stable configuration of GBs has been established, we started to insert the hydrogen atom in different positions in GBs. The insertion energy (in some publications called also the adsorption energy) of a hydrogen atom in the nickel lattice E_H^{Ins} is given in (Eq.4.4):

$$E_H^{Ins} = E_{Ni+H}^{Tot} - E_{Ni}^{Tot} - \frac{1}{2}E_{H_2} \quad (\text{Eq.4.4})$$

E_{Ni+H}^{Tot} is the total energy of nickel lattice with a hydrogen atom, E_{Ni}^{Tot} is the total energy of nickel lattice without hydrogen atom and E_{H_2} is the chemical potential of the molecular hydrogen, the binding energy of one hydrogen atom can be obtained by EAM potential in vacuum [Foiles1987]

($\frac{1}{2}E_{H_2} = -2.36947\text{eV}$). This calculation has indicated that the octahedral site ($E_{Oct}^{Ins} = 0.1775\text{ eV}$) is

more stable than the tetrahedral site ($E_{Tet}^{Ins} = 0.586\text{eV}$). Similar results of EAM have been reported by Zhu *et al.* [Zhu2017]. Thus the segregation energy relative to the octahedral site is written in (Eq.4.5):

$$E_H^{Seg} = (E_{GB+H}^{Tot} - E_{GB}^{Tot}) - (E_{Ni+H}^{Oct} - E_{Ni}^{Tot}) \quad (\text{Eq.4.5})$$

E_{GB+H}^{Tot} is the total energy of GB with a hydrogen atom, E_{GB}^{Tot} is the total energy of GB and E_{Ni+H}^{Oct} is the total energy of the nickel lattice with a hydrogen atom at the octahedral site.

The segregation energy for the different sites in and near the GBs have been determined for the four GBs studied. The energy can be represented as a function of the distance from the GB plane (*figure 4.5*). The minimum of this energy is obtained in the GBs core and depends on the GB character. Additionally this value is an increasing function of the excess volume. Since a large variety of segregation energy can be obtained for some GBs and specifically for large excess volume (see $\Sigma 11\text{-}\{332\}$ as an example). If we are interested in the thickness of GBs from an energy point of view, high energy GBs provide more stable segregation sites and have larger GB thickness as the following relationship: $\Sigma 11\text{-}\{332\}$ ($\approx 16 \text{ \AA}$) $>$ $\Sigma 5\text{-}\{310\}$ ($\approx 10 \text{ \AA}$) $>$ $\Sigma 11\text{-}\{311\}$ ($\approx 8 \text{ \AA}$) $>$ $\Sigma 3\text{-}\{111\}$ ($\approx 6 \text{ \AA}$).

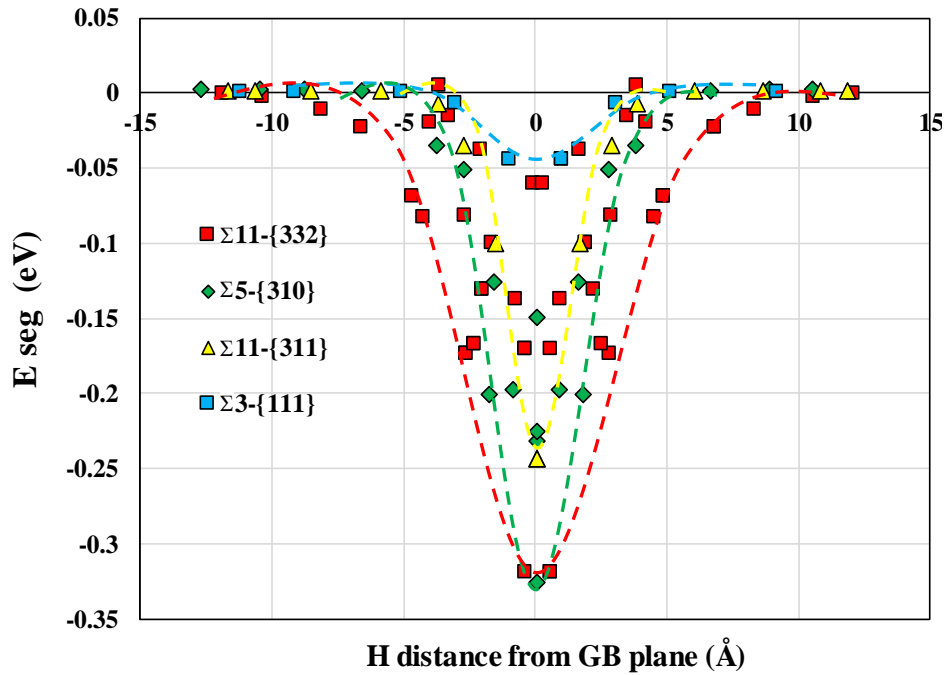


Figure 4.5 – The segregation energy vs the hydrogen distance from the GB plane.

The segregation energy as a function of the hydrogen atomic volume at the segregation site can be now considered (*figure 4.6*). This hydrogen atomic volume occupied by neighboring nickel atoms is calculated using the Voronoi method. The hydrogen atomic Voronoi volume at the octahedral site V_{Oct} is 5.773 \AA^3 . All segregation sites contiguous to the GB region have a higher atomic volume and a more stable segregation state. Concerning the lower energy GBs, the segregation energy is a linear

function of the hydrogen atomic volume, however, this linear relationship is not available for high energy GBs with an atomic volume above 6.6 \AA^3 . Consequently in the following we consider the morphology of the different sites. The segregation sites in the GB region have complicated local geometry structures, thus, we will give the geometry of all the potential segregation sites in GBs core in details.

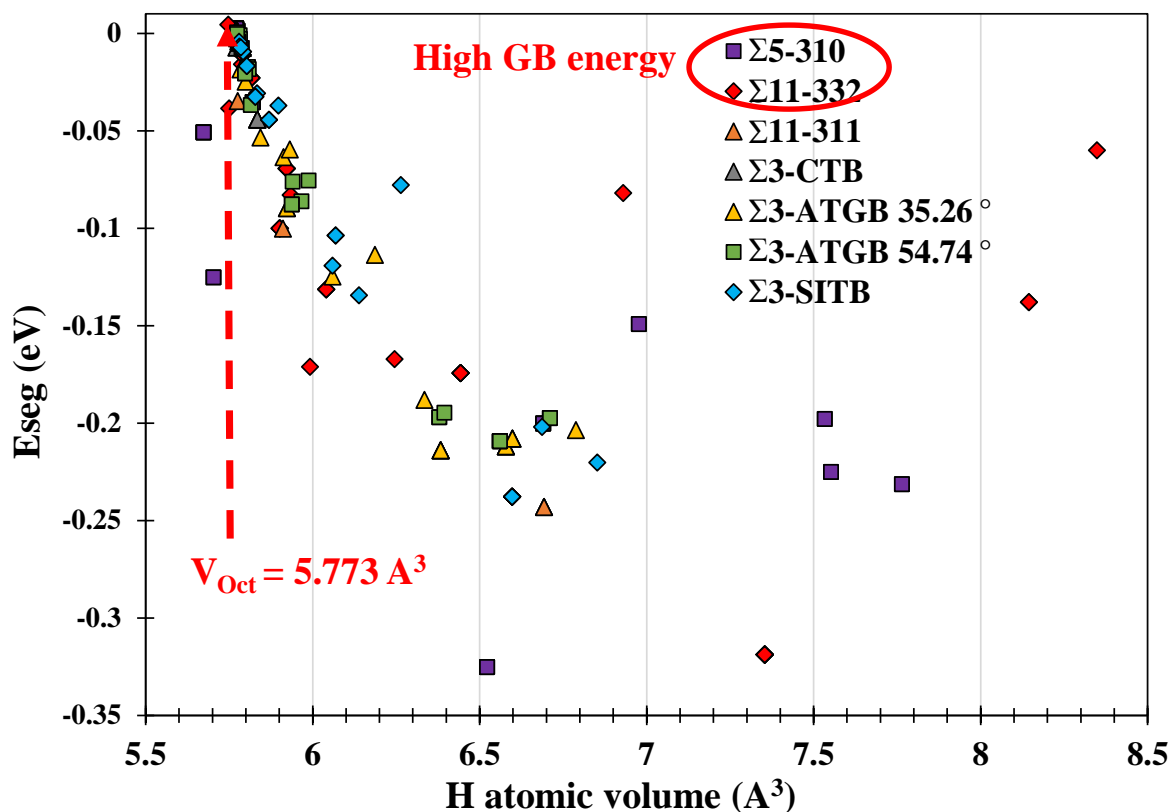


Figure 4.6 – The segregation energy vs the hydrogen atomic volume

The segregation positions and their volume geometry are given in *figure. 4.7*, *figure. 4.8*, *figure. 4.9* and *figure. 4.10* for the four investigated GBs. The position numbers are ranked from the most stable to less stable segregation energy (all position details are given in *Appendix 4.1*). According to the Voronoi tessellation proposed by LAMMPS, the hydrogen volume at the octahedral site in nickel bulk is a cubic form with 14 neighboring atoms. The closer the hydrogen atoms gets to the GB core region, the greater the geometry deformation occurs. The segregation energy and the hydrogen volume size are extremely dependent on the local environment. However, a direct relationship cannot be found among these factors. The morphology of the different sites highlights the fact that the deformation of the site is not isotropic for the most cases. We will discuss this aspect in the next section.

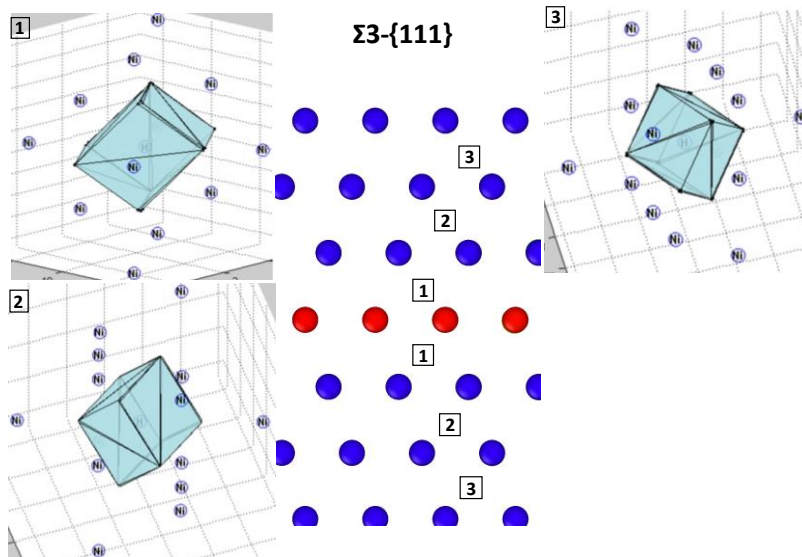


Figure 4.7 – The segregation positions in GB $\Sigma 3\text{-}\{111\}$.

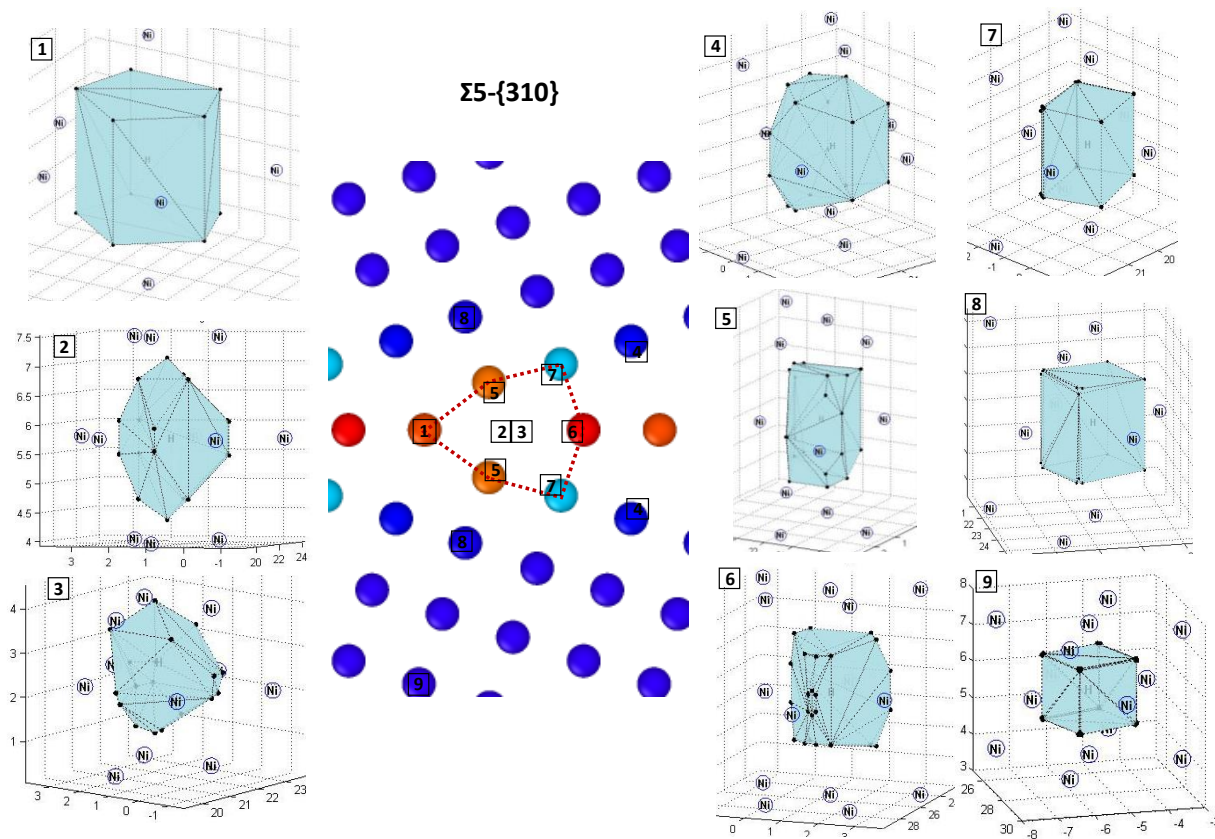


Figure 4.8 – The segregation positions in GB $\Sigma 5\text{-}\{310\}$.

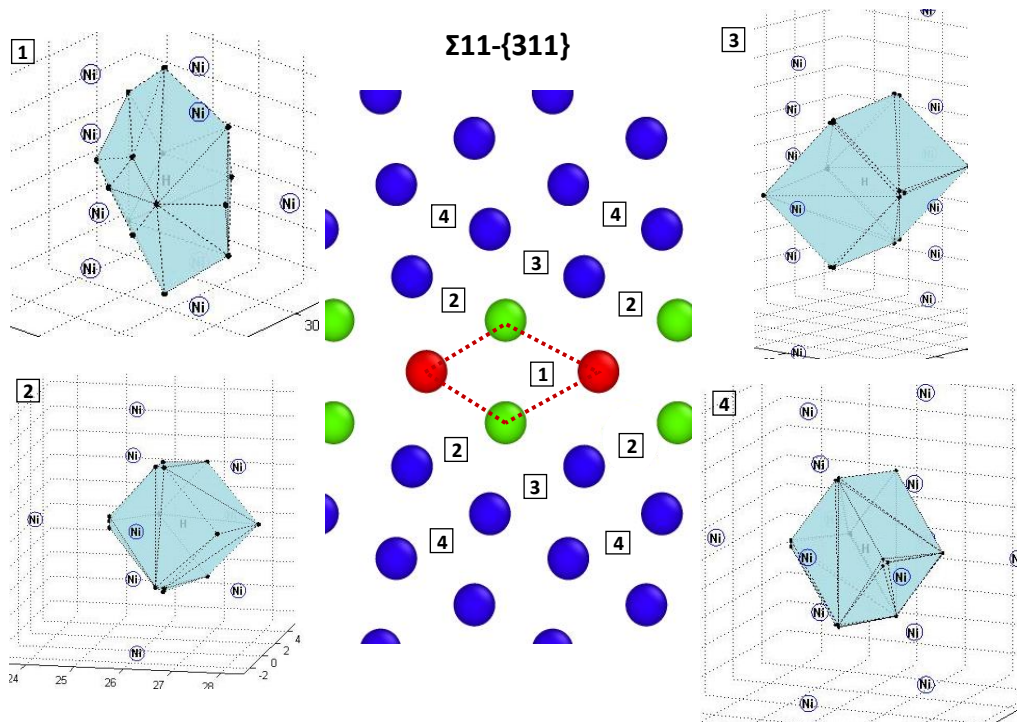


Figure 4.9 – The segregation positions in GB $\Sigma 11\text{-}\{311\}$.

After the consideration of the local volume deformation, the hydrogen atom insertion at different sites can be discussed in term of local energy of hydrogen. This energy is the sum of the kinetic and the potential energy, which differs from the segregation energy only if we have a long range effect associated to the insertion of hydrogen. *Figure 4.11* shows the relationships of the hydrogen atom energy with the segregation energy (a) and with the hydrogen atomic volume (b). Hydrogen atom is more stable at a deep segregation site with high atomic volume. Actually, we have noticed that a part of data have a linear evolution, these sites have a similar cubic form with a relatively low hydrogen atomic volume. This linearity disappears when the distortion becomes significant ($V_H > 6.6 \text{ \AA}^3$).

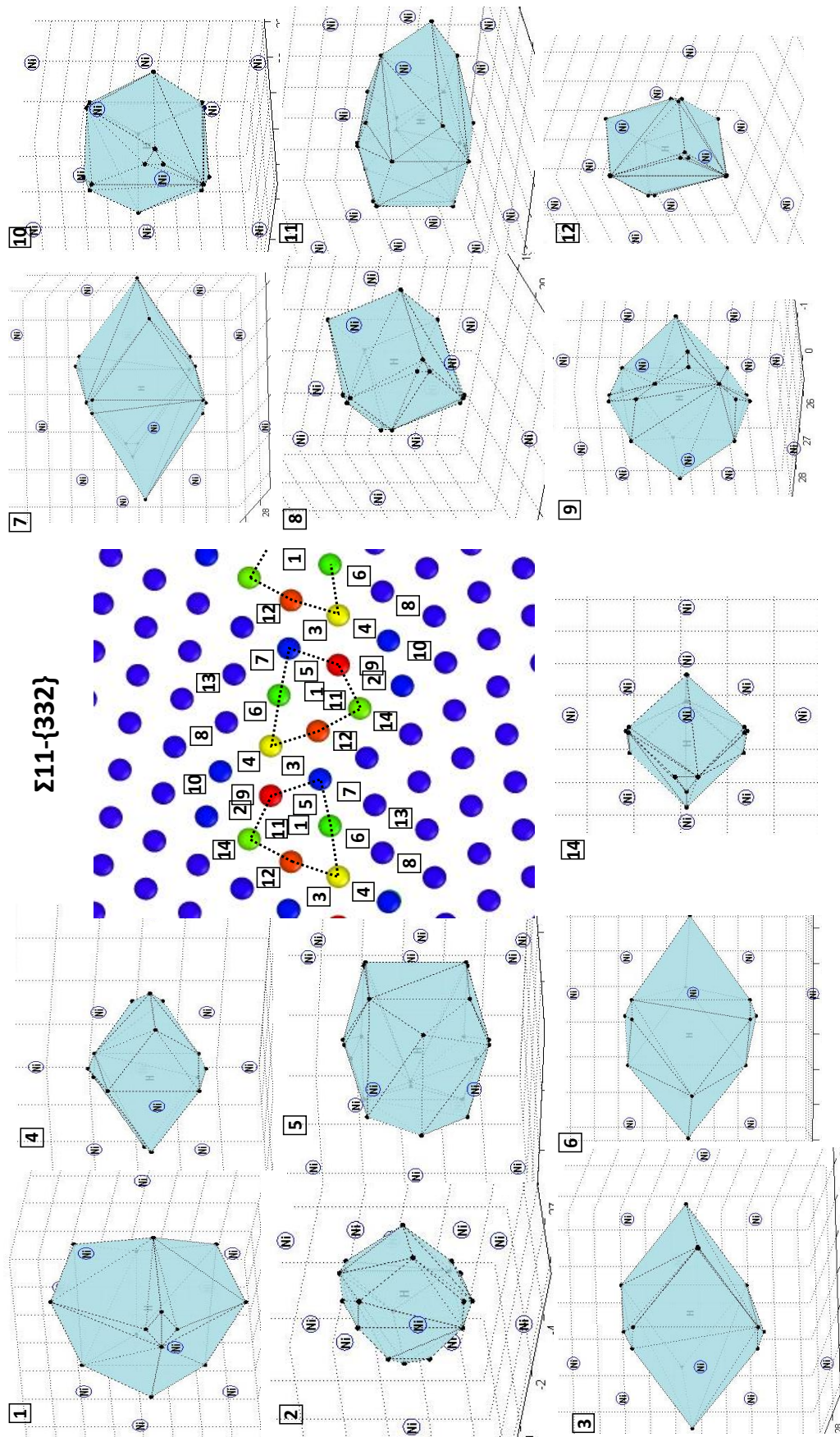


Figure 4.10 – The segregation positions in GB $\Sigma 11\{-332\}$.

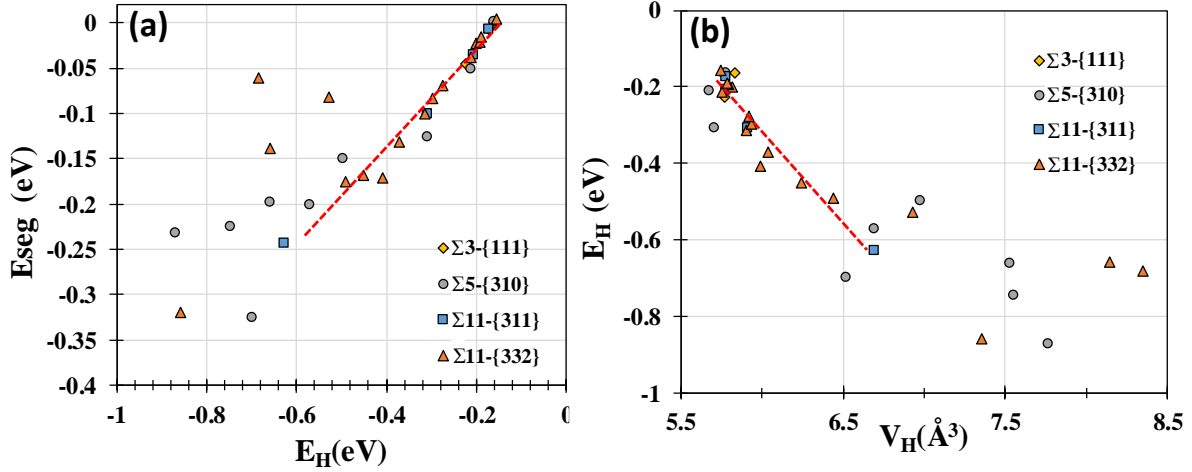


Figure 4.11 – (a) The segregation energy vs hydrogen energy (b) the hydrogen energy vs hydrogen atomic volume.

II.2 Stress states and hydrogen segregation

The insertion of an atom will create a volume expansion in the whole lattice, this variation is composed of two distinct forms – the hydrostatic dilatation (hydrostatic strain) and the distortion of the volume (deviatoric strain). For materials with linear elasticity, the symmetric stress of each atom is calculated and given as an elastic dipole tensor form. The tensor for atom a is given by the following formula, where i and j take on values x, y, z to generate the 6 components of the symmetric tensor (Eq.4.6):

$$\begin{aligned}
 P_{ij} = - \left[& m v_i v_j + \frac{1}{2} \sum_{n=1}^{N_p} (r_{1i} F_{1j} + r_{2i} F_{2j}) \right. \\
 & + \frac{1}{2} \sum_{n=1}^{N_j} (r_{1i} F_{1j} + r_{2i} F_{2j}) + \frac{1}{3} \sum_{n=1}^{N_i} (r_{1i} F_{1j} + r_{2i} F_{2j} + r_{3i} F_{3j}) \\
 & + \frac{1}{4} \sum_{n=1}^{N_d} (r_{1i} F_{1j} + r_{2i} F_{2j} + r_{3i} F_{3j} + r_{4i} F_{4j}) \\
 & + \frac{1}{4} \sum_{n=1}^{N_a} (r_{1i} F_{1j} + r_{2i} F_{2j} + r_{3i} F_{3j} + r_{4i} F_{4j}) + \sum_{n=1}^{N_f} (r_{1i} F_{1j}) \\
 & \left. + K_{\text{space}}(r_{1i}, F_{1j}) \right] \quad (\text{Eq. 4.6})
 \end{aligned}$$

The first term is a kinetic energy contribution for atom a . The second term is a pairwise energy contribution where n loops over the N_p neighbors of atom a , r_1 and r_2 are the positions of the 2 atoms in the pairwise interaction, and F_1 and F_2 are the forces on the 2 atoms resulting from the pairwise interaction. The third term is a bond contribution of similar form for the N_j bonds. There are as well similar terms for the N_i angle, N_d dihedral, and N_a improper interactions. There is also a term for the KSpace contribution from long-range Coulombic interactions [Heyes1994]. Details of how LAMMPS computes the virial for individual atoms for either pairwise or manybody potentials, and includes the effects of periodic boundary conditions is discussed in [Thompson2009].

The elastic dipole tensor characterizes the changes for both the volume and the shape of the interstitial site during the relaxation procedure after the incorporation of the solute in the lattice. Since the lattice deformation around the defect atom occurs principally on the interstitial closest neighboring atoms, we can access the close volume change by calculating the Voronoi atomic volume at each GB interstitial site after the insertion of the hydrogen atom. Thus, the atomic stress σ_{ij} induced from the insertion of the H interstitial are related to the lattice-defect elastic tensor by [Hallil2017]:

$$\sigma_{ij} = \frac{1}{\Omega_H} P_{ij} \quad (\text{Eq.4.7})$$

Where Ω_H is considered as the local atomic volume of the interstitial atom. The atomic stress components are used to calculate the hydrostatic and deviatoric stress tensors, which characterize the isotropic and anisotropic deformations of the interstitial volume due to the insertion of hydrogen. The local hydrostatic stress σ_H and deviatoric stress defined as Von Mises σ_D are given in (Eq.4.8) and (Eq.4.9):

$$\sigma_H = \frac{1}{3}(\sigma_{xx} + \sigma_{yy} + \sigma_{zz}) \quad (\text{Eq.4.8})$$

$$\sigma_D = \sqrt{\frac{(\sigma_{xx} - \sigma_{yy})^2 + (\sigma_{xx} - \sigma_{zz})^2 + (\sigma_{yy} - \sigma_{zz})^2 + 6(\sigma_{xy}^2 + \sigma_{yz}^2 + \sigma_{zx}^2)}{2}} \quad (\text{Eq.4.9})$$

The total strain energy by unit volume U_{Tot} is given in (Eq.4.10), we consider here the Young modulus E and the Poisson ratio ν remain the same with values of the perfect bulk, despite the fact that probably these two parameters are modified in the GBs and with the presence of hydrogen:

$$U_{Tot} = \frac{1+\nu}{3E} \sigma_D^2 + \frac{3(1-2\nu)}{2E} \sigma_H^2 = U_D + U_H \quad (\text{Eq.4.10})$$

Figure 4.12(a) presents local stresses as a function of the hydrogen atomic volume. The hydrostatic stress (absolute value) is significant at a low volume ($V_H < 6.6 \text{ \AA}^3$) and at a quite ‘‘compact

environment” such as an octahedral site in perfect FCC lattice. At these cubic form or similar sites, the deviatoric stress is low due to the small distortion. However, at high volume sites, the hydrostatic stress decreases and at the same time the distortion component of the stress is more significant than the hydrostatic volume change. The contribution of each stress (U_i/U_{Tot}) for the strain energy is given in *figure 4.12(b)*, the hydrostatic stress gives the most contribution to the strain energy particularly for values higher than 2 GPa (Zone I), and in other words high strain energy is at small hydrogen atomic volume with high hydrostatic stress.

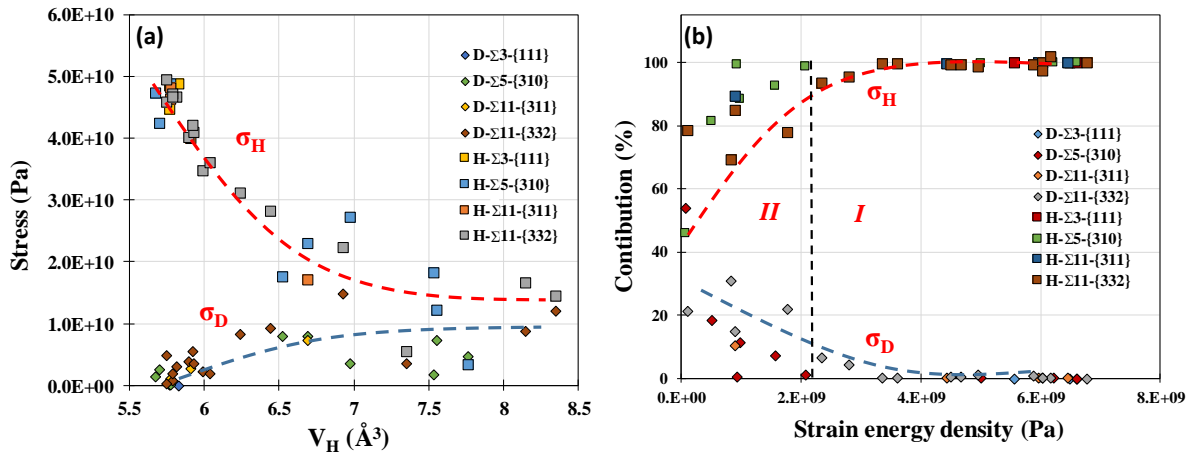


Figure 4.12 – (a) The hydrostatic stress and the deviatoric stress vs the hydrogen atomic volume (b) the contribution of the hydrostatic stress and the deviatoric stress for the strain energy density.

The hydrogen energy versus the strain energy from the insertion of a hydrogen atom is given in *figure 4.13*. Two distinct linear regimes separate for the strain energy density about 2 GPa. The total strain energy is dominated by the hydrostatic stress for the first linear regime called zone I (Hydrogen energy is between -0.15 eV and -0.6 eV), while the other linear regime zone II is due to the contribution of the deviatoric stress (Hydrogen energy is between -0.6 eV and -0.9 eV).

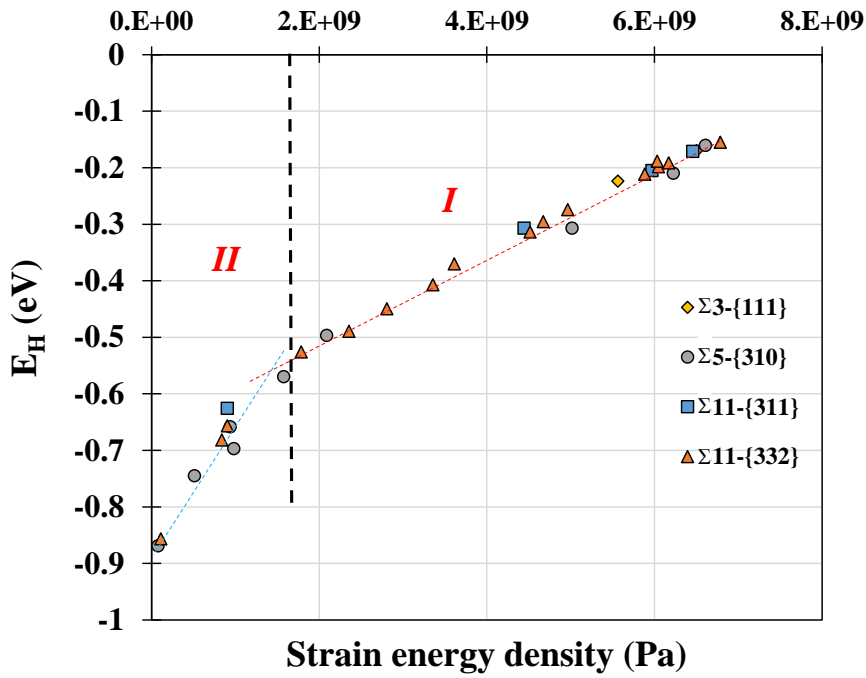


Figure 4.13 – The hydrogen atom energy vs the total strain energy density

Figure 4.14 presents the segregation energy as a function of the strain energy density which is similar to the first linear regime in figure 4.13. The linear relationship starts from the strain energy density about 2 GPa, and this linearity disappears at a low strain energy density range. Indeed, the segregation energy of a site is the difference between the current position and the octahedral site in perfect bulk, thus we lose the linearity of the segregation energy in the GB core because there are many sites around that differ from the octahedral sites in a GB core.

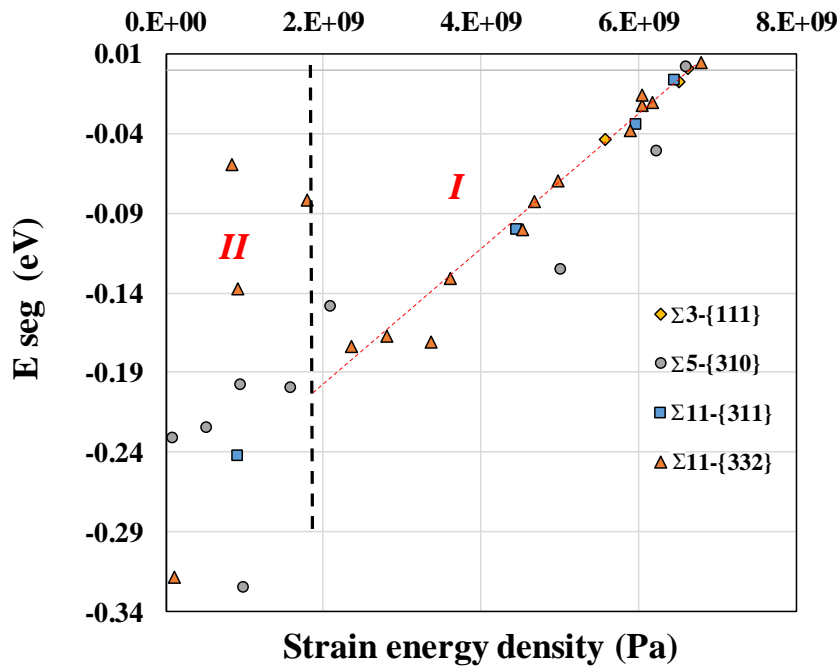


Figure 4.14 – The segregation energy vs the total strain energy density

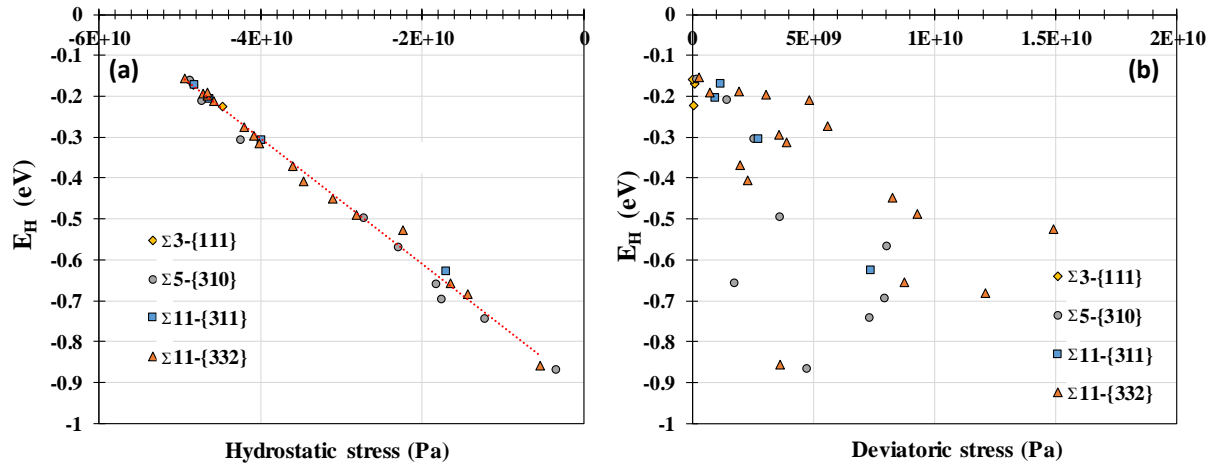


Figure 4.15 – (a) The hydrogen atom energy vs the hydrostatic stress (b) The hydrogen atom energy vs the deviatoric stress

Figure 4.15 (a) indicates that the hydrogen atom energy is a linear function of the hydrostatic stress. However, the deviatoric stress is more dependent on the local environment (figure.4.15 (b)) such as the geometry and its distortion.

A hydrogen atom with a strain energy higher than 2 GPa (in zone I) is located away from the GB and thus has a cubic geometry form. Its segregation site has a low hydrogen atomic volume ($V_H < 6.6 \text{ \AA}^3$), and its contribution to the total strain energy is mostly from the hydrostatic stress, so the linearity appears in this zone. The linearity disappears in the zone II, the complex geometry and its distortion is more significant with a high hydrogen atomic volume ($V_H > 6.6 \text{ \AA}^3$). The deviatoric stress gives a major contribution to the total strain energy since the hydrostatic stress is lower in zone II. Additionally, the high hydrogen atomic volume segregation sites are in the GB core, the calculation of the strain energy densities are based on the elasticity in the perfect nickel bulk with a spread uncertainty due to the difference of elasticity in the GB core and in the nickel bulk and also probably from a slight modification by the presence of a hydrogen atom.

II.3 Segregation concentration

According to the Langmuir–McLean segregation isotherm model without solutes interactions [Lecjek2010, Priester2013, Shen2014], it is possible to establish a relationship between the segregation concentration and the bulk concentration in a binary system. The expression is given in (Eq.4.11):

$$\frac{C_{seg}}{C_{max} - C_{seg}} = \frac{C_{bulk}}{1 - C_{bulk}} \exp\left(\frac{-E_H^{Seg}}{RT}\right) \quad (\text{Eq.4.11})$$

$C_{seg} = C_{Hseg}/C_{Ni}$ is the molar fraction of segregation, $C_{bulk} = C_H/C_{Ni}$ is the molar fraction in the nickel bulk. Hydrogen occupies the octahedral site in the nickel bulk, the unit cell of FCC structure gives the maximum saturation $C_{oct}/C_{Ni} = 1$. Knowing that not every position in grain boundary is available for segregation ($E_H^{Seg} < 0$), thus, a saturation of segregation C_{max} of the boundary occurs and the segregation occupation of each position C_i/C_{max} as a function of C_{bulk} at 300K is given in *figure 4.16*, *figure 4.17*, *figure 4.18* and *figure 4.19* with their corresponding GB unit cells.

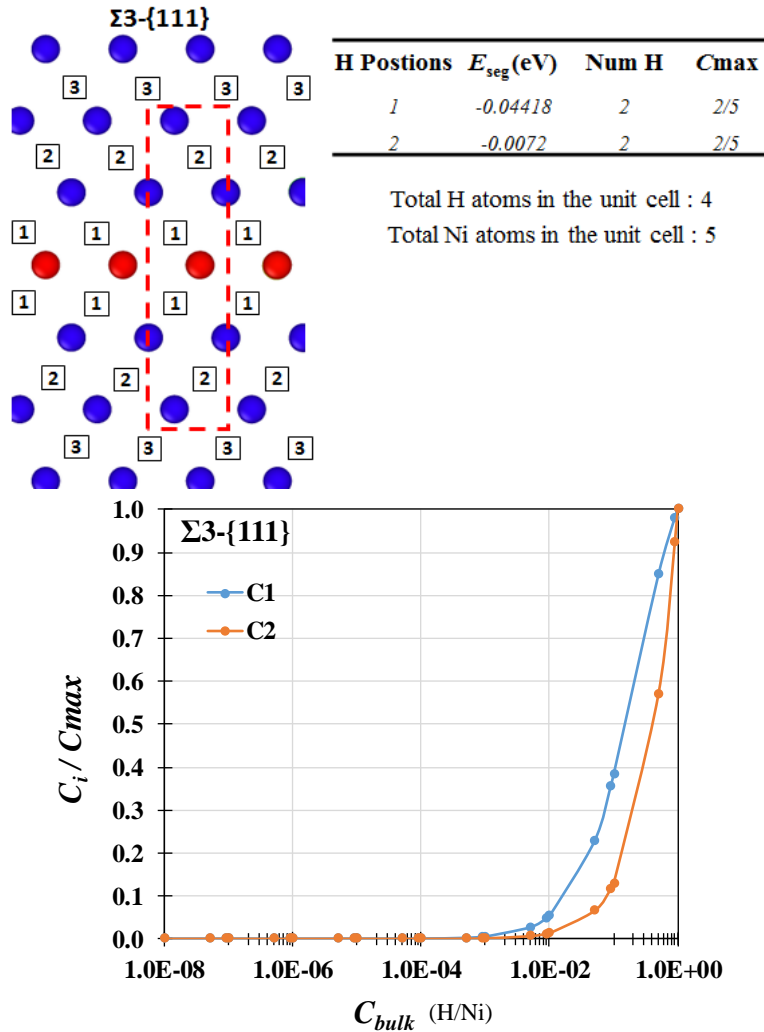


Figure 4.16 – The unit cell for GB $\Sigma 3$ -{111} with position details, and the segregation occupation for 2 positions in GB as a function of the bulk concentration at 300K.

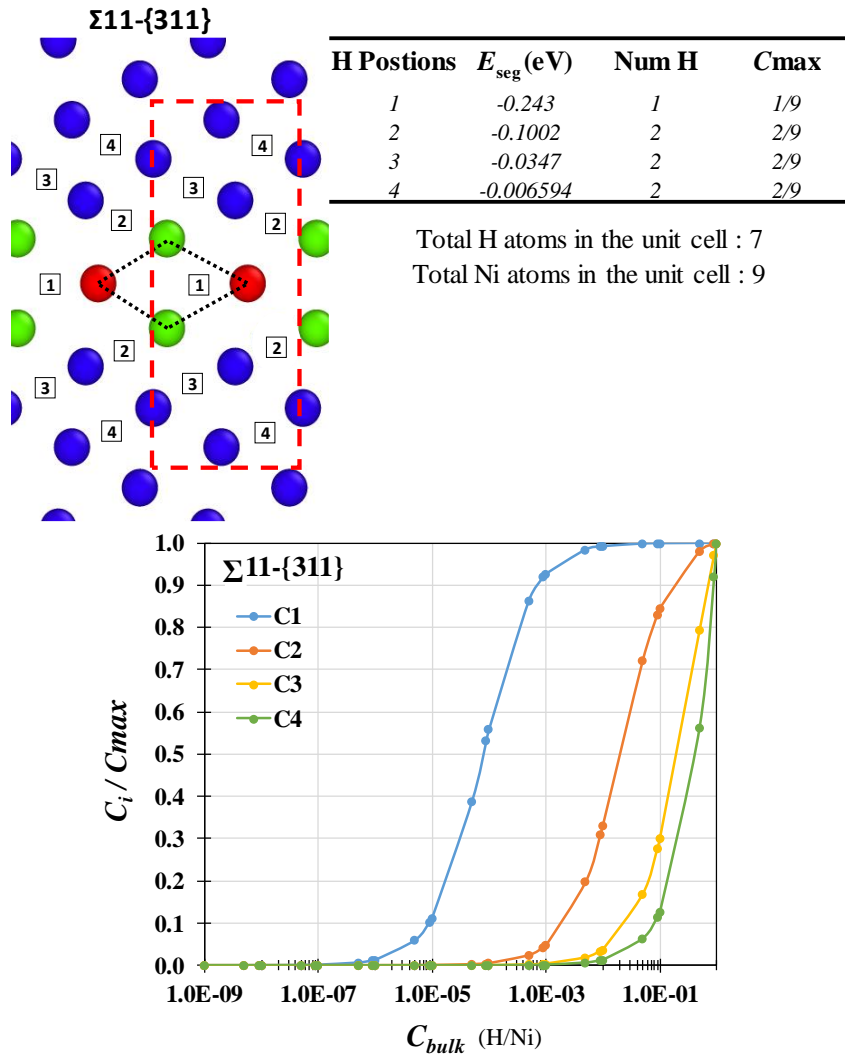
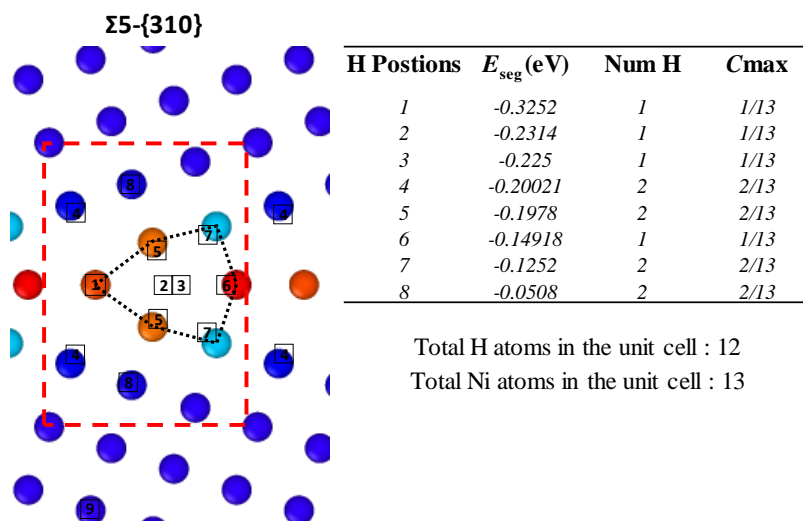


Figure 4.17 – The unit cell for GB $\Sigma 11\{-311\}$ with position details, and the segregation occupation for 4 positions in GB as a function of the bulk concentration at 300K.



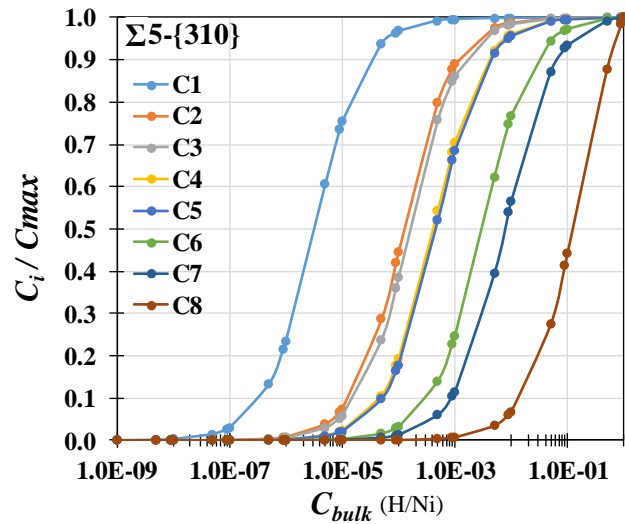


Figure 4.18 – The unit cell for GB $\Sigma 5$ -{310} with position details, and the segregation occupation for 8 positions in GB as a function of the bulk concentration at 300K.

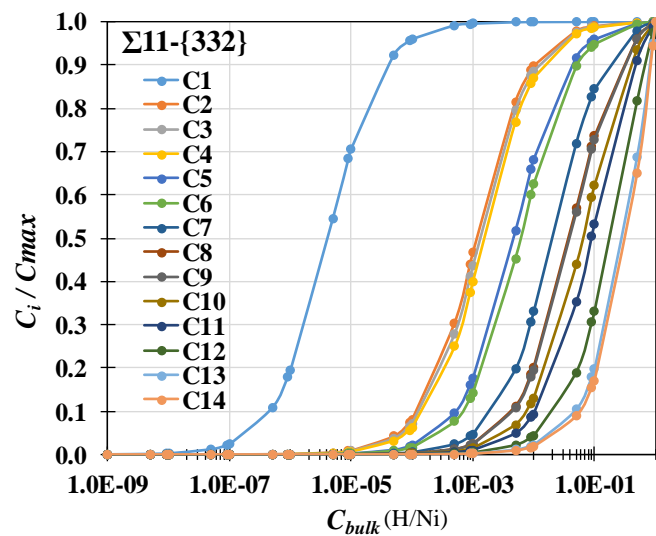
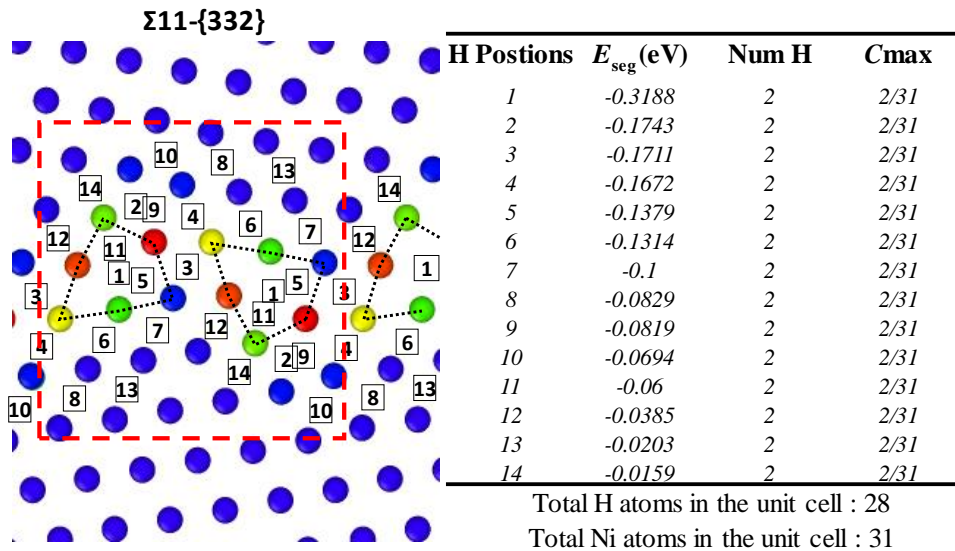


Figure 4.19 – The unit cell for GB $\Sigma 11$ -{332} with position details, and the segregation occupation for 14 positions in GB as a function of the bulk concentration at 300K.

The segregation sites in the high energy GBs such as $\Sigma 11$ -{332} and $\Sigma 5$ -{310} start to be occupied by hydrogen atoms at very low bulk concentration ($C_{bulk} \sim 10^{-7}$ H/Ni). The GB $\Sigma 11$ -{311} starts the segregation around $C_{bulk} = 10^{-6}$ H/Ni while the GB $\Sigma 3$ -{111} starts the segregation around $C_{bulk} = 10^{-3}$ H/Ni. The segregation first takes place at the most stable position C1, then the less stable positions start to segregate hydrogen atoms when the first position is close to saturation (70% -80% occupation). It has been reported that high local concentrations can act as a seed for local hydrides in nickel [Pezold2011, Song2011] because of the attractive H-H interactions. Moreover, EP/TDS experimental data indicates that the limit of hydrogen solubility in nickel single crystal is around $C_{bulk} = 5 \times 10^{-4}$ H/Ni (~ 7.5 wppm at 300 K), we compare thus the segregation in different GBs with a zoom in the limit of solubility in *figure 4.20*.

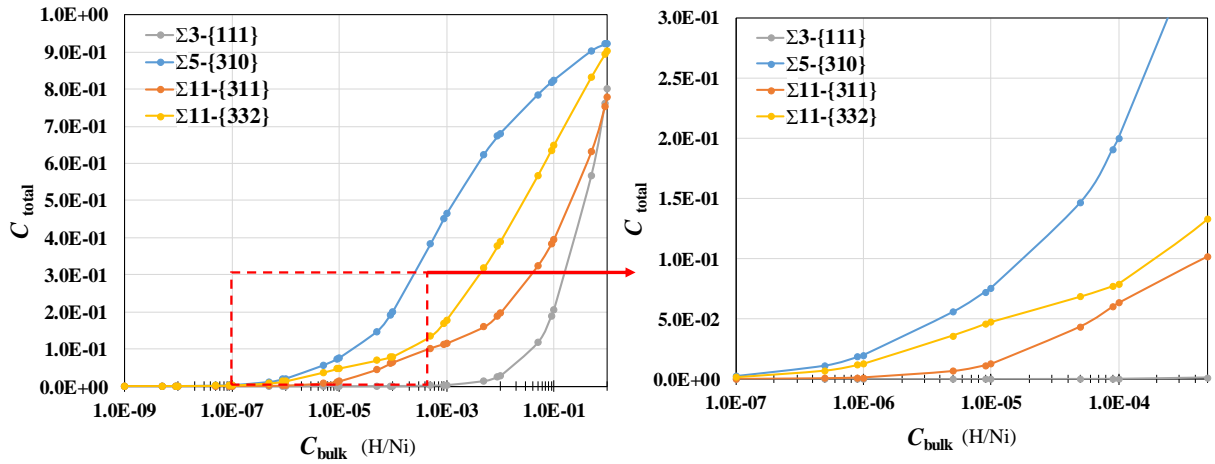


Figure 4.20 – The total segregation concentration $C_{total} = \sum C_i$ in different GBs as a function of the bulk concentration at 300K.

At this range of the bulk concentration ($C_{bulk} \sim 10^{-7}$ to 5×10^{-4} H/Ni), hydrogen segregation is stronger in $\Sigma 5$ -{310} than in $\Sigma 11$ -{332}, the segregation concentration is dominated by the most stable segregation position of which $E_{1seg}^{\Sigma 5-\{310\}} = -0.3252\text{eV} < E_{1seg}^{\Sigma 11-\{332\}} = -0.3188\text{eV}$. Additionally, the GB $\Sigma 3$ -{111} acts as the nickel bulk with no segregation at all.

The GBs with high energy/ excess volume have high segregation densities with various segregation energies. The hydrogen segregation concentration is dominated by the deep segregation sites and these deep segregation sites are often in the GBs core region. The local volume of the segregation sites have been discussed previously, the high local atomic volume and low deformation (low strain energy) sites in the GBs core make it easier to keep a solute hydrogen atom. However this approach is not taken into account the solutes interactions which may change the segregation behavior. Once hydrogen atom is localized in the GBs, it is appropriated to ask how the atom will move or remain trapped.

III. Hydrogen diffusion in GBs –atomic approach

The nudged elastic band method (NEB) method has been used to calculate the minimum energy paths (MEP) and their associated energy barriers. Several stable segregation sites in GBs were looked upon for three principle path directions: (i) the hydrogen atom moves from the bulk site to the GB site, (ii) the hydrogen atom moves between two GB sites along the GB plane, (iii) the hydrogen atom moves between two GB sites along the tilt axis. The first investigation has been carried out in the perfect nickel crystal and $\Sigma 3$ -{111} by A.Hallil and extended to the other GBs. The hydrogen atom moves between octahedral sites through a metastable tetrahedral site in nickel bulk, the energy barriers give EB_{O-T} is 0.47eV in figure 4.21 which is confirmed by the DFT works of Wimmer *et al.* [Wimmer2006] ($EB_{O-T} \sim 0.4664$ eV or 45 KJ/mol). This energy barrier is the reference state, the hydrogen atom is able to move faster if the energy barrier is lower than this reference energy and the entropic contribution is not affected.

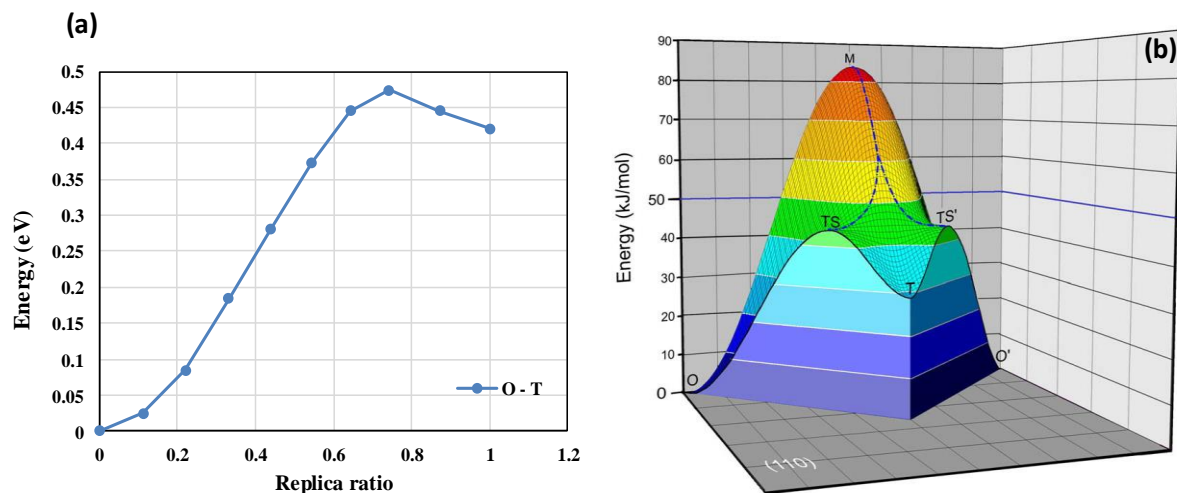


Figure 4.21– (a) Energy barrier from an octahedral site to a tetrahedral site in nickel bulk. (b) Energy hypersurface (electronic energy) of H diffusing in nickel between octahedral interstitial sites. Note the pronounced local minimum at the tetrahedral site (T) and two transition states (TS and TS') along the path from O to O'. The blue dashed-dotted line is the energy divide [Wimmer2006].

$\Sigma 3$ -{111} act as the nickel bulk for its segregation behavior, however the energy barriers of this GB give different characters for the diffusion of hydrogen atom. Figure 4.22 presents the movement of hydrogen atom in the GB core, the energy barrier is calculated with the initial position energy as the reference point. A hydrogen atom can easily cross the GB but slightly slow down along the GB plane.

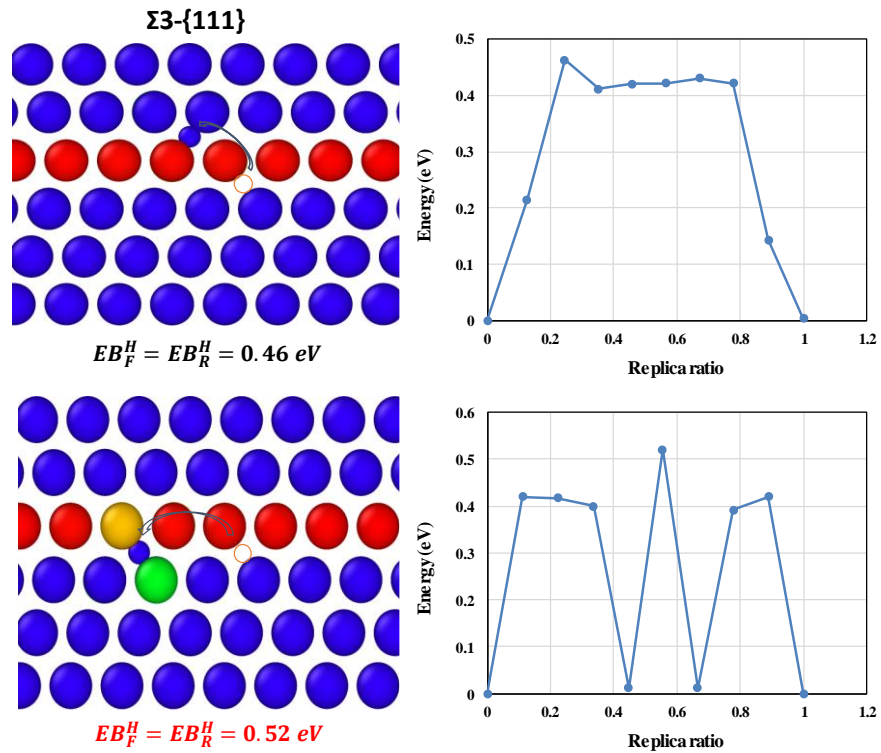


Figure 4.22 – Energy barriers and MEP of hydrogen atoms in GB $\Sigma 3\text{-}\{111\}$, EB_F : Energy barrier forward, EB_R : Energy barrier backward.

Figure 4.23, Figure 4.24 and Figure 4.25 give the MEP and the energy barriers of NEB calculation in $\Sigma 5\text{-}\{310\}$, $\Sigma 11\text{-}\{311\}$ and $\Sigma 11\text{-}\{332\}$ GBs, with the initial position energy as the reference point. We have taken into account several positions such as the most stable segregation sites (type A) and the highest volume sites (type B), A and B positions are the same for the GB $\Sigma 11\text{-}\{311\}$.

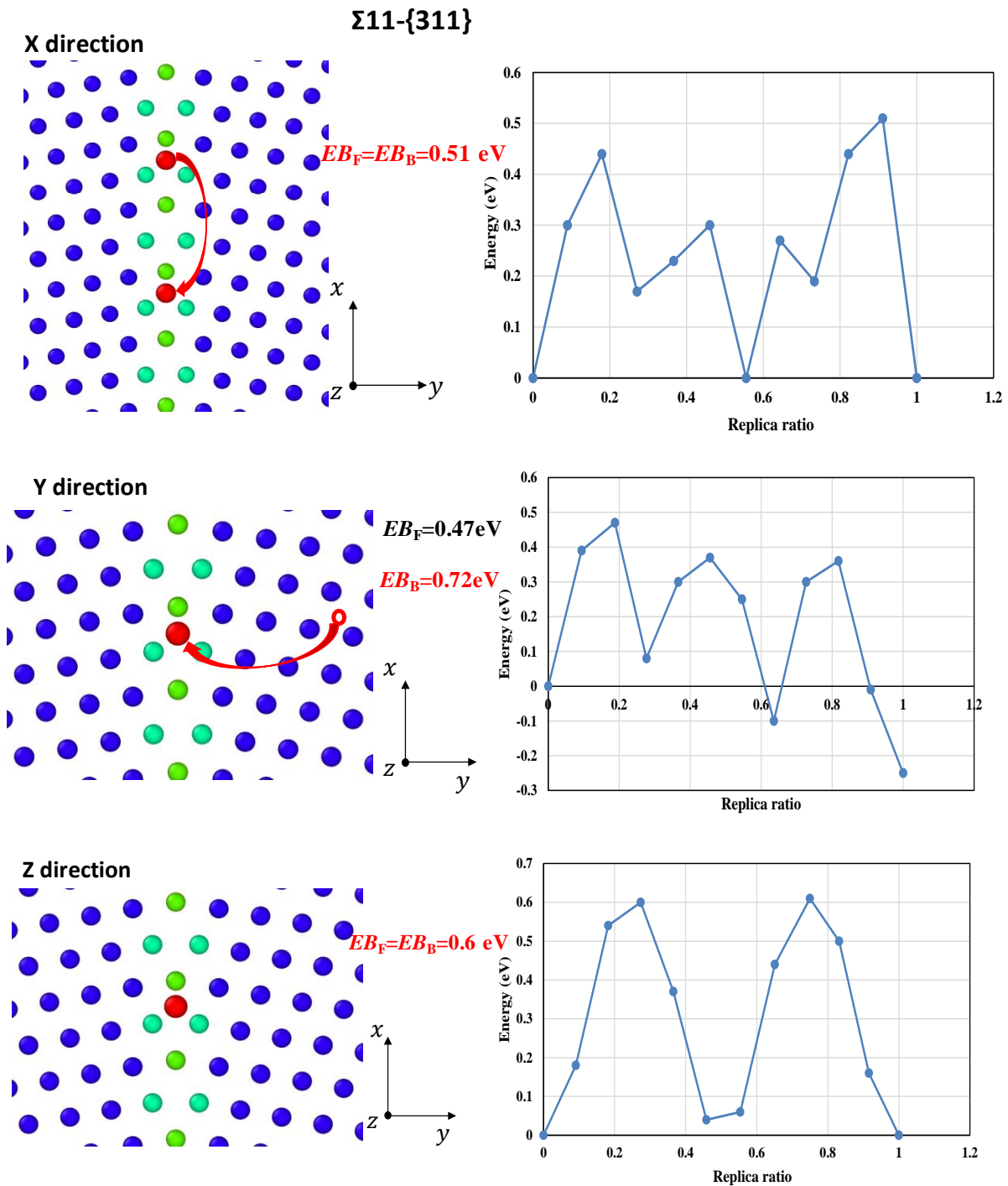


Figure 4.23 – Energy barriers and MEP of hydrogen atoms in GB $\Sigma 11\text{-}\{311\}$, EB_F : Energy barrier forward, EB_B : Energy barrier backward.

For the low energy/excess volume GB $\Sigma 11\text{-}\{311\}$, the hydrogen atom can move easily from the bulk to the GB core, however the energy barriers for other directions are higher than the reference energy in the perfect nickel bulk while the diffusion gets slower in the GB core. This GB has little sites for the hydrogen segregation and its segregation sites are probably trapping sites.

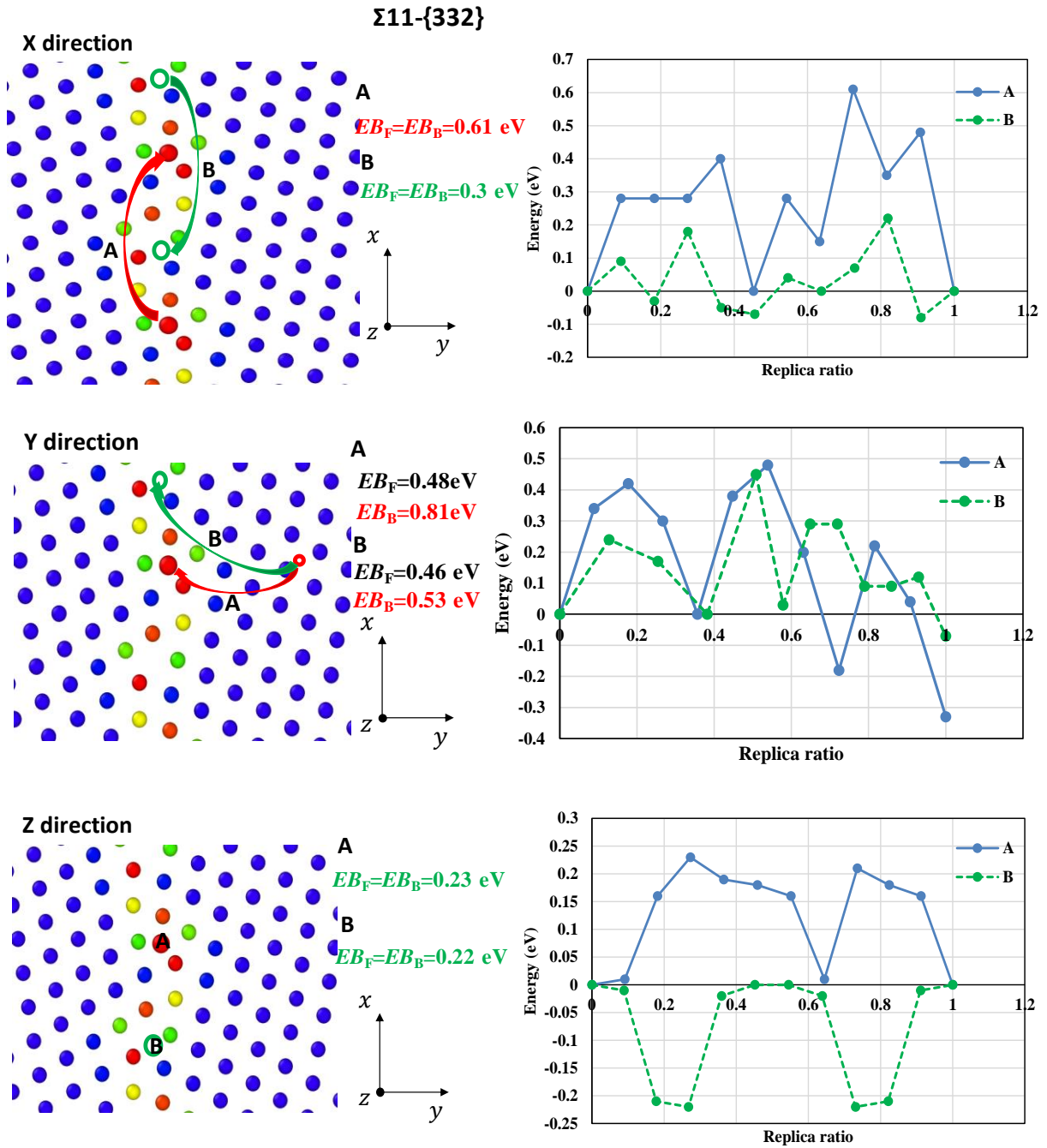


Figure 4.24 – Energy barriers and MEP of hydrogen atoms in GB $\Sigma 11\text{-}\{332\}$, EB_F : Energy barrier forward, EB_B : Energy barrier backward. A is the path between the most stable segregation positions, B is the path between the highest volume positions.

$\Sigma 11\text{-}\{332\}$ is a high energy/excess volume GB, it has several hydrogen segregation sites in the GB core and the energy barriers along the x and z directions are lower than the reference energy in nickel bulk. This GB provides the diffusion paths in two directions.

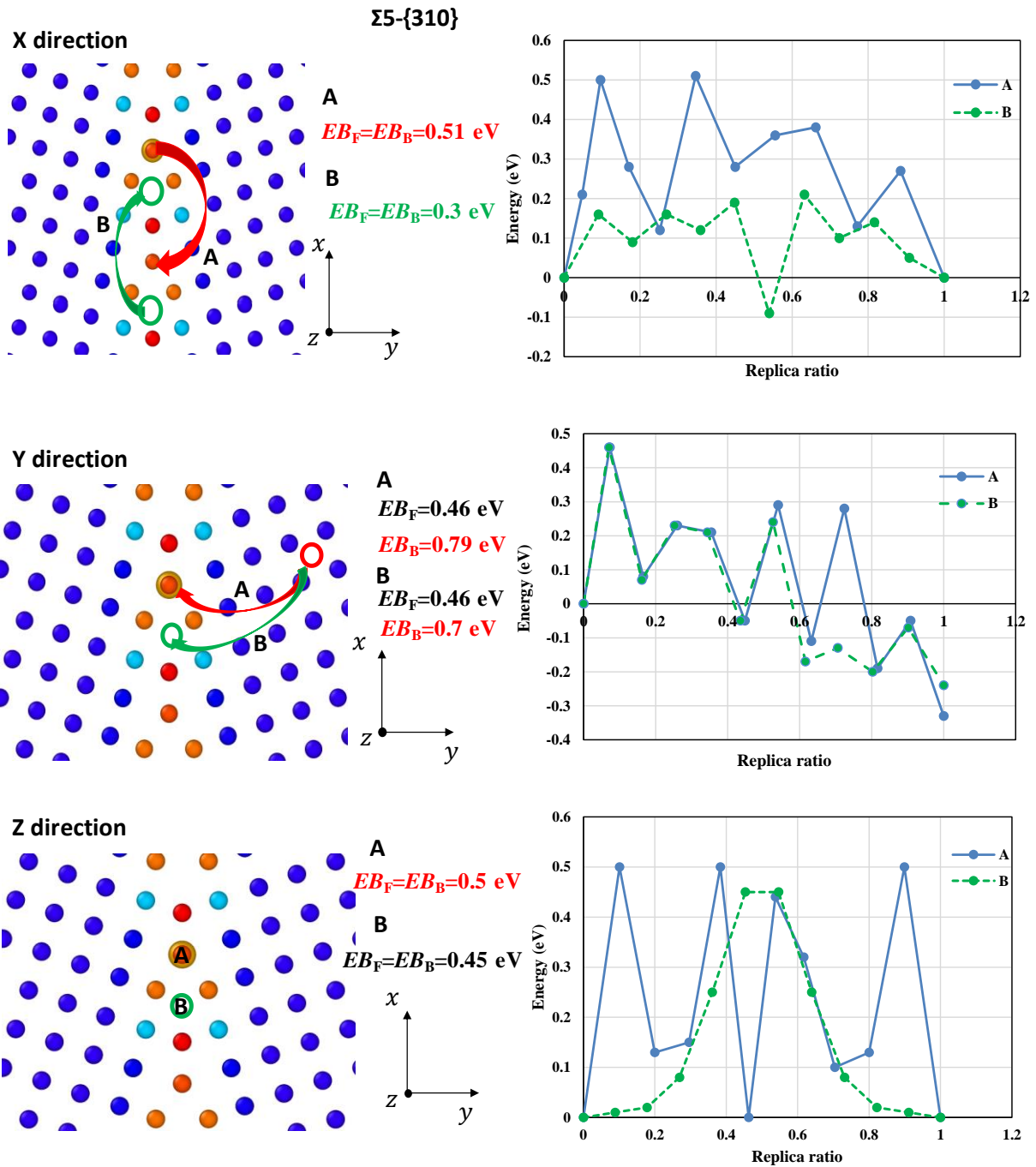


Figure 4.25 – Energy barriers and MEP of hydrogen atoms in GB $\Sigma 5\text{-}\{310\}$, EB_F : Energy barrier forward, EB_B : Energy barrier backward. A is the path between the most stable segregation positions, B is the path between the highest volume positions.

GB $\Sigma 5\text{-}\{310\}$ is the highest energy/excess volume GB in our samples, it has less segregation sites than the GB $\Sigma 11\text{-}\{332\}$ in the GB core. Along the x direction, it exists a diffusion path for which hydrogen atom moves faster at the highest volume sites B. However, the diffusion at the most stable segregation sites A slows down and can be considered as a trapping site.

The energy barrier is able to provide an estimation for the ratio diffusion coefficient in comparison to the diffusion in the perfect nickel bulk (Eq.4.12) [Di Stefano2015]:

$$\frac{D_{GB}}{D_{Bulk}} = \exp\left(\frac{EB_{Bulk} - EB_{GB}}{k_B T}\right) \quad (\text{Eq.4.12})$$

Table 2 – Energy barriers for the most stable segregation position A and the highest volume position B, a brief estimation of ratio D_{GB}/D_{Bulk} is given at 300 K

| GB | X_A | Y_A | Z_A |
|----------------------------|---|--|--|
| $\Sigma 3\text{-}\{111\}$ | $EB_F=EB_B=0.52$ eV $D_{GB}/D_{Bulk}=0.144$ | $EB_F=EB_B=0.46$ eV $D_{GB}/D_{Bulk}=1.4$; | |
| $\Sigma 11\text{-}\{311\}$ | $EB_F=EB_B=0.51$ eV $D_{GB}/D_{Bulk}=0.2$ | $EB_F=0.47$ eV $D_{GB}/D_{Bulk}=1$; $EB_B=0.72$ eV $D_{GB}/D_{Bulk}=6.3 \times 10^{-5}$ | $EB_F=EB_B=0.6$ eV $D_{GB}/D_{Bulk}=6.5 \times 10^{-3}$ |
| $\Sigma 11\text{-}\{332\}$ | $EB_F=EB_B=0.61$ eV $D_{GB}/D_{Bulk}=4.5 \times 10^{-3}$ | $EB_F=0.48$ eV $D_{GB}/D_{Bulk}=6.7 \times 10^{-1}$; $EB_B=0.81$ eV $D_{GB}/D_{Bulk}=1.9 \times 10^{-6}$ | $EB_F=EB_B=0.23$ eV $D_{GB}/D_{Bulk}=1.1 \times 10^4$ |
| $\Sigma 5\text{-}\{310\}$ | $EB_F=EB_B=0.51$ eV $D_{GB}/D_{Bulk}=0.2$ | $EB_F=0.46$ eV $D_{GB}/D_{Bulk}=1.4$; $EB_B=0.79$ eV $D_{GB}/D_{Bulk}=4.3 \times 10^{-6}$ | $EB_F=EB_B=0.5$ eV $D_{GB}/D_{Bulk}=3.1 \times 10^{-1}$ |

| GB | X_B | Y_B | Z_B |
|----------------------------|---|---|--|
| $\Sigma 11\text{-}\{332\}$ | $EB_F=EB_B=0.3$ eV $D_{GB}/D_{Bulk}=7.3 \times 10^2$ | $EB_F=0.46$ eV $D_{GB}/D_{Bulk}=1.4$; $EB_B=0.53$ eV $D_{GB}/D_{Bulk}=9.8 \times 10^{-2}$ | $EB_F=EB_B=0.22$ eV $D_{GB}/D_{Bulk}=1.6 \times 10^4$ |
| $\Sigma 5\text{-}\{310\}$ | $EB_F=EB_B=0.3$ eV $D_{GB}/D_{Bulk}=7.3 \times 10^2$ | $EB_F=0.46$ eV $D_{GB}/D_{Bulk}=1.4$; $EB_B=0.7$ eV $D_{GB}/D_{Bulk}=1.4 \times 10^{-4}$ | $EB_F=EB_B=0.45$ eV $D_{GB}/D_{Bulk}=2$ |

The hydrogen atom in all GBs ($\Sigma 3\text{-}\{111\}$, $\Sigma 11\text{-}\{311\}$, $\Sigma 5\text{-}\{310\}$ and $\Sigma 11\text{-}\{332\}$) can easily move from the nickel bulk to the GB core ($EB_F \approx 0.47$ eV). GBs such as $\Sigma 11\text{-}\{311\}$, $\Sigma 5\text{-}\{310\}$ and $\Sigma 11\text{-}\{332\}$ prevent the hydrogen atom moving from the GB core to the bulk ($EB_B > 0.47$ eV), however $\Sigma 3\text{-}\{111\}$ GB act as the bulk has little influence on this direction.

Figure 4.26 illustrates a distinction (bulk red line) between the accelerated diffusion and the trapping in segregation sites type A and B for different GBs. High energy/excess volume GBs ($\Sigma 11\text{-}\{332\}$ and $\Sigma 5\text{-}\{310\}$) have one or two accelerated diffusion path(s) where the hydrogen atom moves $10^3 \sim 10^4$ faster than the diffusion in the nickel bulk. Indeed, $\Sigma 11\text{-}\{332\}$ is a GB that have more segregation sites in the GB core with two accelerated diffusion paths, and none of these segregation sites has the trapping behavior. While GB $\Sigma 5\text{-}\{310\}$ has only one accelerated diffusion path and the deepest segregation site in this GB is a trapping position the for hydrogen atoms. $\Sigma 11\text{-}\{311\}$ GB presents no accelerated diffusion paths but the tapping sites in the GB core. Similar results in GBs $\Sigma 11\text{-}\{311\}$ and $\Sigma 3\text{-}\{111\}$ have been reported by Du *et al.* [Du2011] in γ -Fe based on the DFT calculations.

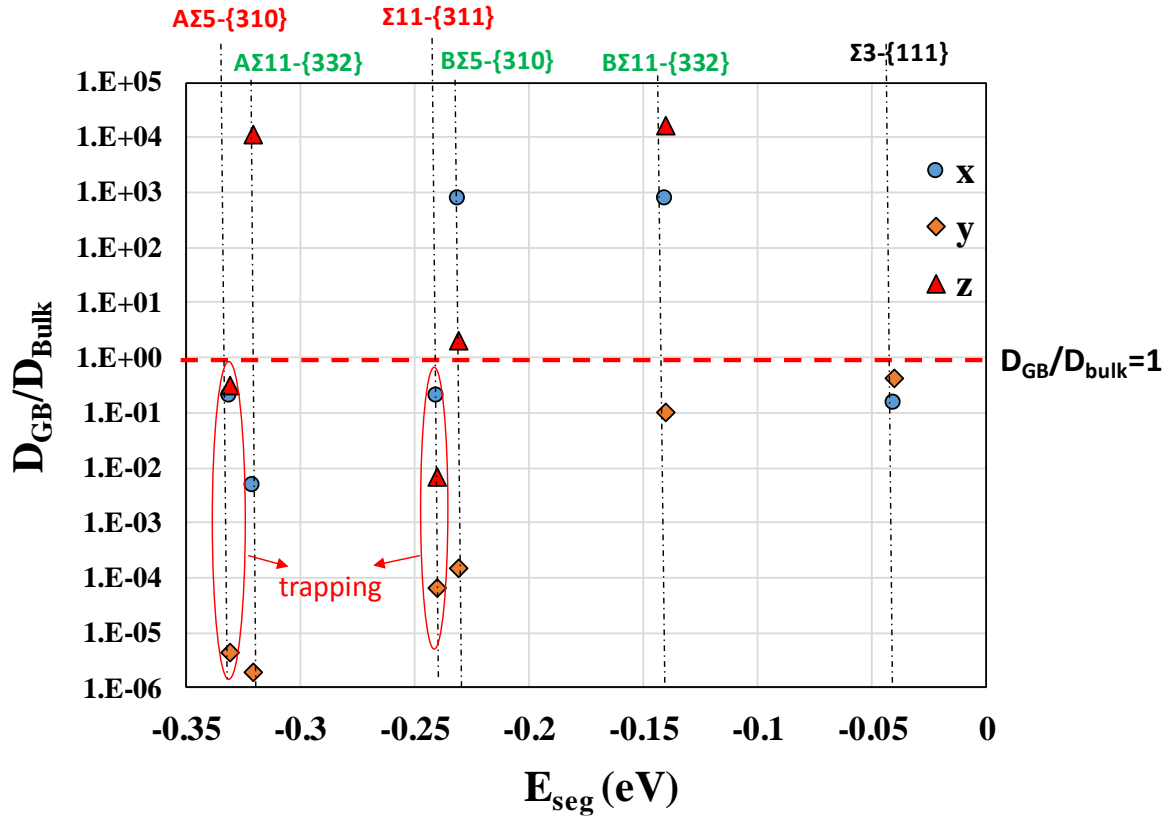


Figure 4.26 – The diffusion coefficient ratio as a function of the hydrogen segregation energy following x, y and z directions for different GBs. Green: GBs have accelerated diffusion path(s), Red: GBs have trapping sites, and Black: GB is similar as the nickel bulk.

IV. Experimental approaches

The experimental tests have been carried out to evaluate the impact of the grain boundary character on the hydrogen trapping and diffusion process. At first, we were interested in the role played by the twin grain boundaries and more precisely the impact of different types of GB on the hydrogen trapping. Thus, we have re-analyzed the results obtained in the thesis of Osman Hoch [Osman Hoch2015] in order to identify the different types of boundaries, a correlation was made with the results of the ToF-SIMS analyzes. In a second step, we have investigated the influence of different types of grain boundaries (or different excess free volume GBs) on the hydrogen transport in bi crystal systems. The accelerated and anisotropic diffusion have been discussed with FEM approaches, moreover, the influence of the stress state on the diffusion process near a GB has been studied based on the dislocation tilt boundary model.

IV. 1 Hydrogen - twin boundaries in nickel polycrystals

This part has been already mentioned in *Chapter I* concerning the influence of Random ($\Sigma > 29$) and Special ($\Sigma < 29$) grain boundaries on the hydrogen trapping processes. The electrochemical hydrogen charging tests were conducted on several polycrystalline nickel samples with grain size 18 and 45 μm . These samples were previously analyzed by EBSD to identify the Random and Special grain boundaries (*figure 4.27*). Micro-hardness indentation were used to identify the different GB areas analyzed by EBSD, a correlation with the hydrogen concentration profile obtained by ToF-SIMS (*figure 4.27(d)*) made it possible to evaluate the influence of these two families of grain boundaries on the trapping of hydrogen.

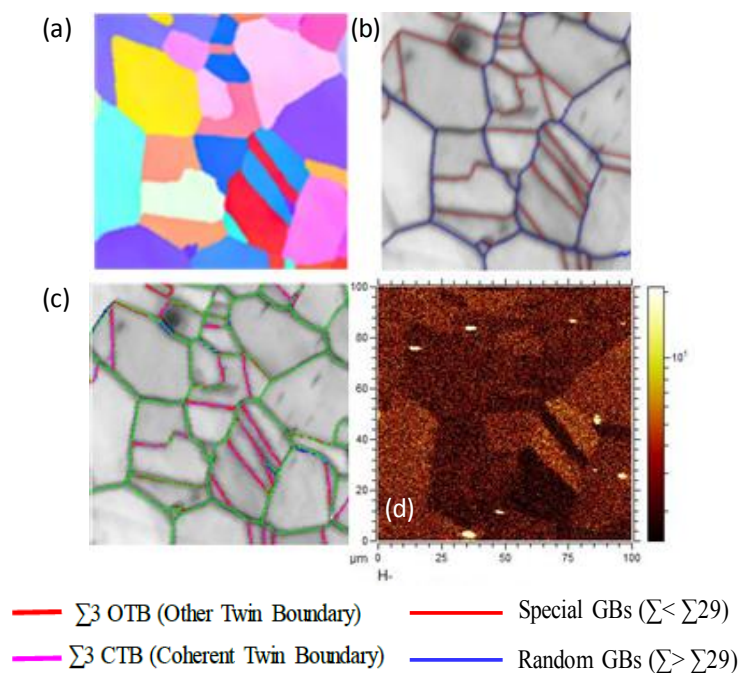


Figure 4.27 – (a) EBSD scan of a polycrystalline nickel, (b) nature of GBs Special/Random, (c) nature of twin GBs coherent and incoherent, (d) hydrogen concentration distribution by ToF-SIMS

The results of this study have shown that the majority of the special grain boundaries have a hydrogen concentration gradient as profile (*Figure 4.28*), whereas this profile is mostly in the form of a gap in the case of Random grain boundaries. [Oudriss2016]. This result allowed to associate the hydrogen trapping to the Special grain boundaries. However, this family of grain boundaries in polycrystalline nickel sample is composed mostly by twin GBs, and these GBs can be latter defined in two categories: coherent and incoherent.

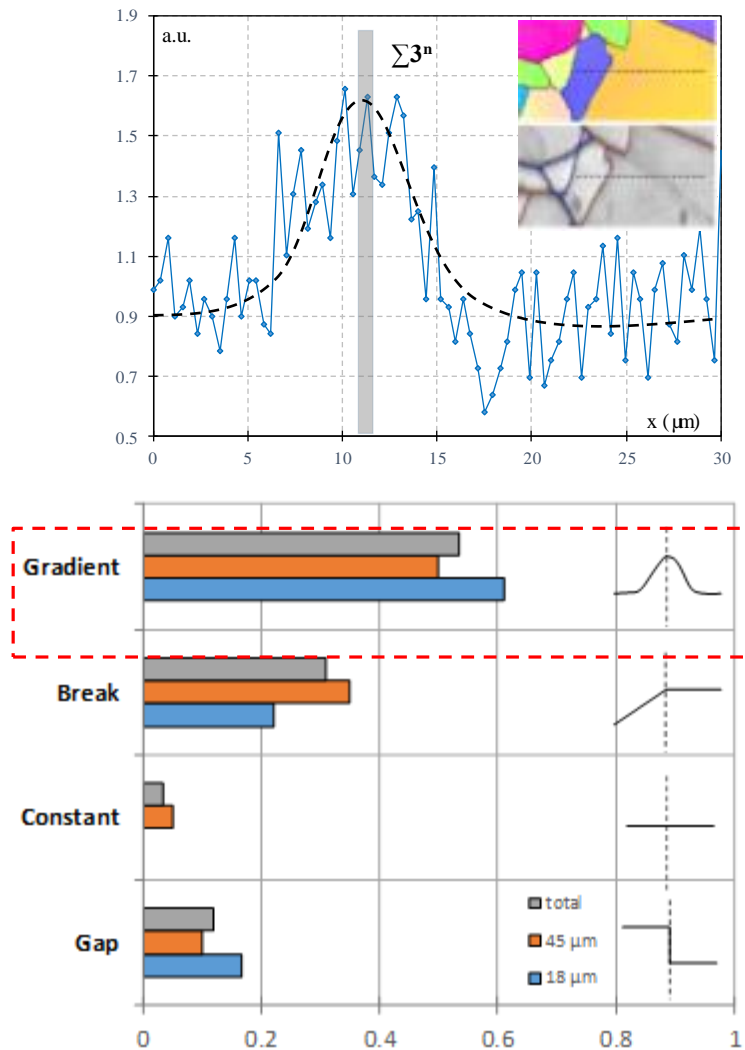


Figure 4.28 – (a) The gradient profile of hydrogen concentration obtained by ToF-SIMS, (b) The hydrogen distribution profile for Special GBs [Osman Hoch2015, Oudriss2012c]

In order to gather more GB information, we proposed to refine these results and to focus more particularly on twin GBs which represent the great majority of Special joints. Thus, using TSL-OIM software, we have identified coherent twin boundary (CTB) and other twin boundary (OTB) according to the two criteria:

- 1) The orientation of the twin is related to the parent with a specific misorientation. For example, the primary recrystallization twin in a face-centered-cubic material is related to the parent by a 60° rotation about the $\langle 111 \rangle$ crystal direction.
- 2) The twinning plane must be aligned with the boundary plane separating the twin from the parent.

Twin boundaries which satisfy the first criterion but not the second are sometimes called incoherent twins, and GBs that satisfy both criteria are coherent twins. Once this analysis was performed, we

correlated the hydrogen concentration profiles obtained by ToF-SIMS with all Special grain boundaries. The results obtained are represented in the form of a histogram.

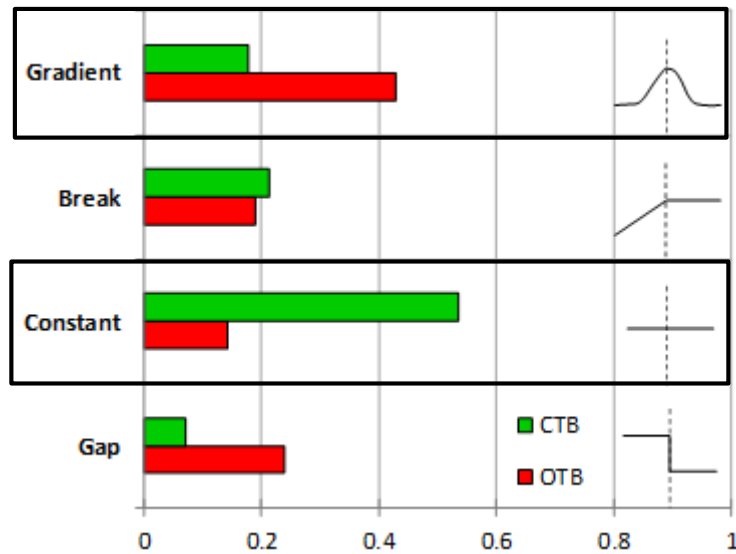


Figure 4.29 - The hydrogen distribution profile for different GB fractions with types CTB and OTB

Considering the hydrogen local profiles around CTB and OTB, a constant for the hydrogen concentration distribution was mainly detected near CTB. In opposite, when OTB fraction is significant a gradient of hydrogen was observed, which can be explained by the hydrogen trapping. This result indicates that the CTB is similar as the crystal bulk, GB segregation or diffusion effect is neglected in this type of GB. These results are in good agreement with our atomistic calculations on the $\Sigma 3\text{-}\{111\}$ (CTB GB).

IV. 2 Hydrogen - GBs in nickel bi crystals

The hydrogen transport in bi crystals and single crystals were compared by hydrogen charging/TDS, the hydrogen charging condition is given in *figure.4.30* to ensure the saturation of hydrogen content. The influence of grain boundaries on the hydrogen transport in nickel is indicated by the difference of hydrogen solubility, due to the production process for nickel bi crystals (see chapter 2), 1-2 wppm initial hydrogen concentration is already present in these samples.

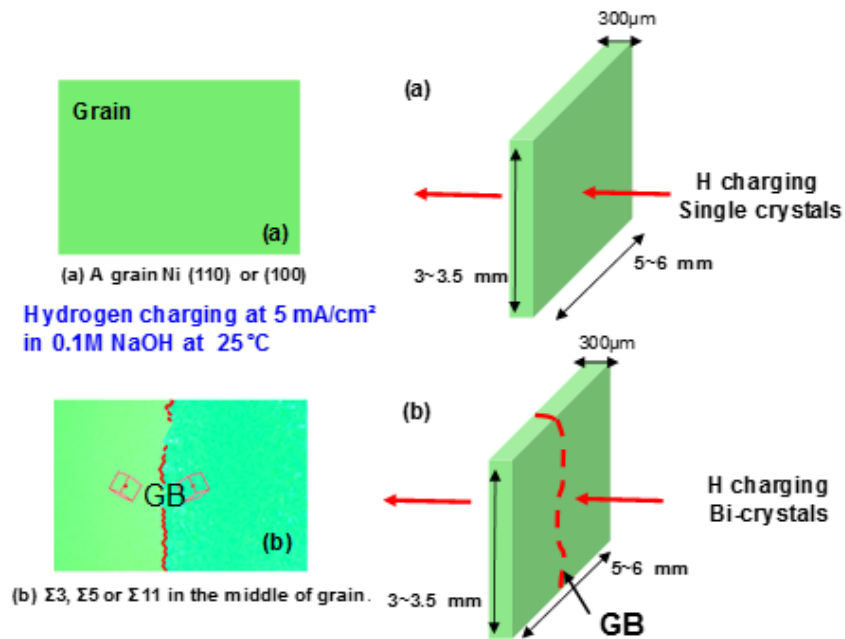


Figure 4.30 – Hydrogen charging conditions for nickel single and bi crystals

The hydrogen solubility as a function of the charging time is given in the *figure 4.31* for the GB $\Sigma 11$ - $\{332\}$ and its grain (equivalent to a single crystal nickel (110)), we keep the same evolution as in the study of the hydrogen solubility for nickel (100) in *chapter 3*. The first result indicates that the bi crystals with a GB $\Sigma 11$ - $\{332\}$ in the center decrease the solubility in comparing to the single crystals, we then choose a charging time around 3 days to compare the hydrogen solubility at the steady state for all types of bi crystals.

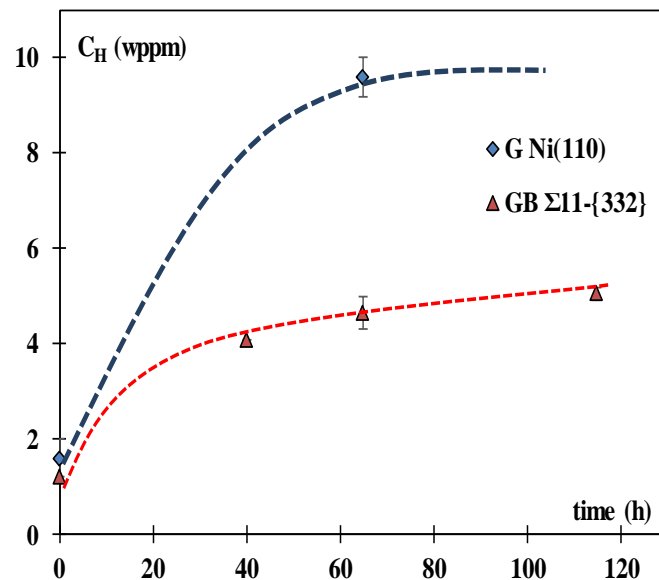


Figure 4.31 – Hydrogen solubility in Grain (nickel (110)) and bi crystals ($\Sigma 11$ - $\{332\}$) vs the charging time

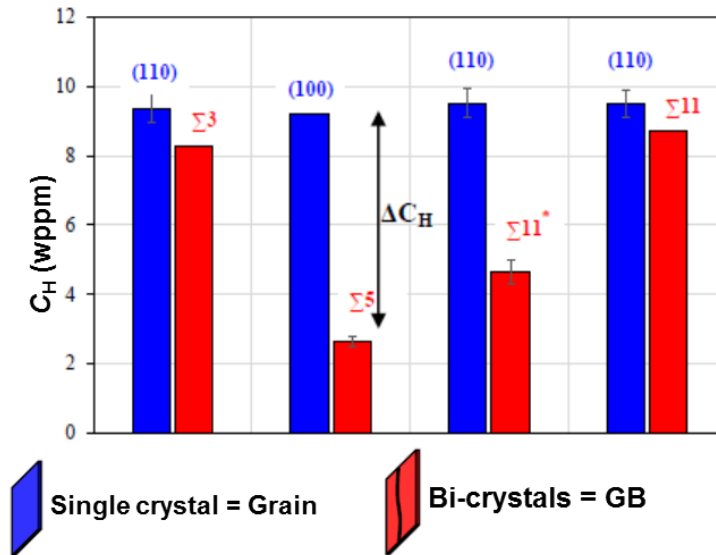


Figure 4.32 – Hydrogen solubility in nickel single and bi crystals after 3 days charging

The difference of hydrogen solubility between single and bi crystals is given in *figure 4.32*, the result shows that different GBs have very different impacts on the hydrogen transport process in nickel, particularly the GBs ($\Sigma 11\text{-}\{332\}$ / $\Sigma 11^*$ and $\Sigma 5\text{-}\{310\}$ / $\Sigma 5$) have sharply decreased the hydrogen solubility in the whole sample.

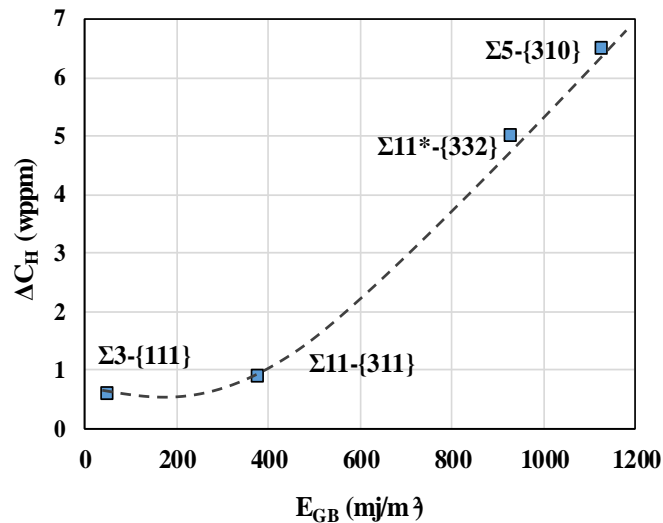


Figure 4.33 – The difference of hydrogen solubility between single and bi crystals as a function of the GB energy.

Figure 4.33 gives a correlation between the solubility difference and the GB energy. High energy/excess volume GBs are more pronounced for their impacts on the hydrogen solubility. These two GBs provide accelerated diffusion paths in the GB core, this point will be discussed later in the following section (IV. 3 FEM approaches).

IV. 3 FEM approaches

IV. 3.1 Pure diffusion

Since high energy GBs have significant influence on the hydrogen solubility, the first part of this study is to investigate if their accelerated diffusion paths are strong enough to change the whole solubility in the sample. We only considered here the anisotropic diffusion in bi crystals based on the experimental data from EP for single crystals and the atomic calculations of the diffusion in GBs. The apparent diffusion tensor was established for nickel single crystals based the crystallographic orientations ([100], [010],[001] in Chapter 3), this tensor is then rotated with a misorientation angle of GB in order to get a fitting to its grain orientations, the diffusion tensors in the grains are given for bi crystals with GBs $\Sigma 11$ -{332} and $\Sigma 5$ -{310}:

$$\overline{\overline{D'}} = \overline{\overline{R}}^T \overline{\overline{D}} \overline{\overline{R}}$$

For GB $\Sigma 5$ -{310}, the rotation is 36.86989 degree around Z direction [001] (see chapter 2)

$$\overline{\overline{D'}} = \begin{pmatrix} 10.8 & 1.4 & 7 \\ 1.4 & 1.2 & 1 \\ 7 & 1 & 6 \end{pmatrix} = \begin{pmatrix} \cos 36.87 & -\sin 36.87 & 0 \\ \sin 36.87 & \cos 36.87 & 0 \\ 0 & 0 & 1 \end{pmatrix}^T \times \begin{pmatrix} 6 & 5 & 5 \\ 5 & 6 & 5 \\ 5 & 5 & 6 \end{pmatrix} \times \begin{pmatrix} \cos 36.87 & -\sin 36.87 & 0 \\ \sin 36.87 & \cos 36.87 & 0 \\ 0 & 0 & 1 \end{pmatrix}$$

For GB $\Sigma 11$ -{332}, the first rotation is 45 degree around Z direction [001] to get the plan {110} and then a rotation 129.52 degree around Y' direction. An illustration of direction indices for the construction of the GB $\Sigma 11$ is given in *figure 4.34*, the misorientation angle 129.52 degree corresponds to the GB plan {332} and the misorientation angle 50.48 degree corresponds to the GB plan {311}.

$$\overline{\overline{A}} = \begin{pmatrix} \cos 45 & -\sin 45 & 0 \\ \sin 45 & \cos 45 & 0 \\ 0 & 0 & 1 \end{pmatrix}^T \times \begin{pmatrix} 6 & 5 & 5 \\ 5 & 6 & 5 \\ 5 & 5 & 6 \end{pmatrix} \times \begin{pmatrix} \cos 45 & -\sin 45 & 0 \\ \sin 45 & \cos 45 & 0 \\ 0 & 0 & 1 \end{pmatrix}$$

$$\overline{\overline{D'}} = \begin{pmatrix} 14.84 & 0 & -3.6 \\ 0 & 1 & 0 \\ -3.6 & 0 & 1.9 \end{pmatrix} = \begin{pmatrix} \cos 129.52 & 0 & \sin 129.52 \\ 0 & 1 & 0 \\ -\sin 129.52 & 0 & \cos 129.52 \end{pmatrix}^T \times \overline{\overline{A}} \times \begin{pmatrix} \cos 129.52 & 0 & \sin 129.52 \\ 0 & 1 & 0 \\ -\sin 129.52 & 0 & \cos 129.52 \end{pmatrix}$$

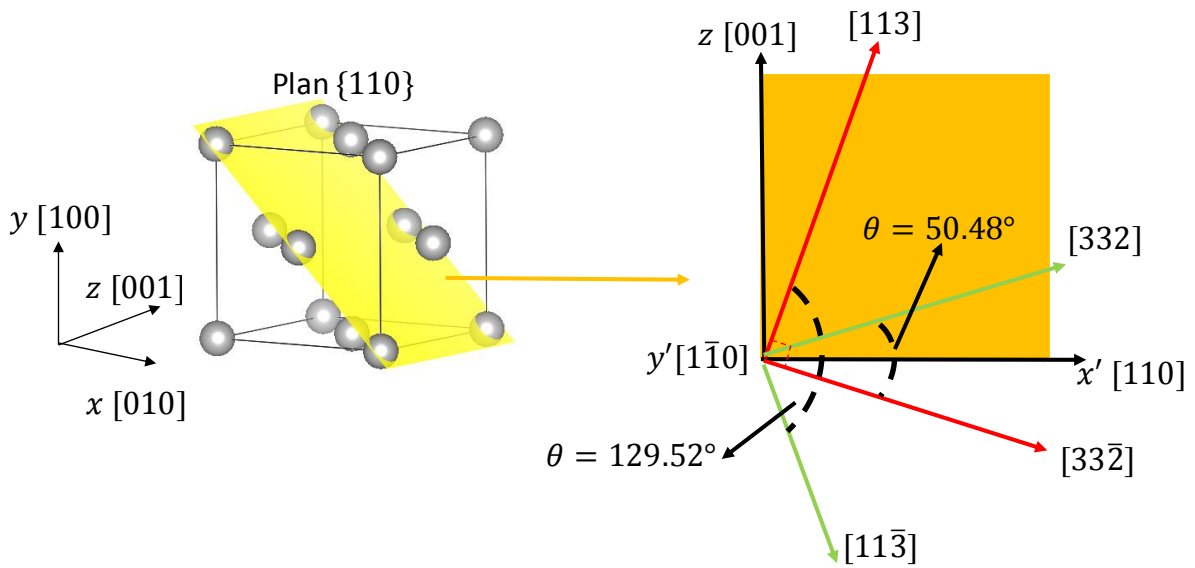


Figure 4.34 – An illustration of direction indices for the construction of the GB $\Sigma 11$.

The atomic calculation shows that GBs can provide accelerated diffusion paths following the x and z directions. The pure diffusion of hydrogen in bi crystals are then simulated with different cases. *Figure 4.35* presents the hydrogen concentration distribution in the membrane. The x direction in the GB is a fast diffusion path, however its influence on the whole membrane can be neglected since the GB fraction is really low. The z direction is the concentration gradient direction. The diffusion is faster following this direction but the concentration distribution at the steady state is the same as in the single crystals. In other words, this type of GB helps to achieve the steady state sooner but has little influence on the whole solubility in the membrane. *Figure 4.36* gives the evaluated hydrogen solubility in the whole membrane for single and three bi crystals cases. The x diffusion is the fast path is similar as the case of GB $\Sigma 5$ -{310}, the GB $\Sigma 11$ -{332} provides the x and z as two fast diffusion paths, and the last case considers that the diffusion is accelerated for all directions in GB. The comparison of hydrogen diffusion between single and bi crystals indicates that the pure GB diffusion has little influence on the whole solubility in the membrane due to its low volume fraction.

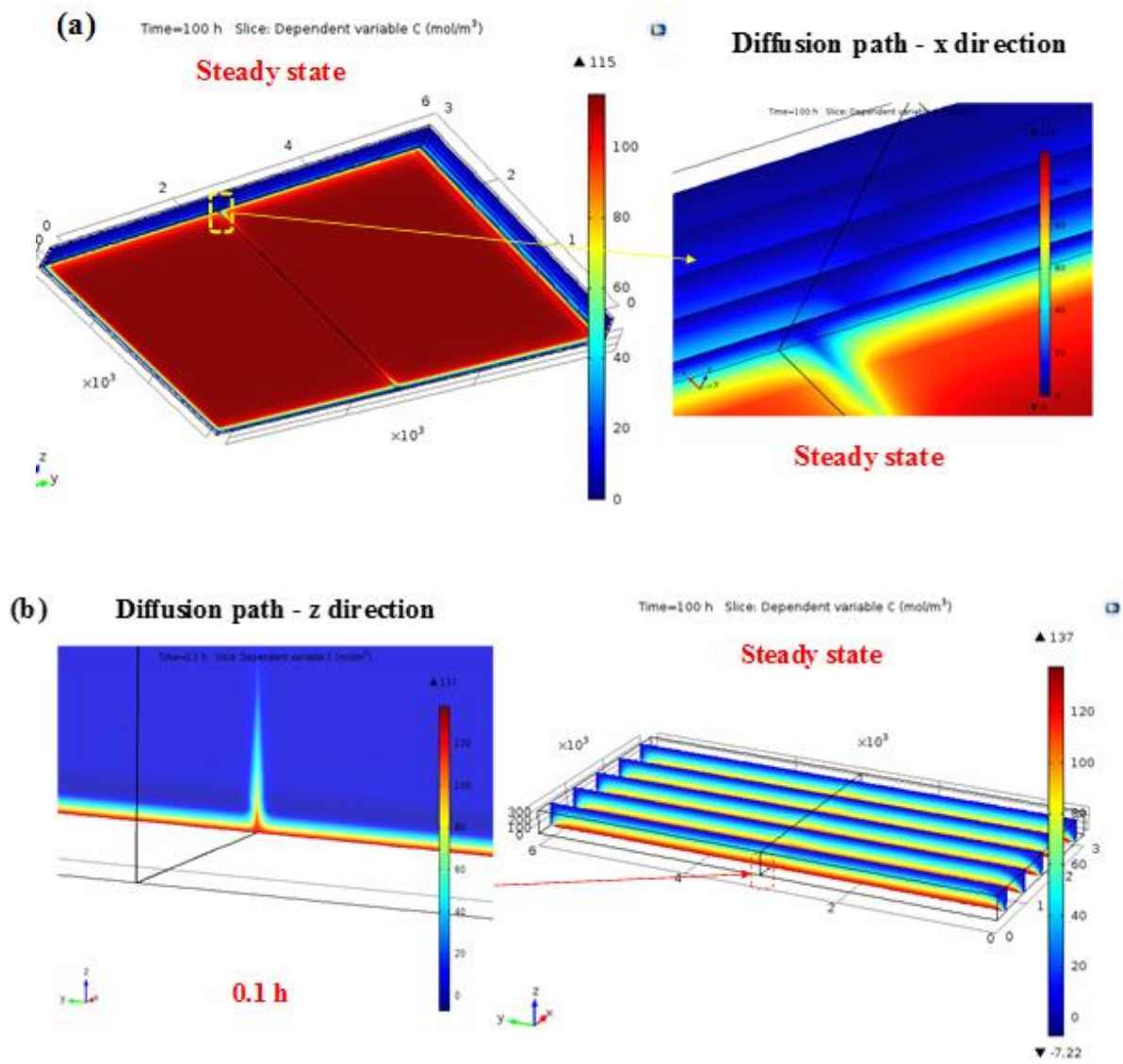


Figure 4.35 – The hydrogen concentration distributions in bi crystals – (a) x diffusion path, (b) z diffusion path

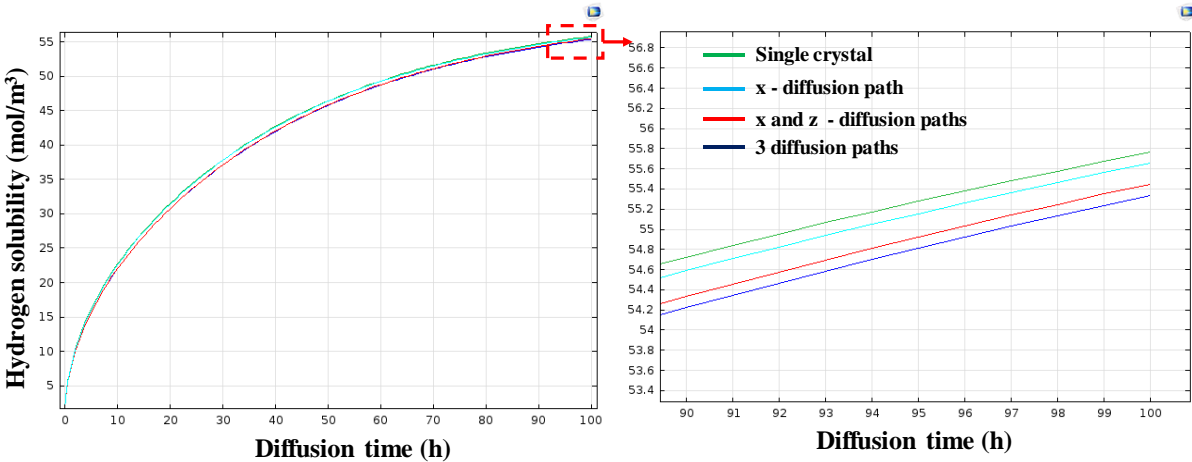


Figure 4.36 – The hydrogen solubility in single and bi crystals vs diffusion time, the results of bi crystals are distinguished by three different diffusion conditions in GB.

We consider now in an extreme case that the diffusion coefficient in GB is infinitely high as an open space, and the hydrogen solubility in membrane is influenced by the scale effects. A scheme of the scale ratio of width/thickness is given in *figure 4.37 (a)*. The reference case considers that there is only one input/output face following the diffusion direction. Then, the hydrogen can enter from one input face and get out from all other faces considering now the scale effects. *Figure 4.37 (b)* gives the relationship between the hydrogen solubility in the whole membrane and the scale ratio by modifying the width distance for different desorption times. The initial state is at the steady state, the desorption is dependent on the solubility at the steady state but is little influenced by the scale effects. For high scale ratios, the solubility in the membrane is close to the reference case, the scale effects are more pronounced for lower scale ratios ($R < 10$) for which the solubility is sharply decreased. However the scale ratio of our experimental sample's dimension is $R = 200$ and the scale effects are not significant.

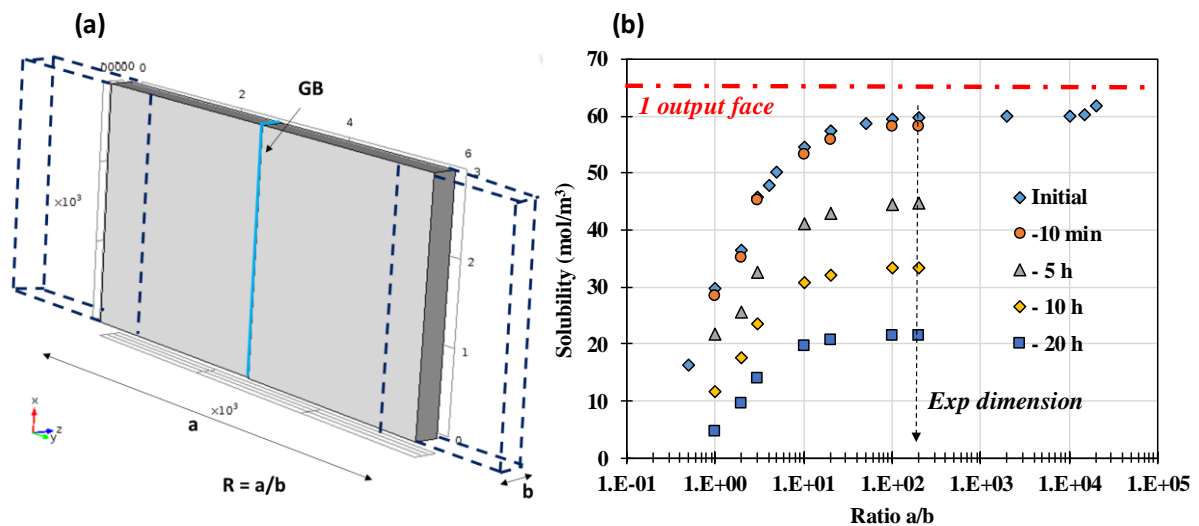


Figure 4.37 – (a) schema of the scale ratio of width/thickness, (b) the hydrogen solubility vs the scale ratio for different desorption times.

Since the GB fraction is really small in bi crystals, the GB diffusion alone is limited to have a significant influence on the hydrogen solubility in the whole sample. *Chapter 3* has highlighted the importance of structural defects and stress state on the hydrogen transport process in nickel, thus some points can be figured out:

- Stress state near GB
- Hydrogen induced vacancy formation near GB
- Hydrogen-dislocation interactions near GB (real GB is full of dislocations)

IV. 3.2 Stress near GB

Since the stress state modifies hydrogen diffusion significantly, we consider here a second stress gradient near the GB. We started from the relationship of the hydrogen flux, which is proportional to the gradient of the chemical potential, and is reduced by hydrostatic stress. So the following expression is obtained:

$$J = -\frac{DC}{RT} \nabla \mu \quad (\text{Eq.4.13})$$

Where C is the hydrogen concentration, D is the diffusion coefficient of hydrogen and μ is the chemical potential defined as follows:

$$\mu = \mu_0 + RT \ln(C) - \sigma_H V_H \quad (\text{Eq.4.14})$$

V_H is the partial molar volume of hydrogen in the metal, σ_H the hydrostatic stress, and the mass balance of total hydrogen might be expressed as:

$$\frac{dC}{dt} + \nabla \cdot J = 0 \quad (\text{Eq.4.15})$$

The combination of equations (Eq.4.13) (Eq.4.14) and (Eq.4.15) gives [Li1966, Bockris1971, Charles2017]:

$$\frac{dC}{dt} - \nabla \cdot (\overline{\overline{D}} \nabla C) + \nabla \cdot \left(\frac{CV_H}{RT} \overline{\overline{D}} \nabla \sigma_H \right) = 0 \quad (\text{Eq.4.16})$$

Now, we introduce the stress σ_H near the GB. It is not possible to get an experimental measurement on the stress state near a GB. The basic idea here is to access an estimation for the stress level based on the models of dislocation for pure tilt GB [Hirth1982, Reed-Hill2009, Priester2013]. By definition, GBs separate stress-free crystallites and do not produce long-range stress fields. The stress components are given as:

$$\sigma_{xx} = -\sigma_0 \sin 2\pi X (\cosh 2\pi Y - \cos 2\pi X + 2\pi Y \sinh 2\pi Y) \quad (\text{Eq.4.17})$$

$$\sigma_{yy} = -\sigma_0 \sin 2\pi X (\cosh 2\pi Y - \cos 2\pi X - 2\pi Y \sinh 2\pi Y) \quad (\text{Eq.4.18})$$

$$\sigma_H = \frac{1}{3} (\sigma_{xx} + \sigma_{yy}) \quad (\text{Eq.4.19})$$

Where

$$\sigma_0 = \frac{\mu b}{2D(1-\nu)(\cosh 2\pi Y - \cos 2\pi X)^2} \quad (\text{Eq.4.20})$$

$X = x/D$, and $Y=y/D$. D is the distance between adjacent tilt GB dislocations (*figure 4.38*), μ the shear modulus ($\mu = 76$ GPa), ν Poisson's ratio ($\nu=0.31$), b the burger vector ($b = 0.3$ nm).

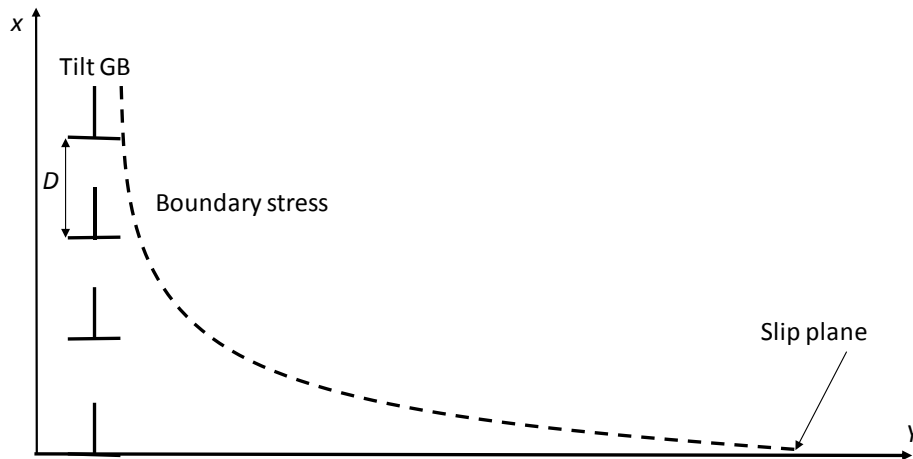


Figure 4.38 – GB stress profile based on the dislocation model.

The boundary hydrostatic stress distribution (absolute value) is given in *figure 4.39*. The stress level near the GB can achieve ~10 GPa and the stress zone is only ~ 10 nm. Considering the GB size in the bi crystal model is 1 μm , the stress zone is proportional to ~10 μm according to this dislocation model.

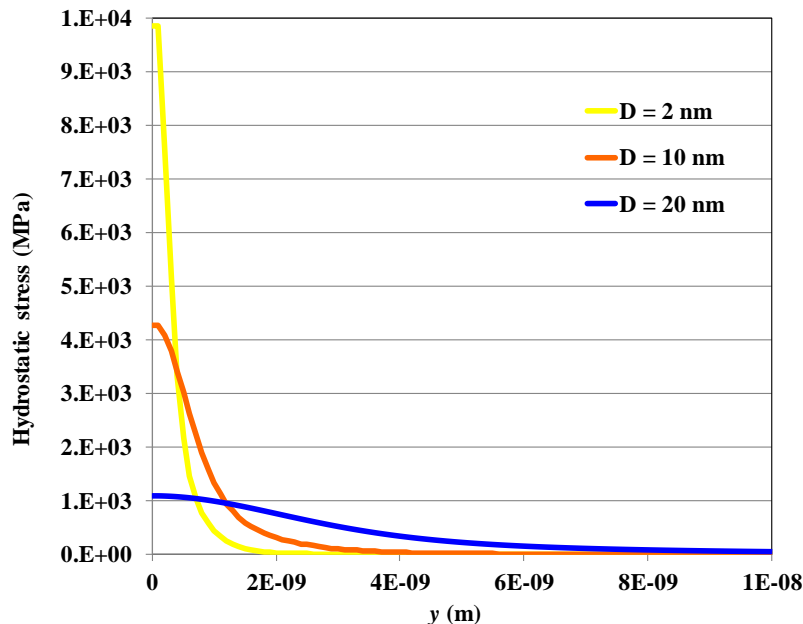


Figure 4.39 – GB stress profile based on the dislocation model for different distance between adjacent dislocations.

In order to fit the bi crystal model with the boundary stress distribution, we consider here the Gaussian distribution which is similar as the boundary stress distribution:

$$S(y) = A \exp\left(-\frac{(y-y_0)^2}{2\sigma^2}\right) \quad (\text{Eq.4.21})$$

A is the stress amplitude, y_0 is the GB position and σ is a factor to modify the stress distribution. This stress function (*figure 4.40*) is applied into equation (Eq.4.16) for the new diffusion simulation. The objective is to investigate the influences of the stress zone size and the stress amplitude on the diffusion process.

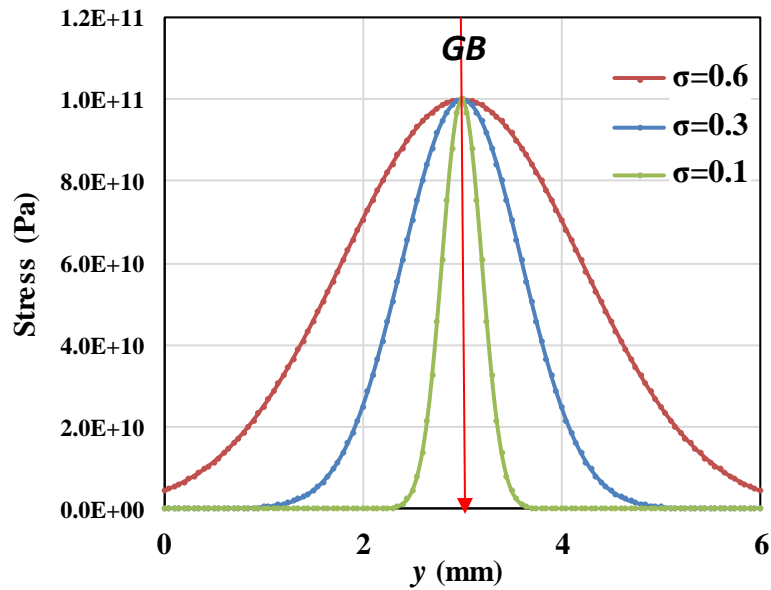


Figure 4.40 – Stress distribution around GB at $y_0 = 3$ mm based on Eq (4.21).

Figure 4.41(a) illustrates that the hydrogen diffusion now is under the influence of two different gradients: the concentration and the stress. A part of the hydrogen concentration following the stress gradient is brought to the GB. Considering the stress level of the dislocation model near the GB is ~ 10 GPa, *figure 4.41 (b)* gives the hydrogen solubility as a function of the diffusion time for different stress zone sizes. Larger stress zone size assists the reduction of the hydrogen whole solubility in the membrane.

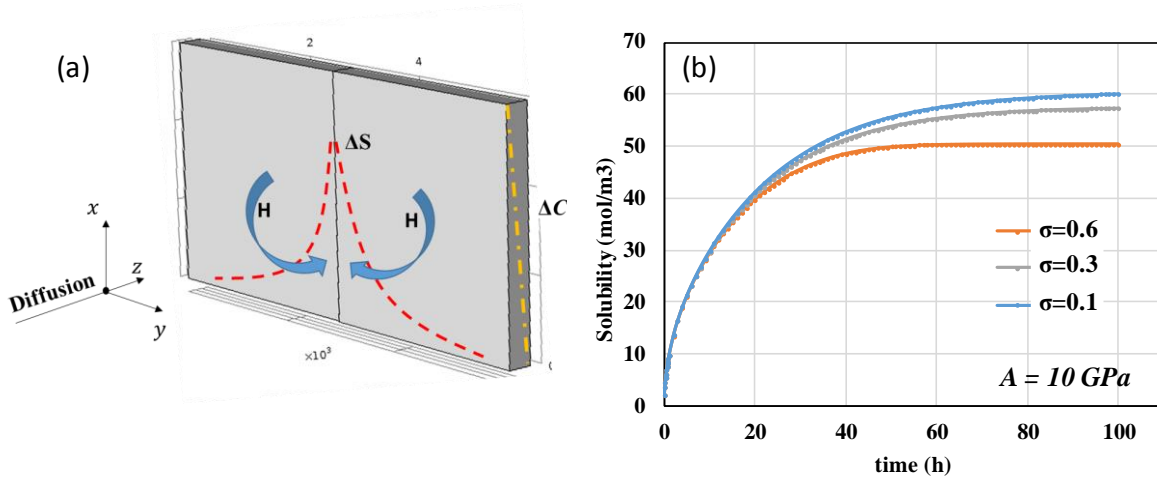


Figure 4.41 – (a) Schematic of two gradients (concentration and stress) in bi crystal model, (b) the hydrogen solubility vs diffusion time for different stress zone sizes.

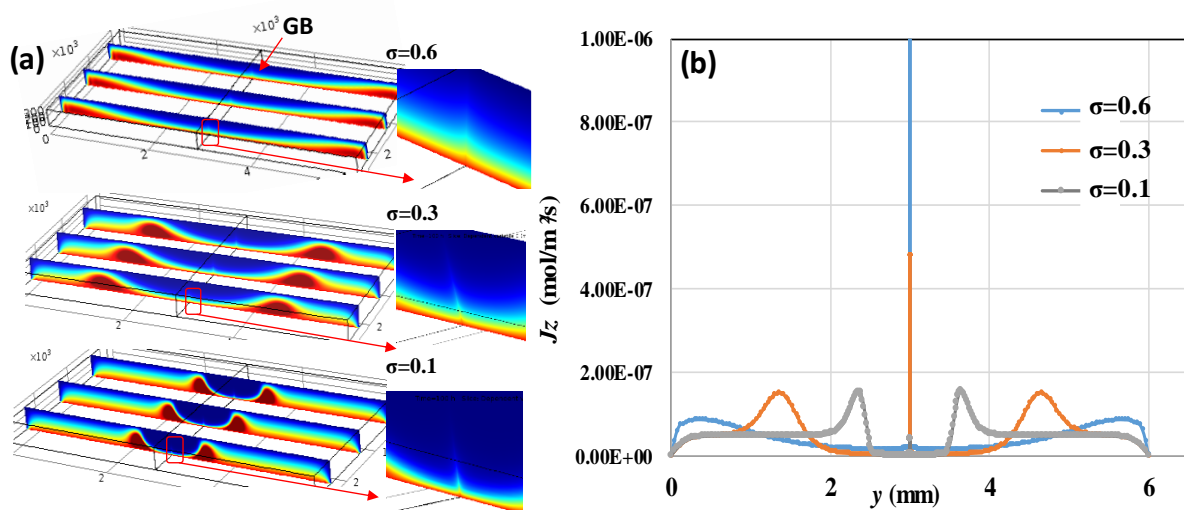


Figure 4.42 – (a) The hydrogen concentration distribution in the membrane, (b) the diffusion flux J_z at the output face following z direction.

The concentration distribution in the membrane is given in *figure 4.42(a)*, the stress zone evacuate the hydrogen concentration towards the GB and the opposite sides, *figure 4.42 (b)* presents the flux J_z on the output side at the steady state. We can see that, the flux is maximum at the GB and minimum in the stress zone. Actually, the concentration distribution or the diffusion flux is directly influenced by the stress gradient (*figure 4.43*), the stress gradient is a symmetry profile around the GB. For a high enough stress level, the concentration distribution is dominated by the length scale of the stress gradient rather than the length scale of the stress zone and the diffusion flux is directed affected by the stress gradient level.

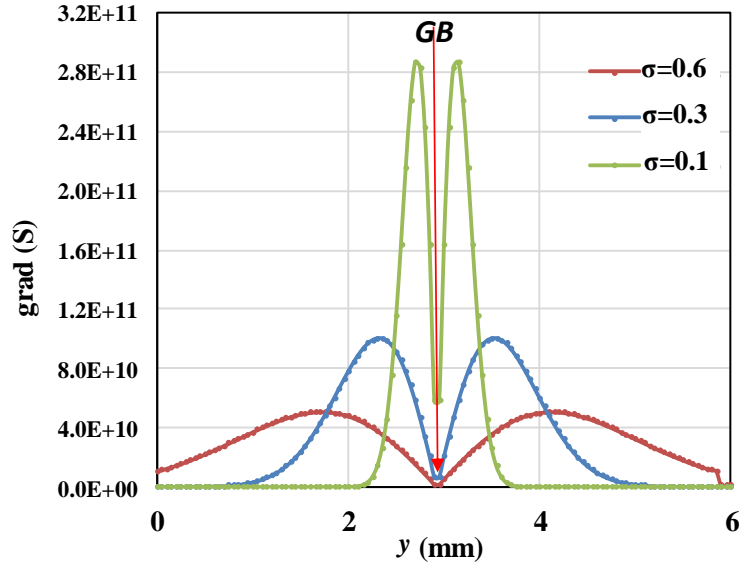


Figure 4.43 – The stress gradient distribution around GB at $y_0 = 3$ mm.

Experimental data indicated that a bi crystal can decrease half hydrogen solubility comparing to a single crystal. This diffusion model considering a Gaussian stress distribution near the GB shows that the experimental data could be fitted at the conditions ($\sigma > 0.6$ and $A > 50$ GPa). However, there is no support that the GB can provide long range stress, ~ 10 μm according to the dislocation model. Furthermore, the stress level higher than 50 GPa seems not reasonable.

Another exponential function has been studied and is given as:

$$S(y) = A \exp\left(-\frac{|y|}{\sigma}\right) \quad (\text{Eq.4.22})$$

y is the GB center here, this exponential function has an objective to modify the stress gradient distribution, and the gradient is particularly centered on the GB. The stress profile near the GB is illustrated in *figure 4.44(a)*, the stress level decreases faster than the Gaussian distribution and the stress gradient has the maximum gradient level near the GB. This function can achieve a decrease of the hydrogen solubility in the whole membrane, however due to the small size of the stress gradient zone (*figure 4.44(b)*), the solubility reduction cannot achieve the experimental observations. This result shows that the influence of the length scale of the stress gradient is more important than the gradient level on the hydrogen concentration distribution.

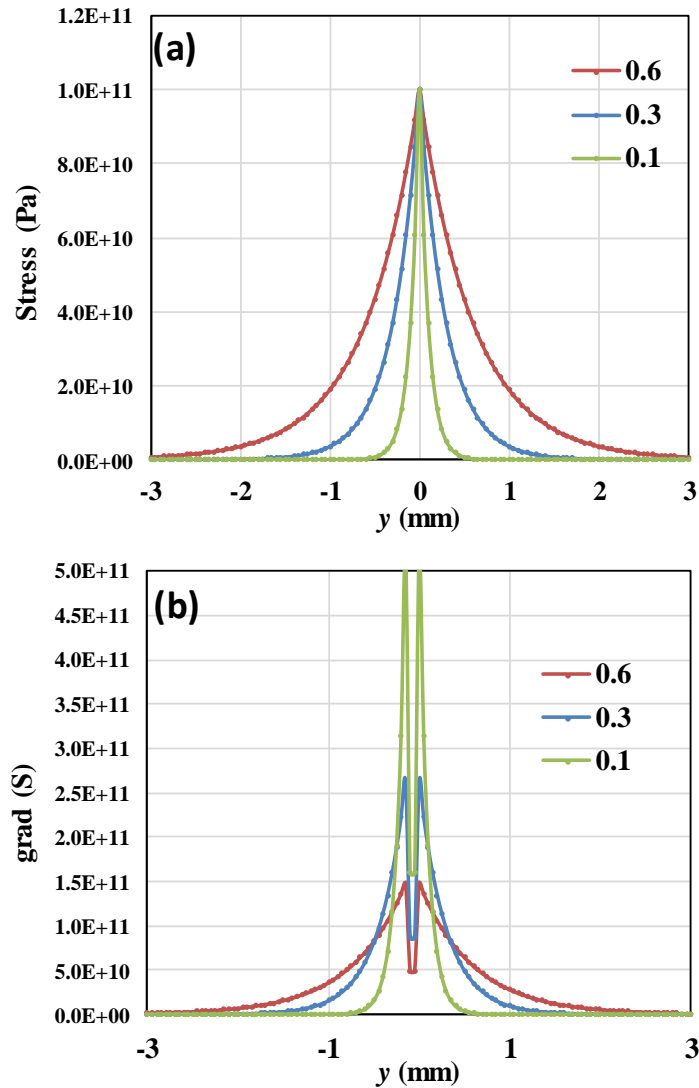


Figure 4.44 – (a) Stress distribution around GB at $y_0 = 0$ mm based on Eq. (4.22). (b) The stress gradient distribution around GB at $y_0 = 0$ mm.

The stress distribution near the GB can modify the hydrogen concentration distribution according to the nature of the stress gradient (zone size and its level). Despite the reduction of the hydrogen solubility in the whole membrane, the experimental observations about the solubility decrease cannot be fully explained. We may consider the influences of microdefects such as vacancies and dislocations on the hydrogen transport in GBs. Previous chapter has demonstrated that the clusters of vacancies have been formed with the hydrogen charging in nickel, and the anisotropic diffusion of hydrogen in the nickel bulk is actually dominated by the clusters of vacancies. In addition, some atomic calculations have indicated that vacancy is easier formed in GB than in the bulk, and the dislocation is also more active in the GB. All these defects could lead to an anisotropic modification of the apparent diffusion coefficient and the stress state, thus a new approach concerning the defects impacts needs to be developed.

V. Summary

The first part of this chapter has focused on the atomic calculations of GBs and their interactions with a hydrogen atom. The GBs with lower energy have a more compact GB plane configuration and low excess volume, in addition, the GB energy increases linearly with the excess volume. The hydrogen atom was inserted at the different positions in GBs in order to investigate the local segregation state, the high excess volume GBs provide more stable segregation sites and have larger GB thickness from an energy point of view. All segregation sites close to the GB core region have a higher atomic volume and a more stable segregation state.

Actually, the hydrogen Voronoi volume at the octahedral site in nickel bulk is a cubic form, the volume geometry for hydrogen atom located close to the GB core region is more or less deformed. The hydrogen segregation is extremely dependent on the local environment, in particular, we have noticed that a part of data of the segregation energy have often a linear evolution with the atomic volume or the hydrogen atom energy, these segregation sites are a similar cubic form with a relatively low hydrogen atomic volume. From a mechanical point of view, the hydrostatic stress is high at these low hydrogen atomic volume sites with a quite “compact environment”. At these cubic form or similar sites, the deviatoric stress is low due to the small distortion. The linear evolution often disappears at high volume segregation sites in the GB core region, the hydrostatic stress decreases while the deviatoric stress increases due to the high distortion. Furthermore, for all segregation sites, the hydrostatic stress has a linear relationship the hydrogen atom energy which is not the case for the deviatoric stress.

An analytical view of the segregation concentration shows that high excess volume GBs have high segregation densities with various segregation energies. The segregation sites start to be occupied by hydrogen atoms at very low bulk concentration, the segregation occurs first at the most stable position, the less stable positions start to segregate hydrogen atoms when the first most stable position is close to the saturation (70% -80% occupation).

The grain boundary diffusion of hydrogen has been studied by the Nudged Elastic Band (NEB) method to find the minimum energy paths (MEP). The high energy/excess volume GBs ($\Sigma 11\text{-}\{332\}$ and $\Sigma 5\text{-}\{310\}$) have one or two accelerated diffusion path(s) which hydrogen atom moves $10^3 \sim 10^4$ faster than the diffusion in nickel bulk. $\Sigma 11\text{-}\{332\}$ is a GB that have more segregation sites in the GB core with two accelerated diffusion paths, and none of these segregation sites has the trapping behavior. While GB $\Sigma 5\text{-}\{310\}$ has only one accelerated diffusion path, and the most stable segregation site in this GB is a trapping position for hydrogen atoms. GB $\Sigma 11\text{-}\{311\}$ presents no diffusion paths but the trapping sites in the GB core. $\Sigma 3\text{-}\{111\}$ GB acts as the nickel bulk with no trapping or

acceleration effects on the hydrogen transport, this finding is supported by the experimental observation of SIMS.

The hydrogen solubility in bi crystals highlighted the important impacts of GBs on the hydrogen transport, particularly the high energy/excess volume GBs ($\Sigma 11\text{-}\{332\}$ and $\Sigma 5\text{-}\{310\}$) have sharply decreased the hydrogen solubility in the whole bi crystal membrane. The first idea was based on the pure anisotropic and accelerated diffusion in the bi crystal system, however this approach is not able to explain the reduction of the hydrogen solubility in the bi crystal membrane. Moreover, based on the dislocation model of tilt type GB, we have estimated the stress state near the GB and considered the diffusion with a stress gradient. The hydrogen concentration distribution is strongly influenced the length scale of stress gradient and the hydrogen solubility could be decreased with this model. Despite a reduction of the solubility in the whole membrane, this approach cannot give a full explanation due to the unreasonable long range stress near the GB and a high stress level.

From another point of view, the influences of microdefects as vacancy and dislocation on the hydrogen transport in the bi crystal system may be considered. It is demonstrated that the clusters of vacancies have been formed with the hydrogen charging in nickel, the anisotropic diffusion in the nickel bulk is dominated by the clusters of vacancies (chapter 3). In addition, based on some atomic calculations, the literature review has highlighted that vacancy is easier formed in GB than in the bulk, and the dislocation is also more active in the GB. It is worthwhile to investigate the grain boundary structure after the hydrogen charging using TEM or HRTEM, the evolution of these defects may give some new indices on the hydrogen transport process.

Chapter 5.

Conclusions and perspectives

In this study, the mobility of hydrogen in nickel has been studied in two elementary systems: single crystals (crystal lattice) and bi-crystals (different grain boundaries), using a methodology combining experimental tools (electrochemical permeation / TDS, TEM, EBSD) and numerical methods (FEM-COMSOL / EAM-LAMMPS).

The reactions of hydrogen at the nickel surface in the alkaline solution are dominated by the Volmer-Tafel mechanism with the identification of kinetic constants. We have also identified the available charging current density range at room temperature and their equivalent fugacity using a conversion model based on the thermodynamic concept. In addition, at this range of potential, the fugacity is close to the real gas pressure.

At first, the diffusivity and solubility of hydrogen in nickel single crystals have been analyzed using the classic Fick's laws to obtain the apparent diffusion coefficient and compare the calculated hydrogen solubility with experimental data. Within a thermodynamic framework, we have demonstrated that the diffusion can be derived from Fick's laws considering the influences of the solute concentration and the stress state. The anisotropic diffusion in nickel single crystals on different crystallographic orientations arises thus from the elastic anisotropy due to the elastic strain field associated with the insertion of solute atoms, the apparent diffusion coefficients could be ranked as follow: $D\langle 111 \rangle > D\langle 110 \rangle > D\langle 219 \rangle > D\langle 100 \rangle$. This analytical calculation indicates that the anisotropy is actually an anisotropic diffusion acceleration if the solute concentration is high enough, however the hydrogen concentration alone is not able to influence this anisotropic behavior. We have considered the impact of hydrogen on the vacancy formation in nickel with the experimental observation by TEM, the clusters of vacancies are actually the key factor on the anisotropic diffusion in nickel single crystals. This last result is a new illustration of the *superabundant vacancies* SAV concept on the impact of hydrogen on material properties (impact of hydrogen concentration and grain orientation on the apparent diffusivity of the solute).

Secondly, grain boundaries structures have been compared to the experimental and numerical approaches in bi crystal systems. TEM observations show that a real grain boundary is full of dislocations, in addition, since the vacancy formation has been observed in nickel single crystals after the hydrogen charging, it can be expected to have more vacancies near the grain boundary core. It is worthwhile to investigate the grain boundary structure after the hydrogen charging using TEM or HRTEM, unfortunately this objective is not achieved in this study.

Another point of view comes from the atomic calculations of grain boundaries and their interactions with a hydrogen atom. The grain boundaries with lower energy have a more compact grain boundary plane configuration and low excess volume, in addition, the grain boundary energy increases linearly with the excess volume. The high excess volume grain boundaries provide more stable segregation sites and have larger grain boundary thickness from an energy point of view. All segregation sites

close to the grain boundary core region have a higher atomic volume and a more stable segregation state.

According to the Voronoi tessellation in LAMMPS, the geometry of hydrogen volume at the octahedral site in nickel bulk is a cubic form, the volume geometry for a hydrogen atom near the grain boundary core region is more or less deformed. The hydrogen segregation is extremely dependent on the local environment, in particular, we have noticed that a part of data of the segregation energy have often a linear evolution with the atomic volume or the hydrogen atom energy, these segregation sites are a similar cubic form with a relatively low hydrogen atomic volume. From a mechanical point of view, the hydrostatic stress is high at these low hydrogen atomic volume with a quite “compact environment”, and the deviatoric stress is low due to the small distortion. The linear evolution often disappears in the grain boundary core with high volume segregation sites due to the high distortion. It is necessary to mention that the calculation is based on the elasticity in the perfect nickel bulk, however, the elasticity in the grain boundary core should be different from the nickel bulk and probably a slight modification by the presence of hydrogen atom. Actually, the influence of the hydrogen concentration on the elasticity is in progress in PhD works of G.Hachet within the laboratory. *Figure 5.1* gives an example of Young’s modulus as a function of the hydrogen concentration of nickel [Hachet2017].

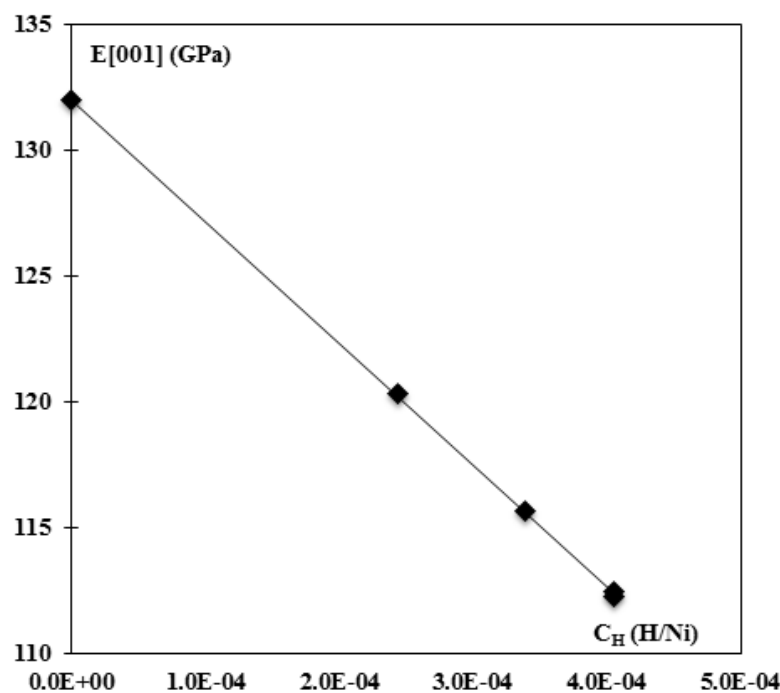


Figure 5.1 – Young’s modulus vs hydrogen concentration at room temperature [Hachet2017]

According to the Langmuir–McLean segregation isotherm model without solutes interactions, an analytical view on the hydrogen segregation concentration shows that high excess volume grain boundaries ($\Sigma 11$ - $\{332\}$ and $\Sigma 5$ - $\{310\}$) have high hydrogen segregation densities with various

segregation energies. The segregation sites start to be occupied by hydrogen atoms at very low hydrogen bulk concentration, the hydrogen segregation occurs first at the most stable position, the less stable positions start to segregate hydrogen atoms when the first most stable position is close to the saturation (70% -80% occupation). Considering the limit of hydrogen solubility in nickel crystals, the hydrogen segregation occurs at a relatively high hydrogen bulk concentration for the low excess volume grain boundary ($\Sigma 11\text{-}\{311\}$), or in some case no segregation at all as the grain boundary $\Sigma 3\text{-}\{111\}$.

The grain diffusion of hydrogen has been studied by the Nudged Elastic Band (NEB) method to find the minimum energy paths (MEP). The high energy/excess volume grain boundaries ($\Sigma 11\text{-}\{332\}$ and $\Sigma 5\text{-}\{310\}$) have one or two accelerated diffusion path(s) where the hydrogen atom moves $10^3 \sim 10^4$ faster than the diffusion in nickel bulk. Indeed, $\Sigma 11\text{-}\{332\}$ is a grain boundary that has more segregation sites in the grain boundary core with two accelerated diffusion paths, and none of these segregation sites has the trapping behavior. While grain boundary $\Sigma 5\text{-}\{310\}$ has only one accelerated diffusion path, and the most stable segregation site in the grain boundary core is a trapping position for hydrogen atoms. Grain boundary $\Sigma 11\text{-}\{311\}$ presents no accelerated diffusion paths but the trapping sites in the grain boundary core. Grain boundary $\Sigma 3\text{-}\{111\}$ acts as the nickel bulk with no trapping or acceleration effects on the hydrogen transport, this finding is supported by the experimental observation of SIMS.

These results of high excess volume grain boundaries could correlate to the ductility of materials with HE by the works of Oudriss *et al.* [Oudriss2014]. A good correlation between the increase of the random grain boundaries fraction and the decrease of the ductility ratio is obtained when the grain size decreases, which the elongation loss (A%) is characterized by a ratio $A\%(H) / A\%$ lower than 1 (*figure 5.2 (a)*). For the grain size range studied (10 to 200 μm) and hydrogen concentration of 120 ppm at., the fracture is brittle and purely intergranular (*figure 5.3*). Consequently, the more appropriate model of HE in the framework of this study seems to be a physical mechanism based on the lowering of the cohesive energy of the interface (grain boundary cohesion) of the metal due to the high mobility of hydrogen in the high excess volume grain boundaries. The evolution of the ductility ratio as a function of hydrogen content for two fractions of CSL grain boundaries is given in *figure 5.2 (b)*, the HE is more pronounced for the high hydrogen concentration probably with high vacancy concentration. The formed clusters of vacancies can promote the formation of nano-cavities along grain-boundaries to favor HE. This result support the idea that high hydrogen flux promotes intergranular fracture more than the hydrogen concentration.

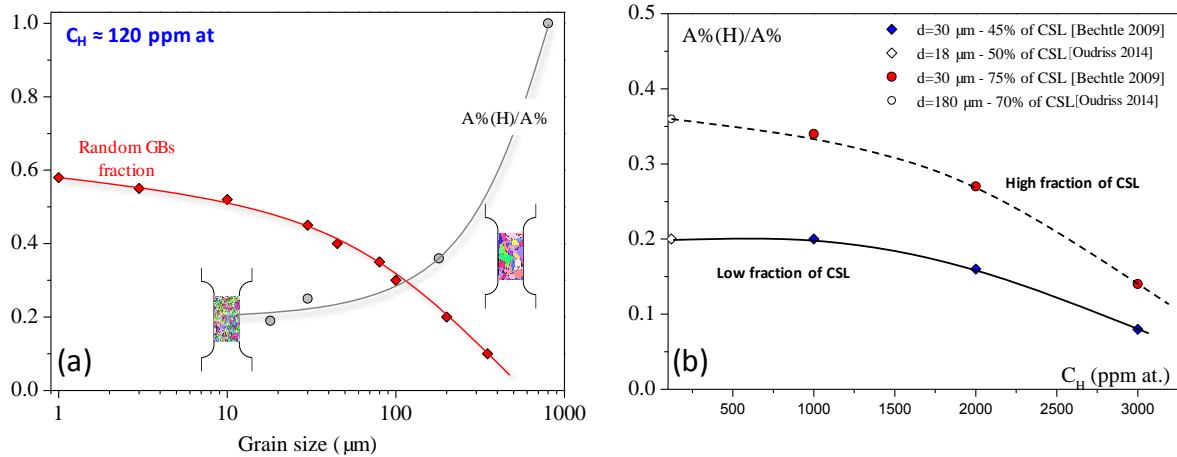


Figure 5.2 – (a) The fraction of the random GBs, f_R , and the ductility ratio $A\%(H) / A\%$ versus the grain size. (b) The ductility ratio $A\%(H) / A\%$ versus the hydrogen concentration for two fractions of CSL GBs. [Oudriss2014]

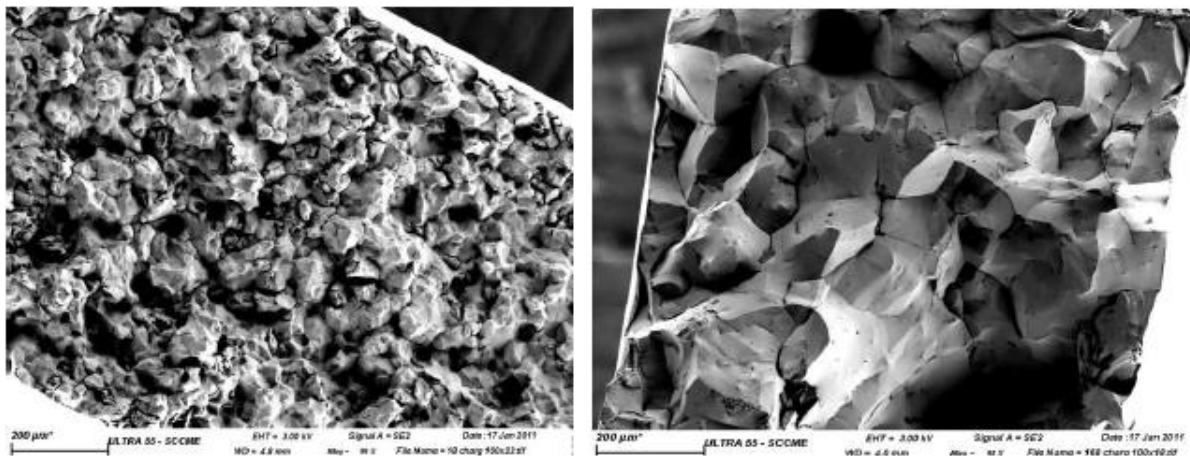


Figure 5.3 – Illustrations of surface fractures obtained by Scanning Electronic Microscopy (SEM) after H cathodic charging of the materials for 3h at 423K: (a) grain size equals to 18 μm , (b) grain size equals to 168 μm . [Oudriss2014]

The hydrogen solubility in bi crystals highlighted the important impacts of grain boundaries on the hydrogen transport, particularly the high energy/excess volume grain boundaries ($\Sigma 11$ - $\{332\}$ and $\Sigma 5$ - $\{310\}$) have sharply decreased the whole hydrogen solubility in the bi crystal membrane. The pure anisotropic and accelerated diffusion in the bi crystal system approach is not able to explain the reduction of the hydrogen solubility. Moreover, based on the dislocation model of tilt type grain boundary, we have estimated the stress state near the grain boundary and considered the hydrogen diffusion with a stress gradient. The hydrogen concentration distribution is strongly influenced by the length scale of the stress gradient and the hydrogen solubility could be decreased with this model. Despite a reduction of the solubility in the whole membrane, this approach cannot give a full explanation due to the unreasonable long range stress near the grain boundary and a high stress level.

From an opinion more close to the experiment, the influences of micro defects as vacancy and dislocation on the hydrogen transport in the bi crystal system may be considered. As highlighted in *chapter 3*, it is demonstrated that the clusters of vacancies have been formed with the hydrogen charging in nickel, the anisotropic diffusion in the bulk is dominated by the clusters of vacancies (*chapter 3*). In addition, the literature review of some atomic calculations have indicated that vacancy is easier formed in grain boundary than in the bulk, and the dislocation is also more active in the grain boundary. It would be more close to the reality considering the impacts of structural defects on the diffusion process, a new model will take into account the vacancy formation on the modification of the apparent diffusion coefficient and the stress state. Hence, it is expected that more vacancies formed near the grain boundary will be observed using TEM. Furthermore, the hydrogen – dislocation – grain boundary interactions remain also questionable.

Recently, scanning Kelvin probe force microscopy (SKPFM), which combines Kelvin probe technology and atomic force microscopy (AFM), has attracted considerable attention because of its capability to detect the variation of contact potential difference induced by hydrogen ingress with high spatial resolution. *Figure 5.4* presents the evolution of hydrogen concentration in the near surface area. It is shown that the hydrogen diffusivity in γ - stainless steel cubic structure depends on the crystallographic orientation [Hua2017].

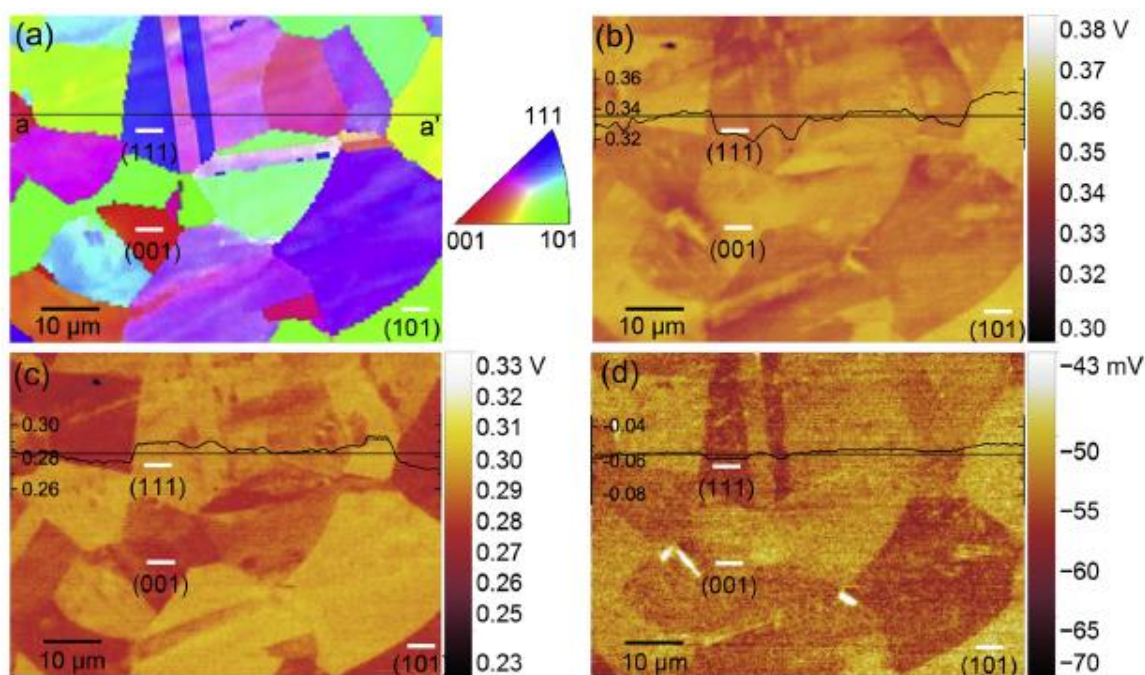


Figure 5.4 - EBSD and SKPFM results obtained from the same area of the hydrogen-charged specimen. (a) EBSD inverse pole image, (b) and (c) Potential difference maps taken at $t=2.8$ h and $t=44$ h after ion milling treatment, respectively. (d) Potential difference map taken after heating at 473 K for 2.5 h. [Hua2017]

Actually, a study on the sample surface preparation is in progress for the SKPFM. This idea is to have a direct observation of the hydrogen concentration evolution near a particular grain boundary. Some

works [Larignon2013a, 2013b] have investigated the hydrogen distribution in cathodically hydrogen-charged aluminum alloy by SKPFM and secondary ion mass spectroscopy (SIMS), and demonstrated that SKPFM appears to be more flexible than SIMS, with the capability of exploring absorbed hydrogen in aluminum alloys at nano-scale. A direct observation of the hydrogen accelerated diffusion and trapping near a grain boundary can be expected with SKPFM high resolution.

Another fashion is a 3D atom distribution detection by Atom Probe Tomography (APT). Localisation of hydrogen atoms at the nanostructural level is a complex nano-analysis task, with few methods able to simultaneously localize the position of hydrogen and quantify its concentration. APT or 3D Atom Probe is the only material analysis technique offering extensive capabilities for both 3D atom-by-atom imaging of materials with a uniquely powerful combination of spatial and chemical resolution at the atomic scale (around 0.1-0.3nm resolution in depth and 0.3-0.5nm laterally). Some works [Haley2014, Seidman2015] based on APT have achieved the detection of 3D distributions of the hydrogen or its isotopic atoms.

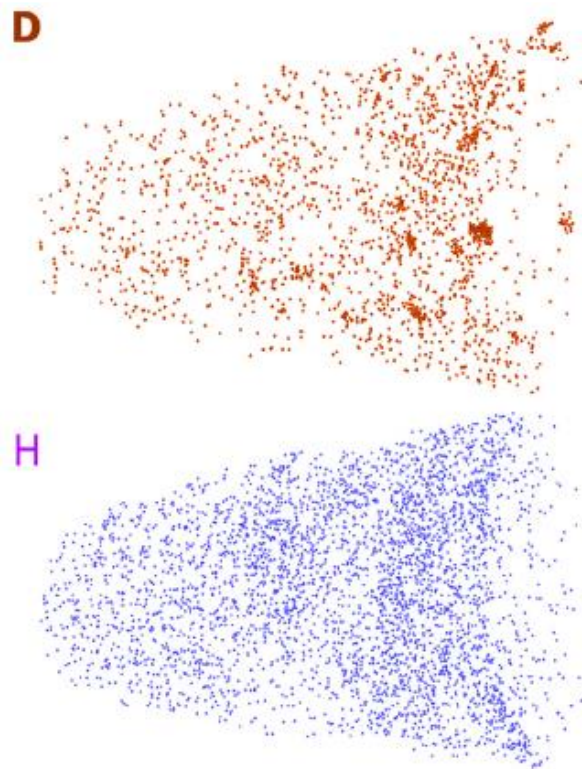


Figure 5.5 - Comparison of Deuterium and Hydrogen distributions for Ag co-deposited sample, showing only the Ag layer. Deuterium and hydrogen distributions are clearly spatially differentiated. [Haley2014]

Figure 5.5 gives an example of 3D distributions for hydrogen atoms and its isotope deuterium, which are clearly spatially differentiated. However, this technique has still some limitations and challenges for the hydrogen detection such as the sample preparation and the test environment. After all, if sufficiently improved from the perspective of sample and test conditions, could provide a clear methodology for visualizing and exploring hydrogen interaction to microstructural features.

Appendix

| | |
|--|-----|
| <u>Appendix 2.1 EBSD and surface preparation</u> | 188 |
| <u>Appendix 2.2 TEM and sample preparation</u> | 190 |
| <u>Appendix 3.1 Diffusion tensor</u> | 194 |
| <u>Appendix 3.2 Sphere inclusion – Eshelby’s solution</u> | 195 |
| <u>Appendix 3.3 Solution for the static displacement waves</u> | 196 |
| <u>Appendix 3.4 Anisotropy of elasticity</u> | 198 |
| <u>Appendix 4.1 Hydrogen atom details at the segregation sites</u> | 200 |

Appendix 2.1 EBSD and surface preparation

The EBSD instrument is coupled to a SEM (scanning electron microscope) Phillips FEI, Quanta 200 FEG / ESEM. The electron microscope operated at a voltage ‘acceleration of 20kV’ with high vacuum (total vacuum of 1×10^{-6} mbar) and has a resolution of 3 nm. This technique consists in placing a sample in microscope chamber perpendicular to the incident electron beam with an inclination of 70° . Among these electrons, some are diffracted by a given family of planes form two cones diffraction. The intersection these cones with the phosphor screen placed opposite the sample, giving rise to pairs of lines Kikuchi (*figure 1*). Data acquisition was then carried out through the IOM-STL software as well as data analyses.

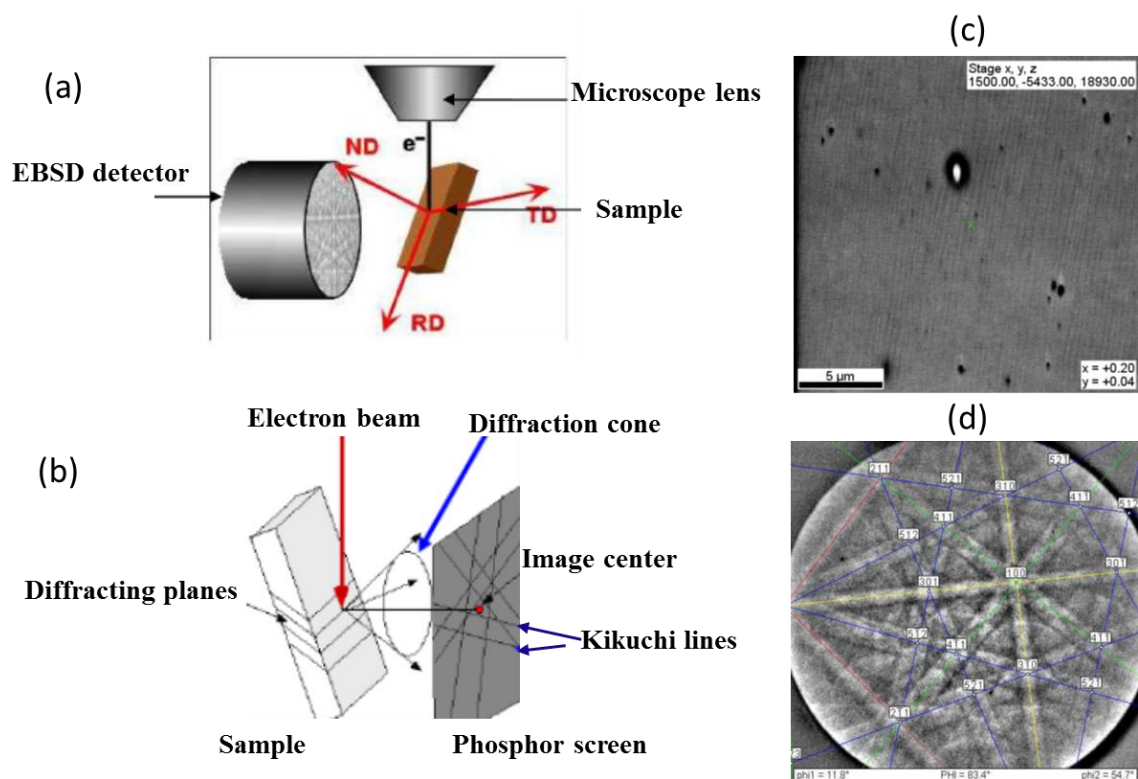


Figure 1 – (a) Sample position relative to the EBSD detector, (b) Diffraction cone and Kikuchi lines, (c) Microstructure image for nickel single crystal, (d) Kikuchi lines for nickel [001]

In order to have a ‘perfect’ surface, the sample is placed at a distance of 18.5mm from one platinum electrode in the beaker containing the electro-polishing solution H_2SO_4 40ml / CH_3OH 280ml. The polishing is done at the temperature of $18^\circ C$. A current density equal to $0.26 A/cm^2$ is applied to sample for 10 min. It also helps to dissolve a thin layer of nickel which has been evaluated about $50 \mu m$. This protocol allows to obtain a surface ‘perfect mirror’ with a roughness below $2 nm$ (*figure 2*).

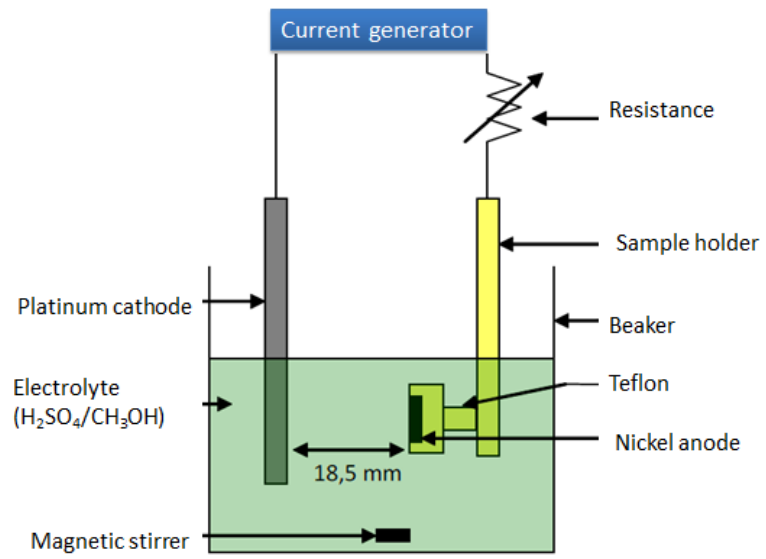


Figure 2 – Experimental setup for electro-polishing

Appendix 2.2 TEM and sample preparation

The transmission electron microscope (TEM) is a very powerful tool for material science. A high energy beam of electrons is gone through a very thin sample, and the interactions between the electrons and the atoms can be used to observe features such as the crystal structure and features in the structure of dislocations and grain boundaries. The used machine is the type JEOL JEM 2011 with a potential 200KV. The electron beam is obtained by heating a LaB6 tip and propagate in the column of the microscope with imposed vacuum about 10^{-7} to 10^{-10} mbar.

The TEM operates on the same basic principles as the light microscope but uses electrons instead of light. Because the wavelength of electrons is much smaller than that of light, the optimal resolution attainable for TEM images is many orders of magnitude (~ 0.1 nm) better than that under a light microscope (~ 0.2 μm).

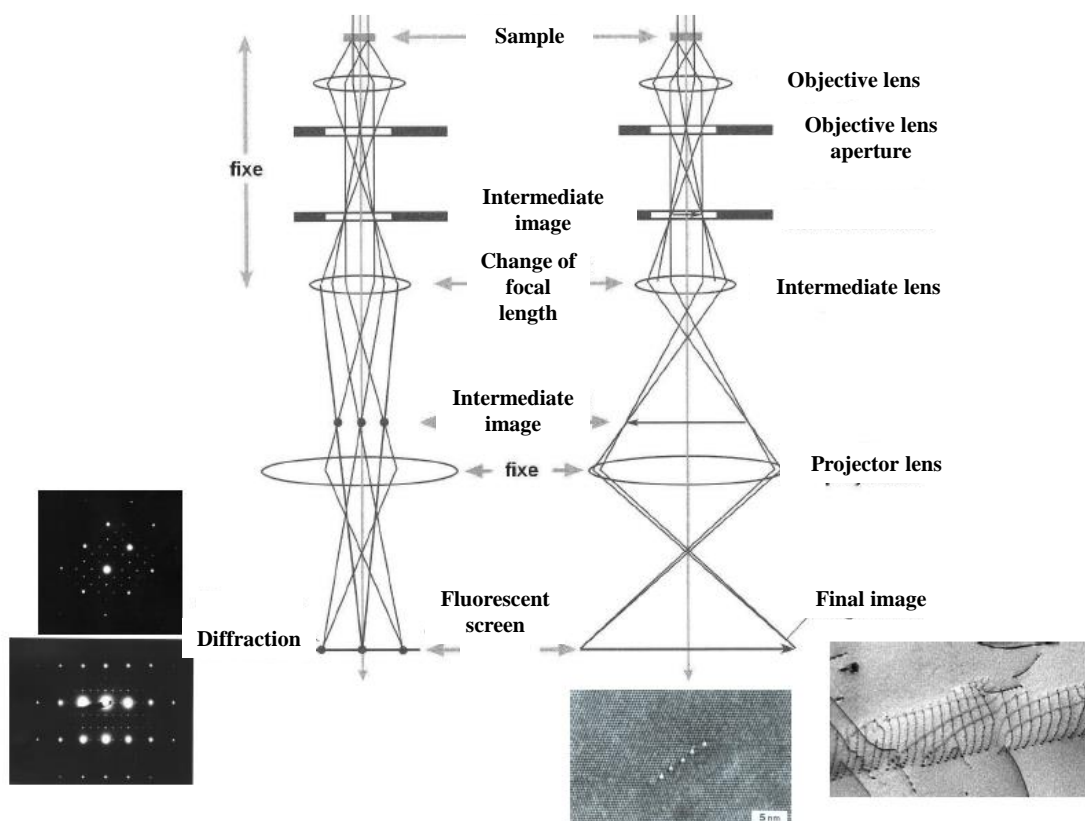


Figure 1 - The electron path to obtain either an image or a diffraction pattern [J. Ruste online]

The beam of electrons from the electron gun is focused into a small, thin, coherent beam by the use of the condenser lens. This beam is restricted by the condenser aperture, which excludes high angle electrons. The beam then strikes the specimen and parts of it are transmitted depending upon the

thickness and electron transparency of the specimen. This transmitted portion is focused by the objective lens into an image on the phosphor screen. Optional objective apertures can be used to enhance the contrast by blocking out high-angle diffracted electrons. The image then passed down the column through the intermediate and projector lenses, is enlarged all the way. The image strikes the phosphor screen and light is generated, allowing the user to see the image. The darker areas of the image represent those areas of the sample that fewer electrons are transmitted through while the lighter areas of the image represent those areas of the sample that more electrons were transmitted through. Another mode is where the electrons scattered in the same direction by the sample are collected into a single point. This is the back focal plane of the objective lens and is where the diffraction pattern is formed.

Preparation of an electron transparent (~ 100-150 nm thick) specimen is both an art and a science. It needs the devising of suitable methods as well as realizing/demonstrating them in a defined process with reproducibility. Also, utmost care is necessary for preparing and handling the specimens, as they are extremely thin and hence prone to bending and breaking. The preparation of GB disc is illustrated in *figure 2*. The edges of chemical treatment sample are rounded by the polishing paper in order to have a circular shape and keep the GB in the middle. Then this circular sample is placed on a steel disc and attached under a screw used as a polishing support. The samples are then thinned by mechanical polishing using abrasive paper in SiC (1200, 2400, and 4000) in order to obtain a circular blade of 3 mm diameter and 100 μm of thickness.

Dimpling is performed to reduce the thickness of the disc in the central portion, in order to make the electron transparent zone on the GB. The dimpling can be performed either on one side or both sides of the disc. A dimple grinder (Model 656, Gatan) is used for dimpling. Its base has a magnetic turntable to which the sample mount can be fixed. It rotates at a constant speed of 3 rpm. It also has a raise/lower cam to which a grinding wheel (phosphor bronze, diameter ~ 15mm) is fixed. This wheel is rotated with variable speeds, orthogonal to the rotation of the turntable. The unit has an inbuilt micrometer and dial indicator for setting up the depth of the dimple and also to examine the progress of the dimpling using a light microscope.

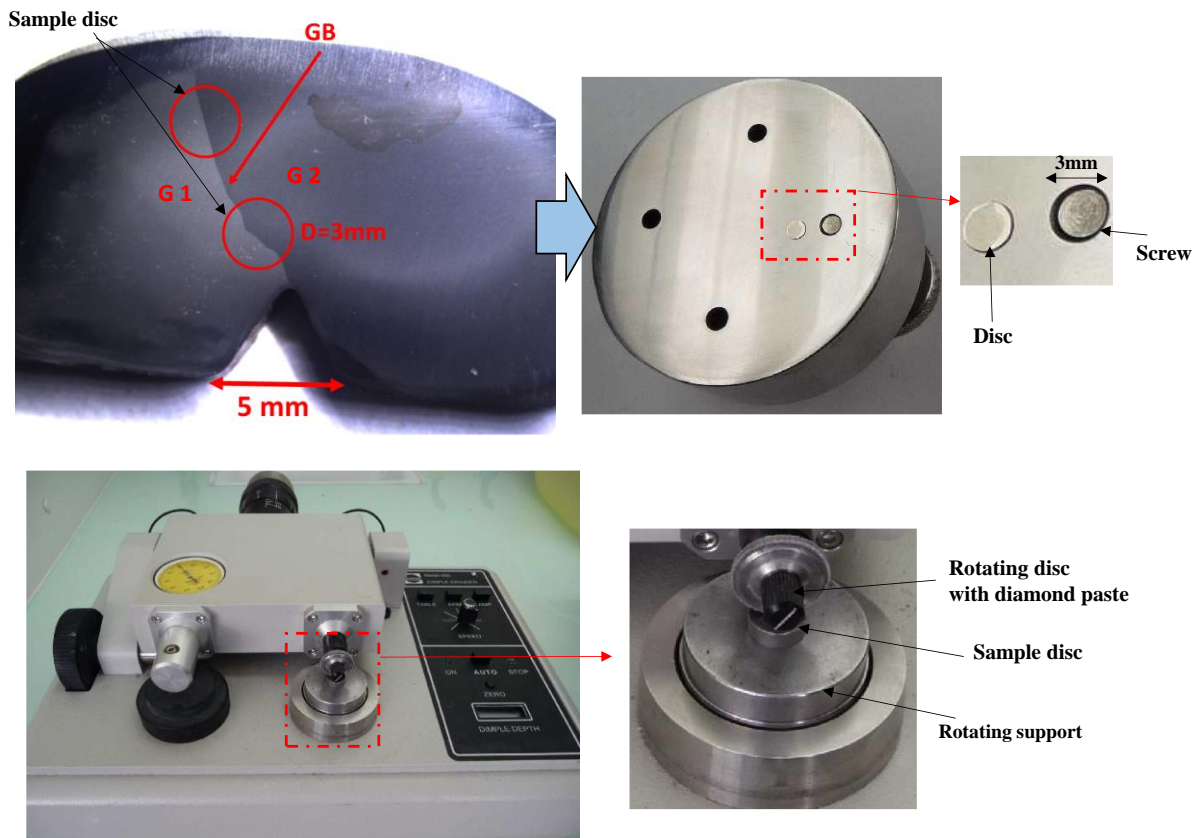


Figure 2 – TEM sample disc preparation (disc preparation +dimple grinder)

The electron transparent zone can be polished by electrochemical action, by keeping it in an electrolyte and applying a suitable potential. The electrolyte, its temperature and the bias voltage are important parameters in controlling the rate of dissolution of the sample. A twin jet electro-polisher (Tenu-pol5 Struers) can be used for electro polishing (*figure 3*), this equipment has a sample holder which can accommodate sample discs with 3 mm diameter. The sample disc acts as the anode. It is positioned between two nozzles, which are acting as cathodes. Both the sample disc and the nozzles are submerged in a suitable electrolyte. A small submersible pump, which is a part of the equipment, pumps jets of the electrolyte through these nozzles on both sides of the sample. The thinning rate in the central portions of the disc is higher than at the edges that are relatively unaffected. Therefore, the perforation occurs preferentially near the central region. The perforation can be identified using a light source and a light sensor that is placed on opposite sides of the sample. The edges near the perforation will have a wedge-shape with those next to the perforation having the desired thickness for *electron transparency*.



Figure 3 – Two jet polishing

For a nickel sample, the solution consists of 75% ethanol (CH_3OH) and 25% nitric acid (HNO_3). Once the solution is cooled to -20°C , the electrolytic polishing may start with a chosen voltage at 13 V, the current density is around 130-150 mA. The electrolytic polishing lasts between 30 seconds and 2 minutes. The priming is detected by a sudden increase in the brightness perceived by a photometric captor close to the polishing zone.

Appendix 3.1 Diffusion tensor

In order to establish the anisotropic diffusion tensor, the reference axis is considered in a crystallographic system ([100], [010], and [001]). The diffusion tensor is written (Eq.1):

$$\bar{D} = \begin{pmatrix} D_{11} & D_{12} & D_{13} \\ D_{21} & D_{22} & D_{32} \\ D_{31} & D_{32} & D_{33} \end{pmatrix} \quad (\text{Eq.1})$$

The hydrogen diffusion coefficient D_n for any orientation \vec{n}_{hkl} of the crystal could be expressed by (Eq. 2):

$$D_n = \vec{n}_{hkl}^T \bar{D} \vec{n}_{hkl} = \begin{bmatrix} h \\ k \\ l \end{bmatrix}^T \begin{pmatrix} D_{11} & D_{12} & D_{13} \\ D_{21} & D_{22} & D_{32} \\ D_{31} & D_{32} & D_{33} \end{pmatrix} \begin{bmatrix} h \\ k \\ l \end{bmatrix} \quad (\text{Eq.2})$$

Thanks to the FCC crystal structure of nickel, the diffusion following a crystallographic direction family $\langle hkl \rangle$ is considered identical, so symmetrical relationship allows us to simplify the diffusion tensor by the expression (Eq.3):

$$D_{11} = D_{22} = D_{33} \quad \text{and} \quad D_{12} = D_{23} = D_{31} = D_{21} = D_{32} \quad (\text{Eq.3})$$

By developing the equation (Eq.2) taking into account the diffusion following orientations [100] and [110], a system of equations (Eq.4; Eq.5) with two unknowns (D_{11} and D_{12}) was obtained. To solve this system of two equations, the development was based on the experimental data of electrochemical permeation tests, using the experimental values of the hydrogen diffusion coefficient $D_{100} = 6 \times 10^{-14} \text{ m}^2/\text{s}$ and $D_{110} = 11 \times 10^{-14} \text{ m}^2/\text{s}$. The trick is to keep the integer number and the diffusion tensor components remain positive.

$$D_{100} = \frac{1}{\sqrt{1}} \times \frac{1}{\sqrt{1}} \times \begin{bmatrix} 1 \\ 0 \\ 0 \end{bmatrix}^T \begin{pmatrix} D_{11} & D_{12} & D_{13} \\ D_{21} & D_{22} & D_{32} \\ D_{31} & D_{32} & D_{33} \end{pmatrix} \begin{bmatrix} 1 \\ 0 \\ 0 \end{bmatrix} \quad (\text{Eq.4})$$

$$D_{110} = \frac{1}{\sqrt{2}} \times \frac{1}{\sqrt{2}} \times \begin{bmatrix} 1 \\ 1 \\ 0 \end{bmatrix}^T \begin{pmatrix} D_{11} & D_{12} & D_{13} \\ D_{21} & D_{22} & D_{32} \\ D_{31} & D_{32} & D_{33} \end{pmatrix} \begin{bmatrix} 1 \\ 1 \\ 0 \end{bmatrix} \quad (\text{Eq.5})$$

Two unknowns D_{11} and D_{12} are given in (Eq.6; Eq.7)

$$D_{11} = D_{100} = 6 \times 10^{-14} \text{ m}^2/\text{s} \quad (\text{Eq.6})$$

$$D_{12} = D_{110} - D_{100} = 5 \times 10^{-14} \text{ m}^2/\text{s} \quad (\text{Eq.7})$$

The diffusion tensor for FCC structure nickel is then determined in (Eq.8)

$$\bar{D} = \begin{pmatrix} D_{11} & D_{12} & D_{13} \\ D_{21} & D_{22} & D_{32} \\ D_{31} & D_{32} & D_{33} \end{pmatrix} = \begin{pmatrix} 6 & 5 & 5 \\ 5 & 6 & 5 \\ 5 & 5 & 6 \end{pmatrix} \times (10^{-14} \text{ m}^2/\text{s}) \quad (\text{Eq.8})$$

Appendix 3.2 Sphere inclusion – Eshelby’s solution

The derivation of Eshelby’s tensor in the isotropic media is detailed in [Mura1987]. For the more general model, the Eshelby’s tensor for an ellipsoidal inclusion with semi-axes a, b, c can be expressed in terms of elliptic integrals.

In the simplest case, a spherical inclusion ($a = b = c$), the Eshelby’s tensor can be simplified to a compact expression (Eq.1):

$$S_{ijkl} = \frac{5\nu-1}{15(1-\nu)} \delta_{ij} \delta_{kl} + \frac{4-5\nu}{15(1-\nu)} (\delta_{ik} \delta_{jl} + \delta_{il} \delta_{jk}) \quad (\text{Eq.1})$$

This tensor does not depend on the sphere’s radius. The components of the tensor are:

$$S_{1111} = S_{2222} = S_{3333} = \frac{7-5\nu}{15(1-\nu)} \quad (\text{Eq.2})$$

$$S_{1122} = S_{2233} = S_{3311} = S_{1133} = S_{3322} = S_{2211} = \frac{5\nu-1}{15(1-\nu)} \quad (\text{Eq.3})$$

$$S_{1212} = S_{2323} = S_{3131} = \frac{4-5\nu}{15(1-\nu)} \quad (\text{Eq.4})$$

Appendix 3.3 Solution for the static displacement waves

The displacement $\bar{u}(\bar{r})$ and the concentration ΔC where \bar{r} is the position vector, are presented as Fourier's forms:

$$\bar{u}(\bar{r}) = i\bar{A}_k C_k \exp(-i\bar{k} \cdot \bar{r}) \quad (\text{Eq.1})$$

$$\Delta C_H = C_k \exp(-i\bar{k} \cdot \bar{r}) \quad (\text{Eq.2})$$

Where $\bar{k} = k\bar{n}$ and \bar{A}_k an unknown vector.

$$\bar{u}_{lm} = \frac{1}{2}(u_{kl} k_m + u_{km} k_l) e^{-ikr} = \frac{1}{2}k(n_m A_{kl} + n_l A_{km}) c_k e^{-ikr} \quad (\text{Eq.3})$$

The combination of the equations (Eq.3) and (Eq.4) leads to an expression of the stress tensor as the function of the concentration of solutes (Eq.A3.35):

$$\sigma_{ij} = C_{ijlm}(\varepsilon_{lm} - L_{lm}\Delta C_H) \quad (\text{Eq.4})$$

$$\sigma_{ij} = C_{ijlm} \left(\frac{1}{2}k(n_m A_{kl} + n_l A_{km}) - L_{lm} \right) \Delta C_H \quad (\text{Eq.5})$$

The equation for the equilibrium state is then:

$$\sigma_{ij} n_j = 0 \quad (\text{Eq.6})$$

$$C_{ijlm} \left(\frac{1}{2}k(n_m A_{kl} + n_l A_{km}) - L_{lm} \right) n_j = 0 \quad (\text{Eq.7})$$

$$\frac{1}{2}(n_m A_{kl} + n_l A_{km}) n_j C_{ijlm} = \frac{1}{k} n_j L_{lm} C_{ijlm} \quad (\text{Eq.8})$$

According to the equation (Eq.8), the component A_k is identified by a simple system of three linear equations (Eq.9):

$$C_{kim} A_{km} = P_{ki} \quad (i=1, 2, 3) \quad (\text{Eq.9})$$

Where $C_{kim} = n_j n_i C_{ijlm}$, $P_{ki} = \frac{1}{k} n_j L_{lm} C_{ijlm}$ and $L_{lm} = \frac{du_{lm}}{dc}$

For a cubic structure, A_k of the equations are simplified because they are characterized by just three elasticities modules C_{11} , C_{12} and C_{44}

$$C_{11} = C_{22} = C_{33} \quad C_{12} = C_{23} = C_{13} \quad C_{44} = C_{55} = C_{66} \quad (\text{Eq.10})$$

And

$$\begin{aligned}
C_{kxx}A_{kx} + C_{kxy}A_{ky} + C_{kxz}A_{kz} &= P_{kx} \\
C_{kxy}A_{kx} + C_{kyy}A_{ky} + C_{kyz}A_{kz} &= P_{ky} \\
C_{kxz}A_{kx} + C_{kyz}A_{ky} + C_{kzz}A_{kz} &= P_{kz}
\end{aligned} \quad (\text{Eq.11})$$

$$C_{kij} = C_{44} + (C_{11} - C_{44})n_i^2 \quad i = j \quad (\text{Eq.12})$$

$$C_{kij} = (C_{12} + C_{44})n_i n_j \quad i \neq j \quad (\text{Eq.13})$$

$$P_{ki} = \frac{1}{3} (C_{11} + 2C_{12}) \frac{1}{v} \frac{dv}{dc} \frac{n_i}{k} \quad (\text{Eq.14})$$

The solution of A_k is given in equation (Eq.15):

$$A_{kx} = \frac{1}{3} \frac{(C_{11} + 2C_{12})}{kD(\bar{n})} (1 + \omega n_y^2)(1 + \omega n_z^2) \frac{1}{v} \frac{dv}{dc} n_x \quad (\text{Eq.15})$$

Where v is the unit cell volume and c is the solute concentration.

The diffusion following one direction is then:

$$D(\bar{n}) = C_{11} + \omega(C_{11} + C_{12})(n_x^2 n_y^2 + n_x^2 n_z^2 + n_y^2 n_z^2) + \omega^2(C_{11} + 2C_{12} + C_{44})n_x^2 n_y^2 n_z^2 \quad (\text{Eq.16})$$

with $\omega = \frac{C_{11} - C_{12} - 2C_{44}}{C_{44}}$. The parameter ω describe the elastic anisotropy for the cubic system, a structure is isotropic if $\omega = 0$.

Appendix 3.4 Anisotropy of elasticity

Taking the anisotropic form of the Y :

$$Y = \left(C_{ijklm} \left(\frac{1}{2} (n_m X_l + n_l X_m) - \delta_{lm} \right) \right) \delta_{ij} \quad (\text{Eq.1})$$

$$\begin{aligned} Y &= C_{111lm} \left(\frac{1}{2} (n_m X_l + n_l X_m) - \delta_{lm} \right) \\ &+ C_{22lm} \left(\frac{1}{2} (n_m X_l + n_l X_m) - \delta_{lm} \right) \\ &+ C_{33lm} \left(\frac{1}{2} (n_m X_l + n_l X_m) - \delta_{lm} \right) \end{aligned} \quad (\text{Eq.2})$$

The complete form of the first term is:

$$\begin{aligned} C_{111lm} \left(\frac{1}{2} (n_m X_l + n_l X_m) - \delta_{lm} \right) &= C_{11111} (n_1 X_1) - C_{11111} \\ &+ C_{11122} (n_2 X_2) - C_{11122} \\ &+ C_{11133} (n_3 X_3) - C_{11133} \\ &+ 2(C_{11112} \left(\frac{1}{2} n_2 X_1 + \frac{1}{2} n_1 X_2 \right)) \\ &+ 2(C_{11113} \left(\frac{1}{2} n_3 X_1 + \frac{1}{2} n_1 X_3 \right)) \\ &+ 2(C_{11123} \left(\frac{1}{2} n_2 X_3 + \frac{1}{2} n_3 X_2 \right)) \end{aligned} \quad (\text{Eq.3})$$

In a cubic case, $C_{11113} = C_{11112} = C_{11123} = 0$, and according to Voigt's notation, the equation (Eq.3) is simplified as:

$$\begin{aligned} C_{111lm} \left(\frac{1}{2} (n_m X_l + n_l X_m) - \delta_{lm} \right) &= -(C_{11} + 2C_{12}) + C_{11} n_1 X_1 \\ &+ C_{12} (n_2 X_2 + n_3 X_3) \end{aligned} \quad (\text{Eq.4})$$

The same of :

$$\begin{aligned} C_{22lm} \left(\frac{1}{2} (n_m X_l + n_l X_m) - \delta_{lm} \right) &= -(C_{11} + 2C_{12}) + C_{11} n_2 X_2 \\ &+ C_{12} (n_1 X_1 + n_3 X_3) \end{aligned} \quad (\text{Eq.5})$$

$$C_{33lm} \left(\frac{1}{2} (n_m X_l + n_l X_m) - \delta_{lm} \right) = -(C_{11} + 2C_{12}) + C_{11} n_3 X_3 \\ + C_{12} (n_2 X_2 + n_1 X_1) \quad (\text{Eq.6})$$

The form of the Y is now:

$$Y = -(C_{11} + 2C_{12}) (3 - (n_1 X_1 + n_2 X_2 + n_3 X_3)) \quad (\text{Eq.7})$$

The term X_i is then:

$$X_1 = \frac{1}{1+\alpha} \left(\frac{C_{11}+2C_{12}}{C_{11}} \right) (1 - \gamma n_2^2) (1 - \gamma n_3^2) n_1 \\ X_2 = \frac{1}{1+\alpha} \left(\frac{C_{11}+2C_{12}}{C_{11}} \right) (1 - \gamma n_3^2) (1 - \gamma n_1^2) n_2 \\ X_3 = \frac{1}{1+\alpha} \left(\frac{C_{11}+2C_{12}}{C_{11}} \right) (1 - \gamma n_1^2) (1 - \gamma n_2^2) n_3 \quad (\text{Eq.8})$$

Where

$$\alpha = -\gamma \phi (n_1^2 n_2^2 + n_2^2 n_3^2 + n_3^2 n_1^2) + \gamma^2 \psi n_1^2 n_2^2 n_3^2$$

$$\gamma = (-C_{11} + C_{12} + 2C_{44}) / C_{44}$$

$$\phi = (C_{11} + C_{12}) / C_{11}$$

$$\psi = (C_{11} + 2C_{12} + C_{44}) / C_{11}$$

The term X_i in the equation (Eq.7) is replaced by (Eq.8):

$$Y = -(C_{11} + 2C_{12}) \left(3 - \frac{C_{11}+2C_{12}}{(1+\alpha)C_{11}} \left(\begin{array}{l} (1 - \gamma n_2^2)(1 - \gamma n_3^2)n_1^2 \\ + (1 - \gamma n_3^2)(1 - \gamma n_1^2)n_2^2 \\ + (1 - \gamma n_1^2)(1 - \gamma n_2^2)n_3^2 \end{array} \right) \right) \quad (\text{Eq.9})$$

$$Y = -(C_{11} + 2C_{12}) \left(3 - \frac{C_{11}+2C_{12}}{(1+\alpha)C_{11}} \left(\begin{array}{l} n_1^2 - \gamma n_1^2 n_3^2 - \gamma n_1^2 n_2^2 + \gamma^2 n_1^2 n_2^2 n_3^2 \\ + n_2^2 - \gamma n_1^2 n_2^2 - \gamma n_3^2 n_2^2 + \gamma^2 n_1^2 n_2^2 n_3^2 \\ + n_3^2 - \gamma n_1^2 n_3^2 - \gamma n_2^2 n_3^2 + \gamma^2 n_1^2 n_2^2 n_3^2 \end{array} \right) \right) \quad (\text{Eq.10})$$

$$Y = -(C_{11} + 2C_{12}) \left\{ 3 - \frac{(C_{11}+2C_{12})[1-2\gamma(n_1^2 n_2^2 + n_2^2 n_3^2 + n_3^2 n_1^2) + 3\gamma^2 n_1^2 n_2^2 n_3^2]}{C_{11}(1+\alpha)} \right\} \quad (\text{Eq.11})$$

Y is isotropic if $\gamma = 0$, for any direction \bar{n} , n_i is the projection on the principle axis in a cubic system as [100], [010] and [001].

Appendix 4.1 Hydrogen atom details at the segregation sites

$\Sigma 3\text{-}\{111\}$

| N° | Voronoi atoms | $V_i(\text{Å}^3)$ | $V_f(\text{Å}^3)$ | $\Delta V(\text{Å}^3)$ | E_H (eV) | E_{seg} (eV) | σ_D (Pa) | σ_H (Pa) | U(Pa) | U_H (Pa) | U_D (Pa) |
|----|---------------|-------------------|-------------------|------------------------|------------|-----------------------|-----------------|-----------------|---------|------------|------------|
| 1 | 12 | 5.45 | 5.77 | 0.32 | -0.22 | -0.04 | 7.8E+07 | -4.5E+10 | 5.6E+09 | 5.6E+09 | 1.1E+04 |
| 2 | 14 | 5.45 | 5.77 | 0.32 | -0.17 | -0.01 | 1.2E+08 | -4.8E+10 | 6.5E+09 | 6.5E+09 | 2.3E+04 |

$\Sigma 11\text{-}\{311\}$

| N° | Voronoi atoms | $V_i(\text{Å}^3)$ | $V_f(\text{Å}^3)$ | $\Delta V(\text{Å}^3)$ | E_H (eV) | E_{seg} (eV) | σ_D (Pa) | σ_H (Pa) | U(Pa) | U_H (Pa) | U_D (Pa) |
|----|---------------|-------------------|-------------------|------------------------|------------|-----------------------|-----------------|-----------------|---------|------------|------------|
| 1 | 9 | 6.60 | 6.69 | 0.10 | -0.63 | -0.24 | 7.4E+09 | -1.7E+10 | 9.0E+08 | 8.1E+08 | 9.5E+07 |
| 2 | 9 | 5.60 | 5.91 | 0.31 | -0.31 | -0.10 | 2.8E+09 | -4.0E+10 | 4.4E+09 | 4.4E+09 | 1.3E+07 |
| 3 | 12 | 5.46 | 5.78 | 0.32 | -0.20 | -0.03 | 9.7E+08 | -4.6E+10 | 6.0E+09 | 6.0E+09 | 1.6E+06 |
| 4 | 14 | 5.46 | 5.78 | 0.32 | -0.17 | -0.01 | 1.2E+09 | -4.8E+10 | 6.5E+09 | 6.5E+09 | 2.5E+06 |

$\Sigma 5\text{-}\{310\}$

| N° | Voronoi atoms | $V_i(\text{Å}^3)$ | $V_f(\text{Å}^3)$ | $\Delta V(\text{Å}^3)$ | E_H (eV) | E_{seg} (eV) | σ_D (Pa) | σ_H (Pa) | U(Pa) | U_H (Pa) | U_D (Pa) |
|----|---------------|-------------------|-------------------|------------------------|------------|-----------------------|-----------------|-----------------|---------|------------|------------|
| 1 | 7 | 6.35 | 6.52 | 0.17 | -0.70 | -0.33 | 8.0E+09 | -1.8E+10 | 9.8E+08 | 8.7E+08 | 1.1E+08 |
| 2 | 11 | 7.84 | 7.76 | -0.08 | -0.87 | -0.23 | 4.7E+09 | -3.5E+09 | 7.3E+07 | 3.4E+07 | 3.9E+07 |
| 3 | 11 | 7.53 | 7.55 | 0.02 | -0.75 | -0.23 | 7.3E+09 | -1.2E+10 | 5.1E+08 | 4.2E+08 | 9.4E+07 |
| 4 | 10 | 6.42 | 6.69 | 0.27 | -0.57 | -0.20 | 8.0E+09 | -2.3E+10 | 1.6E+09 | 1.5E+09 | 1.1E+08 |
| 5 | 12 | 7.30 | 7.53 | 0.23 | -0.66 | -0.20 | 1.8E+09 | -1.8E+10 | 9.4E+08 | 9.3E+08 | 5.4E+06 |
| 6 | 14 | 6.50 | 6.98 | 0.48 | -0.50 | -0.15 | 3.6E+09 | -2.7E+10 | 2.1E+09 | 2.1E+09 | 2.3E+07 |
| 7 | 10 | 5.38 | 5.70 | 0.33 | -0.31 | -0.13 | 2.5E+09 | -4.2E+10 | 5.0E+09 | 5.0E+09 | 1.1E+07 |
| 8 | 10 | 5.35 | 5.67 | 0.32 | -0.21 | -0.05 | 1.4E+09 | -4.7E+10 | 6.2E+09 | 6.2E+09 | 3.7E+06 |

$\Sigma_{11}\{-332\}$

| N° | Voronoi atoms | $V_i(\text{Å}^3)$ | $V_f(\text{Å}^3)$ | $\Delta V(\text{Å}^3)$ | E_H (eV) | E_{seg} (eV) | σ_D (Pa) | σ_H (Pa) | U (Pa) | U_H (Pa) | U_D (Pa) |
|----|---------------|-------------------|-------------------|------------------------|------------|-----------------------|-----------------|-----------------|----------|------------|------------|
| 1 | 9 | 7.43 | 7.35 | -0.08 | -0.86 | -0.32 | 3.6E+09 | -5.5E+09 | 1.1E+08 | 8.4E+07 | 2.3E+07 |
| 2 | 11 | 6.11 | 6.44 | 0.33 | -0.49 | -0.17 | 9.3E+09 | -2.8E+10 | 2.4E+09 | 2.2E+09 | 1.5E+08 |
| 3 | 9 | 5.68 | 5.99 | 0.31 | -0.41 | -0.17 | 2.3E+09 | -3.5E+10 | 3.4E+09 | 3.3E+09 | 9.1E+06 |
| 4 | 9 | 5.84 | 6.24 | 0.40 | -0.45 | -0.17 | 8.3E+09 | -3.1E+10 | 2.8E+09 | 2.7E+09 | 1.2E+08 |
| 5 | 13 | 7.70 | 8.14 | 0.44 | -0.66 | -0.14 | 8.8E+09 | -1.7E+10 | 9.0E+08 | 7.7E+08 | 1.3E+08 |
| 6 | 8 | 5.69 | 6.04 | 0.35 | -0.37 | -0.13 | 2.0E+09 | -3.6E+10 | 3.6E+09 | 3.6E+09 | 6.9E+06 |
| 7 | 11 | 5.56 | 5.90 | 0.34 | -0.31 | -0.10 | 3.9E+09 | -4.0E+10 | 4.5E+09 | 4.5E+09 | 2.6E+07 |
| 8 | 10 | 5.60 | 5.93 | 0.34 | -0.30 | -0.08 | 3.6E+09 | -4.1E+10 | 4.7E+09 | 4.6E+09 | 2.3E+07 |
| 9 | 12 | 6.31 | 6.93 | 0.61 | -0.53 | -0.08 | 1.5E+10 | -2.2E+10 | 1.8E+09 | 1.4E+09 | 3.9E+08 |
| 10 | 11 | 5.58 | 5.92 | 0.34 | -0.27 | -0.07 | 5.6E+09 | -4.2E+10 | 5.0E+09 | 4.9E+09 | 5.5E+07 |
| 11 | 13 | 7.74 | 8.35 | 0.61 | -0.68 | -0.06 | 1.2E+10 | -1.4E+10 | 8.3E+08 | 5.8E+08 | 2.6E+08 |
| 12 | 11 | 5.40 | 5.75 | 0.35 | -0.21 | -0.04 | 4.8E+09 | -4.6E+10 | 5.9E+09 | 5.8E+09 | 4.1E+07 |
| 13 | 14 | 5.47 | 5.79 | 0.32 | -0.19 | -0.02 | 7.3E+08 | -4.7E+10 | 6.2E+09 | 6.0E+09 | 6.5E+06 |
| 14 | 11 | 5.44 | 5.79 | 0.34 | -0.19 | -0.02 | 1.9E+09 | -4.7E+10 | 6.0E+09 | 6.0E+09 | 1.6E+07 |

Reference

A

- [Armbruster1943] M. H. Armbruster, J. Amer; Chem. Soc, 65 (1943) 1043.
- [Aaron1972a] H.B.Aaron &G.F.Bolling. Sciripta Metallurgica Vol.6 pp.553-562. 1972
- [Aaron1972b] H.B.Aaron &G.F.Bolling. Surface science 31 27-49, 1972
- [Atrens1980] A. Atrens *et al.*; Corrosion Science,Vol.20,(1980) pp. 673 to 684
- [Aucouturier1982] M. Aucouturier ; Journal de Physique Colloques, (1982), 43, pp.C6-175-C6-186.
- [Allnatt1993] A.R. Allnatt, A.B. Lidiard, Atomic transport in solids, Cambridge university press, (1993).
- [Arantes1993] D. Arantes *et al.*, Acta Metall. Mater 41,3215–3222 (1993)
- [Angelo1995] J.E. Angelo *et al.*, Modell. Simul. Mater. Sci. Eng. 3 (1995), pp. 289–307.
- [Altunoglu1996] A. K. Altunoglu et N. S. J. Braithwaite, Metall. Trans. A, 27 (1996) 2495-2503.
- [Addach2009] H. Addach, P. Ber çot, M. Rezrazi, J. Takadoum, Corros. Sci., 51 (2009) 263-267.
- [Auger2011] Auger T. Revue de Metall (2011);108:51.
- [Agarwal2016] Agarwal, R. & Trinkle, D. R. Phys. Rev. B. 94, 054106 (2016)

B

- [Bastien1951] P. Bastien and P. Azou:R. Acad. Sci. Paris, 1951, vol. 232, pp. 1845–48.
- [Belyakov1961] Y. I. Belyakov, N. I. Ionov, Sov. Phys-Tech.Phys, 6 (1961) 146.
- [Brandon1966] D.G. Brandon, Acta Metall. 14, 1479 (1966).
- [Blakemore1968] J.S. Balkemore, W. A. Oates, E. O. Hall, Trans. TMS-AIME, 242 (1968) 332.
- [Beck1971] W. Beck, J. O'M.Bockris, M. A. Genshaw, P. K. Subramanyan, Met. Trans, 2 (1971) 883.
- [Bockris1971] J.O. Bockris *et al.*; Acta Metall 1971
- [Beachem1972] C.D. Beachem, Metall. Trans. 3 (2), 441-455 (1972).
- [Boes1976] N. Boes, H. Züchener. Journal of the Less-Common Metals 49 (1976), pp. 223-240.
- [Balluffi1978] R.W. Balluffi, J. Nucl. Mater. 69/70, 240 (1978).
- [Besenbacher1990] F. Besenbacher, *et al.*; J.Fusion Energ. 9 (3), 257-261 (1990).
- [Bakker1990] H. Bakker et al., Diffusion in Solid Metals and Alloy, In : Numerical Data and Functional Relationships in Science and Technology LandoltBörnstein, New Series, (1990) 762p
- [Birnbaum1990] H.K. Birnbaum, Mechanisms of hydrogen related fracture of metals,(1990) pp. 639 – 658 in Hydrogen effects on materials behavior.

[**Brass1990**] A. M. Brass, A. Chanfreau, and J. Chene, in *Hydrogen Effects on Materials Behavior*, edited by N. R. Moody and A. W. Thompson (Minerals, Metals, and Materials Society, Warrendale, PA, 1990), pp. 19–31.

[**Brass 1995**] A. M. Brass, A. Chanfreau, *Acta Mater*, 44, 3823 (1995).

[**Brass1996**] A.M. Brass, A. Chanfreau, *Acta Materialia* 44 (1996), pp. 3823-3831.

[**Birnbaum1997**] H.K. Birnbaum *et al.*; *J. Alloy. Compd.* 253–254 (0), 260-264 (1997).

[**Bockris2000**] J. Bockris: *Modern Electrochemistry: an Introduction to an Interdisciplinary Area* (Plenum Press 2000)

[**Barnoush2008**] A. Barnoush, H. Vehoff, *Corros. Sci.*, 50 (2008) 259-267.

[**Barnoush2010**] A. Barnoush, H. Vehoff, *Acta Mater*, 58 (2010) 5274-5285.

C

[**Cermak1968**] J. Cermak, A. Kufudakis, *Mem. Sci. Rev. Met*, 65 (1968) 375.

[**Combette1970**] P. Combette, P. Azou, *Mem. Sci. Rev. Met*, 67 (1970) 17.

[**Crank1975**] J. Crank, *The mathematics of diffusion*, Clarendon Press, Oxford, (1975).

[**Chen1989**] Chen S P. Srolovitz D J and Voter A F 1989 . *Mater. Res.* 4 62

[**Chen1990**] Chen S P. Voter A F, Albers R C Boring A M and Hays P J 1990 *J. Marer. Res.* 5 955

[**Chanfreau1992**] A. Chanfreau, Chapitre III « Etude de la diffusion de l'hydrogène dans des matériaux chargés et non chargés en hélium, par la méthode de perméation électrochimique », Thèse : Université de Paris-Sud Centre d'Orsay (1992) 308p.

[**Cuitino1996**] A.M. Cuitino and M. Ortiz, *Acta Mater.*, 44, 427 – 436, 1996.147

[**Chêne1999**] J. Chêne et A. M. Brass, *Scr. Mater.*, 40 (1999) 537-542

[**Coudreuse2000**] L. Coudreuse, A.-M. Brass and J. Chêne ; TIB371DUO (ref. article : m176) (2000).

[**Carter2004**] Emily A.carter D.E. Jiang *Acta Materialia* 52 (2004) 4801–4807

[**Carter2010**] Emily A.carter; *J. Mater. Res.*, Vol. 25, No. 2, Feb 2010

[**Connetable2014**] D.Connetable, Y.Wang, D.Tanguy. *Journal of Alloys and Compounds*, vol. 614. (2014) pp. 211-220. ISSN 0925-8388

[**Chen2016**] J.Chen; Avinash.M. Dongare. *J Mater Sci* (2016)

[**Charles2017**] Y.Charles, H.T.Nguyen, M.Gasperini , *Int. J. Hydrogen Energy* 42 (2017) 20336 - 20350

D

[**Daynes1920**] H.A. Daynes, *Proceedings of the Royal Society Series A* 97 (1920), pp. 286-307.

- [Devanathan1962] M. A. V. Devanathan, Z. Stachurski, Proceedings of the Royal Society A, 270 (1962) 90-102.
- [Dus1967] R. Dus, M Smialowski, Acta. Met, 15 (1967) 1611.
- [Donovan1971] J. A. Donovan *et al.*, Quarterly Report: Aprile-June 1971. Report DPST (NASA)-71-2, Dupont, Savannah River Lab, Aiken, S. C, October 1971.
- [Dederichs1978] P.H. Dederichs & K. Schroeder, Phys. Rev. B. 17, 2524–2536 (1978).
- [Dechamps1987] M. Déchamps, F. Baribier and A. Marrouche, Acta Metall. **35** (1), 101-107 (1987).
- [Daw1993] M.S.Daw *et al.*, M. Mater, Sci, Rep. 9, 251(1993)
- [Doyle1995] D.M. Doyle *et al.* Acta Metallurgica et Materialia 43 (1995), pp. 3027-3033.
- [Duparc2000] O. H. Duparc *et al.* Phil. Mag. (2000), Vol. 80, No. 4, 853-870
- [Delafosse2001] D.Delafosse, Eur. J. Mech. A/Solids 20 (2001) 857–872
- [Du2011] Yaojun A. Du *et al.* ; Physical Review B 84, 144121 (2011)
- [Di Stefano2015] D.Di Stefano *et al.* ; Acta Materialia. Vol 98, 1 (2015), Pages 306–312

E

- [Euringer1935] G. Euringer, Zeit. Physik, 96 (1935) 37.
- [Eshelby1954] J.D. Eshelby; J. Appl. Phys. 25, 255–261 (1954).
- [Eshelby1956] J.D. Eshelby; Adv Solid State Phys 1956;3:79.
- [Edwards1957] A. G. Edwards, Brit. J. Appl. Phys, 8 (1957) 406.
- [Eshelby1957] J.D. Eshelby; Proc. R. Soc. A. 241, 1226 (1957).
- [Eichenauer1960] W. Eichenauer, Mem. Sci. Rev. Met, 57 (1960) 943.
- [Eichenauer1965] W. Eichenauer, W. Löser, H. Witte, Z. Metallkde, 56 (1965) 287.
- [Ebisuzaki1967] Y. Ebisuzaki, W. J. Kass, and M. O’Keeffe, J. Chem. Phys. **46**, 1378 (1967).

F

- [Fisher1951] J.C. Fisher, J. Appl. Phys. 22 (1), 74-77 (1951).
- [Friedel1954] Friedel J. Adv Phys (1954);3:446.
- [Fritz1961] J.J. Fritz, H.J. Maria, J.G.Aston.; J. Chem. Phys. 34, 2185 (1961)
- [Fischer1967] W. Fischer, Z. Naturforsch, 22a (1967) 1581.
- [Foiles1987] S.M.Foiles *et al.* J. Less Common Met. 130, 465–473 (1987).
- [Feaugas2003] X. Feaugas et H. Haddou, Metall. Trans. A, 34 A (2003) 2329-2340.
- [Fukai2003] Y.Fukai, *et al.* J. Alloys Compd.356–357, 270–273 (2003).
- [Fukai2005] Y.Fukai, *et al.* J. Alloys Compd. 404–406, 247–251 (2005).

[Fukai2005a] Fukai, Y. *et al.* ; J. Alloys Compd. 404–406, 247–251 (2005).

[Fukai2005b] Fukai, Y. in *The metal-hydrogen system basic bulk properties* (ed. Fukai, Y. *et al.*) 104-113 (2005)

[Foiles2006] S.M. Foiles and J.J. Hoyt, *Acta Mater.* 54 (2006), pp. 3351–3357.

[Frappart2011] S. Frappart, Des éléments de compréhension sur les mécanismes de transport et de ségrégation de l'hydrogène dans les aciers martensitiques trempés et revenus à haute limite d'élasticité
PhD These, Université de la Rochelle.

[Frappart 2012] S. Frappart, X. Feaugas, J. Creus, F. Thebault, L. Delattre et H. Marchebois, *Mater. Sci. Eng., A*, 534 (2012) 384-393.

G

[Gel'd1966] P. V. Gel'd *et al.* ; *Mekhan. Mat*, 2 (1966) 308.

[Gibbs1966] G. Gibbs, *physica status solidi (b)* 16 (1), K27-K29 (1966).

[Grimmer1974] H. Grimmer *et al.* ; *Acta Crystallogr. A* 30 (2), 197-207 (1974).

[Gabrielli2006] C. Gabrielli *et al.* *Journal of Electroanalytical Chemistry* 590 (2006) 1–14

[Guedes2015] D.Guedes ; Etude des mécanismes d'endommagement d'aciers martensitiques associés au SSC (Sulphide Stress Cracking), PhD thesis, Université de La Rochelle.

H

[Hasse1932] L. Luckemeyer-Hasse, H. Schenck, *Arch. Eisenhüttenwes*, 6 (1932) 209.

[Hill1955] H. L. Hill, E. W. Johnson, *Acta Met*, 3 (1955) 566.

[Harrison1961] L.G. Harrison, *Trans. Faraday Soc.* 57 (0), 1191-1199 (1961).

[Hanada1973] R.Hanada: *Scripta Met.* 7, 681 (1973)

[Hanada1976] R.Hanada: In *Effect of Hydrogen on Behavior of Materials*, ed. by A.W.Thompson and I.M.Bernstein (AIME 1976) p. 676

[Hirth1982] John Price Hirth, Jens Lothe-*Theory of dislocations*-Krieger Pub. Co (1982)

[Harris1991] T.M. Harris and M. Latanision, *Metall. Trans. A* 22 (2), 351-355 (1991).

[Heyes1994] D.M. Heyes, *Phys Rev B* 49, 755 (1994)

[Haftbaradaran2011] Haftbaradaran, H., Song, J., Curtin, W.A. &Gao, H. J. *Power Sources*. 196, 361–370 (2011).

[Haley2014] D.Haley *et al.* *Int. J. Hydrogen Energy* 39 (2014) 12221 -12229

[Hickel2014] T. Hickel *et al.*, *JOM* 66 (8), 1399-1405 (2014).

[Hallil2016] A.Hallil *et al.* *Phil.Mag.* Vol 96, (2016) - Issue 20

[Hachet2017] G.Hachet *et al.*, Hydrogen consequences on elastic properties of nickel. *Private Communication*. (2017).

[Hallil2017] A. Hallil, *et al.* J Mater Sci (2017)

[Hua2017] Z.L.Hua *et al.*, Scripta Materialia 131 (2017) 47–50

I

[Ishida 1973] Y. Ishida, M. McLean, Philos. Mag., 27 (1973) 1125-1134.

[Ichimura1991] M. Ichimura *et al.*, Mater. Trans., JIM, 32 (1991) 1109-1114

[Ilin2015] D.Ilin; Simulation of hydrogen diffusion in fcc polycrystals. Effect of deformation and grain boundaries: effect of deformation and grain boundaries. PhD thesis, Université de Bordeaux

J

[Johnson1875] W. H. Johnson: Proceedings of the Royal Society of London, 23 (1875) 168–179.

[Johnson1965] R. A. Johnson, Physical Review Volume 145, Number 2 13 (1966)

[Jones1971] F. G. Jones, R. D. Pehlke, Mrt. Trans, 2 (1971) 2655.

[J.Volkl1975] J.Volkl and G.Alefeld. Diffusion of Hydrogen in Metals, in Diffusion in Solids, ed. by A.S.Nowick, J.J.Burton (Academic Press. New York 1975).

[Juhas1994] M. C. Juhas, L. Priester, M. Biscondi; Materials Science and Engineering, A185 (1994) 71-76

[Jin2015] S.Jin *et al.*; Journal of Nuclear Materials 465 (2015) 135-141

[J.O'Brien2016] S.J.O'Brien and S.M.Foiles; Journal Philosophical Magazine Volume 96, 2016 - Issue 26

[J. Ruste online] <http://micro.icaunais.free.fr/>

K

[Kronberg1949] F.H.W.a.M.L. Kronberg, Trans. AIME 185, 501 (1949).

[Katz1971] L. Katz, M. Guinan, R. J. Borg, Phys. Rev, B4 (1971) 330.

[Koike1981] S. Koike, T. Suzuki: Acta Metall. 29, 553 (1981)

[Kreuser1981] H.Kreuser, Non-equilibrium thermodynamics and its statistical foundations, Clarendon Press; Oxford, (1981).

[Kirchheim1987] Kirchheim, R. & Hirth, J.P.. Acta metall. 35, 2899-2903 (1987).

[Krivoglaz1996] A. Krivoglaz, M. In X-Ray and Neutron Diffraction in Nonideal Crystals. (ed. A. Krivoglaz, M. et al.) 95–99 (Springer-Verlag Berlin Heidelberg, 1996).

- [**Kurtz2003**] De Koning M, Kurtz *et al.* J Nucl Mater (2003);323:281.
- [**Kaxiras2005**] E. Kaxiras and G. Lu; Phys. Rev. Lett. 94, 155501 (2005)
- [**Kirchheim 2007a**] R. Kirchheim, Acta Mater., 55 (2007) 5129-5138.
- [**Kato2009**] D. Kato *et al.*; J. Plasma Fusion Res. SERIES, Vol. 8 (2009)
- [**Kirchheim 2007b**] R. Kirchheim, Acta Mater., 55 (2007) 5139-5148.
- [**Kirchheim2010**] R.Kirchheim., Scripta Materialia 62 (2010) 67–70.
- [**Kharecha2013**] A. Pushker *et al.* Sci. Technol., (2013), 47 (9), pp 4889–4895

L

- [**Li1966**] J.Li, R.Oriani, L.Darken: The thermodynamics of stressed solids, Zeitschrift fur Physikalische Chemie Neue Folge 49, 271–290 (1966)
- [**Ledbetter1976**] H.M.Ledbetter, Acta Metallurgica Volume 24, Issue 10, (1976), P 891-899
- [**Li1978**] J.Li, Metal Trans A, Vols 9A, (1978)
- [**Landau1980**] L.D Landau, E.M Lifshitz. Statistical physics, p129. (1980)
- [**Larche1982**] Larch é F.C. &Cahn, J.W. The effect of self-stress in solids. Acta metall. 32, 1835-1845 (1982).
- [**Louthan1975**] M. R. Louthan, J. A. Donovan et G. R. Caskey, Acta Metall., 23 (1975)745-749
- [**Ladna1987**] B. Ladna and H.K. Birnbaum, Acta Metall. 35 (10), 2537-2542 (1987).
- [**Larche1988**] F.C. Larch é Solid State Phnenomena Vols. 3-4 (1988) pp 205-214
- [**Lynch1988**] S.Lynch; Arm merall. Vol. 36, No. IO, pp. 2639-2661, 1988
- [**Lasia1995**] A. Lasia and D. Gregoire, J. Electrochem. Soc., 142, 3393 ~1995
- [**Luppo1998**] M.I. Luppo, J. Ovejero-Garcia, Materials characterization 40 (1998), pp. 189-196.
- [**Lasia2002**] A. Lasia, in: B.E. Conway, R.E. White (Eds.), Modern Aspects of Electrochemistry, vol. 35, Kluwer/Plenum, New York, 2002, p. 1.
- [**Lezzar2004**] B. Lezzar *et al.* Acta Materialia 52 (2004) 2809–2818
- [**Lasia2006**] A. Lasia; Journal of Electroanalytical Chemistry 593 (2006) 159–166
- [**Liu 2009**] Y.-L. Liu *et al.*; Phys. Rev. B. 79 (17),172103 (2009).
- [**Lejcek2010**] Pavel Lejcek, Grain Boundary Segregation in Metals-Springer-Verlag Berlin Heidelberg (2010)
- [**Lekbir2012**] C. Lekbir, Effet de la déformation plastique du nickel monocristallin sur l'état d'équilibre de l'hydrogène en surface et subsurface. Science et Génie des Matériaux, PhD These : Université de La Rochelle.
- [**Lynch2012**] S.Lynch; Corros Rev 30 (2012): 105–123

[**Legrand2013**] E.Legrand ; Approche numérique des transitions d'échelles appliquées à la diffusion et au piégeage de l'hydrogène dans des métaux de structures hétérogènes. PhD These, Université de la Rochelle.

[**Larignon2013a**] C. Larignon, *et al.*, Scr. Mater. 68 (2013) 479–482.

[**Larignon2013b**] C. Larignon, *et al.*, Electrochim. Acta. 110 (2013) 484–490.

[**Liu2014**] Q.Liu, A.D. Atrens, Z. Shi, Kim Verbeken, Andrej. Atrens; Corrosion science 87 239-258 ; 2014

[**Li2017**] J.Li *et al.* Scientific Reports, (2017) 7:45041

M

[**McLean1957**] McLean D. Grain boundaries in metals. London: Oxford University Press; (1957).

[**McBreen1966**] J. McBreen, L. Nanis, W. Beck, Journal of the electrochemical society 113 (1966), pp. 1218-1222.

[**McLellan1973**] R. McLellan, J. Phys. Chem. Solids 34, 1137 (1973).

[**Matter1979**] H. Matter, J. Winter, and W. Triftshiiuser, Appl. Phys. 20, 135-140 (1979)

[**Makenas1980**] B. Makenas, H. Birnbaum, Acta. Metall. 28, 979–988 (1980)

[**McLellan1984**] REX B. McLellan and P. L. Sutter Acta metall. Vol. 32. No. 12 pp. 2233-2239. (1984)

[**Mutschele1987**] T. Mutschele and R. Kirchheim Scripta Metallurgica Vol. 21, pp. 135-140, 1987

[**Mura1987**] T. Mura, Micromechanics of defects in solids, Martinus Nijhoff Publishers, (1987).

[**Matsui1990**] H. Matsui, M. Koiwa: Acta Metall. 38, 1175 (1990)

[**Moody1991**] N.R. Moody *et al.* Mat. Res. Soc. Symp. Proc. Vol. 229. (1991) Materials Research Society

[**Mishin1995**] I. Kaur, Y. Mishin, W. Gust, *Fundamentals of Grain and Interphase Boundary Diffusion*, John Wiley and Sons, Ltd., 1995

[**Mishin2001**] Y. Mishin *et al.* Phil. Mag. A. 81, 2591–2612 (2001).

[**Mao2002**] J. Mao, R. McLellan; J. Phys. Chem. Solids 63, 2029–2036 (2002).

[**Mehrer2007**] H. Mehrer Diffusion in solids: Fundamentals, methods, materials, diffusion-controlled processes, springer series in solid state science 155, (2007).

[**Marcus2011**] P.Marcus, Corrosion mechanisms in theory and practice-CRC Press (2011)

[**Matsumoto2011**] R.Matsumoto *et al.*, Progress in nuclear science and technology, Vol. 2, pp.9-15 (2011)

[**Martin2012**] Martin ML, Auger T, Johnson DD, Robertson IM. J Nucl Mater (2012);426:7.

[**Metsue2014**] A.Metsue, *et al.*, J. Chem. Phys. 140, 104705 (2014).

[**Metsue2016**] A.Metsue, Oudriss, A. X.Feaugas;. J. Alloys Compd. 656, 555-567 (2016)

N

- [Nagumo2004] M. Nagumo, Mater. Sci. Tech. Ser. 20 (8), 940-950 (2004).
[Nam2009] H-S. Nam and D.J.Srolovitz; Acta Mater (2009);57:1546.
[Nazarov2012] R.Nazarov, T. Hickel, J. Neugebauer; Phys. Rev. B. 85, 144118 (2012).
[Nazarov2014] R.Nazarov, T. Hickel, J. Neugebauer; Phys. Rev. B. 89, 144108 (2014)

O

- [Oriani1972] R. Oriani: A mechanistic theory of hydrogen embrittlement of steels, Ber. Bunsenges. Phys. Chem 76, 848–857 (1972)
[Oriani1993] R. A. Oriani; The Physical and Metallurgical Aspects of Hydrogen in Metals. in ICCF4, Fourth International Conference on Cold Fusion. 1993.
[Olmsted2009] D.L. Olmsted, S.M. Foiles, and E.A. Holm, Acta Mater. 57 (2009), pp. 3694–3703.
[Oudriss2012a] A. Oudriss, *et al.* Scripta Mater. 66 (1), 37-40 (2012).
[Oudriss2012b] A. Oudriss *et al.* Acta Mater. 60, 6814–6828 (2012).
[Oudriss2012c] A. Oudriss, Influence des h á érog á n é t é s m é t a l l u r g i q u e s s u r l e s p r o c e s s u s d e d i f f u s i o n e t d e p i é g e a g e d e l ’ h y d r o g è n e d a n s l e n i c k e l , P h D t h e s i s , U n i v e r s i t é d e L a R o c h e l l e .
[Oudriss2014] A. Oudriss, *et al.*, Procedia Mater. Sci. 3, 2030-2034 (2014).
[Osman Hoch2015] B. Osman Hoch *et al.* Computational Materials Science Vol.97 (2015) P 276-284.
[Osman Hoch2016] B. Osman Hoch; Modelling of hydrogen diffusion in heterogeneous materials: implications of the grain boundary connectivity, PhD thesis, Université de La Rochelle.
[Oudriss2016] A. Oudriss, *et al.*, Materials Letters 165 (2016) 217–222

P

- [Pines1940] B.J. Pines; J Phys (Moscow, Acad USSR) (1940);3:309.
[Pressouyre1980] G. Pressouyre: Trap theory of hydrogen embrittlement, Acta Metall. 28, 895–911 (1980)
[Pyun1989] S.I. Pyun, R.A. Oriani. “The permeation of hydrogen through the passivating films on iron and nickel”, *Corrosion Science* **29** (1989), pp. 485-496.
[Philibert1991] J. Philibert, Atom Movements – Diffusion and mass transport in solids, Les editions de Physique, Les Uilis, 1991.
[Palumbo1990a] G. Palumbo and K.T. Aust, Acta Metall. Mater. **38** (11), 2343-2352 (1990a).
[Palumbo1990b] G. Palumbo, S. J. Thorper et K. T. Aust, Scr. Metall., 24 (1990) 1347-1350.

- [**Plimpton1995**] S.J. Plimpton, Fast parallel algorithms for short-range molecular dynamics, *J. Computat. Phys.* 117 (1995), pp. 1–19
- [**Poulat2000**] S. Poulat, J. Thibault, L. Priester, *Interface Science* 8, 5 (2000)
- [**Pedersen2009**] A. Pedersen *et al.* 2009 *New J. Phys.* 11 073034
- [**Priester2006**] L. Priester, *Les joint de grains : de la th éorie à l'ing énierie*, EDP Sciences ed. (2006).
- [**Pezold2011**] J.V. Pezold *et al.*; *Acta Materialia* 59 (2011) 2969–2980
- [**Priester2013**] L. Priester, *Grain Boundaries-From Theory to Engineering*-Springer Netherlands (2013)

R

- [**Read1950**] W.T. Read and W. Shockley, *Phys. Rev.* 78 (3), 275-289 (1950).
- [**Ransley1955**] C. E. Ransley, D. E. J. Tablot, *Z. Metallkde*, 46 (1935) 328.
- [**Ryabchikov1964**] L. M. Ryabchikov, *Ukr. Fiz. Zh*, 9 (1964) 303.
- [**Robertson1973**] W. M. Robertson, *Z. Metallkde*, Bd 64 (1973) H.6.
- [**Robertson1998**] I. M. Robertson, D. Teter: *J. Microsc. Res. Tech.* 42, 260 (1998)
- [**Randle1999**] V. Randle and P. Davies, *Interface Science* 7 (1), 5-13 (1999).
- [**Robertson2001**] I. M. Robertson: *Engineering Fracture Mechanics* 68, 671–692 (2001)
- [**Reed-Hill2009**] Reza Abbaschian, Robert E. Reed-Hill, *Physical metallurgy principles fourth edition*, (2009)
- [**Robertson2014**] I.M. Robertson *et al.* *Current Opinion in Solid State and Materials Science* 18 (2014) 227–243
- [**Rohrer2015**] S. Rohrer *et al.*; *Acta Materialia* 88 (2015) 346–354

S

- [**Sieverts1911**] A. Seiverts, *Z. Phys. Chim*, 77 (1911) 591.
- [**Sieverts1929**] A. Seiverts, *Z. Metallkde*, 21 (1929) 37.
- [**Smittenberg1934**] J. Smittenberg, *Rec. Trav. Chim, Pays-Bas*, 53 (1934) 1065.
- [**Smoluchowski1952**] R. Smoluchowski, *Phys. Rsv.* 87 (1952) 482.
- [**Suzuoka1961**] T. Suzuoka, *T. Jpn. I. Met.* 2 (1), 25-32 (1961)
- [**Schenck1966**] H. Schenck, K. W. Lange, *Arch. Eisenhüttenwes*, 37 (1966) 809.
- [**Schenck1966**] H. Schenck, K. W. Lange, *Z. Metallkde*, 57 (1966) 378.
- [**Scherrer1967**] S. Scherrer, G. Lozes, B. Deviot, *C. R. Acad. Sci*, 264 B (1967) 1499.
- [**Sosnowska1971**] I. Sosnowska *et al.* *VOr. UME* 27, NUMBER 2 *PHYSICAL REVIEW LETTERS* (1971)

- [**Stafford1974**] S.W.Stafford, R.B.McLellan; *Acta Metal.* vol. 22, (1974)
- [**Siegel1978**] R.W. Siegel, *J. Nucl. Mater.* 69/70, 117 (1978).
- [**Schaefer1987**] H.-E. Schaefer *et al.* *Sci. Forum* 15–18, 111 (1987)
- [**Sofronis1995**] P. Sofronis et H. K. Birnbaum, *J. Mech. Phys. Solids*, 43 (1995) 49-90.
- [**Sutton1995**] A.P. Sutton and R.W. Balluffi, *Interfaces in Crystalline Materials* (Clarendon Press, Oxford, 1995).
- [**Sepa2001**] D Sepa *et al.* ; *Journal of Electroanalytical Chemistry*, Volume 512, Issues 1–2, 5 October 2001, Pages 16-26
- [**Sofronis2001**] P. Sofronis, Y. liang et N. Aravas, *Eur. J. Mech. A/Solids*, 20 (2001) 857-872.
- [**Suzuki 2003**] A. Suzuki and Y. Mishin, *Interface Science* **11** (1), 131-148 (2003).
- [**Sahal2006**] M. Sahal, Influence d'une pr éd éformation plastique sur la r éactivit é anodique du nickel polycristallin dans le milieu acide sulfurique, PhD These, Université de La Rochelle.
- [**Song2011**] J. Song and W.A. Curtin; *Acta Materialia* 59 (2011) 1557–1569
- [**Solanki2012**] K.N.Solanki *et al.*; *metallurgical and materials transactions A* volume 44a, (2013),1365
- [**Shen2014**] X.J Shen, Tanguy, Dome and Connetable, Damien; (2014) *Philosophical Magazine*, vol. 94 (n °20). pp. 2247-2261. ISSN 1478-643
- [**Seidman2015**] Yoon-Jun Kim, D.N. Seidman, *Microsc. Microanal.* 21, 535–543, (2015)
- [**Song2016**] J.Song *et al.* *Physical review letters*; PRL 116, 075502 (2016)
- [**Scully2017**] J.R. Scully and K. Lutton; *Reference Module in Chemistry, Molecular Sciences and Chemical Engineering*, 2017

T

- [**Troiano1960**] A. Troiano: The role of hydrogen and other interstitials in the mechanical behavior of metals, *Trans. ASM* 52, 54–80 (1960)
- [**Tanabe1986**] T. Tanabe, K. Sawada et S. Imoto, *Trans. Jpn. Inst. Met.*, 27 (1986) 321-327.
- [**Tseng1988**] D. Tseng, Q. Y. Long et K. Tangri, *Scr. Metall.*, 22 (1988).
- [**Teter2001**] D. F. Teter, I. M. Robertson, H. K. Birnbaum; *Acta Mater.* 49, 4313–4323 (2001)
- [**Tavares2002**] S.S.M Tavares *et al.*; *Journal of Alloys and Compounds* 347 (2002) 105–109
- [**Tateyama2003**] Y. Tateyama, T. Ohno; *Physical Review B* 67, 174105 (2003)
- [**Tal-Gutelmacher2004**] E. Tal-Gutelmacher and D. Eliezer; *Materials Transactions*, Vol. 45, No. 5 (2004) pp. 1594 to 1600
- [**Tschopp2007**] M.A.Tschopp and D.L.Mcdowell; (2007) *Philosophical Magazine*, Vol. 87, No. 25, 3871–3892
- [**Toshihiko2008**] M.Toshihiko, D.Yusuke, N.Akihiro, *Journal of the society of materials science, Japan*, Vol. 57, No. 8, pp. 774-779, (2008).
- [**Takai2008**] K. Takai, H. Shoda, H. Suzuki and M. Nagumo, *Acta Mater.* 56 (18), 5158-5167 (2008).

[Thompson2009] A. Thompson, S. J. Plimpton, W. Mattson, *J Chem Phys*, 131, 154107 (2009)

[Tschopp2012] M.A. Tschopp *et al.*, *Physical Review B* 85, 064108 (2012)

V

[Vökl1975] J. Vökl et G. Alefeld. *Diffusion in Solids*. A. S. Nowickel al. New York, Academic Press (1975) 231-302.

[Vehoff1997] H. Vehoff: *Hydrogen in Metals III* (Springer Berlin / Heidelberg 1997) Chap. Hydrogen related material problem, pp. 215–274

W

[Whipple1954] R.T.P. Whipple, *Philos. Mag. Series 7* 45 (371), 1225-1236 (1954).

[Wriedt1970] H. A. Wriedt, R. A. Oriani, *Acta Metall.* 18, 753–760 (1970)

[Wayman1989] M.L. Wayman, G.C. Weatherly; *Bulletin of Alloy Phase Diagrams* Vol. 10 No. 5 (1989) 579

[Wolf1990] D. Wolf, *J. Mater. Res.* 5, 1708 (1990)

[Wolf1991] U. Wolf *et al.*; *Mat. Res. Soc. Symp. Proc.* Vol. 238. 1991

[Wipf1997] H. Wipf, in *Hydrogen in Metals III*, (Springer, 1997), pp. 51-91.

[Watanabe1994] T. Watanabe, *Mater. Sci. Eng. A* 176 (1-2), 39-49 (1994).

[Wimmer2006] E. Wimmer *et al.*, Temperature-dependent diffusion coefficients from ab initio computations: Hydrogen in nickel, LM-06K021, (2006).

Y

[Yoshioki1976] S. Yoshioki. *J. Phys. F. Metal Phys.* 6, 957–963 (1976).

[Young1978] F.W. Young, *J. Nucl. Mater.* 69/70, 310 (1978).

[Yao1991a] J. Yao, J.R. Cahoon. *Acta Metall. Mater.* 39, 111–118 (1991).

[Yao1991b] J. Yao, J.R. Cahoon. *Acta Metall. Mater* 39 (1991), pp. 119-126.

[Yang2005] F.Q. Yang; Interaction between diffusion and chemical stresses. *Mater. Sci. Eng., A*. 409, 153–159 (2005).

[Yazdipour2012] N. Yazdipour *et al.*; *Comput. Mater. Sci.*, 56 (2012) 49-57

Z

[Zhang2000] W.S. Zhang, X.W.Zhang, Z.L. Zhang, J. Alloys Compd. 302 (2000) 258–260

[Zakroczymski2006] T. Zakroczymski, Electrochim. Acta, 51 (2006) 2261-2266.

[Zhevnenko2011] S.N. Zhevnenko *et al.*; J Mater Sci (2011);46:4248.

[Zhu2017] Zhu *et al.* npj Computational Materials 3, 28, 2017

Apport de l'ingénierie du joint de grain dans la problématique de la fragilisation par l'hydrogène de nature inter-granulaire

Résumé:

La mobilité de l'hydrogène dans les métaux est un paramètre clef pour la compréhension des mécanismes de base de la fragilisation par l'hydrogène (FPH). Cette problématique est directement associée aux mécanismes de diffusion et de piégeage de l'hydrogène au sein d'un réseau cristallin. Ces derniers dépendent des diverses hétérogénéités microstructurales et en particuliers des défauts cristallins présent au sein du matériau. Dans le cadre de nos travaux nous nous sommes restreint à étudier la diffusion et le piégeage de l'hydrogène au sein de deux systèmes élémentaires : des monocristaux et des bi-cristaux de nickel. Nous avons développé une méthodologie associant des outils expérimentaux (Perméation électrochimique/TDS, METHR, EBSD) et numériques (FEM-COMSOL/EAM-LAMMPS). Les résultats obtenus sur monocristaux montrent une dépendance du coefficient de diffusion de l'hydrogène avec l'orientation cristallographique et la teneur en hydrogène. L'analyse thermodynamique du système nickel-hydrogène-lacune démontre une dépendance du potentiel chimique de l'hydrogène à l'état de contrainte induit par la formation d'amas de lacunes associés à la présence de l'hydrogène. Le caractère anisotrope de la diffusion est alors expliqué par l'anisotropie des propriétés d'élasticité du réseau cristallin et la présence de ces amas. D'autre part nous avons caractérisés les processus de diffusion et de piégeage de l'hydrogène pour des bicristaux de nickel présentant différents volumes libres. L'énergie de ségrégation de l'hydrogène dépend de la nature du site (volume libre locale et énergie mécanique associée à l'incorporation du soluté). La diffusion de l'hydrogène est influencée directement par la nature de joint de grain (excès de volume et distribution des sites). Nos résultats, à l'échelle atomique, montrent une corrélation entre la solubilité et le volume libre du joint de grain. Les joints de grains avec un volume libre important présentent des chemins de diffusion plus favorable pour hydrogène que dans le réseau cristallin et en dans le même temps un nombre plus important de sites de ségrégation.

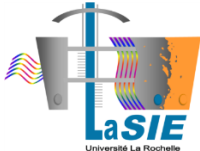
Mots clés : Diffusion anisotrope, joints de grains, hydrogène, nickel, lacunes, contraintes.

Contribution of the grain boundary engineering in the problem of intergranular hydrogen embrittlement

Abstract:

The mobility of hydrogen in metals is a key parameter for understanding the basic mechanisms of hydrogen embrittlement (HE). This problem is directly related to the mechanisms of diffusion and trapping of hydrogen within a crystal lattice. These mechanisms depend on the various microstructural heterogeneities and in particular the crystalline defects. In our work, we have focused on the diffusion and trapping of hydrogen in two elementary systems: nickel single crystals and bi-crystals. We developed a methodology combining experimental tools (electrochemical permeation / TDS, HRTEM, EBSD) and numerical methods (FEM-COMSOL / EAM-LAMMPS). The results obtained on the single crystals show a dependence of the diffusion coefficient of hydrogen with the crystallographic orientation and the hydrogen content. The thermodynamic analysis of the nickel-hydrogen-vacancy system shows a dependence of the chemical potential of hydrogen with the stress state induced by the formation of clusters of vacancies associated with the presence of hydrogen. The anisotropic character of the diffusion is then explained by the anisotropy of the elastic properties of the crystal lattice and the presence of these clusters. Moreover, we have characterized the processes of diffusion and trapping of hydrogen for nickel bi-crystals with different free volumes. The segregation energy of hydrogen depends on the nature of the site (the local free volume and the mechanical energy associated with the incorporation of solute). The diffusion of hydrogen is directly influenced by the nature of the grain boundary (the free volume and the distribution of the segregation sites). Our results, at the atomic scale, show a correlation between the solubility and the free volume of the grain boundary. The grain boundaries with a higher free volume have more favorable diffusion paths for hydrogen than in the crystal lattice and at the same time more segregation sites.

Keywords: Anisotropic diffusion, grain boundaries, hydrogen, nickel, vacancies, stress.

| | | |
|---|---|---|
|  | <p>Laboratoire des Sciences de l'Ingénieur pour l'Environnement UMR-CNRS 7356 Bat. Marie-Curie, av. Michel Crépeau 17042 LA ROCHELLE CEDEX</p> |  |
|---|---|---|